Universitat de València
DEPARTAMENT DE FÍSICA ATÒMICA
MOLECULAR I NUCLEAR

Optics Studies and Performance Optimization for a Future Linear Collider: Final Focus System for the e^-e^- Option (ILC) and Damping Ring Extraction Line (ATF)

TESIS DOCTORAL

María del Carmen Alabau Pons

Febrero de 2010

Dra. ANGELES FAUS GOLFE, Científico Titular del Consejo Superior de Investigaciones Científicas (CSIC),
Dr. PHILIP BAMBADE, investigador en el Laboratoire de l'Accélérateur Linéaire (Université Paris-Sud IN2P3/CNRS),

CERTIFICAN:

Que la presente memoria *Optics Studies and Performance Optimization for a Future Linear Collider: Final Focus System for the e^-e^- Option (ILC) and Damping Ring Extraction Line (ATF)* ha sido realizada bajo nuestra dirección en el Departamento de Física Atómica Molecular y Nuclear de la Universidad de Valencia por Dña. María del Carmen Alabau Pons y constituye su Tesis para optar al Grado de Doctor en Física.

Y para que así conste, firmamos el presente Certificado.

Fdo: Angeles Faus Golfe

Fdo: Philip Bambade

A la memoria de Jesús Alabau

Acknowledgements

I would like to thank the *Instituto de Física Corpuscular (IFIC)-CSIC-Universitat de València* and the *Laboratoire de l'Accélérateur Linéaire (LAL)* for giving me the opportunity to make this work in the field of accelerator physics and for the financial support.

In particular I want to sincerely acknowledge Dr. Angeles Faus-Golfe and Dr. Philip Bambade for their support, supervision and for making this work possible.

I would like to thank Dr. Daniel Schulte and Dr. Andrea Latina for the interesting and fruitful collaboration in the realistic simulations including dynamic imperfections in the ILC BDS.

Many thanks to my colleagues Dr. Javier Resta, Dr. Manqi Ruan, Dr. Olivier Dadoun, Dr. Cécile Rimbault, Dr. Julien Brossard and Yves Renier for their support and for being always willing to help on anything.

I want also to thank the whole ILC group at *LAL* for their hospitality.

I truly want to thank François Touze and Guy le Meur for all the work concering the modeling of the ATF magnets, and for the willingness they always have.

I would like to thank the entire ATF and ATF2 group at KEK for the support and for making possible the experiments, in particular thanks to Prof. Junji Urakawa, Prof. Toshiaki Tauchi, Dr. Nobuhiro Terunuma, Dr. Kiyoshi Kubo, Dr. Toshiyuki Okugi and Dr. Takashi Naito. I particular, I want to express my gratitude to Dr. Shigeru Kuroda for his enormous help and patience during all the experiments.

Thanks to the SLAC group who installed the OTR monitor in the Extraction Line of ATF, particularly to Douglas McCormick always willing to help us in the operation and realignment of the instrument.

I would like to aknowledge Mark Woodley for the enormous help during the experiments, for providing very useful tools for the modeling of the accelerator and his always willingness.

Thanks to Dr. Robert Appleby, Dr. James Jones and Anthony Scarfe for the collaboration during the experiments.

I would like to thank Dr. Frank Zimmermann, Dr. Rogelio Tomás, Prof. Philip Burrows, Dr. Juan Fuster and Prof. Toshiaki Tauchi for their fruitfull comments to my work and for reading the manuscript.

I want to thank all my colleagues and friends at IFIC for their support, specially to Juan José García for sharing the office with me and being always ready to help on anything.

I want to sincerely thank Vicent for encouraging me to start this work and for his support.

I would like to thank my family, specially my parents, for being always there, with inconditional support.

Finally, with affection, special thanks to Sergio for the enormous support and patience.

Contents

Resumen

Introducción

Los aceleradores de partículas han jugado un papel crucial desde principios del siglo pasado en la comprensión de los componenetes elementales de la materia y las interacciones entre ellos. Adentrarse en el estudio del mundo subatómico a escalas cada vez menores requiere aceleradores que operen a mayores energías. El gran colisionador llamado *Large Hadron Collider* (LHC), que operará en la *European Organization for Nuclear Research* (CERN) a partir de 2009, proporcionará colisiones de protones con energías en el centro de masas de 14 TeV [1]. Con la creación de partículas que se produce a tan altas energías se pretende estudiar la física más allá del Modelo Estándar de las partículas elementales, y dar respuesta a cuestiones como la existencia del bosón de Higgs, la existencia de partículas supersimétricas, o explicar el origen de la gran diferencia de masa entre las partículas elementales, o la naturaleza de la materia oscura.

Existe consenso general en la comunidad de física de partículas en que un colisionador electrón-positrón (e^+e^-) sería el siguiente paso para complementar los estudios del LHC. Las colisiones e^+e^- proporcionan un ambiente experimental más limpio, permitiendo medidas más precisas que en el caso de colisiones protón-protón, ya que la colisión se produce entre partículas elementales puntuales [2, 3]. Además, hay un claro acuerdo sobre que dicho futuro colisionador sería lineal, ya que los colisionadores e^+e^- están limitados en energía debido a la emisión de radiación sincrotrón por parte de las partículas relativistas en las trayectorias curvilíneas.

Los mayores retos en la construcción de dicho futuro colisiondador e^+e^-, son las altas energías que se deben alcanzar en una máquina en la que el haz pasa una sola vez, a diferencia de los colisionadores circulares, y las pequeñas emitancias y dimensiones del haz requeridas en el punto de interacción para alcanzar luminosidades del orden de 10^{34}-10^{35} $\mathrm{cm}^{-2}\mathrm{s}^{-1}$.

Durante las ltimas décadas se ha investigado en dos grandes proyectos para la construcción de un futuro colisionador lineal cuya diferencia más importante es la tecnología utilizada para la aceleración del haz de partículas: el *International Linear Collider* (ILC) [2] y el *Compact Linear Collider* (CLIC) [4].

El diseño del CLIC, que se está desarrollando en el CERN, está basado en cavidades aceleradoras construídas con un material conductor normal (no superconductor), que operan a frecuencias de 12 GHz y que requieren enormes campos eléctricos de 100 MV/m para acelerar haces a energías de 3 TeV en el punto de interacción, limitando la longitud total del acelerador a unos 48 km. Se está desarrollando una nueva tecnología para alcanzar estos enormes gradientes del campo eléctrico, basada en un diseño de aceleración de dos haces, en el cual el haz principal se acelera gracias a la energía suministrada durante el frenado de un haz secundario. En el CERN se está construyendo un prototipo para

probar la viabilidad de esta innovadora técnica de aceleración [5].

El proyecto del ILC, desarrollado como fruto de una colaboración internacional, proporcionaría haces e^+e^- con una energía en el centro de masas de 500 GeV (con posibilidad de aumentar a 1 TeV). El diseño está basado en cavidades aceleradoras superconductoras de radiofrecuencia, que operarían a 1.3 GeV, con un gradiente medio del campo eléctrico de 31.5 MV/m y una longitud total de 31 km.

Además de colisiones e^+e^-, en el ILC se consideran otras opciones de colisión, como electrón-fotón ($e^-\gamma$), fotón-fotón ($\gamma\gamma$) y electrón-electrón (e^-e^-). Las colisiones e^-e^- permiten una alta polarización para ambos haces, y ofrecen algunos canales interesantes para la física, como por ejemplo, estudios de super-simetría, proporcionando un medio ideal para medidas de la masa umbral de producción de s-electrones [13, 16].

A pesar de que para proporcionar colisiones e^-e^- no se requieren grandes cambios en el acelerador o el detector, la optimización del diseño y de los parámetros del haz en el punto de interacción se ha realizado para las colisiones e^+e^-, y se puede presentar un deterioro en el funcionamiento en modo e^-e^-. En la primera parte de esta tesis se ha realizado un estudio de las principales diferencias entre ambas colisiones, para evaluar la viabilidad de adaptación y optimizar el sistema de focalización final o *Final Focus System* (FFS) para colisiones e^-e^-.

Para alcanzar la alta luminosidad requerida en un futuro colisionador lineal con un consumo eléctrico aceptable, se deben crear haces muy intensos (del orden de 2×10^{10} partículas por paquete) con emitancias muy pequeñas (del orden de 0.04 pm·rad), que deben preservarse a lo largo del acelerador, y los haces deben focalizarse fuertemente hasta alcanzar dimensiones verticales en el punto de interacción del orden del nanómetro. Esto requerirá especificaciones sin precedentes en cuanto a alineamiento y estabilización del FFS, para mantener los haces en colisión en el punto de interacción con tolerancias del orden de medio nanómetro. Se han construido numerosas instalaciones y aceleradores en las últimas décadas para ahondar en el estudio de las especificaciones requeridas en los diferentes sub-sistemas del *Beam Delivery System*, como el FFS [23, 25].

En 1996 se completó la construcción en KEK, Japón, de la llamada *Accelerator Test Facility* (ATF), un anillo de amortiguamiento o *Damping Ring* (DR), construido para conseguir haces con emitancias extremadamente pequeñas requeridos en un futuro colisionador lineal [6]. En la actualidad, estos haces son inyectados en la *Accelerator Test Faciliy 2* (ATF2), completada en 2008 como fruto de una colaboración internacional, que es un prototipo de FFS a menor escala que el diseñado para el ILC para focalizar los haces hasta dimensiones verticales de 37 nm, y que utiliza el mismo sistema de corrección local de la cromaticidad prevista en el ILC o CLIC [8]. En el DR de ATF se han alcanzado emitancias del orden de 6 pm·rad a 1.3 GeV [7], pero la emitancia alcanza valores anómalamente grandes después de la extracción del DR, en la línea que transporta el haz a ATF2 [9, 11]. En las segunda parte de esta tesis se ha realizado un estudio de la preservación de la emitancia a lo largo de esta línea de extracción, así como de la no linealidad del campo magnético en los imanes implicados en la extracción que pueden causar dicho aumento de la emitancia.

Estudios de la óptica y optimización del sistema de focalización para la opción e^-e^- en el ILC

Se ha llevado a cabo un estudio de las principales diferencias entre la colisión e^+e^- y e^-e^- para evaluar la viabilidad de adaptación y optimizar el sistema de focalización final para el modo de operación e^-e^-.

Efectos de la interacción haz-haz

Una de les diferncies importantes entre ambas colisiones es debida a la interacción de las partículas de un haz con el campo electromagnético del haz opuesto. En el caso de colisiones e^+e^- se produce una focalización mutua entre los haces, produciendo un aumento de la luminosidad [39]. En cambio, en las colisiones e^-e^- la repulsión entre los haces aumenta las dimensiones transversales efectivas de éstos, disminuyendo la luminosidad pico, que es aproximadamente el 20% de la luminosidad obtenida en colisiones e^+e^-. Además, en este caso la luminosidad es mucho más sensible a desplazamientos residuales en el punto de interacción que en el caso de colisiones e^+e^-.

Cuando los haces se encuentran en el punto de interacción con un desplazamiento relativo entre ellos, hay una fuerza electromagnética neta que produce una deflexión de la trayectoria de ambos [44]. Esta deflexión es importante cuando el desplazamiento es vertical, debido a la forma plana de los haces, siendo la dimensión vertical del orden de 100 veces menor que la horizontal [43]. Para desplazamientos relativamente pequeños, la relación entre éstos y la deflexión producida es lineal, y su valor se utiliza como señal principal para mantener los haces alineados en el punto de interacción a niveles de medio nanómetro. Los ángulos después de la colisión, cuyos valores típicos pueden alcanzar unos 150 μrad, se obtienen midiendo las posiciones de los haces unos pocos metros más allá del punto de interacción. Esta información es utilizada en un sistema de corrección por retroalimentación para corregir la posición relativa en el punto de interacción de los siguientes paquetes [56].

Una característica importante de las colisiones e^-e^- es que la pendiente de esta curva de deflexión en función del desplazamiento inicial es mucho más grande que en el caso de colisiones e^+e^-, lo que podría influir en el funcionamiento del sistema de corrección por retroalimentación o *feedback*.

Simulación simplificada del sistema de alineamiento

Se ha llevado a cabo un estudio del impacto en el funcionamiento del sistema de alineamiento por retroalimentación de esta curva de deflexión mucho más abrupta de las colisiones e^-e^-. De acuerdo con medidas del movimiento del suelo en diferentes emplazamientos, los desplazamientos entre los haces producidos al inicio de cada tren de paquetes en el ILC puede ser del orden de cientos de nanómetros, mientras que las amplitudes correspondientes a la frecuencia entre los paquetes son despreciables comparadas con el tamaño de éstos [54]. Se han realizado simulaciones simplificadas del sistema de corrección para ambas colisiones, teniendo en cuenta estos desplazamientos.

En el caso de colisiones e^-e^- la corrección de los desplazamientos al inicio de cada tren es más lenta que para el caso de colisiones e^+e^-, ya que la pendiente especificada que relaciona los ángulos de salida con la corrección aplicada al siguiente paquete es mayor para evitar la sobre-corrección de los desplazamientos pequeños entre los paquetes. A

pesar de esto, la corrección de los desplazamientos al inicio de cada tren se puede realizar en un número de paquetes correspondiente a una fracción despreciable del tren, por lo que la luminosidad media del tren no se ve afectada.

En cambio, para desplazamientos producidos por la vibración introducida entre sucesivos paquetes, del orden de fracciones de la dimensión del haz, la luminosidad en el caso de colisiones e^-e^- es aproximadamente la mitad que en el caso e^+e^-. Esta gran sensibilidad de la luminosidad incluso a desplazamientos muy pequeños entre los haces, es debida a la fuerte perturbación entre los haces durante la colisión.

Optimización de los parámetros del haz

La interacción entre los haces durante la colisión viene caracterizada por el parámetro de perturbación, conocido como *disruption parameter*, que se define como la relación entre la desviación típica de la dimensión longitudinal del haz y la distancia focal efectiva. Con el fin de disminuir la perturbación entre los haces, se ha realizado una optimización de los parámetros del haz, por medio de simulaciones que incluyen la interacción entre los haces durante la colisión. Se han obtenido diferentes conjuntos de parámetros disminuyendo la dimensión longitudinal del haz en factores en el intervalo 0.5-0.7, y optimizando las dimensiones transversales del haz de manera que se maximice la luminosidad limitando la energía perdida por *beamstrahlung* a aproximadamente 5%, ya que estos parámetros cumplen las especificaciones de los diferentes conjuntos de parámetros propuestos para el ILC.

Estos parámetros alternativos propuestos tienen una luminosidad pico mayor, con hasta un 40% de aumento comparado a la luminosidad con parámetros nominales para colisiones e^-e^-. Algunos de los conjuntos de parámetros propuestos también presentan menor sensibilidad a los desplazamientos entre los haces en el punto de interacción, por lo que la luminosidad media en un tren para diferentes amplitudes de desplazamientos entre los haces aumenta con estos parámetros, en comparación con los nominales.

Simulación del sistema de alineamiento incluyendo imperfecciones dinámicas

Se ha realizado una simulación más completa del sistema de alineamiento por retroalimentación para verificar que las amplitudes y la distribución del movimiento del suelo asumidas en la simulación simplificada son aceptables. Para ello, se ha incluido en la simulación un generador de movimiento del suelo basado en medidas experimentales, que incluye correlaciones espaciales y temporales.

Los elementos magnéticos a lo largo del sistema de focalización final se han desalineado para diferentes intervalos de tiempo sucesivos, y el haz se ha transportado a lo largo de la línea. En esta simulación, tanto la posición relativa de los haces en el punto de interacción como el ángulo con el que llegan a este putno es corregido paquete a paquete.

El desalineamiento de los imanes produce no sólo desplazamientos de los haces en el punto de interacción, sino que además aumenta el tamaño de los haces por efectos ópticos, disminuyendo así la luminosidad. Los resultados de la simulación indican que después de tan sólo un segundo, la luminosidad máxima que se puede recuperar es aproximadamente del 90%. Este pequeño deterioro es debido al aumento del tamaño del haz por efectos ópticos a lo largo de la línea. Este comportamiento es comun a las colisiones e^+e^- y e^-e^-. Después de aproximadamente 5 minutos, este deterioro es muy importante, siendo imposible recuperar más del 30-40% de la luminosidad. En este caso se necesitan otros

sistemas más lentos de alineamiento de la trayectoria así como de los propio imanes.

Estudios de la óptica del sistema

Se han realizado estudios de la óptica del sistema de focalización y de la línea de extracción con el fin de evaluar la capacidad de adaptación de éstos a los parámetros propuestos para el modo de operación e^-e^-. Los estudios se han realizado para ambas zonas de interacción, con ángulo de cruce pequeño (2 mrad) y grande (20 mrad) en el punto de interacción propuestas para el ILC en el momento de este estudio.

Para obtener las nuevas funciones betatrónicas en el punto de interacción, se debe modificar la desmagnificación del sistema de focalización. Pero ésto estropearía la compleja optimización llevada a cabo para minimizar las aberraciones cromáticas y geométricas del sistema, por lo que el cambio en la desmagnificación se realiza ultilizando cuadrupolos que se encuentran a la entrada del sistema de focalización y reajustando los sextupolos, y no por medio de los potentes cuadrupolos situados justo antes del punto de interacción, que son los responsables principales de la gran cromaticidad del sistema antes de aplicar las correcciones. Este método es viable con los parámetros propuestos, ya que están dentro del rango de parámetros especificados para el ILC.

Se han realizado estudios de la óptica de la línea de extracción y de la potencia perdida a lo largo de ésta con los parámetros propuestos para la colisión e^-e^-, obteniendo resultados comparables a los obtenidos para colisiones e^+e^- con los parámetros dentro del rango especificado para el ILC.

En el caso de 2 mrad de ángulo de cruce, la adaptación para las colisiones e^-e^- es más complicada. El haz después de la colisión atraviesa el último quadrupolo de la línea del haz incidente, y no lo hace centrado, por lo que sufre una desviación de la trayectoria que ayuda a extraer el haz. En el caso de colisiones e^-e^- este esquema sólo funciona si se invierten las polaridades de la última pareja de cuadrupolos y sextupolos. Los estudios preliminares indican que este esquema puede funcionar para el modo de operación e^-e^- sin modificar la magnitud de la fuerza de los quadrupolos, con tal de conservar la misma geometría para la extracción que en el caso e^+e^-, pero esto produce haces menos planos en el punto de interacción, lo que reduce considerablemente la luminosidad [61]. Esta pérdida de luminosidad se puede recuperar disminuyendo la dimensión longitudinal del haz, pero para obtener mejoras importantes se requeriría una reoptimización del sistema de focalización [26]. Esto no será necesario, ya que en 2007 se decidió que el ángulo de cruze para el ILC sería de 14 mrad, cuya geometría es muy similar a la de 20 mrad.

Efecto de las no linealidad del campo magnético sobre la emitancia en la línea de extracción de ATF

Mientras que las pequeñas emitancias verticales, del orden de 6 pm·rad, son consistentemente reproducidas en el DR de ATF, la emitancia vertical medida en la sección dedicada a diagnóstico del haz de la línea de extracción ha sido durante años aproximadamente un factor 3 mayor de lo esperado [9, 11]. Se ha realizado un estudio de una de las posibles causas de este anómalo aumento de la emitancia, como es la no linealidad del campo electromagnético de los imanes implicados en la extracción del haz.

El proceso de extracción del haz del DR se inicia por medio de un elemento magnético dipolar de tipo *kicker*, y a continuación el haz pasa nominalmente desplazado en la di-

rección horizontal respecto al centro del imán a través de dos quadrupolos centrados en el DR (QM6R y QM7R). Además, a continuación pasa a través de tres elementos magnéticos de tipo septum (BS1X, BS2X y BS3X), y pasa por el primero de estos muy cerca del borde del conductor por restricciones de la geometría, ya que este imán está situado muy cerca del DR, lo que podría significar que el campo presentara alguna perturbación en este punto. A partir de aquí, el DR y la línea de extracción continuan en canales separados completamente. Aunque la órbita en ATF es normalmente estable manteniéndose en niveles del orden de 100 μm, el haz podría tener un desplazamiento absoluto de la órbita de unos pocos milímetros, tanto en el plano horizontal como en el vertical después de la extracción. La no linealidad del campo magnético de los imanes, junto con los desplazamientos al pasar a través de éstos, podría causar un aumento significativo de la emitancia vertical.

Modelización de los imanes implicados en la extracción del haz

Con el ánimo de cuantificar el efecto de la no linealidad del campo electromagnético en el haz extraído, se ha llevado a cabo un estudio detallado del mapa del campo mangético para los imanes que intervienen en la extracción con el código PRIAM, utilizando la geometría y los parámetros explícitos para cada uno de dichos imanes [72].

Los mapas del campo magnético obtenidos se han ajustado mediante una función polinómica en el plano complejo para obtener así una representación continua en forma de expansión multipolar local alrededor del punto de extracción en cada elemento magnético.

La contribución más importante en cuanto a las no linealidades del campo electromagnético parece provenir del cuadrupolo QM7R. Dicha contribución en el caso del elemento QM6R es despreciable, como era de esperar, ya que el desplazamiento del haz respecto al centro del imán es muy pequeño, 0.65 cm, mientras que en el caso de QM7R este desplazamiento horizontal es de 2.25 cm, pasando el haz cerca del polo del imán. En el caso del septum BS1X, la contribución a la no linealidad obtenida es también despreciable, a pesar de que la órbita de referencia pasa cerca del conductor. En el caso de los septum BS2X y BS3X la órbita nominal pasa incluso más alejada del conductor que en el caso del septum BS1X, por lo que no hay indicios de que estos elementos presentaran no linealidades significativas.

Simulaciones incluyendo la no linealidad del campo magnético

Los cálculos analíticos del aumento de la emitancia del haz al pasar a través del cuadrupolo QM7R desplazado verticalmente por distancias pequeñas, del orden del milímetro, y teniendo en cuenta la componente sextupolar del campo electromagnético en el punto de extracción obtenido del mapa del campo, indican que el aumento en la emitancia vertical es importante, pudiendo llegar a incrementarse aproximadamente en un factor 3.

Para realizar un estudio más completo y estudiar el efecto de los órdenes superiores de la no linealidad, se han realizado simulaciones transportando un haz de partículas ideal a través de la línea de extracción, teniendo en cuenta las expansiones multipolares de los campos obtenidas [73].

Los resultados indican que el efecto principal en el aumento de la emitancia vertical viene del cuadrupolo QM7R, como era de esperar por los mapas del campo obtenidos. La no linealidad del campo en este imán sería despreciable si el haz pasara verticalmente

alineado por el centro, pero causa un aumento importante en la emitancia, de aproximadamente un factor 3 cuando pasa desplazado aproximadamente un milímetro. La magnitude de este aumento también varía con la trayectoria horizontal, aumentando o disminuyendo dependiendo de si la trayectoria del haz extraído se aleja o se acerca al centro del quadrupolo. Este aumento de la emitancia puede ser reducido en un factor aproximadamente 2 para 2 mm de desplazamiento horizontal hacia el centro del imán.

Medidas experimentales

Para completar los estudios analíticos y las simulaciones, se ha llevado a cabo un programa experimental en ATF para estudiar la dependencia del aumento de la emitancia con la trayectoria del haz extraído [74].

Con el objetivo de estudiar la emitancia para diferentes trayectorias del haz en el canal de extracción, se ha modificado la trayectoria por medio de kickers en la zona de extracción, anulando a continuación la modificación en el DR para no producir perturbaciones en el haz en el anillo.

En la sección de diagnóstico de la línea de extracción hay cinco instrumentos para la medida del tamaño transversal del haz, del tipo *wire scanner*, para permitir medidas de la emitancia. Pero en el momento de este estudio, no fué posible conseguir un avance de fase de la función betatrónica entre los diferentes instrumentos adecuado para realizar dichas medidas de una manera fiable, por lo que se tuvo que utilizar un método alternativo para el diagnóstico. Éste consistía en la medida del tamaño vertical del haz con un monitor de radiación óptica de transición u *Optical Transition Radiation* (OTR), situado justo después de la extracción, a continuación de los septum. A partir de la medida de la talla y de la función betatrónica obtenida a través de un modelo de la óptica del acelerador, se infiere la emitancia vertical en esta posición para las diferentes trayectorias del haz extraído. En paralelo se realizaron medidas de la talla del haz en el DR, por medio de un monitor de radiación sincrotrón de rayos-X, para las diferentes trayectorias con el objetivo de poder discernir entre alteraciones del haz debidas al cambio de trayectoria en la extracción de las variaciones propias producidas en el DR.

Los resultados de dos de los experimentos, realizados en diciembre de 2007 y a finales de mayo de 2008, muestran que el aumento de la emitancia después de la extracción es claramente visible. Sin embargo este aumento es menor que el predicho por las simulaciones considerando un haz pasando a través del cuadrupolo QM7R con la trayectoria horizontal nominal. Las medidas pueden ser reproducidas por la simulación asumiendo desplazamientos horizontales de la trayectoria de unos pocos milímetros (1.6 y 2.7 mm en diciembre y mayo, respectivamente), pasando el haz más cerca del centro del cuadrupolo, donde se reduce la no linealidad del campo. Con la instrumentación disponible en 2007 y 2008 en la línea de extracción no era posible monitorizar la posición del haz en posiciones cercanas al cuadrupolo QM7R o los septums. Sin embargo, el procedimiento de puesta en marcha y ajuste del DR está basado principalmente en la maximización de la eficiencia de transmisión, por lo que los desplazamientos durante cada periodo de toma de medidas podrían ser diferentes. Para verificar los resultados obtenidos, hubiera sido muy útil la realización del experimento con desplazamientos horizontales de la órbita de extracción, pero desafortunadamente no se dispuso del suficiente tiempo con haz para realizar dichas medidas.

Las medidas realizadas en otras tres ocasiones, en marzo y en la primera mitad de mayo de 2008, muestran valores del tamaño del haz después de la extracción anormal-

mente grandes (con un factor de aumento de aproximadamente 3), incluso antes de producir ninguna perturbación en la trayectoria. Además, el tamaño del haz variaba significativamente en el DR, lo que puede indicar que la perturbación en la región de extracción estaba afectando al haz almacenado. Por estas razones, es muy difícil obtener conclusiones a partir de los resultados de estos experimentos. Estos haces anormalmente grandes podrían deberse a una dispersión anómala en la región de extracción. Tampoco se pueden excluir otros efectos derivados de desplazamientos en el canal de extracción incluso mayores de los considerados.

Después de los experimentos descritos en esta tesis, la línea de extracción de ATF ha sido reconfigurada y parcialmente reconstruida para conducir el haz a la línea de focalización final, ATF2. Algunas de las mejoras en este nuevo diseño son la reducción de la dispersión en la región de extracción, y la optimización de la línea de manera que se pueden obtener avances de fase adecuados entre los intrumentos de medida en la sección de diagnóstico para permitir las medidas de emitancia. Además, el cuadrupolo QM7R ha sido reemplazado por otro similar pero con apertura mayor para el que las medidas y las simulaciones indican que la no linealidad del campo magnético en la posición del haz extraído es despreciable.

Conclusiones

Uno de los retos más importantes en el diseño y operación de un futuro colisionador lineal de leptones es alcanzar las pequeñas dimensiones y emitancias del haz necesarias para conseguir la gran luminosidad requerida para los experimentos. Esto supone tolerancias sin precedentes en cuanto a la estabilización y el alineamiento tanto del acelerador como de los haces.

En el ILC los haces deben mantenerse en el punto de interacción con desplazamientos verticales relativos del orden del nanómentro. Un sistema de alineamiento rápido corrige las posiciones relativas de cada paquete con la información del paquete precedente, haciendo uso de la relación lineal entre el desplazamiento relativo de los haces al encontrarse en el punto de interacción y la desviación de la trayectoria producida por la interacción entre ambos.

En la primera parte de esta tesis se ha realizado un estudio del impacto en el funcionamiento del sistema de alineamiento de la gran pendiente de esta curva para el caso de colisiones e^-e^- comparado con las colisiones e^+e^-. Para ello se han realizado simulaciones tanto simplificadas como otras incluyendo un modelo de vibraciones dinámicas a lo largo del acelerador basado en medidas temporales y espaciales en un emplazamiento determinado.

Se ha observado que debido a esta pendiente más pronunciada de la curva, la corrección de la posición de los haces en las colisiones e^-e^- debe hacerse aproximadamente un factor 7 más lenta que en el caso e^+e^- para evitar sobrecorrección. Sin embargo esta corrección puede hacerse en un número de paquetes despreciable comparado con el número de paquetes por tren, por lo que no hay un impacto importante en la luminosidad media del tren.

A pesar de que esta pendiente tan acentuada no resulta ser un problema para el funcionamiento del sistema de alineamiento, la fuerte perturbación entre los haces produce una disminución importante de la luminosidad para desplazamientos verticales relativos entre los haces del orden de la fracción de la dimensión vertical del haz. Se han propuesto

unos parámetros alternativos a los nominales para el caso de colisiones e^-e^- reduciendo la dimensión longitudinal de los haces, de manera que disminuya la fuerte perturbación entre ambos, reduciendo así la sensibilidad de la luminosidad con los pequeños desplazamientos.

También se ha realizado un estudio de la óptica del FFS y de la línea de extracción, encontrando que éstos pueden adaptarse fácilmente a los parámetros propuestos, sin necesidad de reacer la complicada corrección de la cromaticidad en el FFS y sin tener que cambiar la geometŕia de la extracción.

En la segunda parte de la tesis se ha realizado un estudio de la preservación de la emitancia en ATF durante la extracción del haz del DR. La medida de la emitancia en la sección de diagnóstico situada inmediatamente después de la extracción ha sido durante años aproximadamente un factor 3 más grande que en el DR.

Se ha realizado un estudio de los campos magnéticos en los diferentes imanes implicados en la extracción del haz, para quantificar la no linealidad del campo magnético en la zona del haz extraído. Se ha encontrado una no linealidad importante en el quadrupolo QM7R, en el que el haz extraído pasa horizontalmente desplazado, y cerca de un polo.

Los resultados de simulaciones incluyendo esta no linealidad indican que sta puede causar un aumento en la emitancia vertical del orden de un factor 3 cuando el haz pasa desplazado verticalmente respecto al centro del imán. Además, las simulaciones indican que este factor de aumento es muy sensible a desplazamientos horizontales del haz. Aunque la órbita en ATF es normalmente estable manteniéndose en niveles del orden de 100 μm, el haz podría tener un desplazamiento absoluto de la órbita de unos pocos milímetros, tanto en el plano horizontal como en el vertical después de la extracción.

En el programa experimental llevado a cabo en ATF se ha observado un aumento de la emitancia al desplazar el haz verticalmente durante la extracción. Sin embargo este aumento es menor que el predicho por las simulaciones cuando el haz pasa horizontalmente por la posición nominal de extracción. Las medidas pueden ser reproducidas por la simulación asumiendo desplazamientos horizontales de la trayectoria de unos pocos milímetros (de entre 1.5 y 3 mm), pasando el haz más cerca del centro del cuadrupolo, donde se reduce la no linealidad del campo.

Los resultados de este estudio muestran que la estabilización de la órbita es crucial no sólo en el plano vertical sino también en el horizontal. Además hay indicios de que hay una anómala dispersión en la zona de extracción, lo que aumentaría los tamaños del haz.

En ATF se ha cambiado el cuadrupolo en cuestión por otro con mayor apertura para el que la no linealidad es despreciable en la zona del haz extraído. Sin embargo la estabilización del haz y la dispersión en la zona de extracción van a ser estudiadas en más detalle en ATF durante la puesta en marcha de ATF2.

Chapter 1

Introduction

Since the beginning of the last century, particle accelerators have revealed many secrets of matter and of the sub-atomic world, and human knowledge has arrived at the concept of the Standard Model of particle physics. But there is a missing particle in this model, the Higgs boson. Moreover, the search for physics beyond the Standard Model, for example super-symmetry, motivates new high-energy accelerators at even higher energies to solve questions not understood at present, as for instance the hierarchy of different mass scales in physics or the nature of dark matter.

The Large Hadron Collider (LHC), currently under commissioning, will operate at the European Organization for Nuclear Research (CERN) to find answers to many questions left open by the Standard Model. It will be the most powerful particle accelerator ever built when it starts operation in 2009, providing proton-proton collisions with a center-of-mass energy of 7 TeV initially to be increased to 14 TeV with a luminosity $\mathcal{L} \sim 10^{34}$ $\mathrm{cm}^{-2}\mathrm{s}^{-1}$ in the following years [1].

There is a general consensus among the particle physics community that an electron-positron (e^+e^-) collider would be the next step to complement the studies of the proton-proton (pp) collider. Electron-positron colliders provide a cleaner experimental environment and hence more precise measurements because the collision is produced between point-like elementary particles [2, 3].

Circular e^+e^- colliders are limited in energy by the synchrotron radiation emission in bending sections, so the next high-energy e^+e^- collider must be a linear collider.

The biggest challenges in the construction of such a linear collider, are the high beam energies that have to be reached in this single pass machine, and the small emittances and beam spot sizes required at the interaction point to achieve the required luminosities of the order of 10^{34}-10^{35} $\mathrm{cm}^{-2}\mathrm{s}^{-1}$.

Two big projects are presently under study for the construction of a future linear collider in the tera-electron-volt scale, to work in concert with the LHC: the International Linear Collider (ILC) [2] and the Compact Linear Collider (CLIC) [4].

The CLIC project, developed at CERN, is based on normal conducting travelling-wave accelerating structures, operating at a frequency of 12 GHz and with very high electric fields of 100 MV/m to keep the total length to about 48 km for a colliding beam energy of 3 TeV. To reach these high electric fields, an innovative technology based on a two-beam accelerator scheme has been proposed in which a second beam, the drive beam, is decelerated and supplies energy to the main accelerating beam. The 3^{rd} generation CLIC Test Facility (CTF3) is presently under construction at CERN to prove the feasibility of this new acceleration technology by 2010 [5].

The ILC project, developed as a fully international scientific project, would consist of two linear accelerators that face each other, with a center-of-mass energy of 500 GeV (upgradeable up to 1 TeV), based on 1.3 GHz Superconducting Radio-Frequency (SCRF) accelerating cavities, with an average accelerating gradient of 31.5 MV/m and a total length of about 31 km.

In order to achieve the required high luminosity with an acceptable electric power consumption, very intense beams ($\sim 2 \times 10^{10}$ particles per bunch) have to be strongly focused to nanometer scale transverse sizes at the interaction point (IP).

The Accelerator Test Facility (ATF) at KEK (Japan) is a Damping Ring (DR) built to demonstrate the small emittance beams needed for future linear colliders [6]. It has achieved world records for the normalized vertical emittance, with values as small as 3×10^{-8} m at 1.3 GeV [7]. ATF2 is a prototype final focus system, recently completed as a result of an international collaboration to study the feasibility of focusing and stabilizing the damped ATF beam down to the nanometer scale [8]. The ATF2 final focus system is a down-scaled version that uses the same principle of local chromaticity correction as the ILC and CLIC projects, which is detailed in Chapter 2.

In addition to e^+e^- collisions, alternative options are under consideration at the ILC, as the electron-photon (eγ), photon-photon ($\gamma\gamma$) and electron-electron (e^-e^-) collisions. In a Photon Collider (PC), electron beams are converted into photon beams by inverse Compton scattering off a laser. New and interesting physics measurements become accessible with the resulting beam collisions, as for example the study of Higgs boson production in the s-channel, s-leptons or QCD measurements [12].

Unlike for the PC, for the e^-e^- option there are no major changes required in the interaction region or the accelerator. The e^-e^- collisions allow large polarization for both beams, thus almost pure e_L,e_R initial states, and provide some interesting channels for physics [13, 14]. As an example, they offer a good discovery potential for states with exotic quantum numbers and for super-symmetry studies, providing in particular an ideal environment for s-electron threshold mass measurements. The unique quantum numbers of the e^-e^- initial state imply that production cross sections at threshold for identical s-electrons are proportional to β, the velocity of the produced s-electrons, hence rising much more sharply than in e^+e^- collisions, for which cross sections rise as β^3 [15]. In particular, the s-electron mass may be measured to a precision of 100 MeV with a total integrated luminosity of 1 fb^{-1} in e^-e^- collisions, while more than 100 fb^{-1} are needed in e^+e^- collisions for a similar precision [16]. On the other hand, threshold scans are sensitive to the luminosity spectrum, hence requiring careful optimization.

Although the e^-e^- option can be implemented without major changes in the accelerator, a study of the main differences between both e^+e^- and e^-e^- collisions is needed to assess the relative luminosity performance.

There are in particular important differences due to the beam-beam effects. The strong electromagnetic fields that the bunches experience during collisions cause a mutual focusing, called pinch effect, which enhances the luminosity in the case of e^+e^- collisions. The opposite is true for e^-e^- collisions, where the luminosity is reduced by mutual defocussing, or anti-pinching. But not only the peak luminosity is affected, the luminosity also drops rapidly with the vertical offsets between the bunches at the IP, hence increasing the sensitivity of e^-e^- collisions to such offsets.

With beam sizes in the nanometer scale, maintaining them aligned at the IP with a precision of the order of half a nanometer is important to maintain luminosity. A specific feedback system is designed with this aim, based on the dependence of the deflection

of the colliding beams with the IP offset. Beam-beam effects make this deflection curve steeper for the e^-e^- collision, which can make feedback correction more difficult.

In the first part of this thesis report a study of the luminosity performance for the e^-e^- option and an optimization of the beam parameters, taking into account the requirements for the beam-beam based feedback system, are presented.

The main components of the ILC design, and the main changes needed for the e^-e^- mode of operation are summarized in Chapter 2. The differences between the e^+e^- and e^-e^- collisions due to the beam-beam effects are shown in Chapter 3.

In Chapter 4, simplified as well as more realistic versions of the simulations used to study the feedback system at the IP are presented. The results obtained are used in the optimization of the beam parameters at the IP for the e^-e^- option.

Optics studies to achieve the desired parameters for the e^-e^- option and studies of the extraction line of the corresponding spent beam are presented in Chapter 5.

The second part of this thesis is dedicated to the study of the preservation of the small beam emittances reached at the ATF DR along the transport to the ATF2 final focus beamline. One of the main goals of ATF2 is the establishment of the hardware and beam handling technologies pertaining to achieving and measuring such small beams, reproducibly and in stabilized conditions. The nominal vertical beam size is specified to be 37 nm at the ATF2 final focus point [8]. For this, beams with the smallest vertical emittances must both be provided by the ATF DR and preserved throughout the different sections of the optical transport.

Since several years, the vertical beam emittance measured in the original Extraction Line (EXT line), that extracts the beam from the ATF DR, and which was reconfigured to transport the electron beam to the recently commissioned ATF2 final focus beam line, has been significantly larger than the emittance measured in the DR itself [9–11]. There are also indications that the emittance increases with beam intensity. This long-standing problem has motivated studies of possible sources for this anomalous emittance growth, as well as the study of the proper emittance measurement process and reconstruction, which are complicated and could induce some uncertainties in themselves. One possible contribution, that is studied in this thesis report, is the non-linearity of the magnetic fields in the extraction region experienced by the beam when passing off-axis through magnets centered in the DR, and shared by both the DR and the EXT line.

In order to quantify the effect on the emittance of the non-linearities in the magnets involved in the extraction, the computation of the magnetic field has been done from the geometry of these magnets. The obtained field maps have been fitted by a polynomial function in order to get a continuous representation. The results are shown in Chapter 6.

Tracking simulations have been carried out and indicate that these non-linear fields can produce a significant vertical emittance growth whilst passing displaced with respect to the reference trajectory. The orbit stabilization in ATF achieves levels of about 100 μm, but the beam orbit itself can arrive to the extraction region with displacements of a few mm, because of systematic orbit distortions in the DR. Such distortions can be expected from mechanical drifts between re-alignments and from known imbalances in the configuration of bending magnets, which are only partially corrected at present.

An experimental program has been performed in order to assess the results of the simulations and to study the correlation between the emittance growth and the orbit displacements during the beam extraction. Results from simulations and measurements are presented in Chapters 7 and 8, respectively.

Finally, some conclusions are drawn in Chapter 9.

Chapter 2

Towards a future linear collider: the ILC design

Searching for physics beyond the Standard Model requires a new generation of particle accelerators in the TeV center-of-mass energy scale. During the last decades, many R&D activities have been dedicated to the study of different technologies for a future linear collider which would complement the studies of the Large Hadron Collider at CERN. The design of the International Linear Collider (ILC), based on the superconducting acceleration technology, is presented, with special emphasis on the Beam Delivery System (BDS), on which this work is focused.

2.1 Linear colliders and test facilities

One way of probing physics beyond the Standard Model is the direct search and study of new particles produced in the TeV energy range. Particle physicists worldwide have reached a consensus that an e^+e^- collider will be needed to complement the results obtained at the LHC [17].

Circular e^+e^- colliders are limited in energy by the synchrotron radiation emission in bending sections, as the energy loss increases with the fourth power of the energy of the circulating beam. The highest centre-of-mass energy in e^+e^- collisions (209 GeV) was reached at the Large Electron Positron (LEP) collider at CERN. In this circular machine, each beam was loosing about 3% of its energy per turn, which had to be replaced by the Radio Frequency (RF) acceleration system. The biggest superconducting RF system built so far, which provided a total of 3640 MV per revolution, was just enough to keep the beam in LEP at its nominal energy. Thus, a future e^+e^- collider operating at an energy significantly above that of LEP, must be a linear collider.

The Stanford Linear Collider (SLC) at SLAC is the only linear collider built so far. It operated during more than ten years until 1998, delivering e^+e^- beams at approximately 45.6 GeV with a maximum luminosity of $3 \times 10^{30}\ cm^{-2}s^{-1}$. The SLC did not consist however, of two opposing machines, since it used a single linac to accelerate both electron and positron beams, then separating them at the linac exit and turning them around and bringing them into head-on collisions with the so-called “arc” transport lines. This scheme was possible for the SLC due to its small beam energy, but it is not feasible for beam energies of the order of hundreds of GeV.

The high center-of-mass energy together with the high luminosities required, are the

biggest challenges for a future linear collider. In such a single pass machine, very high electric fields are required to reach the high energies while keeping the length of the collider within reasonable limits, and such high fields can be achieved only in pulsed operation. In a circular machine the counter-rotating beams collide with a high repetition frequency, as for instance, 44 *kHz* in the case of LEP. In a linear collider, the repetition frequency would be typically 5-100 *Hz*, which means that to reach the high luminosity required with an acceptable power consumption, very intense beams have to be provided, with very small emittances and beam spot sizes at the Interaction Point (IP).

During the last decades there has been a very active research on the next generation of linear colliders, and to support the R&D activities several test facilities have been operated. A number of design proposals have been presented, where the primary variable is the design of the main linear accelerators, which in turn drives design variations in other systems, as damping rings, etc.

Any proposed technology for a future linear collider must achieve an acceptable high gradient and an acceptably high efficiency of conversion from AC power to beam power to minimize construction and operating costs. Different design concepts have been under investigation for several years. One, developed by the TESLA collaboration, is based on a low-frequency (1.3 *GHz*), long-pulse, superconducting RF system, with an average acceleration gradient of 23.4-35 MV/m [18]. The other, a result of joint research by the Japan Linear Collider and Next Linear Collider (JLC/NLC), is based on a high-frequency (11.4 GHz, short-pulse, normal conducting RF system, with an average acceleration gradient of $50 MV/m$ (loaded) [19, 20].

In 2004, the International Technology Recommendation Panel (ITRP) recommended the superconducting RF technology for the ILC, and it was endorsed by the International Committee for Future Accelerators (ICFA). Many institutes around the world involved in linear collider R&D united in a common effort to produce a global design for the ILC, which culminated with the publication in August 2007 of the ILC Reference Design Report [2]. The ILC is designed with a 200-500 *GeV* center-of-mass energy, with possibility to upgrade up to 1 TeV. The basic element of the accelerating technology is a nine-cell SCRF 1.3 *GHz* niobium cavity, with an acceleration gradient of 31.5 MV/m. Eight or nine cavities are mounted together in a string and assembled into a common low-temperature cryostat or cryomodule. This SCRF technology has been demonstrated in proof of principle, and some of these cryomodules are installed and operated at the Vacuum Ultra-Violet Free-Electron Laser (FLASH) facility in Hamburg [21], that was realized as an extension of the TESLA Test Facility (TTF). FLASH is a prototype of the future European X-Ray Laser (XFEL) presently under construction at DESY, where an electron beam will be accelerated by means of the TESLA technology up to about 18 *GeV* to create high brilliant ultrashort X-Ray flashes [22].

In parallel, during the last 25 years, another design concept for a future linear collider has been developed, with an innovative acceleration technique. The CLIC project, which was initiated at CERN, is based on normal conducting travelling-wave accelerating structures, operating at a frequency of 12 *GHz* and with very high gradients of 100 MV/m to keep the total length to about 48 *km* for a colliding beam energy of 3 *TeV* [4]. Such high fields require high peak RF power, of about 275 *MW* per active metre of accelerating structure. The use of individual RF power sources, such as klystrons, to provide such a high peak RF power is not really possible, and hence a novel power source has been developed. This innovative technique consists on a two-beam accelerator scheme in which a second beam, the drive beam, is decelerated and supplies energy to the main

accelerating beam. To transfer the energy to the main beam, the drive beam passes trough novel Power Extraction and Transfer Structures (PETS), where it excites strong electromagnetic oscillations, i.e. the beam looses its kinetic energy to electromagnetic energy. This RF energy is extracted from the PETS and sent via waveguides to the accelerating structures in the parallel main beam. The PETS are travelling-wave structures like the accelerating structures for the main beam, but with different parameters. The 3^{rd} generation CLIC Test Facility (CTF3) is presently under construction at CERN to demonstrate the generation scheme for the CLIC drive beam by 2010 [5]. CTF3 consists of a 150 MeV electron linac, followed by a series of two rings, the delay loop and the combiner ring. This part of CTF3 is a scaled-down version of the complex required to generate the CLIC drive beam. It will demonstrate the principle of the novel bunch-interleaving technique using RF deflectors to produce the compressed drive-beam pulses. The compressed beam, of 32 A of beam current, a bunch repetition frequency of 12 GHz and a pulse length of 140 ns, is then sent to the CLIC Experimental Area (CLEX). This houses several beam lines, including the extraction of RF power from the drive beam and transfer of this RF power to the accelerating structure, where the CLIC accelerator scheme will be tested. CLIC foresees the construction in stages, starting at the lowest energy required by the physics, with successive energy upgrades that can potentially reach the 5 TeV.

Both ILC and CLIC projects keep on progressing with their research activity, pending a decision based on physics results from the LHC, which could provide information about the most interesting energy range to be explored in a future linear collider.

The critical issue for a linear collider in the TeV scale is to achieve the high luminosity that the experiments demand. For this, extremely low beam emittances have to be reached and preserved along the accelerator and for which the beam has to be focused down to a few nanometers in the vertical dimension at the IP. This will require unprecedented specifications for alignment and stabilization, to maintain the beams colliding at the IP with tolerances of the order of half a nanometer. To this end, several international test facilities have been built and planned to address key performance goals of beam delivery sub-systems [23]. The Final Focus Test Beam (FFTB) was built in 1993 by an international collaboration to investigate the factors that limit the size, how small the beams can be made in a reliable and stable manner, and the stability of the beam at the IP. It reached 70 nm *rms* vertical beam sizes, and entailed an important progress in instrumentation and feedback control systems to ensure stability of these small beam bunches [24, 25].

The Accelerator Test Facility (ATF) was built in 1996 to establish the technologies associated with producing small emittance electron beams needed for a future linear collider. It now provides such beams to the ATF2 final focus beam line which is presently being commissioned. ATF2 was built as an international collaboration. It is a prototype final focus system which uses the same principle of local chromaticity correction as the ILC and CLIC projects [26]. The ATF DR has achieved world records for the normalized vertical emittance, with values as small as 1.5×10^{-8} m at 1.3 GeV. One of the main goals of ATF2 is the establishment of the hardware and beam handling technologies pertaining to achieving and measuring small beams of 37 nm at the final focus point in a reproducible and stable manner. Both ATF and ATF2 serve the mission of providing many R&D activities in the fields of instrumentation and feedback systems for beam control and stabilization at the nanometer scale.

2.2 The ILC baseline design

The ILC is designed to have a continuous center-of-mass energy range between 200 GeV and 500 GeV, and a peak luminosity of $\mathcal{L} \sim 2 \times 10^{34}\ cm^{-2}s^{-1}$, consistent with producing 500 fb^{-1} in the first four years of operation. In addition, the machine should be upgradeable to a center-of-mass energy of 1 TeV. It has been designed to achieve an energy stability and precision of 0.1%, and to have 80% electron polarization at the IP as well as an option for 60% positron polarization. Furthermore, alternative options for ($\gamma\gamma$) and electron-electron (e^-e^-) collisions are under consideration.

2.2.1 Beam parameters

The nominal ILC beam parameter set has been chosen to optimize between known accelerator physics and technology challenges throughout the whole accelerator complex, as beam instability and kicker hardware constraints in the DR, beam current, beam power and pulse length limitations in the main linacs, emittance preservation, and acceptable levels of background and kink instability issues at the IP. The ILC has been designed such that each subsystem accommodates a range of beam parameters, resulting in flexible operating parameters that will allow identified problems in one area to be compensated for in another. For instance, operating with low bunch charge, with low power (decreasing the number of bunches per train) or with a resulting large vertical *rms* beam size at the IP, could be compensated for by other beam parameters going towards more challenging extremes of the supported range, in order to maintain the peak luminosity close to the nominal value. In the case that all the subsystems would work with the most favorable performance, the operating parameters could be set such that they would allow higher luminosity. The nominal IP beam parameters as well as the design ranges are presented in Table 2.1 [2].

The IP beam parameter sets corresponding to the low charge (Low Q), large vertical beam size (Large Y), low power (Low P) and high luminosity (High $\mathcal{L}$), as well as the nominal ones proposed during the First ILC Workshop in 2004 [27], and which are used in this study, are shown in Table 2.2.

2.2.2 Main components of the ILC

In the baseline configuration of the ILC, electrons and positrons are accelerated up to 250 GeV in two linear machines facing each other, and then collided at the IP, where detectors are located.

A schematic of the main components of a generic linear collider is shown in Fig. 2.1. Electron and positron beams are created and pre-accelerated to a few GeV before being injected in the respective Damping Rings, where the beam emittance is reduced by radiation damping. The beam is then compressed longitudinally to the required bunch length at the IP, and is accelerated in the Main Linacs up to the desired energy. It then goes to the Beam Delivery System, where the beam halo is collimated, and is strongly focused to the required beam sizes at the IP where the detector is located. The Extraction Line transports the disrupted beam after the collision to the dump.

Table 2.1: Nominal and design range of IP beam parameters for the ILC at 500 GeV center-of-mass energy [2]. The minimum and maximum columns do not represent consistent set of parameters, but only indicate the span of the design range for each parameter.

IP Beam Parameters (ILC RDR, 2007)				
Parameter	**Symbol/Units**	**Min**	**Nom**	**Max**
Bunch charge	N_b ($\times 10^{10}$)	1	2	2
Bunches per train	n_b	1260	2625	5340
Normalized H emitt	$\epsilon^*_{x,N}$ (μm·rad)	10	10	12
Normalized V emitt	$\epsilon^*_{y,N}$ (μm·rad)	0.02	0.04	0.08
H β-function at IP	β^*_x (mm)	10	20	20
V β-function at IP	β^*_y (mm)	0.2	0.4	0.6
rms H beam size	σ^*_x (nm)	474	640	640
rms V beam size	σ^*_y (nm)	3.5	5.7	9.9
rms bunch length	σ_z (μm)	200	300	500
Luminosity	$\mathcal{L}$ (10^{34}cm$^{-2}s^{-1}$)		2.0	
Beamstrahlung E_{loss}	δ_B (%)	1.7	2.4	5.5

Table 2.2: IP beam parameter sets corresponding to the low charge (Low Q), large vertical beam size (Large Y), low power (Low P) and high luminosity (High $\mathcal{L}$) options, as well as the nominal ones for the ILC at 500 GeV center-of-mass energy proposed during the First ILC Workshop in 2004 [27].

IP Beam Parameters (First ILC Workshop, 2004)						
Parameter	**Symbol/Units**	**Nom**	**LowQ**	**LargeY**	**LowP**	**High$\mathcal{L}$**
Bunch charge	N_b ($\times 10^{10}$)	2	1	2	2	2
Bunches per train	n_b	2820	5640	2820	1330	2820
Normalized H emitt	$\epsilon^*_{x,N}$ (μm·rad)	10	10	12	10	10
Normalized V emitt	$\epsilon^*_{y,N}$ (μm·rad)	0.04	0.03	0.08	0.035	0.03
H β-function at IP	β^*_x (mm)	21	12	10	10	10
V β-function at IP	β^*_y (mm)	0.4	0.2	0.4	0.2	0.2
rms H beam size	σ^*_x (nm)	655.2	495.3	495.3	452.1	452.1
rms V beam size	σ^*_y (nm)	5.7	3.5	8.1	3.8	3.5
rms bunch length	σ_z (μm)	300	150	500	200	150
Luminosity	$\mathcal{L}$ (10^{34}cm$^{-2}s^{-1}$)	2.12	2.00	1.78	2.01	5.16
Beamstrahlung E_{loss}	δ_B (%)	2.2	1.8	2.4	5.7	7.0

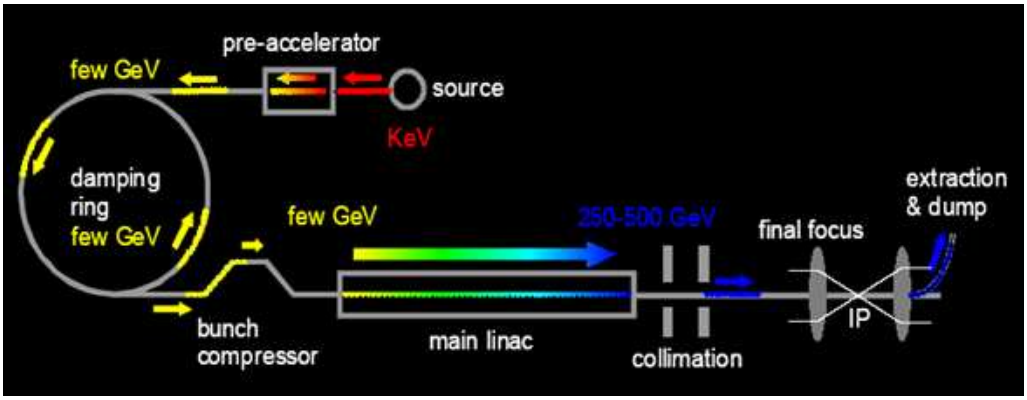

Figure 2.1: Scheme of the main components of a linear collider [37].

Fig. 2.2 shows a schematic view of the overall layout of the ILC, indicating the location of the major subsystems. Both damping rings are centrally located around the interaction region. The plane of the damping rings is elevated by approximately 10 m above of that of the Beam Delivery System (BDS) to avoid interference. To upgrade the machine to center-of-mass energy of 1 TeV, the linacs and the beam transport lines from the damping rings would be extended by another 11 km each. Certain components in the BDS would also need to be augmented or replaced.

The main components of the ILC are:

Electron source

The beam is produced by a laser illuminating a photo-cathode in a DC gun. Two independent laser and gun systems provide redundancy and create a 140-160 keV electron beam with a bunch charge of 4.5-5 nC and a bunch length of 1 ns. The bunching system compresses the beam down to about 20 ps and it is then pre-accelerated to 76 MeV by means of normal-conducting structures. The normalized transverse emittance is 70 μm·rad. The beam is then accelerated to 5 GeV in a superconducting linac. Before injection into the damping ring, superconducting solenoids rotate the spin vector into the vertical, and a separate superconducting RF structure is used for energy compression. Fig. 2.3 shows the schematic view of the polarized electron source.

Positron source

To produce positrons, electrons accelerated up to about 150 GeV are first passed through a 150 m helical undulator to produce the required high-energy photons (of roughly 10 MeV), and returned to the electron linac. These photons are then converted in a titanium alloy target into electron-positron pairs. A normal conducting L-band RF and solenoidal focusing system captures the positrons and accelerates them to 125 MeV, and the remaining electrons and photons are separated from the positrons and dumped. The positrons are accelerated to 400 MeV in a normal conducting L-band linac with solenoidal focusing. The beam is transported to the central injector complex, and accelerated to 5 GeV using superconducting L-band RF. Before injection into the DR, superconducting solenoids rotate the spin vector into the vertical, and a separate superconducting RF structure is used for energy compression, as in the electron case.

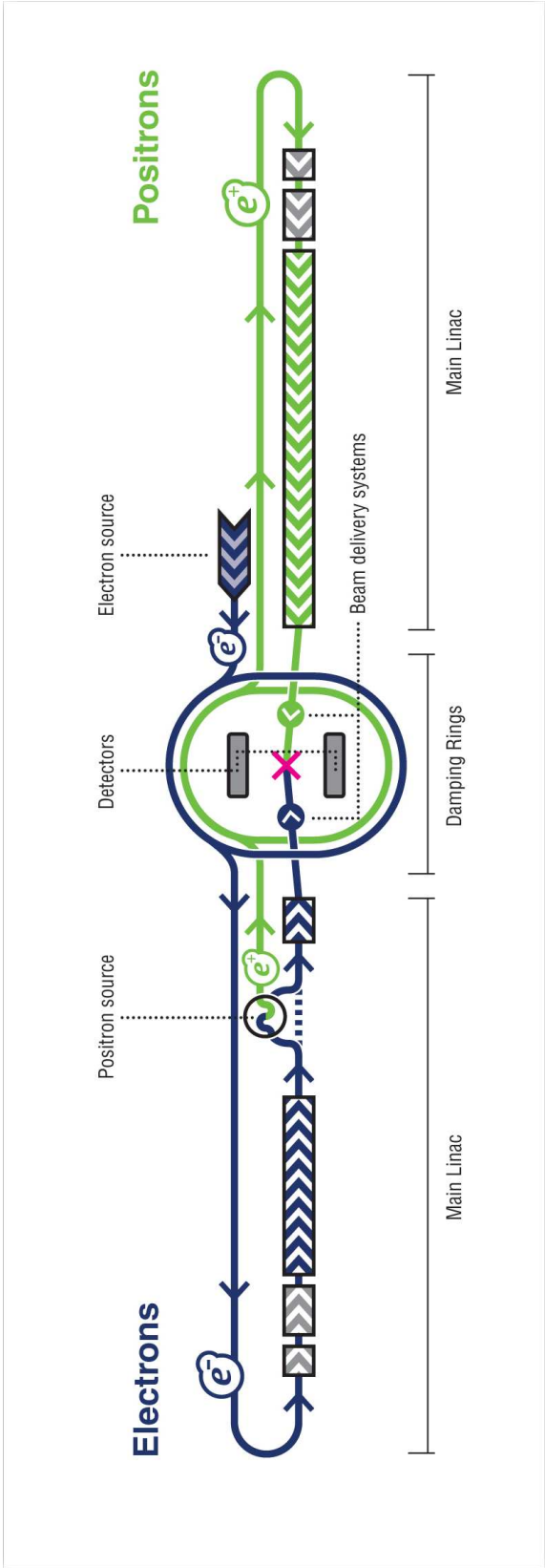

Figure 2.2: Schematic layout of the ILC complex for 500 GeV center-of-mass energy [2].

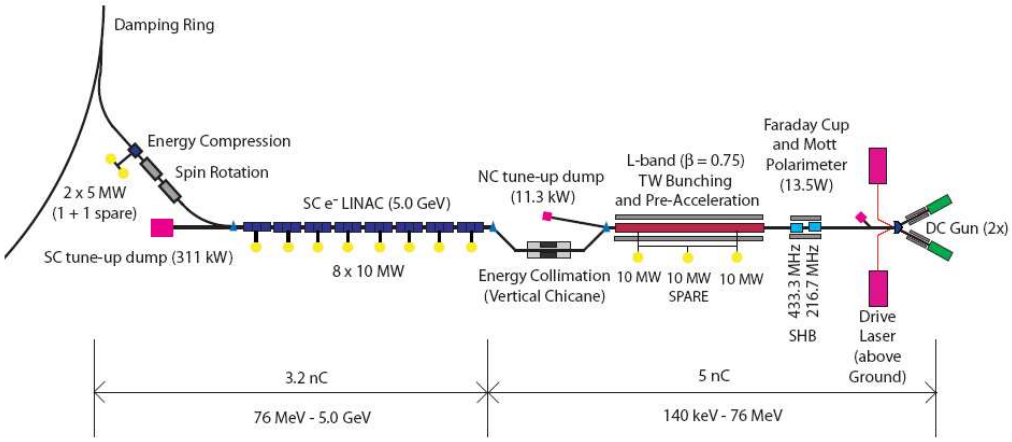

Figure 2.3: Schematic view of the polarized electron source [2].

The positron source system also includes a "Keep Alive Source" to generate a low intensity (approximately 10%) beam of positrons at 400 MeV that can be injected into the superconducting L-band linac. This allows various beam feedbacks to remain active if the main electron beam, and hence the undulator based positrons, is lost.

Fig. 2.4 shows the schematic layout of the positron source.

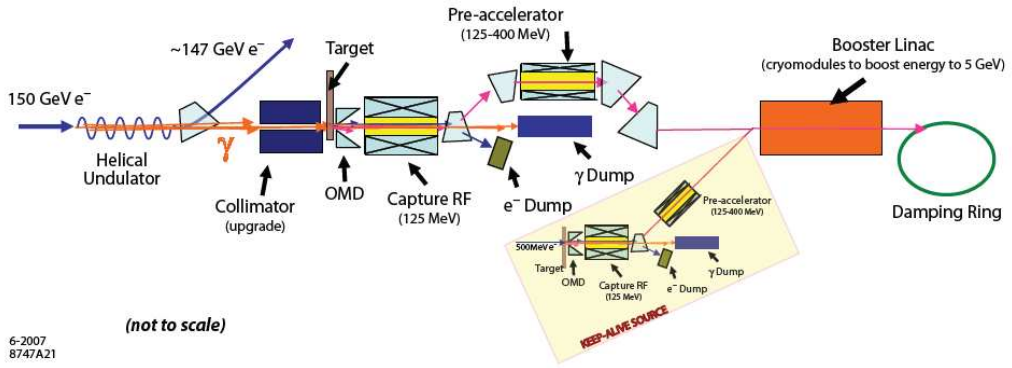

Figure 2.4: Overall layout of the positron source [2].

Damping ring (DR) for electron and positron beams

Damping rings of 6.7 km circumference store the electron and positron beams, operating at a beam energy of 5 GeV. The two rings are housed in a single tunnel near the center of the site, with one ring positioned above the other. Each damping ring must be capable of storing a full bunch train (roughly 3000-6000 bunches) and reducing the phase space volume of the bunches (the so-called longitudinal and transverse emittances) to the required level within the 200 ms interval between machine pulses. To achieve the short damping time necessary to reduce the emittances (by roughly five orders of magnitude in the case of the positron vertical emittance) within the allowed 200 ms interval, superconducting wigglers of total length roughly 200 m are used in each damping ring.

Ring to main linac (RTML)

The ILC RTML is responsible for transporting and matching the beam from the DR to the entrance of the main linac. The layout of the RTML is identical for both electron and positron beams, and is shown in Fig. 2.5. It consists on an approximately 15 km long 5 GeV transport line, betatron and energy collimation systems to reduce the halo density by 3-4 orders of magnitude, a spin rotator to orient the beam polarization to the direction required by the experimental physicists, and a two-stage bunch compressor to compress the beam bunch length by a factor of 30-45, down to a few hundred microns as required at the IP.

Compressing the beam is achieved by first introducing an energy correlation along the bunch using a superconducting RF section. The beam is then transported through a dispersive lattice formed by bending magnets (wigglers); the relative path length differences for the low and high energy parts of the bunch cause the bunch to compress longitudinally, or more precisely, to rotate in longitudinal phase space.

The bunch compressor includes acceleration from 5 GeV to 13-15 GeV in order to limit the increase in fractional energy spread associated with bunch compression.

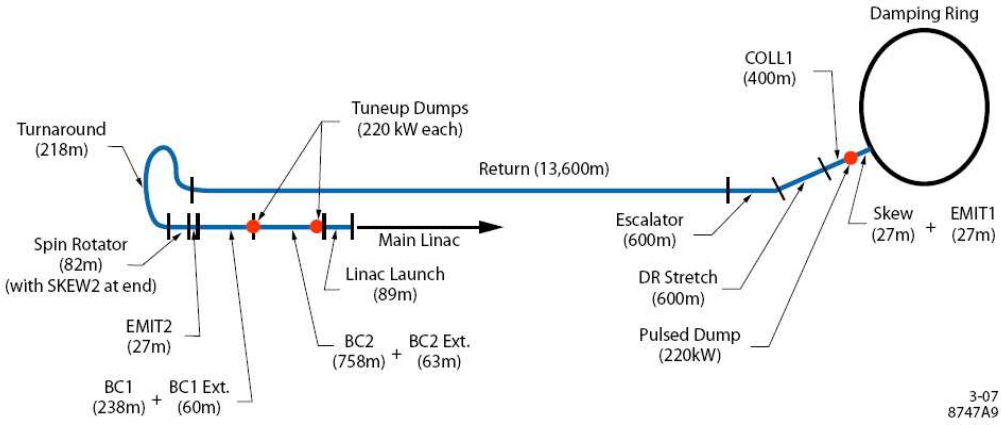

Figure 2.5: Schematic layout and location of the various sub-beamlines of the RTML [2].

Main Linac

The two main linacs accelerate the electron and positron beams from their injected energy of 15 GeV up to the final beam energy of 250 GeV, over a total length of 23 km. This must be accomplished while preserving the small bunch emittances, which requires precise orbit control based on data from high resolution beam position monitors.

The linacs utilize L-band (1.3 GHz) superconducting technology, with nine-cell standing-wave niobium cavities operating at an average gradient of 31.5 MV/m, in which the fundamental mode consists of a longitudinal electric field. Figure 2.6 shows one of the nine-cell niobium cavities for the ILC. The modules use liquid helium to cool the cavities to 2 K. The linacs are composed of RF units. Each unit comprises three contiguous superconducting RF cryomodules containing 26 nine-cell cavities each. The layout of the RF unit is illustrated in Fig. 2.7. The positron and electron linacs contains 278 and 282 RF units, respectively.

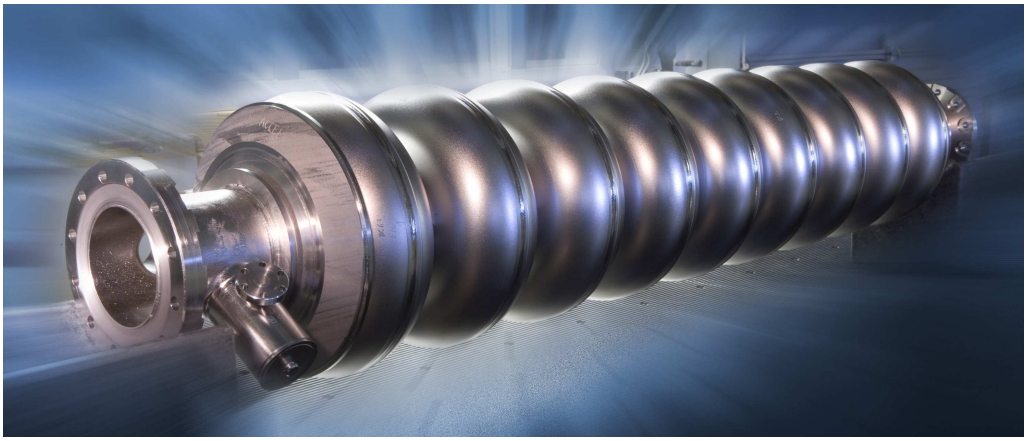

Figure 2.6: TESLA nine-cell 1.3 GHz superconducting niobium cavity from ACCEL Corp. in Germany for ILC. (Courtesy Fermilab Visual Media Services).

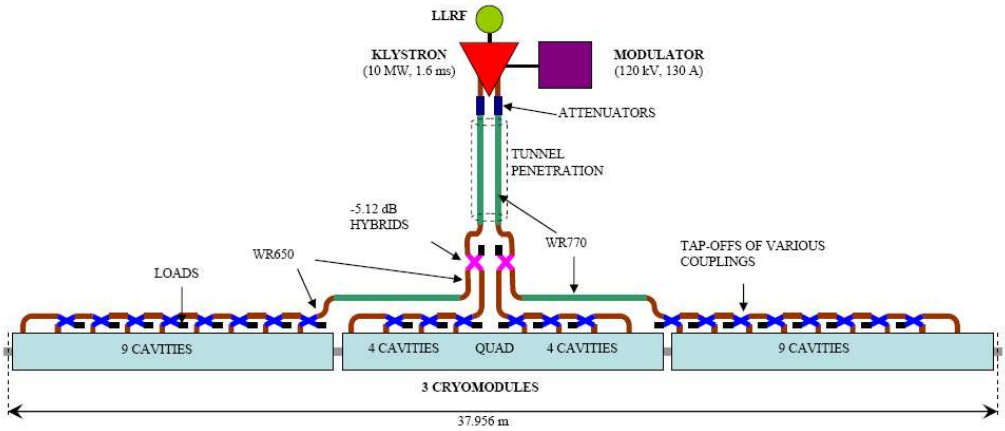

Figure 2.7: Schematic layout of the RF unit that forms the main linac [2].

Beam Delivery System (BDS)

The BDS is responsible for transporting the beam from the exit of the high energy linacs to the IP, providing the strong focusing required to produce the nanometer-sized beams at this point (about 5.7 and 640 nm in the vertical and horizontal dimensions respectively), and then transporting the spent beams after the collision to the main beam dumps. In addition, it has to accommodate several systems for beam diagnostics, machine protection against mis-steered beams and collimation systems to remove any large amplitude particles (beam halo) from the linac to minimize background in the detector. The layout of the BDS is shown in Figs. 2.8 and 2.9.

Two interaction regions with different crossing angle schemes have been studied for the ILC design. The first region with small (2 mrad) crossing angle geometry and the second one with a large (20 mrad) crossing angle [28]. Fig. 2.10 shows a scheme of that.

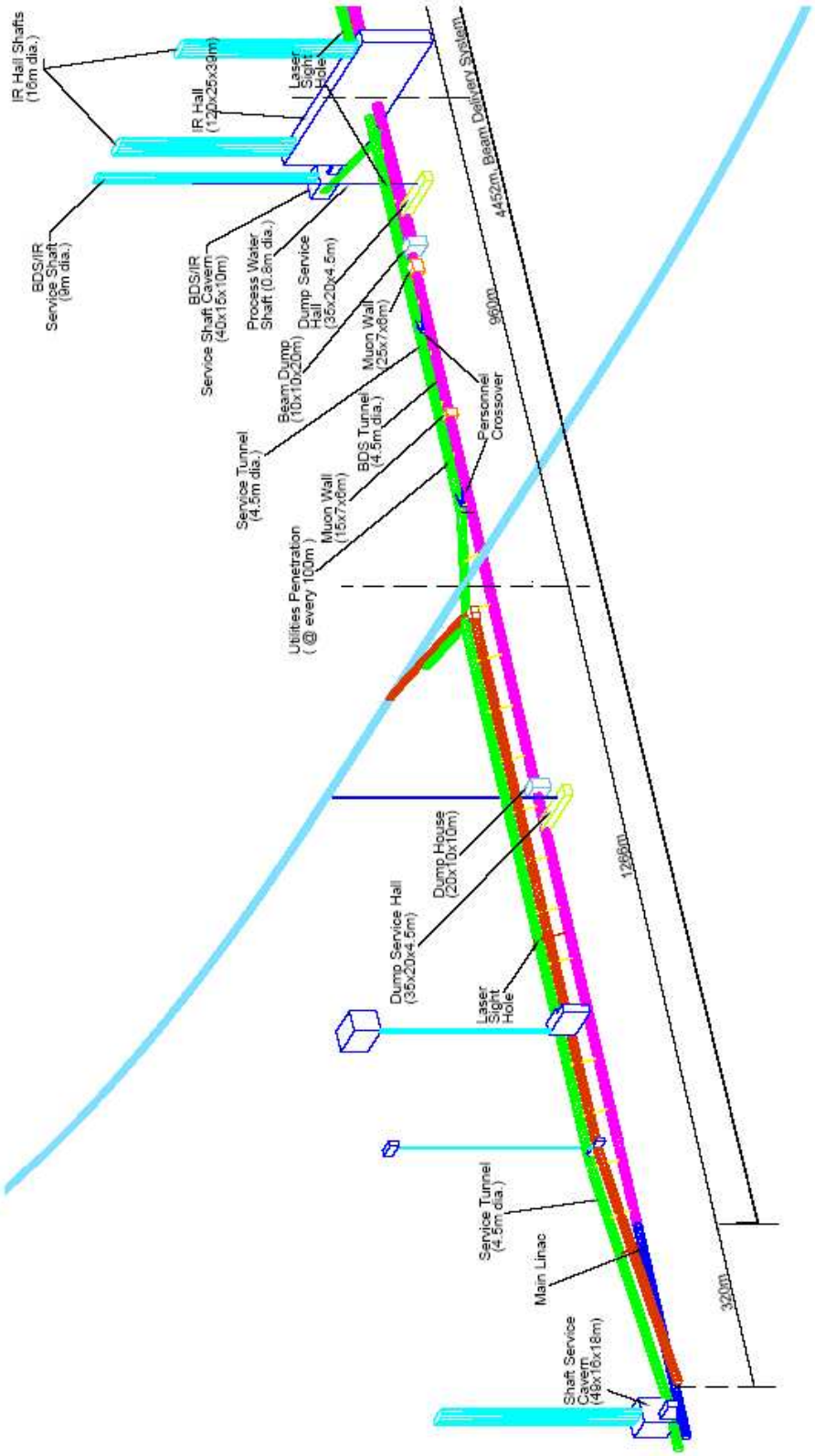

Figure 2.8: Schematic layout of the BDS, beam and service tunnels (shown in magenta and green), shafts and experimental hall [2]. The plane of the damping rings (light blue line) is elevated by approximately 10 m above that of the BDS.

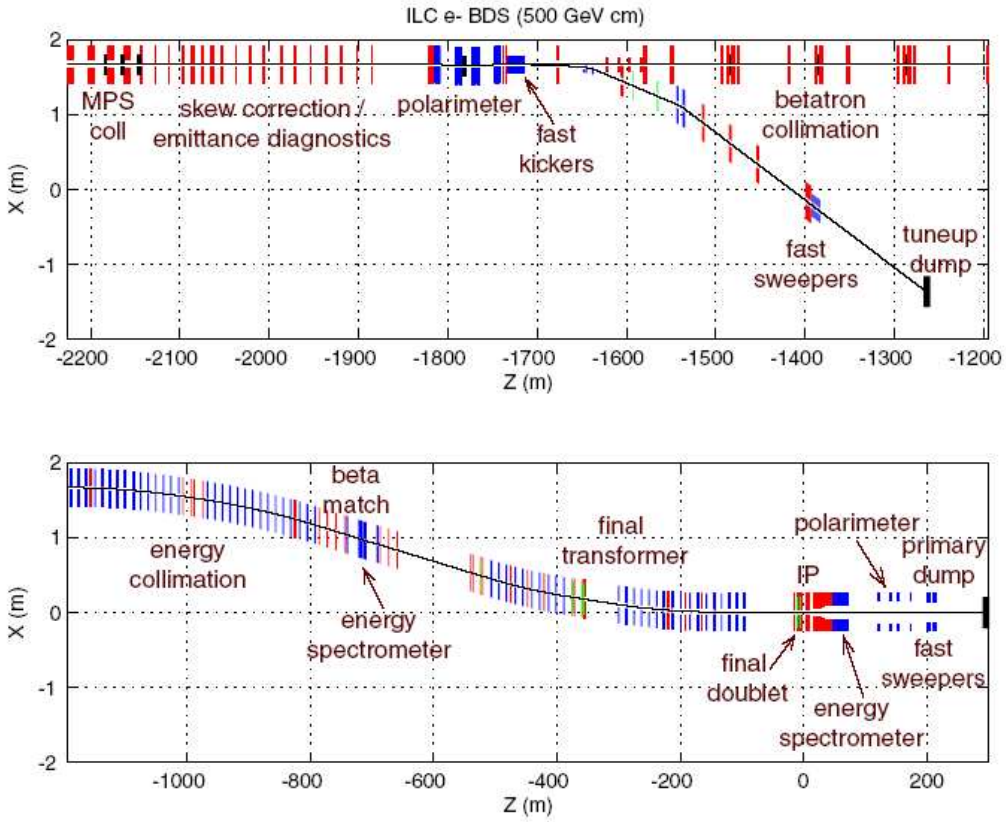

Figure 2.9: Schematic layout of the BDS, showing functional subsystems, starting from the linac exit; X and Z refer to the horizontal position of the elements and the distance measured from the IP, respectively [2].

The small crossing angle geometry offers some advantages from the detector point of view, while in the large crossing angle option the extraction of the spent beam is much easier because the incoming and outgoing beam lines don't have any common magnets. On the other hand crab-cavities are needed to recover the luminosity loss due to the crossing angle between the bunches at the IP [29]. A re-design of the head-on crossing scheme originally presented in the TESLA TDR [30] has also been pursued to overcome several of its problems.

Finally, a single collision point with a total 14 mrad crossing angle has been adopted as baseline configuration for the ILC [2]. It serves two detectors through a sophisticated system so-called "push-pull", in which both are moveable. The detectors are pre-assembled on the surface and then lowered into the interaction region hall when the hall is ready for occupancy. A major issue of this scheme is to maintain the calibrations of the detectors and beam lines after each move.

The design of the 14 mrad interaction region is rather similar to the large crossing-angle geometry with 20 mrad, and presents rather similar performances. This geometry provides space for separate extraction lines but requires crab cavities to rotate the bunches in the horizontal plane for effective head-on collisions.

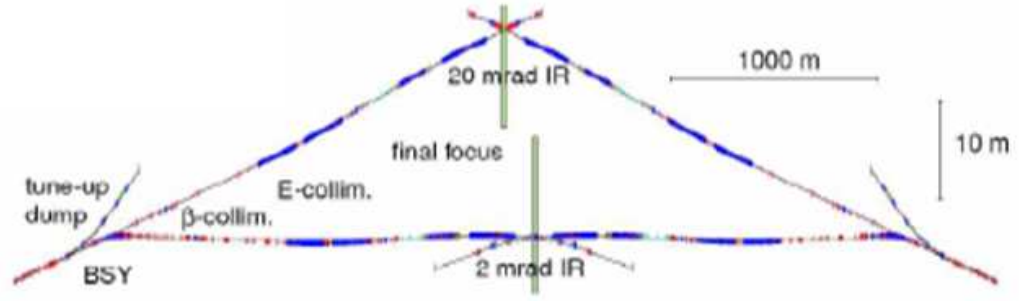

Figure 2.10: Proposed layout for two interaction regions with small (2 mrad) and large (20 mrad) crossing angle geometries at the ILC.

The main subsystems of the BDS, starting from the exit of the main linac are:

Diagnostics, Tune-up dump and Machine Protection

The initial part of the BDS, from the end of the main linac to the collimation system, is known for historical reasons as the Beam Switch Yard. It allows emittance, polarimeter and energy diagnostics of the beam at the exit of the linac, skew corrections and comprises a section to match the beam into the Collimation System. In addition, mis-steered beams must be detected and safely extracted in order to protect the downstream systems and the detector.

Collimation System (CS)

The interactions of the beam halo with the detector components and the synchrotron radiation produced in the quadrupoles near the IP can cause a large amount of background in the interaction region. The collimation system must remove any particles in the beam halo such that no particles are lost in the last several hundred meters of beamline before the IP, and all synchrotron radiation passes cleanly through the IP to the extraction line. This is achieved in two stages by means of a betatron and an energy collimation section.

The betatron collimation system has two spoiler/absorber horizontal and vertical pairs located at high beta points, providing single-stage collimation at each of the final doublet (FD) and IP betatron phases. The spoilers, which are some fraction of a radiation length of material, scrape the halo with minimal heating and enlarge the beam angular spread via multiple Coulomb scattering. The beam size increases and thus the machine is also protected from mis-steered beams. In a second step, the enlarged beam is then absorbed in the thick (>20 radiation lengths) secondary collimators (absorbers, masks, protection collimators) placed in the shadow of their spoiler partner (see Fig. 2.11).

The downstream energy collimators help to remove the degraded energy particles originating from the betatron collimation but not absorbed there. The energy collimation section has a single spoiler located at the central high dispersion point.

The collimation system has to be designed to remove the halo generating synchrotron radiation photons to a certain “collimation depth”, the maximum allowed amplitude of the particles at the entrance of the FD [32]. In terms of the nominal core beam size, collimation depths for the ILC design are approximately 8-10σ_x in the horizontal plane and about 60-80σ_y in the vertical plane [33].

The machine protection issue is a severe constraint on the design, due to the intense beams. Mis-steered beams, with power of ≈20MW would produce instantaneous beam power densities of many GW/mm^2. For a spoiler to survive from a direct hit from the beam, the beam sizes are enlarged, which requires β-functions of the order of a kilometer. This makes the system longer, and imposes tight tolerances on the magnet alignment.

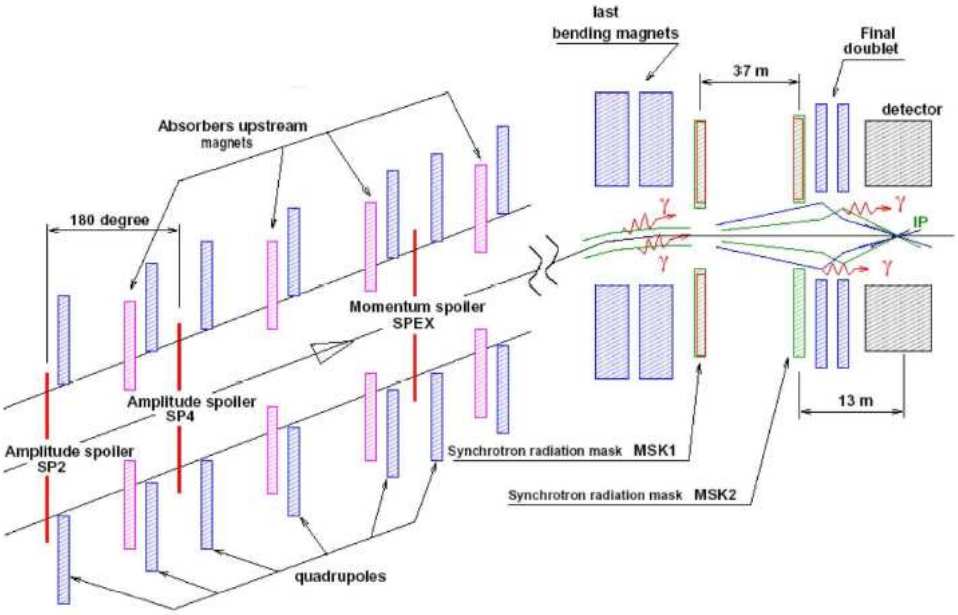

Figure 2.11: Sketch of the ILC Collimation System [31].

The optics of the BDS, starting from the entrance of the CS to the IP is shown in Fig. 2.12.

Final Focus System

After the beam halo has been collimated, the beam is strongly demagnified at the FFS to achieve the small transverse beam sizes at the IP, in particular in the vertical plane, ($\sigma_y^* \sim 5.7$ nm, $\sigma_x^* \sim 640$ nm), by means of strong quadrupoles. Since particles of different energies have different focal points, even a relatively small energy spread of about 0.1% significantly dilutes the beam size, unless adequate corrections are applied. The design of the FFS is thus mainly driven by the need to cancel the chromaticity induced by these strong magnets. The ILC FFS is designed to correct the chromaticity locally, placing sextupoles close to the strong quadrupoles, in a scheme known as “Raimondi scheme”.

In addition, the FFS includes a matching section at the entrance of the system, with an energy spectrometer, additional absorbers for the small number of halo particles which escape the collimation section, tail folding octupoles (to reduce the amplitude of beam halo particles by means of non-linear focusing, while keeping the core untouched [34, 35]), the crab cavities and additional collimators for machine protection or synchrotron radiation masking of the detector.

More details about the FFS design and the local chromaticity correction can be found in section 2.3.

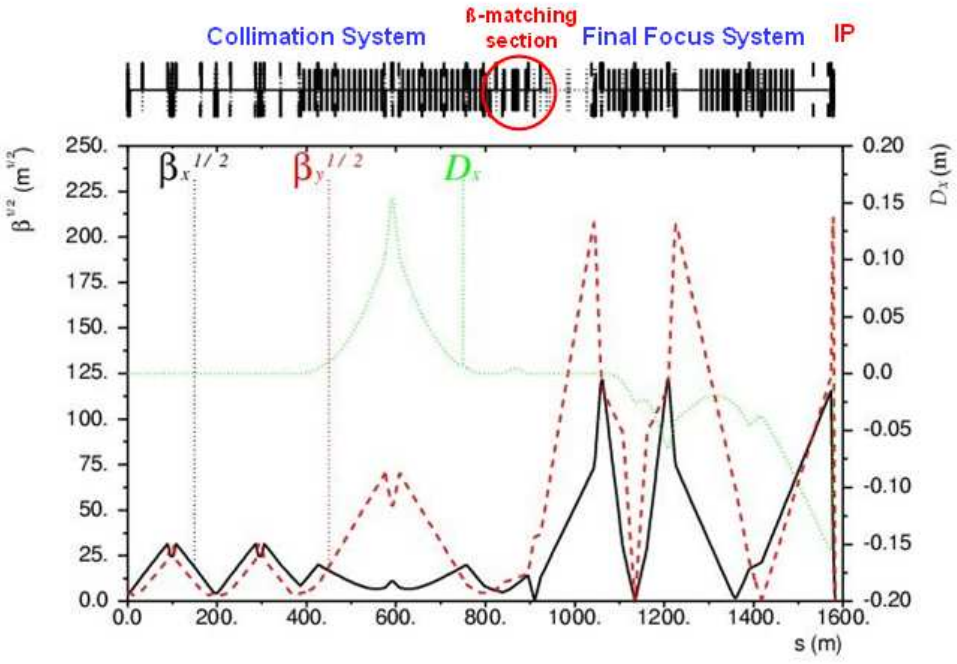

Figure 2.12: Horizontal and vertical β-functions ($\beta_{x,y}$) and horizontal dispersion (D_x) versus longitudinal coordinate s, for the ILC BDS (from the entrance of the CS to the IP) for the nominal parameters at 500 GeV center-of-mass energy (see Table 2.2). A sketch with the elements of the different parts of the BDS is also shown.

Extraction line and dump

The disrupted beam after the collision is transported to the dump in a dedicated extraction line, in which post-collision beam diagnostics can be carried out. Fig 2.13 shows the optics of the ILC extraction line for the nominal parameters of the baseline configuration.

After the collision, the beam has a large angular divergence and huge energy spread with very low energy tails, and it has to be transported to the dump with acceptable beam losses. The extraction line is designed such that particles with momentum offsets up to 60% can be transported to the dump. As there is no net bending in the extraction line, the charged particle dump can also act as a dump for beamstrahlung photons with angles up to 0.75 mrad.

The extraction line comprises a vertical chicane to allow energy spectrometer measurements, and a second vertical chicane located at a secondary focal point where a Compton polarimeter is located. The diagnostic section is followed by a 100 m long drift to allow adequate transverse separation between the dump and the incoming line.

2.3 The Final Focus System (FFS)

Once the beam-halo has been collimated, the Final Focus System provides the beam focusing to achieve the β-functions required at the IP.

The luminosity in a linear collider increases by decreasing the transverse beam sizes (it scales as $1/(\sigma_x^*\sigma_y^*)$), but also the energy loss by beamstrahlung increases (as $1/(\sigma_x^* +$

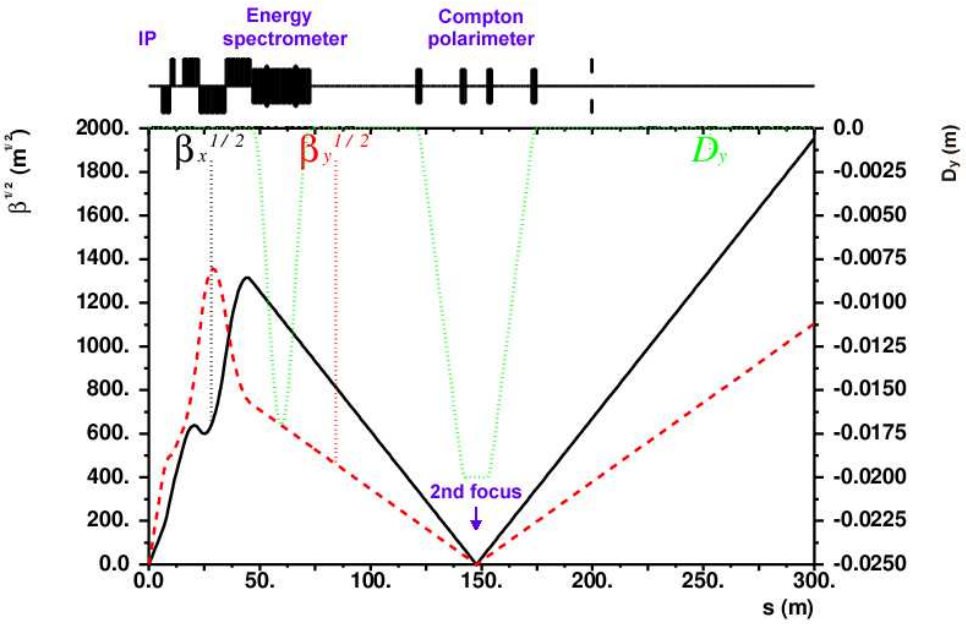

Figure 2.13: Horizontal and vertical β-functions ($\beta_{x,y}$) and vertical dispersion (D_y) versus longitudinal coordinate s for the ILC extraction line for the nominal parameters at 500 GeV center-of-mass energy. A sketch with the main elements to allow beam diagnostics is also shown.

$\sigma_y^*)^2$). Therefore, future linear colliders are designed to collide "flat beams" with $\sigma_x^* >> \sigma_y^*$, in order to maximize the luminosity while keeping the energy loss by beamstrahlung at acceptable levels (see Section 3.4). This exploits the naturally flat emittances from the DR. However, an important demagnification is still required in the vertical plane.

At the IP typical vertical β-functions are of the order of 0.4 mm (see Table 2.1), while at the exit of the linac the β-functions are several meters (in the present baseline ILC configuration, $\beta_y^{linac} = 23.5\ m$). The beam must be demagnified by a factor of $\sqrt{\beta_{linac}/\beta_y^*} \approx$ 300. The simplest way to achieve this is by means of a telescope structure with point-to-point focusing. Considering the vertical plane for simplicity, from Fig. 2.14 it is easily derived in the thin lens approximation that the demagnification factor is $M = f_1/f_2$ where f_1 and f_2 are the focal lengths of the lenses. Actually, the thin lenses in the figure must focus in both planes, and then are each formed by two quadrupoles, a focusing and a defocusing one. The last pair before the IP is called the Final Doublet (FD). The design of the corresponding magnets is constrained by the required effective focal lengths of that system, especially in the vertical plane, where it is closely related to the l^* parameter, the distance between the last (defocusing) quadrupole of the FD and the IP. In the present design, l^* ranges from 3.5 to 4.5 meters. Very strong superconducting quadrupoles form the FD, with gradients of the order of hundreds of Tesla per meter.

If there would be no energy spread in the beam, a telescope could serve as a final focus. But energy spread introduces chromaticity, and particles with different energies passing through such strong lenses will be focused to different longitudinal points along the beam line, increasing the beam size at the IP [36]. The correction of this chromatic aberration makes the FFS much more complex.

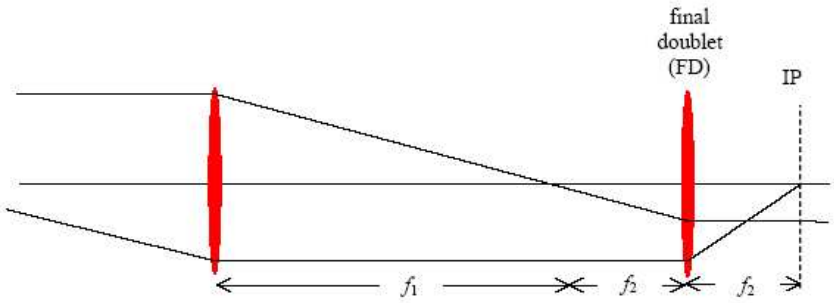

Figure 2.14: Telescope optics for a final focus system

Particles of different energies passing through a quadrupole are focused differently because the kick from the magnetic field depends on the particle momentum. Consider a focusing quadrupole in the vertical plane. The dependence of the quadrupole strength K with the momentum particle p can be written as:

$$K = \frac{e}{p}\frac{\partial B_x}{\partial y} = \frac{e}{p_0(1+\delta)}\frac{\partial B_x}{\partial y} = \frac{K_Q}{(1+\delta)} \approx K_Q\left(1-\delta+\delta^2-\ldots\right), \tag{2.1}$$

where $\delta = (p - p_0)/p_0$ is the relative momentum deviation with respect to the reference particle, and e is the electron charge. Taking the first order term in δ,

$$K \approx K_Q\,(1-\delta)\,. \tag{2.2}$$

The vertical kick dy' received by a particle passing through the thin section of the quadrupole, ds, is given by [36]:

$$dy' \approx -K_Q(1-\delta)yds = (-K_Q y + K_Q\delta y)ds. \tag{2.3}$$

The first term of Eq. (2.3) gives a kick to the particle proportional to the distance to the center of the magnet, *i.e.*, focuses the particle in the vertical plane, while the second term, proportional to the momentum deviation, has a defocusing effect, which results in an increase of the beam size (see Fig. 2.15).

Equivalently for the horizontal plane, for which the strength of the quadrupole has the same value but the opposite sign, the kick dx' received by the particle is given by:

$$dx' \approx K_Q(1-\delta)xds = (K_Q x - K_Q\delta x)ds, \tag{2.4}$$

where also here in addition to the defocusing term, a focusing one proportional to the deviation with respect to the nominal momentum appears.

In order to quantify the increase of the beam size produced by this chromatic aberration, let's consider the simplified case of the off-momentum particle in Fig. 2.15 passing through a thin lens quadrupole of length $l_Q \to 0$, holding the integrated strength $k_Q = K_Q l_Q$ constant.

Assuming that the IP angle θ is small, the particle will have a finite displacement at the IP given by

$$\Delta y^* \approx l^*\Delta\theta, \tag{2.5}$$

where $\Delta\theta$ is the associated change in IP angle due to the energy deviation of the particle.

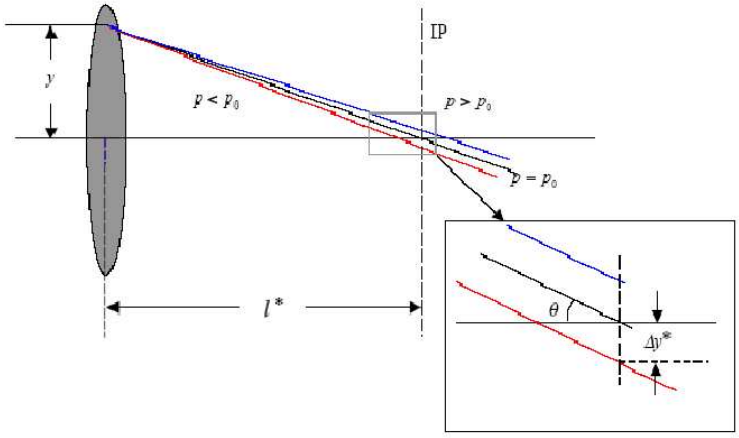

Figure 2.15: Chromatic aberration from the strong final doublet for a particle with on and off-momentum respect to the nominal value [37].

From Eq. 2.3 the change in IP angle can be deduced, since

$$\theta + \Delta\theta \approx -k_Q y + k_Q \delta y. \tag{2.6}$$

Thus, Eq. 2.5 becomes

$$\Delta y^* \approx l^* k_Q \delta y, \tag{2.7}$$

and considering that the vertical position in the quadrupole is $y = l^*\theta$,

$$\Delta y^* \approx l^{*2} k_Q \delta\theta. \tag{2.8}$$

Taking into account that the focal length of the thin quadrupole is given by $l^*=1/k_Q$, the equation becomes

$$\Delta y^* \approx l^* \delta\theta. \tag{2.9}$$

To estimate the impact of this aberration on the *rms* vertical beam size, the *rms* aberration Δy^*_{rms} has to be calculated. Assuming that there is no initial correlation between energy and angle, it becomes

$$\Delta y^*_{rms} \approx l^* \theta_{rms} \sigma_\delta, \tag{2.10}$$

where θ_{rms} and σ_δ correspond to the *rms* angle and energy spread, respectively.

Dividing Eq. 2.10 by the nominal beam size at the IP, σ^*_y,

$$\frac{\Delta y^*_{rms}}{\sigma^*_y} \approx l^* \frac{\theta_{rms}}{\sigma^*_y} \sigma_\delta. \tag{2.11}$$

and using the standard relations $\theta_{rms} = \sqrt{\epsilon/\beta}$ and $\sigma = \sqrt{\epsilon\beta}$, valids as there is no dispersion at this location, the increase on the vertical beam size can be expressed as

$$\frac{\Delta y^*_{rms}}{\sigma^*_y} \approx \frac{l^*}{\beta^*_y} \sigma_\delta \approx W_y \sigma_\delta, \tag{2.12}$$

where W_y is the vertical chromaticity that can be approximated by l^*/β_y.

In the case of the ILC, where $l^* \approx 3.5$ m, $\beta^*_y \approx 0.4$ mm and $\sigma_\delta \approx 0.1\%$, the increase

on the vertical beam size would be a factor of

$$\frac{\Delta y^*_{rms}}{\sigma^*_y} \approx 9, \tag{2.13}$$

which means that the chromatic aberration would completely dominate the IP vertical beam size, and thus it is essential to correct it.

2.3.1 Chromaticity correction

The correction of the chromaticity is performed by means of sextupoles located in dispersive regions, hence requiring prior placement of dipole magnets. Two different conceptual designs of the FFS have been developed over the last decades, which differ in the scheme used for the chromatic correction. A non-local correction scheme [38], experimentally verified for the SLC and later for the Final Focus Test Beam (FFTB) at SLAC, and a compact correction scheme proposed 10 years ago for the next generation of linear colliders as ILC and CLIC [26].

In the non-local correction scheme, the chromaticity is compensated upstream of the final telescope, in a dedicated chromatic correction section which consists of sextupoles combined with dipoles (to create horizontal dispersion) (Fig. 2.16 bottom). In addition, pairs of sextupoles separated with minus unit optical transformations ($-I$) are used to compensate the geometric aberrations introduced by the former sextupoles. The main disadvantage of this scheme is that it is quite long. In addition, the chromatic correction section requires large β-functions and dispersion, which imposes tight tolerances on the magnet alignment. Moreover, the chromatic kick generated by the sextupoles must be transported over many quadrupoles before arriving at the FD which leads to the generation of high-order aberrations ultimately limiting the momentum acceptance, or optical bandwidth, of the system.

The local correction scheme has been proposed in order to overcome these disadvantages, and has been implemented in the baseline configuration of the ILC. It will be tested experimentally in the ATF2 facility at KEK. The local correction consists in placing the sextupoles close to the strong quadrupoles (FD) where the chromatic aberration is created (Fig. 2.16 top). One arranges to have non-zero horizontal dispersion at the FD by means of a dipole. At the IP the dispersion is zero, but not its slope. However this does not affect the IP beam size, only the divergence.

The kick that a sextupole, focusing in the vertical plane, provides to a particle can be written as

$$dx' = \frac{1}{2} K_S \left(x^2 - y^2\right) ds, \tag{2.14}$$

$$dy' = -K_S\, xy ds. \tag{2.15}$$

where $K_S = (e/p_0)\left(\partial B_y^2/\partial x^2\right)$, is the strength of the sextupole.

Taking into account that the dispersion introduced in the lattice produces a displacement proportional to the momentum deviation with respect to the ideal particle, and substituting the horizontal and vertical displacements by the total coordinates:

$$x = x_\beta + D_x \delta \tag{2.16}$$

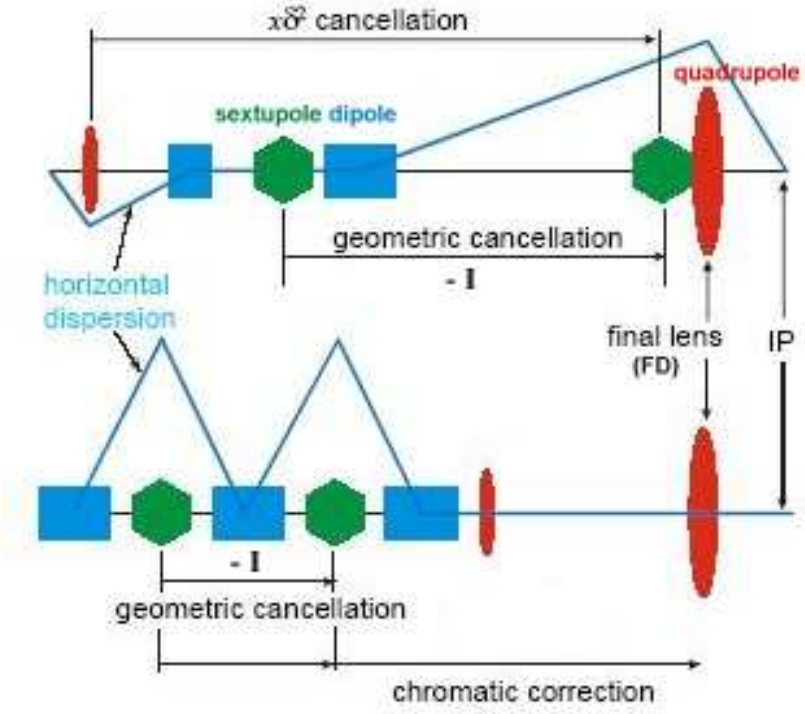

Figure 2.16: Two Final Focus design concepts [32]. Top: the compact local correction scheme for the ILC. Bottom: the non-local correction scheme used in the SLC and the FFTB. The rectangles and the hexagons represent bending magnets and sextupoles, respectively.

and,

$$y = y_\beta \tag{2.17}$$

Eqs. (2.14) and (2.15) can be rewritten as:

$$dx' = \left[D_x \delta x_\beta + \frac{1}{2} D_x^2 \delta^2 + \frac{1}{2}\left(x_\beta^2 - y_\beta^2\right)\right] K_S \, ds, \tag{2.18}$$

$$dy' = -\left(D_x \delta y_\beta + x_\beta y_\beta\right) K_S \, ds. \tag{2.19}$$

If $K_S D_x = K_Q$ is specified, the terms of these equations in xδ and yδ vanish, hence cancelling the chromatic aberration[1]. In the vertical plane, the compensation is quite straightforward, but in the horizontal plane, it is a bit more complicated.

In the presence of horizontal dispersion, the horizontal kick received by a particle from a quadrupole is, rewriting Eq. (2.4):

$$dx' \approx \left(K_Q D_x \delta + K_Q x_\beta - K_Q D_x \delta^2 - K_Q \delta x_\beta\right) ds. \tag{2.20}$$

The first two terms of this equation provide the focusing for the particle at a distance $x = x_\beta + D_x \delta$ from the quadrupole center. The fourth term is the chromatic aberra-

[1]The possible variation of the β-functions between each FD quadrupole and its nearby sextupole is omitted for simplicity.

tion which is compensated with the sextupoles, once $K_S D_x = K_Q$ is specified. But a second-order horizontal dispersion term appears, proportional to δ^2, of which just a half is compensated by this procedure. In order to compensate fully this non-linear dispersion, one must impose that the entire chromaticity of the FFS be created once more upstream of the FD, in a non-dispersive region. In this way, the sextupoles run twice stronger and compensate it as well.

The pure geometric (δ-independent) terms from the sextupoles, must still be canceled, and this requires a pair of sextupoles upstream at the same phase as the ones in the FD, with a $-I$ transformation between the sextupoles, but in a non-dispersive region (see Fig. 2.16 top).

In addition, octupoles and decapoles can be placed in the FFS in order to correct higher order term aberrations [35].

The main advantage of this local chromaticity correction scheme is that it is much shorter compared with the conventional designs and that it involves fewer quadrupoles and sextupoles. Even though its chromaticity is larger than in the older schemes (since it had to be doubled to cancel the second order dispersion), the corresponding correction is done more locally. Thus, fewer sextupole kicks need to be transported through many elements, which in turn reduces the number of bandwidth limiting higher-order terms which are generated. As a result, the FD can accommodate larger chromaticities, which allows increasing the focal length, and hence moving the FD further away from the IP. The latter can be advantageous for the detector.

The optics of the ILC FFS is shown in Fig. 2.17, for the nominal parameters in Table 2.2.

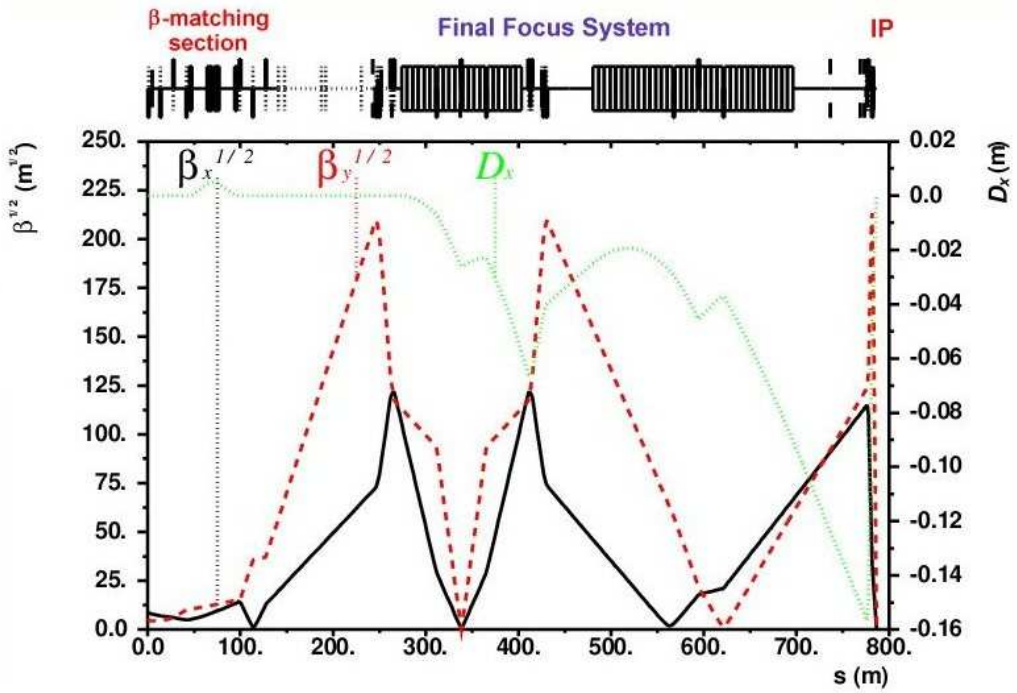

Figure 2.17: Optical functions of the ILC FFS, for the nominal parameters at 500 GeV center-of-mass energy (see Table 2.2).

2.4 e^-e^- mode of operation

Alternative collision modes to the standard e^+e^- are under consideration at the ILC, such as the e^-e^-, eγ and $\gamma\gamma$ collisions. These modes are important for some physics channels [12–14]. In the collisions that involve photons, electron beams are converted into photons by laser backscattering. For a photon collider (PC) some important changes in the interaction region are needed to accommodate the optical cavities and more complex beam extraction scheme.

For the e^-e^- collider, on the other hand, only minor changes to the hardware of the e^+e^- machine and detector are needed. The positron source has to be switched off and electrons must be driven directly to the machine. The accelerating RF phase must be shifted by 180°, and the magnet polarities have to be inverted. Fig. 2.18 shows a sketch of the main changes needed for the e^-e^- mode of operation.

Even though when inverting the polarities of the magnets for the positron line, electrons are driven to the IP with the same beam parameters and thus with the same geometric luminosity $\mathcal{L}_0$ compared to the e^+e^- collisions, the effective luminosity is smaller due to the beam-beam effects (see Chapter 3), *i.e.*, to the repulsion that a bunch experiences from the opposite one during the collision. An optimization of the beam parameters for the e^-e^- collisions has been done in order to decrease the disruption between the bunches in the collision to improve the luminosity performance (see Chapters 3 and 4). In order to achieve these proposed beam parameters at the IP, some magnet strengths in the FFS must be changed. The detailed studies are presented in Chapter 5.

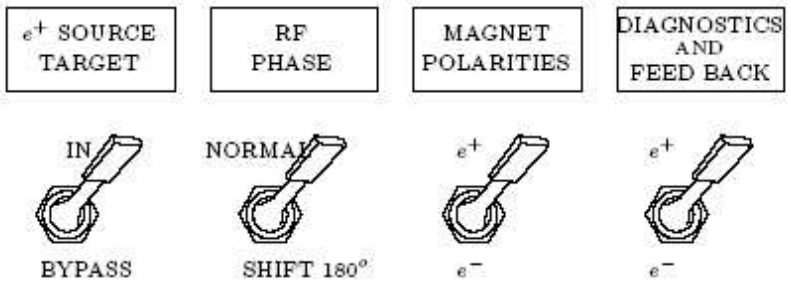

Figure 2.18: Sketch of the main changes to switch to the e^-e^- mode of operation [12].

Chapter 3

Luminosity performance and beam-beam effects

In future linear collider designs, beam-beam effects due to the interaction between the very intense beams become important. The luminosity in e^+e^- collisions is enhanced by the mutual focusing force that the bunches experience at the IP. However the beam-beam interaction also gives rise to other non-desirable effects such as the emission of synchrotron radiation by the deflected particles. The beams suffer a strong deflection when colliding with an initial transverse offset between them, which degrades the luminosity. These deflection angles serve to monitor the offsets between the beams at the IP, and feedback systems based on this have been developed. Contrary to the e^+e^- collisions, in the e^-e^- case, the repulsion between the bunches degrades the luminosity performance, and beams with small transverse offsets experience stronger deflections compared to e^+e^- collisions. A study of the beam-beam effects for both e^+e^- and e^-e^- collisions, their dependence on the beam parameters, and their impact on the luminosity and on the deflection angles is presented in this chapter.

3.1 Design Luminosity

The luminosity, together with the center-of-mass energy, is the key parameter for a high-energy physics collider experiment.

The luminosity, $\mathcal{L}$, is defined as the ratio between the event rate and the cross-section for a given event. In a linear collider, the luminosity is proportional to the charge of the colliding bunch population N_{b1} and N_{b2} (N_b^2 if N_{b1}=N_{b2}), to the number of bunches per train, n_b and to the repetition frequency f_{rep} of the trains, and inversely proportional to the effective transverse beam area. Assuming that the two colliding bunches have the same transverse spot sizes and charge, the luminosity $\mathcal{L}$ can be written as:

$$\mathcal{L} = \left[f_{rep} n_b N_b^2 \int \psi_+(x,y)\psi_-(x,y)dxdy \right] H_D(\sigma_z, \beta^*), \tag{3.1}$$

where $\psi(x,y)$ is the particle probability distribution in the transverse plane. The indices + and − refer to positron and electron beams, respectively. The expression between the brackets is the so-called geometric luminosity, $\mathcal{L}_0$ which considers only the overlap of the nominal probability distributions of the bunches at the IP, without taking into account the mutual focusing from their interaction. The latter is represented in the so-called luminos-

ity enhancement factor H_D, that depends on the bunch length σ_z and the β-function at the IP β^*[1]. This factor has a typical value of 2 for most future linear collider designs, and increases the luminosity in the case of e^+e^- collisions. It will be described in more detail in Section 3.2.3.

For Gaussian beams, the transverse particle distributions can be written as:

$$\psi(x,y;\sigma_x,\sigma_y) = \frac{1}{2\pi\sigma_x\sigma_y} exp\left[-\frac{x^2}{2\sigma_x^2} - \frac{y^2}{2\sigma_y^2}\right], \tag{3.2}$$

where σ_x and σ_y are the horizontal and vertical *r.m.s.* beam sizes. If there is no transverse tilt between the two distributions, *i.e.* the two beams collide head-on, from the integral of the Eq. (3.1), the expression of the luminosity for a linear collider is:

$$\mathcal{L} = \frac{f_{rep} n_b N_b^2}{4\pi\sigma_x^*\sigma_y^*} H_D, \tag{3.3}$$

where σ_x^* and σ_y^* are the transverse *r.m.s.* spot sizes at the IP.

Introducing the center-of-mass energy E_{cm} in Eq. (3.3) and considering the power of the beams, $P_{beam} = n_b N_b E_{cm} f_{rep}$, it can be rewritten as:

$$\mathcal{L} = \frac{P_{beam} N_b}{4\pi\sigma_x^*\sigma_y^* E_{cm}} H_D = \frac{1}{4\pi E_{cm}} (\eta_{RF} P_{RF}) \left(\frac{N_b}{\sigma_x^*\sigma_y^*} H_D\right), \tag{3.4}$$

where P_{RF} is the *RF* power and η_{RF} is the *RF* to beam power conversion efficiency.

In order to achieve high luminosities with a reasonable *RF* power, going to very small transverse beam sizes is required.

3.2 Beam-beam effects

The extremely high charge densities of the beams at the IP leads to significant beam-beam effects. During the collision the particles of one beam interact with the strong electromagnetic fields generated by the opposing beam and this causes the so-called "pinch" effect in the case of e^+e^- collisions, which results in a reduction of the effective beam sizes and an increase of the luminosity, while the opposite is true for the e^-e^- collisions, where by "anti-pinching" the luminosity is decreased.

The electric field generated by a bunch close to the beam center increases approximately linearly with the transverse coordinates (see Fig. 3.1), and the mutual beam-beam focusing can hence be assimilated to a very thin quadrupole [39]. The effective focal length of the beam in the transverse coordinates, $f_{x,y}$ can be written as:

$$\frac{1}{f_{x,y}} = \frac{2N_b r_e}{\gamma} \frac{1}{\sigma_{x,y}\left(\sigma_x + \sigma_y\right)}, \tag{3.5}$$

where $r_e = e^2/(4\pi\epsilon_0 m_e c^2)$=2.81794×$10^{-15}$ m is the classical electron radius and $\gamma = m_0 c^2$ is the relativistic parameter.

For the case of the ILC, the vertical focal length is of the order of 30 μm. When dealing with such strong lenses, not only the slope of the trajectory of a test particle changes as it crosses the opposite bunch, but there is also an appreciable change in the transverse

[1] Strictly speaking H_D also depends on the crossing angle in case it is not compensated through crab-crossing.

position, or impact parameter. Thus, the bunch can not be treated any more with the 'thin lens' approximation, but the finite bunch length has to be taken into account.

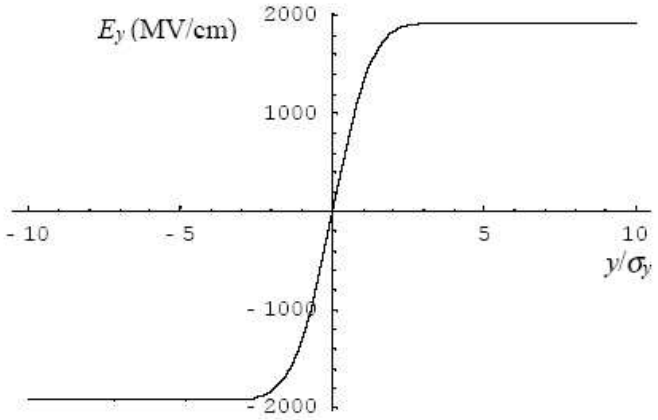

Figure 3.1: Typical electric field from a flat beam ($\sigma_x >> \sigma_y$) at the IP of a linear collider, with σ_x=500 nm, σ_y=5 nm, σ_z=300 μm and N=10^{10} [40].

3.2.1 Disruption

The magnitude of the beam-beam effects is often quantified by the so-called disruption parameter, $\mathcal{D}_{x,y}$, defined as the ratio between the *r.m.s.* of the bunch length, σ_z, and the effective focal length, and which represents the relative change in the impact parameter while crossing the opposite bunch:

$$\mathcal{D}_{x,y} \equiv \frac{\sigma_z}{f_{x,y}} = \frac{2r_e N_b \sigma_z}{\gamma \sigma_{x,y}\left(\sigma_x + \sigma_y\right)}. \tag{3.6}$$

If the disruption parameter is small, $f_{x,y} >> \sigma_z$, the beam acts as a 'thin lens', while if it is high, $\mathcal{D}_{x,y} >> 1$, the focal length is shorter than the bunch length, leading to a pinch enhancement which can lead to an instability that reduces the luminosity in the presence of small beam offsets if it is too strong. For the case of the ILC, with nominal parameters, $\mathcal{D}_y \sim 10$ and $\mathcal{D}_x \sim 0.08$.

3.2.2 Beam-beam deflections

In addition to the strong focusing experienced by the beams during the collision under high disruption, if the bunches are displaced transversely before collision, the center-of-mass of each bunch is deflected by the beam-beam force. This is illustrated in Fig. 3.2.

In the case of flat beams ($\sigma_x^* >> \sigma_y^*$) with a significantly large vertical disruption, the deflection between beams with a small initial vertical offset is important. The relation between the initial displacement and the outgoing angle of the beam is useful for monitoring the beam position [41]. Sophisticated feedback systems have been developed based on this to maintain the beams aligned at the IP.

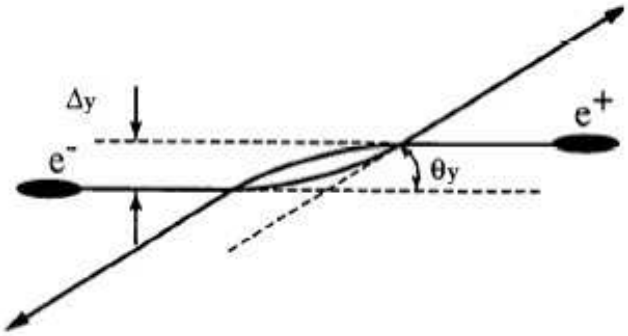

Figure 3.2: Beam-beam deflections caused by the interaction between both bunches with an initial vertical offset between them.

3.2.3 Luminosity enhancement factor

The luminosity enhancement factor is defined as the ratio of the effective luminosity, taking into account disruption, to the geometrical luminosity

$$H_D = \frac{\mathcal{L}}{\mathcal{L}_0} = \frac{\sigma_x \sigma_y}{\sigma_{x,eff}\sigma_{y,eff}}, \tag{3.7}$$

where $\sigma_{x,eff}$ and $\sigma_{y,eff}$ are the effective beam sizes resulting from the beam-beam interaction.

The luminosity enhancement factor $H_D = f(\mathcal{D}_x, \mathcal{D}_y)$ is not calculable analytically (unless $\mathcal{D}_{x,y} << 1$) because the dynamics of the beam-beam interaction is non-linear. Simulations with codes which includes this beam-beam interaction are thus needed [39]. For the case of round beams, where $\mathcal{D}_x = \mathcal{D}_y = \mathcal{D}$, the following expression was fitted to such simulations [42]:

$$H_D = 1 + \mathcal{D}^{1/4}\left(\frac{\mathcal{D}^3}{1+\mathcal{D}^3}\right)\left[ln\left(\sqrt{\mathcal{D}}+1\right) + 2ln\left(\frac{0.8\beta^*}{\sigma_z}\right)\right], \tag{3.8}$$

where β^* is the β-function at the IP.

A similar behavior of the enhancement factor as a function of the disruption is found for flat beams [43]. In this case, H_D is obtained as a function of the horizontal and vertical parameters $H_{D_x} = f(\mathcal{D}_x, \beta_x^*)$ and $H_{D_y} = f(\mathcal{D}_y, \beta_y^*)$, which have similar expressions as Eq. 3.8, being functions of the horizontal and vertical disruption parameters and β-functions, respectively.

The following general scaling behavior of H_D as a function of the ratio between the transverse beam sizes $R = \sigma_x/\sigma_y$ is found [43]:

$$\begin{aligned} H_D &= H_{D_x}^{1/2} H_{D_y}^{f(R)}, \\ f(R) = \tfrac{1+2R^3}{6R^3} &= \begin{cases} 1/2, & R \to 1 \\ 1/3, & R \to \infty. \end{cases} \end{aligned} \quad . \tag{3.9}$$

For round beams, $H_D = H_D^{1/2} H_D^{1/2}$, and the Eq. 3.8 is obtained directly. In this case, the effective beam size $\sigma_{eff} = \sigma_{x,eff} = \sigma_{y,eff}$ is given by:

$$\sigma_{eff} = \sigma H_D^{-1/2}, \quad R = 1. \tag{3.10}$$

In the flat beam limit ($R \to \infty$), $H_D = H_{D_x}^{1/2} H_{D_y}^{1/3}$, and the horizontal beam size is assumed to be fixed, obtaining a vertical effective beam size:

$$\sigma_{y,eff} = \sigma_y H_D^{-1/3}, \quad R \gg 1. \tag{3.11}$$

This less than quadratic dependence can be appreciated intuitively. In the round beam case, the change of beam size in each of both transverse directions would enhance the luminosity, as the focusing effects in the two dimensions are fully coupled. In a non-round beam, the charge distribution is mainly determined by its major dimension, σ_x, and a significant disruption or focalization power affects the perpendicular dimension. The lack of horizontal disruption entails a milder pinch effect for the flat beams.

A quantitative difference from both cases is that the enhancement can be expected by at most a factor of 2 for flat beams, while higher values can be obtained for round beams.

3.2.4 Hourglass effect

The last term in the square bracket in Eq. 3.8 represents a limitation in the achievable beam size for a given bunch length. The vertical β-function (smaller than the horizontal one in the case of flat beams) can be understood as a "depth of focus" for the bunch. Beams with bunch lengths greater than the "depth of focus" ($\sigma_z > \beta_y$) experience an increase in effective transverse beam sizes leading to a decrease in luminosity. This is known as the *hourglass effect* because the longitudinal beam profile around the focusing point has a narrow waist in the center of the bunch, like an hourglass tilted by 90° (see Fig. 3.3). Consequently it is important to have $\sigma_z \leq \beta_y$.

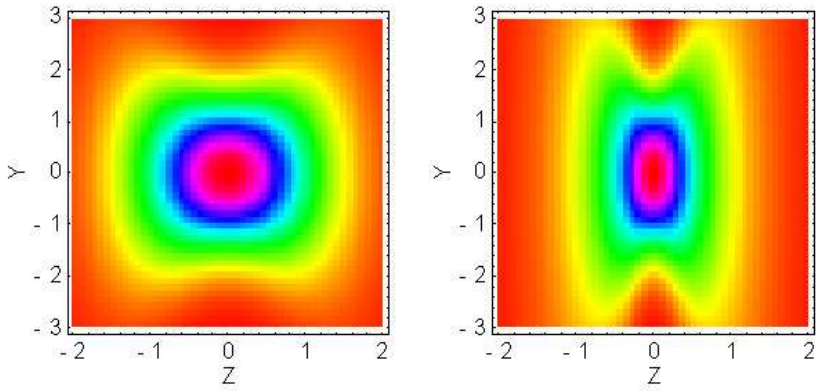

Figure 3.3: The *hourglass effect* [40]. Density plots of the bunch at the IP in the $z - y$ plane for the case of (left) $\sigma_z = \beta_y$ and (right) $\sigma_z = 3\beta_y$. (Units are in terms of the nominal beam size).

3.3 Luminosity degradation by beamstrahlung

The deflection of the particle trajectories by the electromagnetic fields of the opposite beam during the collision produces the pinching that enhances the luminosity but is also responsible for other non-desirable effects. The bent particles emit synchrotron radiation, which in this context, as caused by the beam-beam effects, is called beamstrahlung [44].

Fig. 3.4 shows a trajectory of a typical incident particle as it traverses the opposite bunch off-axis. The particle's trajectory is bent towards the axis by the focusing action of the opposite bunch.

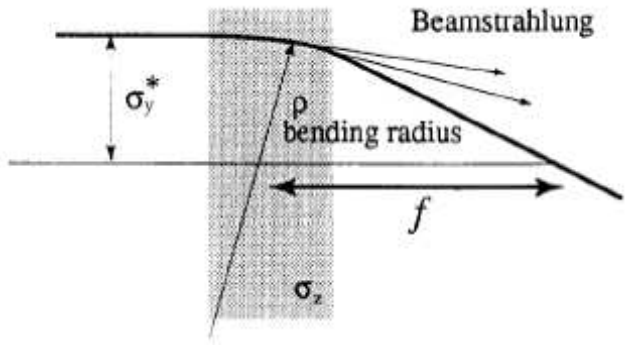

Figure 3.4: Trajectory of a typical incident particle through the opposite bunch is bent during the passage. The particle radiates beamstrahlung photons in the process.

The power emitted by the radiation, P_γ, increases for decreasing bending radius, ρ of the particle trajectory, and is given by:

$$P_\gamma = \frac{2}{3}\frac{e^2 c}{4\pi\epsilon_0}\frac{\beta^4\gamma^4}{\rho^2}, \tag{3.12}$$

where ϵ_0 is the electric permitivity of vacuum.

As a consequence of such an energy loss, the peak luminosity is degraded, inducing a luminosity spectrum, and the emitted photons can also increase the background in the detector. One of the most important processes is the e^+e^- pair creation. Another detrimental effect is the high disruption after the collisions, which makes the transport along the extraction line quite difficult.

The *r.m.s.* relative energy loss during the collision due to beamstrahlung is approximately given by:

$$\delta_B \approx 0.86\frac{e r_e^3}{2m_0c^2}\left(\frac{E_{cm}}{\sigma_z}\right)\frac{N_b^2}{\left(\sigma_x+\sigma_y\right)^2} \tag{3.13}$$

and typical energy loss values for linear colliders are between 2 and 16%.

3.4 Flat beams in future linear colliders

Beamstrahlung energy loss is a critical factor in future linear colliders due to the high beam intensities at the IP. Decreasing the transverse beam sizes in order to increase the luminosity increases also the energy loss by beamstrahlung. From Eqs. 3.4 and 3.13, it is desirable to make $\left(\sigma_x\sigma_y\right)$ small to maximize the luminosity while keeping $\left(\sigma_x+\sigma_y\right)$ large to reduce the relative energy loss δ_B. In order to achieve this compromise, the future linear collider designs consider "flat beams", with $\sigma_x^* >> \sigma_y^*$. As a result, the beamstrahlung is only a function of the horizontal beam size:

$$\delta_B \approx 0.86\frac{e r_e^3}{2m_0c^2}\left(\frac{E_{cm}}{\sigma_z}\right)\frac{N_b^2}{\sigma_x^2}, \tag{3.14}$$

and thus, the horizontal beam size σ_x^* can be set, to fix the δ_B, and the vertical beam size made as small as possible to achieve high luminosity.

Combining Eqs. 3.4 and 3.14 the luminosity scaling law can be expressed in terms of the beamstrahlung energy loss:

$$\mathcal{L} \propto \frac{\eta_{RF} P_{RF}}{E_{cm}^{3/2}} \frac{\sqrt{\delta_B \sigma_z}}{\sigma_y}. \tag{3.15}$$

From this equation it is derived that the luminosity increases with the bunch length, but taking into account the *hourglass effect* (see section 3.2.4), the bunch length and the vertical β-function are constrained by the relationship $\sigma_z^* \leq \beta_y^*$. Going to the limit where β_y^*=σ_z^* in order to maximize the luminosity and writing the vertical beam size in terms of the normalized vertical emittance, $\epsilon_{y,N}$, the final luminosity scaling law is:

$$\mathcal{L} \propto \frac{\eta_{RF} P_{RF}}{E_{cm}} \sqrt{\frac{\delta_B}{\epsilon_{y,N}}} H_D. \tag{3.16}$$

Thus, in linear colliders, flat beams are foreseen with small vertical emittances in order to maximize the luminosity while keeping an acceptable RF power and energy loss by beamstrahlung.

3.4.1 Fundamental limits: the Oide effect

As seen in Section 3.2.4, there is a limitation in the achievable beam size at the IP for a given bunch length, since the vertical β-function has to be at least as large as the bunch length ($\beta_y \geq \sigma_z$). Assuming that the bunch could always be compressed further, it could be thought that one could indefinitely also reduce the vertical beam size. But there is a fundamental limit for the minimum transverse beam sizes achievable in a given optical system, due to the emission of synchrotron radiation in the FD, which produces an increase of the beam size. This is called the Oide effect [45].

Particles with high amplitudes are strongly deflected in the quadrupoles of the FD, and as a consequence, they emit synchrotron radiation, losing energy in the process. These particles passing now through the quadrupoles are over-focused, increasing thus the transverse beam sizes. This is analogous to the discussion on the FD chromatic aberration (see section 2.3), with the difference that in this case, the momentum error is created in the FD itself. The more the $\beta_{x,y}^*$ is reduced, the bigger is the corresponding β-function at the FD, increasing this effect. Thus, there should be a minimum value of $\beta_{x,y}^*$ corresponding to a minimum beam size $\sigma_{x,y}^*$, below which, the effect of the radiation becomes dominant.

The vertical beam size including the Oide effect can be expressed as

$$\sigma_y^* = \sqrt{\beta_y^* \epsilon_{y,N} + \Delta\sigma_{yOIDE}^2}. \tag{3.17}$$

Taking into account the vertical and horizontal motion inside the final quadrupole, $\Delta\sigma_{yOIDE}^2$ can be expressed as [46]

$$\Delta\sigma_{yOIDE}^2 \approx \frac{15\sqrt{\pi} c_u r_e \lambda_e \gamma^5 \sigma_{y'}^{*2}}{32} \int ds L_y^c(s)^2 |\kappa(s)|^3 \times$$
$$\times \left[\sigma_{x'}^{*2} R_{12}^2(s) + \sigma_{y'}^{*2} R_{34}^2(s)\right]^{1/2} \left[\sigma_{x'}^{*2} R_{12}^2(s) + 7\sigma_{y'}^{*2} R_{34}^2(s)\right], \tag{3.18}$$

where $c_u = 55/(24\sqrt{3})$, $\sigma^*_{x'/y'} = (\epsilon_{x/y,N}/\beta^*_{x/y})^{1/2}$, κ is the strength of the final quadrupole in units of m^{-2}, $R_{12}(s)$ and $R_{34}(s)$ are the optical transport matrix elements between the entrance of the final quadrupole and the IP and $L^c_y(s)$ is the chromatic length given as

$$L^c_y(s) = \int ds\kappa(s)R_{34}(s)^2. \tag{3.19}$$

For an FD where the final quadrupole is vertically focusing and horizontally defocusing, R_{12} and R_{34} are given by the following expressions

$$R_{12}(s) = \frac{sinh\left(\sqrt{|\kappa|}s\right)}{\sqrt{|\kappa|}} + l^* cosh\left(\sqrt{|\kappa|}s\right), \tag{3.20}$$

$$R_{34}(s) = \frac{sin\left(\sqrt{\kappa}s\right)}{\sqrt{\kappa}} + l^* cos\left(\sqrt{\kappa}s\right), \tag{3.21}$$

where l^* is the free distance from the final quadrupole to the IP.

Assuming only vertical motion, $\sigma^*_{x'}$=0,

$$\Delta\sigma^2_{yOIDE} \approx 4.2 r_e \lambda\!\!\!^{-}_e \gamma^5 \sigma^{*5}_{y'} \int ds L^c_y(s)^2 |\kappa(s)|^3 R^3_{34}(s), \tag{3.22}$$

which is the equation derived by K. Oide in [45]. The minimum vertical beam size (ignoring the horizontal movement) is given by

$$\sigma^*_{y,min} \approx 1.83\,(r_e \lambda\!\!\!^{-}_e F)^{\frac{1}{7}}\,\epsilon^{\frac{5}{7}}_{y,N}, \tag{3.23}$$

corresponding to the minimum β-function:

$$\beta^*_{y,min} \approx 2.39\,(r_e \lambda\!\!\!^{-}_e F)^{\frac{2}{7}}\,\epsilon^{\frac{3}{7}}_{y,N}, \tag{3.24}$$

where $\lambda\!\!\!^{-}$ is the Compton wavelength, and F is a factor dependent on the parameters of the FD design, with a typical value of approximately 7. It has to be noted that the minimum vertical beam size achievable is independent of the beam energy.

Tracking simulations including synchrotron radiation generated in the quadrupoles show that the horizontal design beam parameters for the ILC, (see Table 2.2) are not so far from this limit [47]. The energy spread created by reducing the horizontal β-function further, would have an impact also in the vertical coordinate, increasing the vertical beam size.

3.5 Simulations of beam-beam effects for e^+e^- and e^-e^- collisions

Simulations of both e^+e^- and e^-e^- collisions have been carried out with the GUINEA-PIG code [48] to compare the respective luminosity performances and deflection curves. GUINEA-PIG is a program dedicated to simulating the beam-beam interaction in high energy linear colliders such as ILC and CLIC. This computing tool is used to predict the luminosity and to study the backgrounds from secondary particles produced in the collisions, in order to optimize several aspects of the designs of both the machine and the detectors [49].

As an example of these simulations, Fig. 3.5 shows the luminosity as a function of the vertical offset between the beams for e^+e^- and e^-e^- collisions, using idealized Gaussian beam distributions for the nominal ILC beam parameters at 500 GeV center-of-mass energy (see Table 2.2). The reduction of the peak luminosity for e^-e^- collisions compared with the e^+e^- case is about 80%. Moreover, the repulsion between the bunches causes the luminosity to drop with the vertical offsets much more rapidly for the e^-e^- collisions. This higher sensitivity of the e^-e^- collisions to the vertical beam offsets, can be observed also in the deflection of the beams during the collision. Fig. 3.6 compares the vertical deflection curves for both kinds of collision.

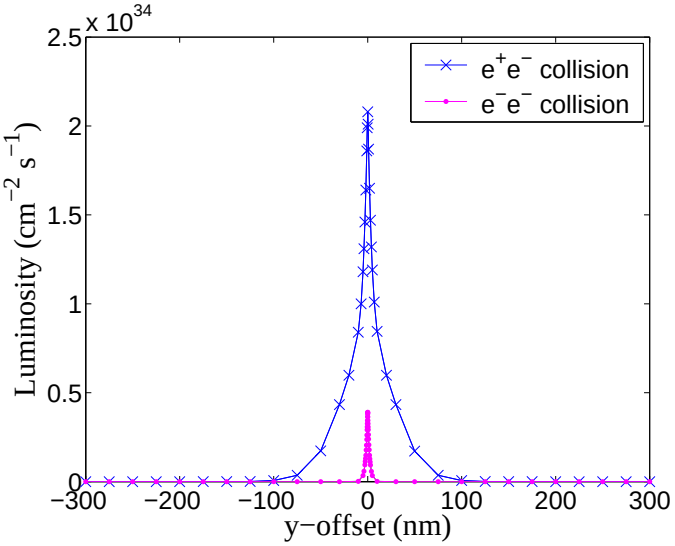

Figure 3.5: Luminosity versus vertical half beam-beam offset, for e^+e^- and e^-e^- collisions simulated with GUINEA-PIG, using idealized Gaussian beam distributions with ILC nominal parameters in Table 2.2 at 500 GeV in the center-of-mass.

The approximately linear dependence of the deflection angles with the vertical offsets (for relatively small offsets) is used to monitoring the offsets between the bunches at the IP (see Section 3.2.2). The time structure of the trains at the ILC, with a time-spacing of 300 ns between bunches, allows to implement a fast feedback system which corrects these displacements, based on the information of the previous bunches. But as shown in Fig. 3.6, the beam-beam deflection curve for e^-e^- collisions is much steeper than the e^+e^- one. This could affect the performance of the beam-based feedback system used to maintain the beams aligned at the IP.

Simulations of the beam-based feedback system have been carried out in order to compare the performance for both e^+e^- and e^-e^- collisions (see Chapter 4). Studies of the impact of the beam parameters on the beam-beam effects for the e^-e^- collisions and the consequences on luminosity and feedback performances have also been done.

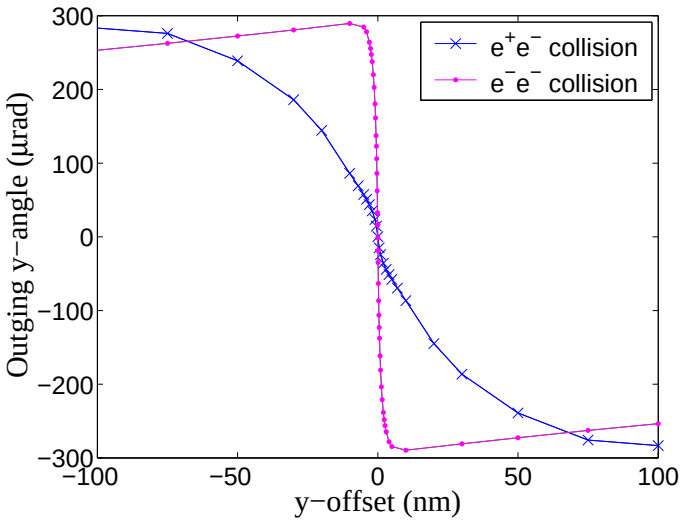

Figure 3.6: Vertical deflection angle versus vertical half beam-beam offset, for e^+e^- and e^-e^- collisions simulated with GUINEA-PIG, using idealized Gaussian beam distributions with ILC nominal parameters in Table 2.2 at 500 GeV in the center-of-mass.

Chapter 4

Beam-based IP position feedback simulation

Misalignments in the lattice magnets induce perturbations of the beam trajectory with respect to the ideal trajectory which can increase the transverse beam sizes at the IP and introduce offsets between the beams at the collision point. Sophisticated feedback systems are foreseen to mitigate these effects at the ILC and to avoid the resulting degradation of the luminosity. To maintain the beams aligned within half a nanometre at the IP, a feedback system is essential. The main signal used to infer the correction is the transverse kick that the misaligned beams experience due to the strong interaction between the bunches at the IP. For e^-e^- collisions the slope of the deflection curve as a function of the misalignment at the IP is much steeper than for e^+e^- collisions. In addition, the luminosity for the e^-e^- collisions decreases with the vertical offsets more rapidly than in the e^+e^- case.

Both these effects are taken into account to compare the feedback performances in both modes. A specific parameter optimization is also studied for the e^-e^- mode, by reducing the disruption parameter.

4.1 Effect of magnet misalignments on the beam dynamics

Misalignments in the lattice magnets produce two unwanted effects which reduce the luminosity performance. On the one hand, the beams can be kicked and arrive at the IP with transverse offsets which reduce the luminosity. For the e^-e^- collisions, the reduction of the luminosity with the offsets is greater than for e^+e^- collisions, as shown in section 3.5. On the other hand, magnet misalignments can also produce increases in the transverse beam sizes at the IP, which also reduce the luminosity.

The main sources of relative beam-beam offsets at the IP are the misalignment of the lattice quadrupoles. Beams passing through the center of a quadrupole experience transverse focusing forces that are symmetric, and don't produce the displacement of the beam center. But a beam passing through a quadrupole with a displacement with respect to the ideal beam trajectory Δy_Q, receives a kick that induces a betatron oscillation of the beam center [50]. This oscillation can produce a beam offset at the IP, Δy^*. If the quadrupole is located at a distance s_0 upstream from the IP, the offset can be expressed as

$$\Delta y^* = R_{34}(s_0 \rightarrow IP)\Delta y' = \sqrt{\beta_y^* \beta_y(s_0)}\sin(\phi_y^* - \phi_y(s_0))K_Q l_Q \Delta y_Q, \tag{4.1}$$

where β_y and ϕ_y are the vertical β-functions and the betatron phases, $R_{34}(s_0 \rightarrow IP)$ is the (3,4) element of the transport matrix from the quadrupole to the IP and $\Delta y' = K_Q l_Q \Delta y_Q$ is the deflection due to the quadrupole offset, where $K_Q = (1/B\rho)(\partial B_y/\partial x)$ and l_Q are the strength and the length of the quadrupole.

The FD is located at $\pi/2$ phase advance from the IP, which is the focal point of the optical system. If $\beta_y^* << 1$, the β-function at the FD is approximately given by $\beta_y^{FD} \approx f_y^2/\beta_y^*$, and taking into account that $K_Q l_Q = 1/f_y$, Eq. 4.1 can be expressed as

$$\Delta y^* \approx \frac{\sqrt{\beta_y^* \beta_y^{FD}}}{f_y} \Delta y_{FD} \approx \Delta y_{FD}, \tag{4.2}$$

which means that offsets of the beam with respect to the magnet center are translated one to one to offsets at the IP. The last quadrupole in the FD, focusing in the vertical plane, has the tightest tolerance for misalignments with respect to the beam axis.

Misalignments of the lattice magnets not only introduce offsets of the beams at the IP. In addition, they can enlarge the transverse beam sizes, reducing the luminosity performance. A typical source for an increase of the vertical beam size is the relative vertical offset between the beam and a sextupole. The variation of the beam size at the IP induced by a sextupole focusing in the horizontal plane with a relative offset Δy_S between the beam and the sextupole, located at a distance s_0 from the IP can be obtained by transporting the sextupole kick with the matrix element $R_{34}(s_0 \rightarrow IP)$. The vertical deflection is given by

$$\Delta y'(x) = K_S l_S x \Delta y_S, \tag{4.3}$$

where $K_S = (1/B\rho)(\partial^2 B(x)/\partial x^2)$ is the strength of the sextupole.

The *r.m.s.* beam size increase is obtained by integrating over the x direction:

$$\Delta\sigma_y^* = \Delta y_S \sigma_x K_S l_S |R_{34}(SX \rightarrow IP)|. \tag{4.4}$$

It has to be noted that a coupling between the vertical and the horizontal planes is introduced. Quadrupole magnets tilted can also introduce this coupling between both planes.

Quadrupoles with a vertical offset are sources of vertical dispersion. The kick that a particle experiences from a quadrupole displaced by Δy_Q, depends on the energy of the particle, and can be expressed as

$$\Delta y' = -\frac{K_Q l_q \Delta y_Q}{1+\delta} \approx -K_Q l_Q \Delta y_Q (1-\delta). \tag{4.5}$$

The particle offset at the IP is given by

$$\Delta y^* \approx R_{34}\Delta y' + R_{36}\Delta\delta + T_{346}\Delta y'\Delta\delta \tag{4.6}$$

where T_{346} is the second-order transport matrix element that couples the energy spread δ and the vertical deflection y' to the vertical coordinate y. Thus, the increase of the *r.m.s.* vertical beam size can be expressed, through second-order, as

$$\Delta\sigma_y^* = \Delta y_Q K_Q l_Q \sigma_\delta |R_{34} - T_{346}|, \tag{4.7}$$

where σ_δ is the relative *r.m.s.* energy spread.

A study of the misalignment tolerances of the elements of the FFS has been done. Figures 4.1 and 4.2 show respectively the vertical beam displacement and beam size at the IP for different vertical misalignments of the elements in the FFS. The results were obtained by tracking the beam through the FFS with the PLACET simulation [51], using idealized Gaussian beam distributions at the entrance and nominal ILC beam parameters at 500 GeV center-of-mass energy.

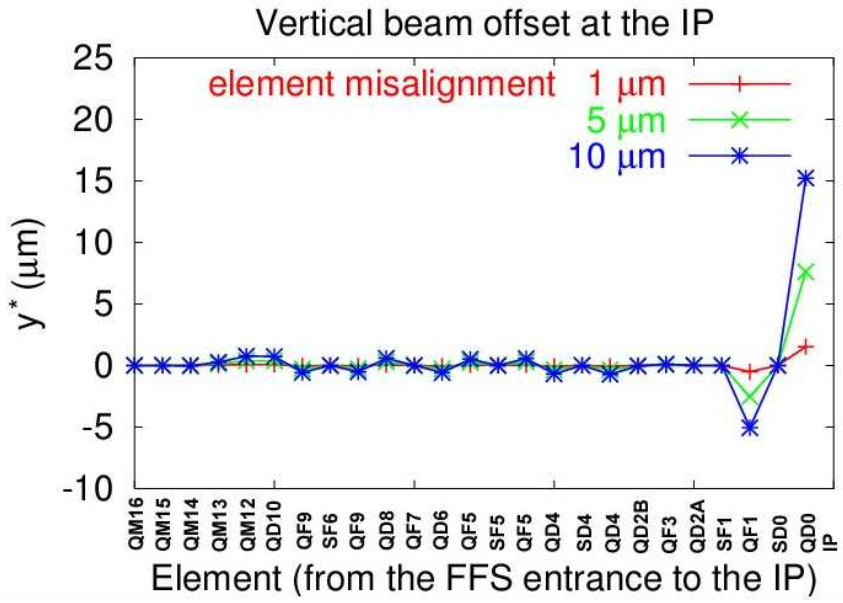

Figure 4.1: Vertical beam displacement at the IP for different vertical misalignments of the elements in the FFS. Idealized Gaussian beam distributions are used as input, with nominal ILC parameters at 500 GeV center-of-mass energy.

4.2 Sources of magnet displacements

An important source of magnet displacement is ground motion, which is transmitted to the lattice elements by their support structures. The ground motion can be divided into two frequency ranges. On the one hand "slow" frequencies below $f_{cut} \approx f_{rep}/25$, where f_{rep} is the pulse repetition frequency, that is 5 Hz for the ILC, and on the other hand "fast" frequencies above f_{cut} [52].

The slow ground motion is dominated by the tidal motion of the earth surface, mainly due to the gravitational attraction of the moon and sun, but is also influenced by temperature variations and atmospheric activities. There is an empirical diffusive model which describes the ground motion below approximately a tenth of hertz, called the ATL law. Here, the *r.m.s.* of the relative displacement Δy between two points separated by a distance L is proportional to the time T, and can be expressed as

$$\langle \Delta y^2 \rangle = ATL, \tag{4.8}$$

where A is a constant that depends on the specific conditions and on the geology of the site, and is in the range of 10^{-5} to 10^{-9} $\mu m^2 s^{-1} m^{-1}$.

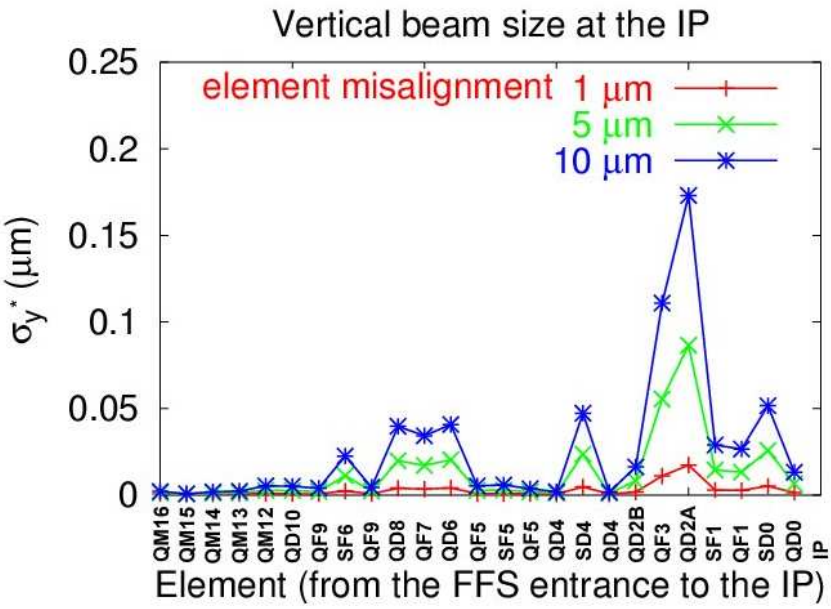

Figure 4.2: Vertical beam size at the IP for different vertical misalignments of the elements in the FFS. Idealized Gaussian beam distributions are used as input, with nominal ILC parameters at 500 GeV center-of-mass energy.

The fast ground motion, above approximately 1 Hz consists of elastic waves propagating at velocities in the order of a few km/s. The power of this fast motion decrease rapidly with the frequency, approximately as $(1/f^4)$. In addition to the natural sources of ground motion, the so-called *cultural noise* related to the human activity has to be considered. Accelerators are commonly built in deep tunnels to attenuate the cultural noise. Moreover, water pumps, ventilation systems, air flows and power supply systems in the tunnel can increase the ground motion by a factor of 10 during operation.

Complex feedback systems are foreseen in order to maintain aligned the lattice magnets, and to correct for displacements between the colliding bunches. The ground motion at high frequencies that cannot be efficiently suppressed by the fast intra-train feedback system has fortunately very small amplitudes. Slow ground motion can be efficiently suppressed by feedback. The beam-based IP position feedback system maintains the beams aligned at the IP, and the accumulated misalignments of the lattice magnets are corrected by another slow feedback system [53].

Ground motion models

The ground motion can be represented by a two-dimensional power spectrum $P(w,k)$ which will carry all the necessary information about the spatial and temporal correlations. Several ground motion models have been built, based on the results of measurements. These models include ATL diffusive motion, slow systematic motion, natural micro-seismic motion, and fast cultural noise [54]. Three models have been created, with different levels of noise. A low noise model A has been built based on measurements at the LEP tunnel. An intermediate noise model B, based on measurements at the SLAC shallow tunnel and at the Aurora deep mine near FNAL, has been created, and a high

noise model C, based on measurements in the shallow HERA tunnel. Fig. 4.3 shows the integrated ground motion spectra for these three models, both for the absolute motion, and for differential motion for points separated by 50 m.

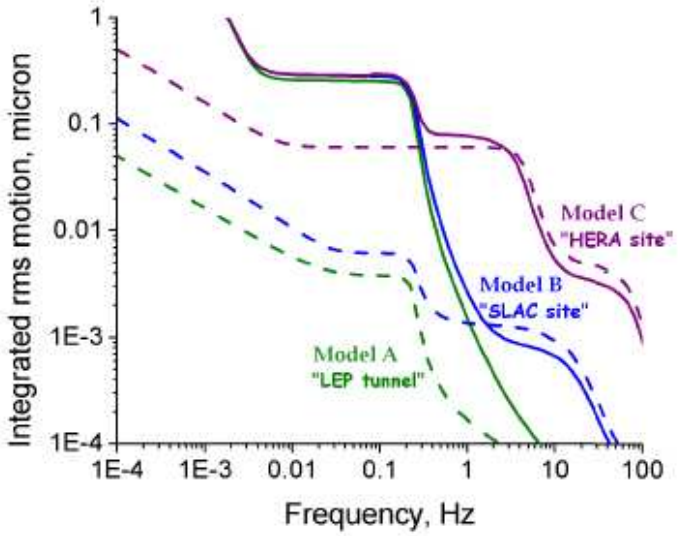

Figure 4.3: Integrated ground motion spectra based on models for “LEP tunnel” (model A), “SLAC site” (model B) and “Hera site” (model C). Absolute motion (solid curves) and differential motion for points separated by 50 m (dashed curves) [55].

The spatial properties of the ground motion are studied in terms of the correlation of motion between two points separated in space. The relatively long wavelength of the ground motion does not affect the beam if this wavelength is much longer than the betatron length.

The spectra created to approximate the ground motion are useful tools to evaluate the performance of a linear collider if the response functions of the beam line and the feedback are available.

4.3 Feedback systems and stability

Future high energy linear colliders require vertical beam sizes in the nanometre scale. Maintaining the stability of the beam and the lattice magnets is essential since small vertical offsets of a fraction of the beam size at the collision point noticeably degrade the luminosity performance.

Beam-based orbit feedback loops are foreseen at the ILC to maintain the size and position of the beams at the collision point. All of the feedback loops use beam position monitors with micrometer-level resolution to detect the beam position, and dipole magnets or stripline kickers to deflect the beam.

To correct the position and the angle of the beam at the IP, fast intra-train feedback systems are used, which can apply a correction to the beam between bunches of a single train. The signals detected on early bunches in the train are used to correct the subsequent bunches. Slower train-by-train feedback systems are required to maintain aligned the lattice magnets and to correct the beam trajectories, which operate at the 5 Hz repetition rate of the ILC.

4.3.1 Intra-train beam-based IP position and angle feedback system

The IP position feedback system is foreseen to maintain the beams aligned at the collision point with half a nanometre of tolerance. The offset of the beams at the IP is determined by measuring the deflection from the beam-beam interaction. This interaction is so strong that nm-level offsets produce deflections with typical amplitudes of tens of microradians, that are big enough to be measured with a beam position monitor (BPM) with micron-level resolution, a few meters downstream of the IP. The approximately linear dependence of the deflection angles on the vertical offsets, for relatively small offsets, (see Fig. 3.2), is used to compute the offset at which the collision occurred, and to correct the next bunch. The corrector is a dipole that induces a kick on the incoming beam, and it is placed at a $\pi/2$ betatron phase advance from the IP, close to the FD, because in this case the dipole kick induces a maximum offset. A sketch of the feedback system is shown in Fig. 4.4.

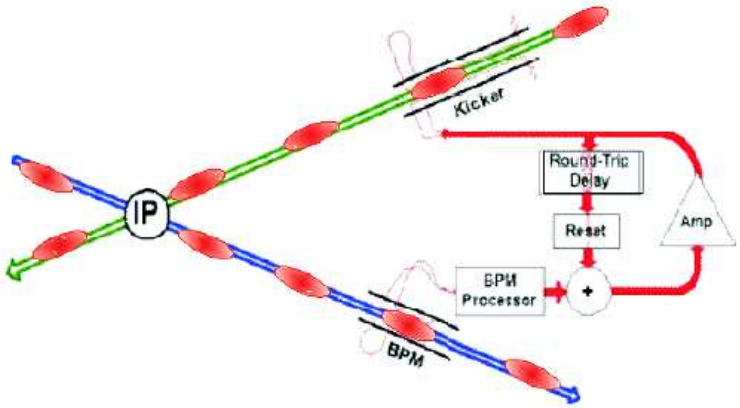

Figure 4.4: Sketch of the IP position beam-based feedback system. A beam position monitor (BPM) downstream of the interaction point measures the offset of the beam after the collision and allows calculating the deflection angle. This information is fed into the corrector that introduces a kick to the incoming beam [56].

The angle of the beams at the IP is determined by measuring the beam positions at locations $\pi/2$ out of phase with the IP. At these locations the beam offsets are relatively large so micron resolution is sufficient to directly measure the beam position to infer the IP angle. The orbit is corrected by means of a kicker located at the entrance of the FFS, at $n\pi$ phase-advance from the IP, which causes a latency of about 4 bunch spacings.

4.4 Simplified simulation of the beam-based IP position feedback system

The beam-beam deflection curve for e^-e^- collisions is much steeper than the e^+e^- one, as shown in Fig. 3.6. This could affect the performance of the beam-based feedback system used to maintain aligned the e^-e^- beams at the IP. A simplified simulation of the beam-based feedback system has been carried out in order to compare the performance for both e^+e^- and e^-e^- collisions.

Hypothesis of work for the simplified simulation

At the ILC, trains are delivered with a frequency of 5 Hz, and have a duration of ∼1 ms, with 2820 bunches spaced by 307.7 ns. Looking at the amplitudes of the ground motion models for the frequencies corresponding to the time scale in which the trains are delivered, it is possible to conclude that offsets of the order of hundred nanometres could affect the beginning of each train (see Fig. 4.3). On the contrary, amplitudes corresponding to the frequency of the bunch spacing are much smaller, and correspond to a negligible fraction of the vertical beam size.

For the simulation, initial offsets at the beginning of each train of the order of hundred nanometres are introduced at the IP and a random Gaussian noise of a fraction of the vertical beam size is added pulse-to-pulse to account for uncorrelated jitter from injection or other sources. In addition a 10% error in the correction is introduced to represent the measurement resolution. For the correction, the conversion of the angle into the offset at the IP is done by a proportional factor between these quantities, and the correction is done bunch-to-bunch with the information of only the precedent bunch. To obtain the luminosity and the out-going angle corresponding to the relative position between the bunches, a parametrization of the curves shown in Fig. 3.5 has been done, and they are obtained by interpolating, to avoid running the GUINEA-PIG program for each collision, as this would take a lot of time. Nominal beam parameters at 500 GeV center-of-mass energy are considered for both e^+e^- and e^-e^- collisions.

Simplified simulation for e^+e^- and e^-e^- collisions with nominal parameters

Fig. 4.5 shows the feedback response for different proportional factors between the angle and the offset at the IP for the case of e^+e^- collisions. An offset of 200 nm for each beam at the beginning of the train was used, and a bunch-to-bunch jitter of 0.1 nm. As seen in Fig. 4.5 left, the smaller the slope relating the out-going angle with the IP offset, the faster the correction. But if this factor is too small, an over-correction occurs and there is an amplification of the jitter. It is necessary to find a compromise to carry out the correction as fast as possible without amplifying the residual offset.

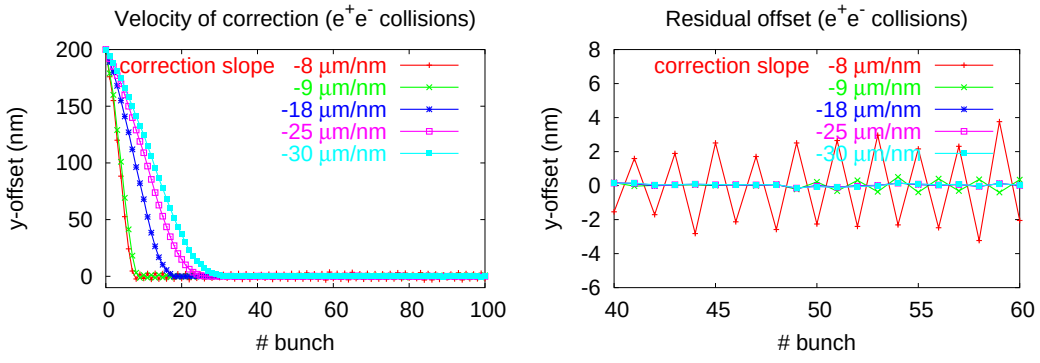

Figure 4.5: Left: Feedback response simulation with different correction slopes for e^+e^- collisions with nominal parameters at 500 GeV center-of-mass energy. Right: Zoom of the residual offset once the correction has aligned the beams. The simulation was done for an initial offset of 200 nm for each train, and with 0.1 nm of bunch-to-bunch jitter.

The simulation was done for the e^-e^- case with the same assumptions as for the e^+e^-

simulation. The results are shown in Fig. 4.6. Due to the much steeper deflection curve, the correction must be done much slower compared with the e^+e^- case. Otherwise, the jitter is strongly amplified due to the large over-correction. While 20 or 30 bunches are enough for correcting the initial offset in the e^+e^- case, 100 or 150 bunches are needed to correct the offset without amplifying the residual jitter for the e^-e^- collisions under the same conditions. But in either case trains are long compared to the number of bunches needed to correct the relative offset between the beams: even for the e^-e^- case, it is only 5% of the train.

The simulation of the feedback has been done for different initial train offsets for a given bunch-to-bunch jitter. The results indicate that the average train luminosity is almost independent of the initial offset (see Fig. 4.7). The lower speed of correction for the e^-e^- collision due to the steeper deflection curve turns out not to be a problem.

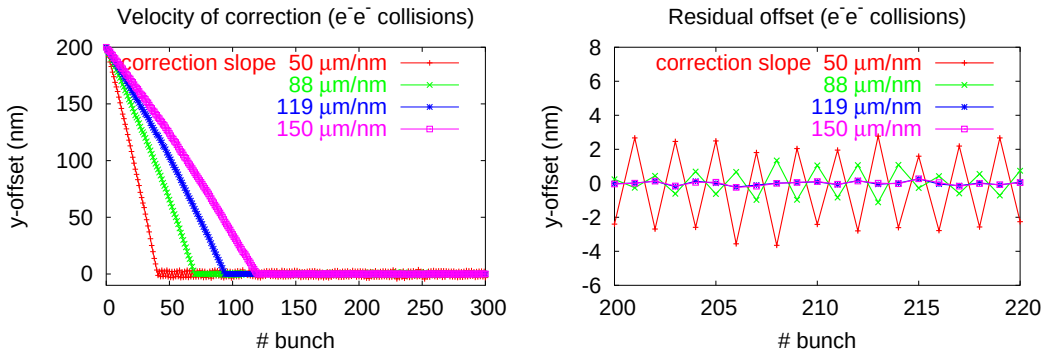

Figure 4.6: Left: Feedback response simulation with different correction slopes for e^-e^- collisions with nominal parameters at 500 GeV center-of-mass energy. Right: Zoom of the residual offset once the correction has aligned the beams. The simulation was done for an initial offset of 200 nm for each train, and with 0.1 nm of bunch-to-bunch jitter.

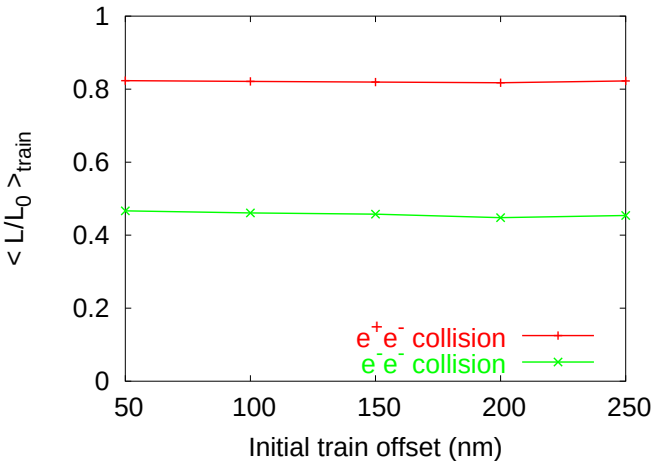

Figure 4.7: Average relative train luminosity versus different initial offsets applied to each train. The feedback simulation was done for a 2 nm bunch-to-bunch jitter.

The feedback response for different bunch-to-bunch jitters for e^+e^- and e^-e^- collisions is shown in Fig. 4.8, for an initial offset of 100 nm applied to each train. The

correction slope does not need to be optimized for each value of the bunch-to-bunch jitter applied, since it has been optimized for both e^+e^- and e^-e^- collisions such that it is big enough to avoid the amplification of the small jitter values by over-correction. The luminosity decreases more rapidly for the e^-e^- case due to the higher sensitivity to the beam-beam offsets compared with the e^+e^- collision. For 1 nm jitter the average luminosity loss for the e^+e^- collisions is ~10%, while more than 30% is lost in the e^-e^- case.

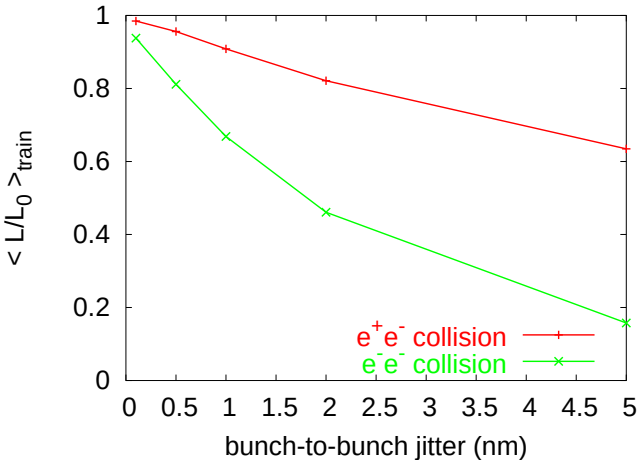

Figure 4.8: Average relative train luminosity versus different bunch-to-bunch jitter applied. The feedback simulation was done with a 100 nm initial offset for each train.

The steeper deflection curve for e^-e^- collisions is not really a problem for the feedback performance, but the luminosity decreases more rapidly with uncorrelated jitter amplitudes than for e^+e^- collisions, due to the repulsion between the beams. An optimization of the beam parameters for the e^-e^- collision, decreasing the disruption parameter between the beams, has been done (see section 4.5.1) to reduce the sensitivity to jitter.

4.5 Feedback simulation with different beam parameters

4.5.1 Beam parameter optimization for e^-e^- collisions

While luminosity in e^+e^- collisions is enhanced for a moderately high disruption between the bunches, for e^-e^- collisions the opposite is true. Large vertical disruption parameters should be avoided in this case. This is also important to reduce the high sensitivity of the luminosity to the vertical beam-beam offsets. In the case of flat beams, the absolute value of the vertical disruption parameter $\mathcal{D}_y$ (see section 3.2.1), scales as:

$$\mathcal{D}_y \propto \frac{N_b \sigma_z}{\sigma_x^* \sigma_y^*}. \tag{4.9}$$

To decrease $\mathcal{D}_y$, σ_z can be reduced and the product of σ_x^* and σ_y^* can be increased. The latter would also decrease the nominal luminosity $\mathcal{L}$, though not as fast as the geometric luminosity $\mathcal{L}_0$, that scales as:

$$\mathcal{L} = \mathcal{L}_0 H_D \propto \frac{N_b^2}{\sigma_x^* \sigma_y^*} H_D, \tag{4.10}$$

since the repulsion between the bunches is reduced, and thus, the decrease on the geometric luminosity would be partially compensated by the increase of the enhancement factor. It is worth noting that to shorten the bunch length is challenging, and that it is done at the expense of the energy spread, which is increased through the phase dependent acceleration in the bunch compression system (see Section 2.2.2).

In Table 4.1 several beam parameter sets studied in the case of the e^-e^- mode are shown. Parameter sets 2 and 3 are proposed with half of the nominal bunch length, reducing the disruption and with higher luminosity compared with the nominal parameters. The luminosity can be increased at the expense of a higher beamstrahlung energy loss. The transverse beam sizes have been optimized computing the luminosity with the GUINEA-PIG code in order to enhance the luminosity as much as possible while keeping the maximum energy loss by beamstrahlung at 5%. The latter scales as:

$$\delta_{\mathcal{B}} \propto \frac{N_b^2}{\sigma_x^{*2}\sigma_z}. \tag{4.11}$$

The luminosity for parameter set 3 is almost 50% larger than for the nominal one. The increase for parameter set 2 is only 25%, but the sensitivity to vertical IP offsets is smaller than for parameter set 3, because the beam is rounder which decreases the disruption.

Table 4.1: Luminosity and beamstrahlung energy loss for e^-e^- collisions with different beam parameter sets at 500 GeV in the center-of-mass energy. The nominal values for the bunch length and the transverse beam sizes at the IP are σ_{z0} =300 μm and $\sigma^*_{x0/y0}$ =655.2/5.7 nm and the nominal intensity is $N_{b0} = 2\times10^{10}$ particles.

	nominal	**set 1**	**set 2**	**set 3**	**low Q**
N_b/N_{b0}	1	1	1	1	0.5
σ_z/σ_{z0}	1	0.7	0.5	0.5	0.5
σ^*_x/σ^*_{x0}	1	0.7	0.8	0.9	0.7
σ^*_y/σ^*_{y0}	1	1.5	1.5	1	0.6
ϵ_x(μm·rad)	10	10	10	10	9.6
ϵ_y(μm·rad)	0.04	0.04	0.04	0.04	0.03
β^*_x(mm)	21.0	10.3	13.4	17.0	10.0
β^*_y(mm)	0.4	0.9	0.9	0.4	0.2
L ($\times10^{33}$) ($cm^{-2}s^{-1}$) for Δy_{IP} = 0 *nm*	3.9	4.6	4.9	5.8	3.0
L ($\times10^{33}$) ($cm^{-2}s^{-1}$) for Δy_{IP} = 2 *nm*	2.4	3.7	4.4	4.4	1.8
δ_B (%)	2.24	4.9	5.0	4.3	2.2

Since reducing the bunch length can present technical difficulties in the bunch compressor, parameter set 1 is also proposed with a bunch length 0.7 times the nominal one. This parameter set gives an increase of ~18% for the luminosity with respect to the nominal one, and also has a small sensitivity to vertical IP offsets thanks to its rounder beams.

Finally, a fourth set of parameters, called "low Q" in Table 4.1, is presented with half of the bunch charge N_b, while keeping the same number of bunches per train. Reducing the bunch charge drastically impacts the luminosity because of the quadratic scaling (see

Eq. 4.10). To recover part of the luminosity loss, both the bunch length and the horizontal and vertical β-functions are reduced by half. Such a parameter set could be important for early ILC operation and flexibility.

4.5.2 Feedback simulation with the alternative parameters

The simplified feedback simulation carried out with the nominal parameters in section 4.4 has been repeated to check the performances with the proposed beam parameter sets 1, 2 and 3 in Table 4.1. The average train luminosity, normalized to the peak luminosity with nominal parameters is shown in Fig. 4.9 for different amplitudes of the bunch-to-bunch jitter applied to each beam.

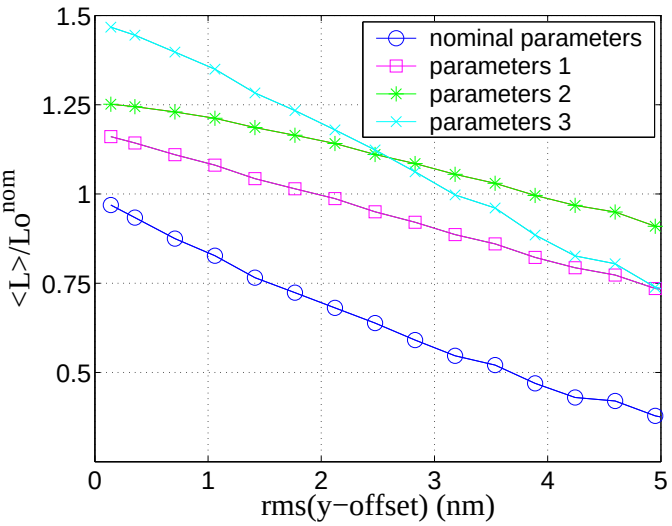

Figure 4.9: Average train luminosity normalized to the peak luminosity of the nominal beam parameter set for e^-e^- versus r.m.s. vertical offset difference between the beams. The results shown include a 100 nm initial offset for each train.

As expected from the beam parameter optimization, parameter sets 1 and 2, with bunch lengths 0.7 and 0.5 times the nominal one respectively, have increased peak luminosity and smaller sensitivity to the vertical IP offsets compared with the nominal one. Parameter set 3 has the highest peak luminosity, but with similar sensitivity to the offsets as for the nominal case.

4.6 Realistic beam-based feedback simulation

4.6.1 Generation of ground motion

In order to verify that the assumptions on the ground motion amplitudes considered in the simplified simulation of the feedback system carried out in section 4.4 are acceptable, a more realistic simulation has been carried out. It has been performed for the case of nominal beam parameters for both e^+e^- and e^-e^- collisions. This simulation has been done with the tracking code PLACET [51] which allows to misalign every element of the BDS of both lines based on a ground motion Monte Carlo generator built from measurements taken at different sites and including both spatial and temporal correlations.

Three ground motion models are available, with different levels of noise (see section 4.2). For the simulation, the elements of both BDS lines are misaligned applying the intermediate noise model B [52]. The time interval used to sample the ground motion was 0.2 s, corresponding to the frequency at which trains are delivered.

To check the misalignments produced by this model along the lattice as function of time, the *r.m.s.* displacements for 50 seeds of the generator were calculated. Fig. 4.10 and Fig. 4.11 show, respectively, the difference and the sum of the vertical misalignments produced at each element in the electron line with respect to the same element in the positron one, for successive time intervals.

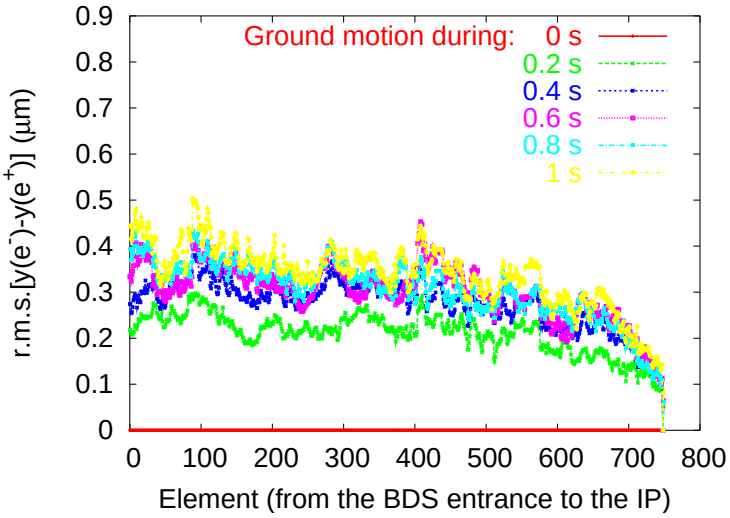

Figure 4.10: Difference in misalignment of each BDS element in the e^- line with respect to the same element in the e^+ one. Ground motion model B was applied at successive time intervals. The results are the *r.m.s.* of 50 seeds.

The fact that the sum of the misalignments is bigger than the difference between corresponding elements of the e^- and e^+ lines indicates that there is a certain level of spatial coherence in the ground vibration. When the elements are displaced in the same direction, both beams move together at the IP.

The simulation of the beam-based IP position feedback system, is only sensitive to the difference between the beams at the IP, while other deviations of the trajectories with respect to the ideal trajectory should be corrected upstream, with a slower feedback which maintains the magnets correctly positioned along the beam lines, or through appropriately placed magnetic correctors. As will be shown, such corrections, while not essential to keep the beams in collision at the IP, are important to maintain the optical quality of the beam spot, and hence the luminosity.

The closer the elements are to the IP, the smaller are the misalignments produced. For elements far away from the IP, the misalignments with respect to the same element of the opposite line become larger. However, as shown in Figs. 4.1 and 4.2, tolerances also tend to be more relaxed in this case.

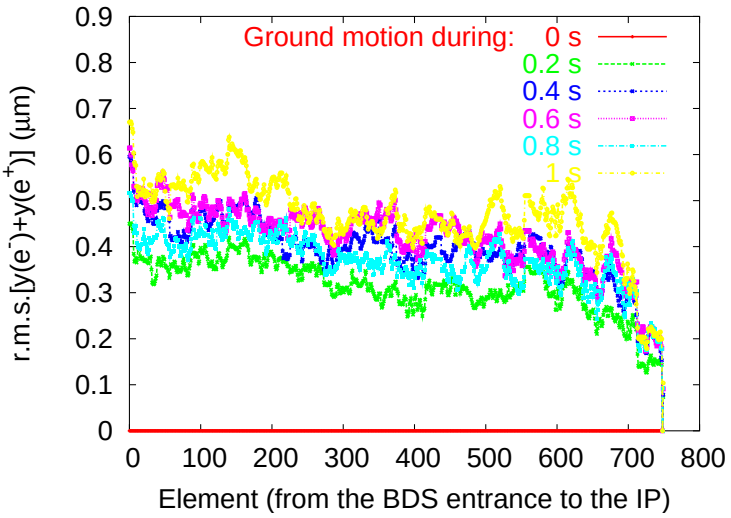

Figure 4.11: Sum of the misalignments of each BDS element in the e^- line with respect to the same element in the e^+ one. Ground motion model B was applied at successive time intervals. The results are the *r.m.s.* of 50 seeds.

4.6.2 Beam-based IP position feedback simulation

For the simulation of the IP position feedback, after tracking the beams through the BDS lattices misaligned by the ground motion with the code PLACET [51], the beam-beam collision is simulated with the code GUINEA-PIG [48] to obtain the outgoing angle that will serve to compute the correction. The beam position of the next bunch is corrected with a kicker located upstream of the IP just before the FD[1]. The operation is repeated bunch-to-bunch.

Figs. 4.12 and 4.13 illustrate the feedback responses for different individual seeds, for e^+e^- and e^-e^- collisions, respectively. The average luminosity performance as a function of time is obtained with typically 50 such seeds. Such results are shown in Fig. 4.14. The correction for the e^-e^- collisions is slower compared with the e^+e^- ones as the slope relating the outgoing angle with the IP offsets for the e^-e^- case is ~6 times the one for e^+e^- , which is needed to avoid noise amplification.

Another important observation is that the larger a ground motion is applied, the more important are the misalignments in the lattice, and the smaller is the final luminosity which can be recovered with the beam-beam deflection based IP position feedback. Although 70 or 80% of the luminosity can be recovered after 1 s, the deterioration of the beam sizes due to the optical effects caused by upstream misalignments makes it impossible to recover more than about 30 or 40% of the luminosity after *e.g.* 300 s, and other feedback loops are required.

[1]If the kicker would be placed upstream of the FD, it could cause the beam to pass off-axis in the sextupoles used for the local chromaticity correction (see section 4.1), leading to unwanted optical effects on the IP spot sizes. The location of the kicker in the simulation upstream of the IP, just before the FD, is an idealized position to avoid this effect. In the real design, there is not enough space before the FD, and the kicker is placed in the middle of the FD (between SD0 and QF1). This causes some limitations on the range of corrections which can be applied.

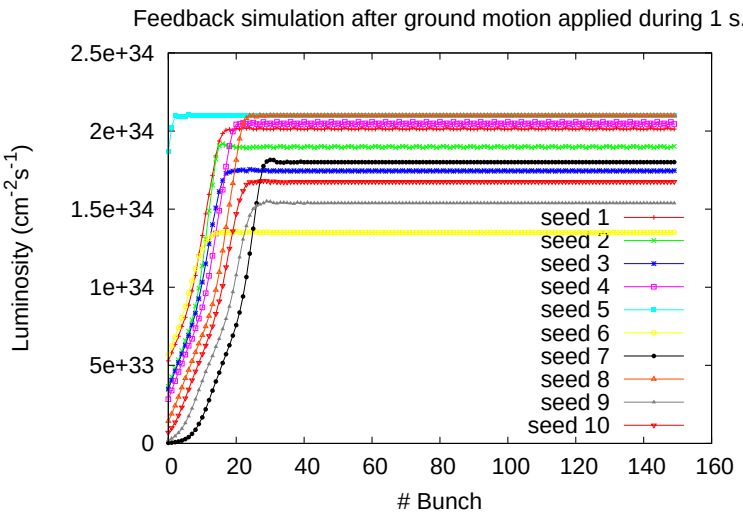

Figure 4.12: Feedback simulation for different individual seeds for e^+e^- collisions with ground motion model B applied during 1 s along the BDS.

4.6.3 Feedback simulation including IP angle correction

The IP angle correction has been included in the simulation in order to correct the position of the beams along the Final Focus System (FFS), and thus mitigate the beam size increase produced by passing off-axis through the sextupoles, in order to check if the nominal luminosity can be recovered after the correction of the beam offsets at the IP, at least for misalignments produced by the ground motion applied during some seconds or minutes.

The angle at the IP is corrected with a kicker located at the entrance of the FFS, at $n\pi$ phase-advance from the IP. The angle is corrected by zeroing the signal in a BPM located at a phase $\pi/2$ downstream from the kicker.

Figure 4.15 illustrates the feedback responses for ground motion applied during successive time intervals, for e^+e^- (left) and e^-e^- (right) collisions, including both IP position and angle correction. The average relative luminosity is also calculated over 50 seeds.

The results indicate that about 20 % more of luminosity can be recovered for e^+e^- collisions by correcting the IP angle compared to the case where only the IP position correction was considered (see Figs. 4.14 and 4.15). In the case of the e^-e^- collisions with the nominal e^+e^- parameters, the big sensitivity to the vertical offsets at the IP means that there is less improvement correcting the angle. The correction of the IP angle would also benefit e^-e^- collisions when beam parameters with reduced disruption at the IP were under consideration. Fig. 4.16 compares the maximum luminosity that can be recovered as a function of time for e^+e^- and e^-e^- collisions, after the bunch corrections corresponding to Fig. 4.15 have been performed. For the cases where the ground motion is applied during a longer time, the luminosity recovered in the case of e^-e^- collisions is smaller than in the e^+e^- case, and the errors are much bigger. This is due to the fact that in the e^-e^- case, the luminosity has not been completely recovered, and more than 250 bunches are needed for that. The luminosity cannot be recovered to 100% of the nominal value after a few seconds of ground motion applied solely with position and angle feedback, due to optical effects along the FFS, responsible for increasing of the beam size at the IP, but the feedback performance is rather similar for e^+e^- and e^-e^- collisions. The correlation

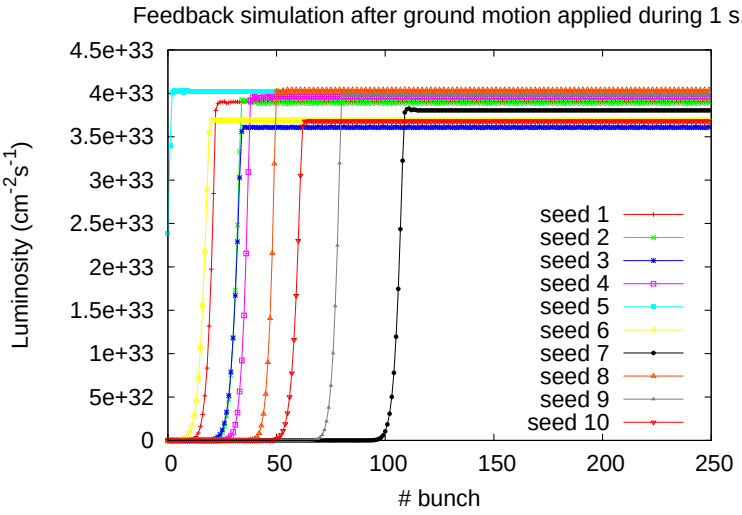

Figure 4.13: Feedback simulation for different individual seeds for e^-e^- collisions with ground motion model B applied during 1 s along the BDS.

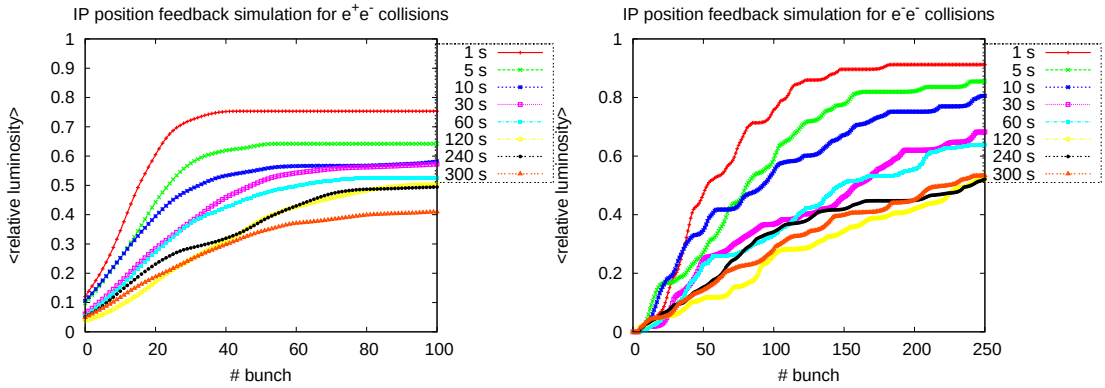

Figure 4.14: Feedback simulation for the e^+e^- (left) and e^-e^- (right) collisions with ground motion model B applied during different times along the BDS. The average relative luminosity is calculated over about 50 seeds.

between the vertical beam size at the IP and the luminosity is shown in Fig. 4.17 top. The luminosity loss is directly related to the increased beam size since there is no significant residual offset between the beams at the IP, and the offsets are not correlated with the luminosity, as shown in Fig. 4.17 bottom.

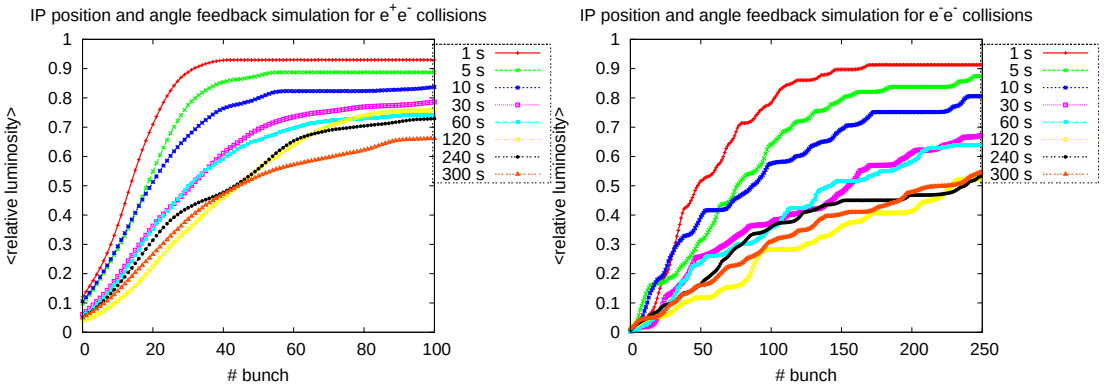

Figure 4.15: Beam-based IP position and IP angle feedback simulation for e^+e^- (left) and e^-e^- (right) collisions with ground motion model B applied during different times along the BDS. The average relative luminosity is calculated over 50 seeds.

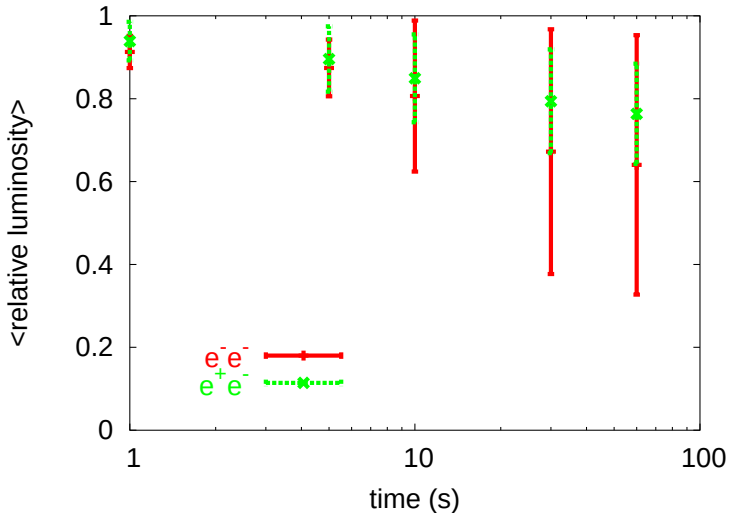

Figure 4.16: Average relative luminosity for e^+e^- and e^-e^- collisions as function of time after the beam-based IP position and angle feedback system has recovered the maximum luminosity achievable after the bunch corrections corresponding to Fig. 4.15. About 50 seeds are used in the simulation.

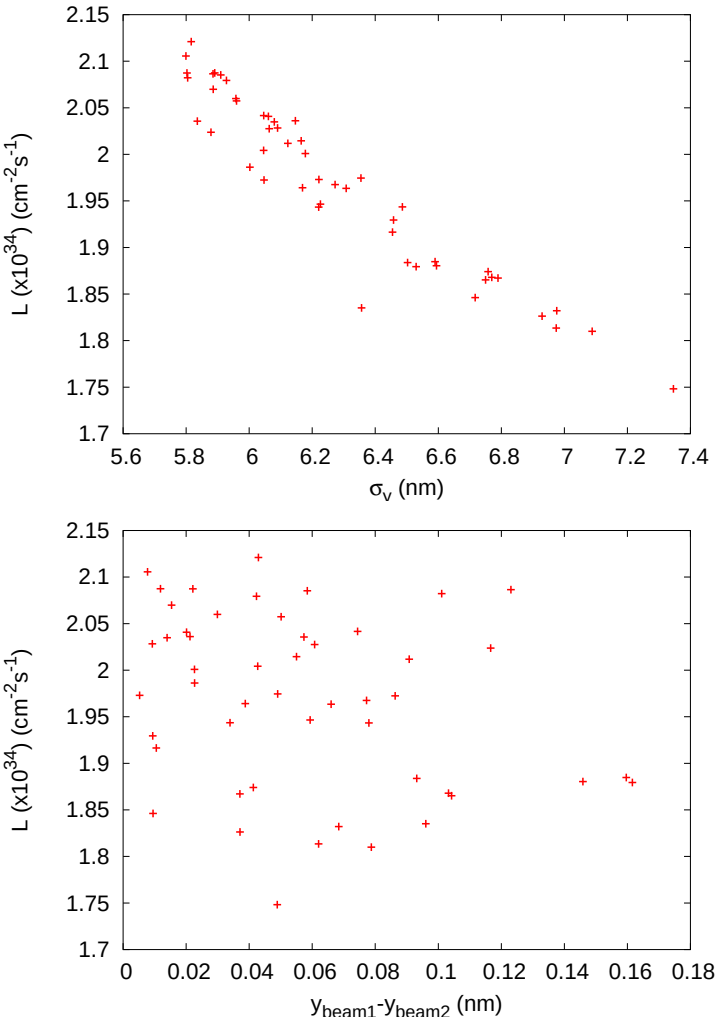

Figure 4.17: Luminosity versus the combined vertical beam sizes of both e^- and e^+ beams at the IP (top) and luminosity versus the vertical position difference of both beams at the IP (bottom). Feedback simulation carried out for e^+e^- collisions under the effect of the misalignments produced by the ground motion after 1 s.

Chapter 5

Optics studies for the e^-e^- option

Optics studies have been done to verify the feasibility of adapting the BDS and the extraction line for the e^-e^- option at the ILC with the proposed alternative beam parameters which reduce the disruption between the bunches (see section 4.5.1). The studies have been done both for the large (20 mrad) and small (2 mrad) crossing-angle geometries. The latter presents specific difficulties due to the fact that the incoming and the outgoing lines have some magnets in common (see Figs. 2.10 and 5.19).

5.1 Optics studies for the 20 mrad crossing angle geometry

5.1.1 Final Focus System

Obtaining new β-functions at the IP

To obtain the proposed beam parameters described in section 4.5.1 to decrease the disruption between the beams for the e^-e^- collisions, new β-functions must be obtained at the IP. This could be achieved by changing the demagnification of the FFS, but this would spoil the careful correction of geometric and chromatic aberrations achieved in this accelerator section (see Section 2.3). Instead changes in the β-functions at the IP are obtained by re-matching the phase space of the beam injected into the FFS, using quadrupoles in the so-called matching section upstream of the FFS (see Fig. 2.12). The sextupoles are also slightly re-fitted to optimize the correction of the chromatic and geometric aberrations (cancelling out the second order terms T_{126}, T_{346}, T_{122}, T_{324} and T_{166} over the BDS). With this method, in which the demagnification of the FFS is not changed, the range of β-functions achievable at the IP is limited, but a full re-optimization of the higher order terms in the FFS optics is avoided.

The matching of the quadrupoles and sextupoles to obtain new β-functions at the IP has been done with the program MAD [57], using the version 2006a of the ILC BDS FFS optics for the nominal parameters at 500 GeV center-of-mass energy [58]. The obtained transverse β-functions and the horizontal dispersion of the BDS for the parameter sets 1, 2 and 3 in Table 4.1 are shown in Figs. 5.1, 5.2 and 5.3 respectively (the optics for the nominal parameters is also shown for comparison in Fig. 5.4).

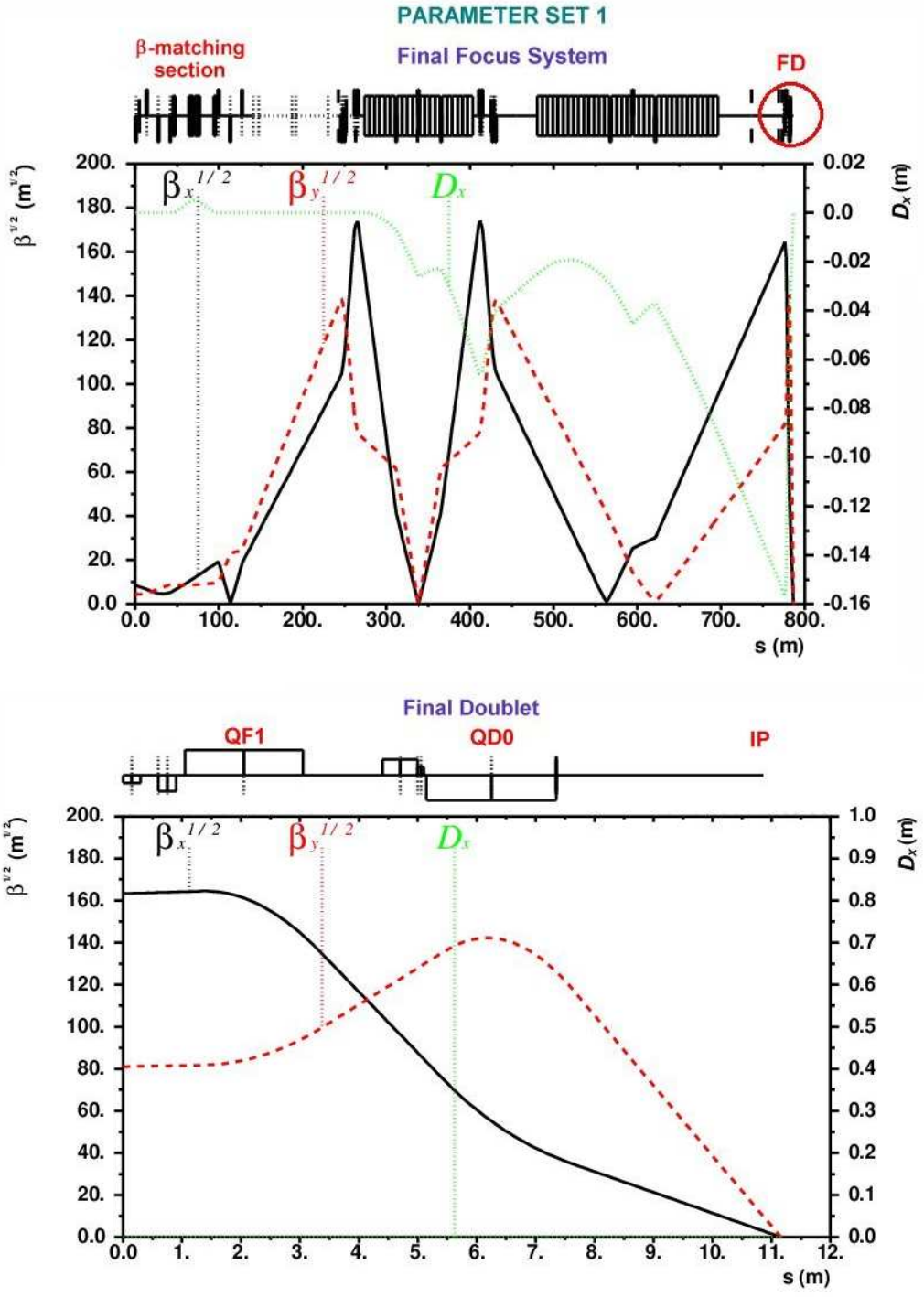

Figure 5.1: Optical functions of the ILC FFS (top) for the parameter set 1 in Table 4.1 (β_x^*=10.3 mm, β_y^*=0.9 mm). A zoom of the optical functions of the FD region is also shown (bottom).

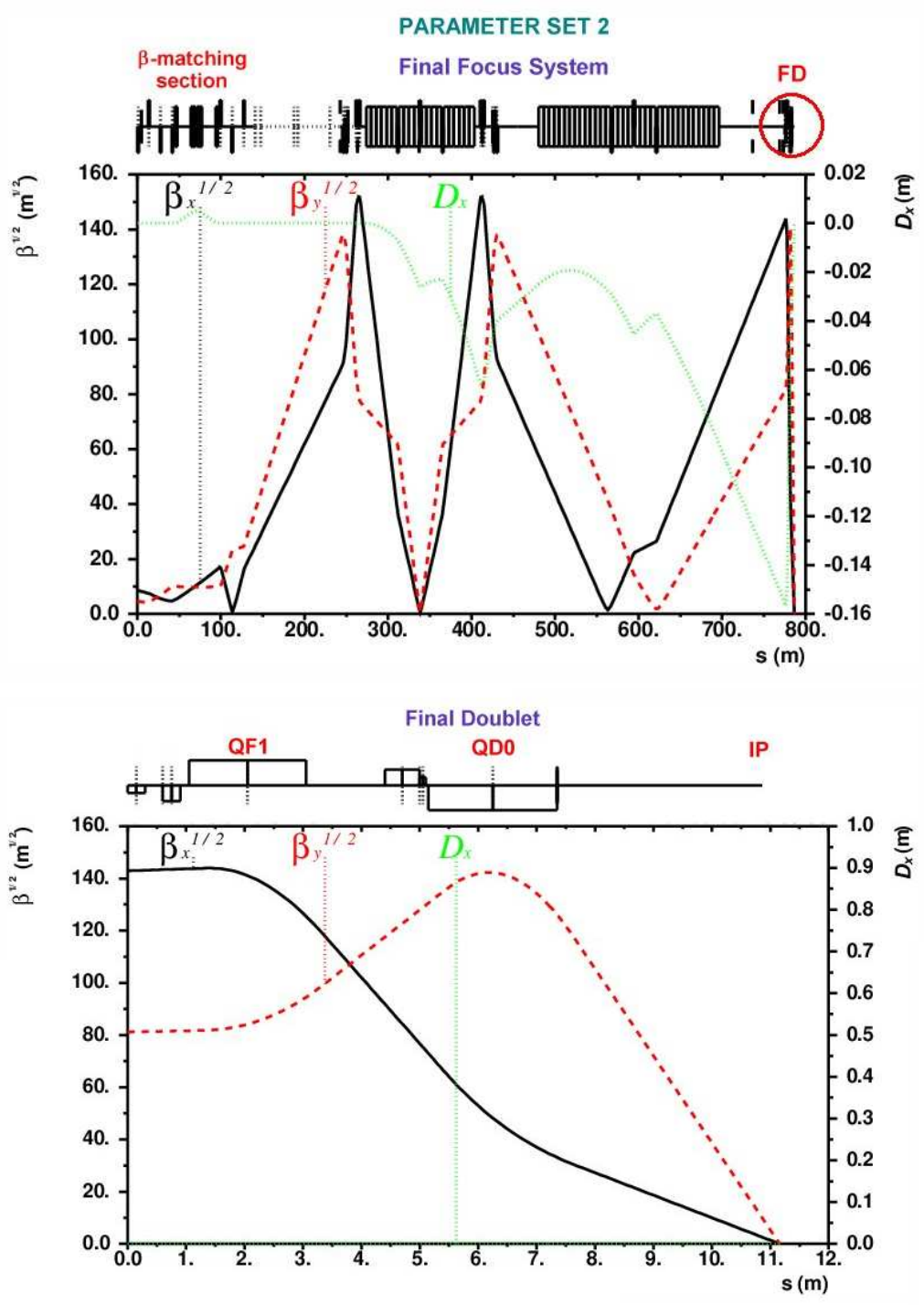

Figure 5.2: Optical functions of the ILC FFS (top) for the parameter set 2 in Table 4.1 (β_x^*=13.4 mm, β_y^*=0.9 mm). A zoom of the optical functions of the FD region is also shown (bottom).

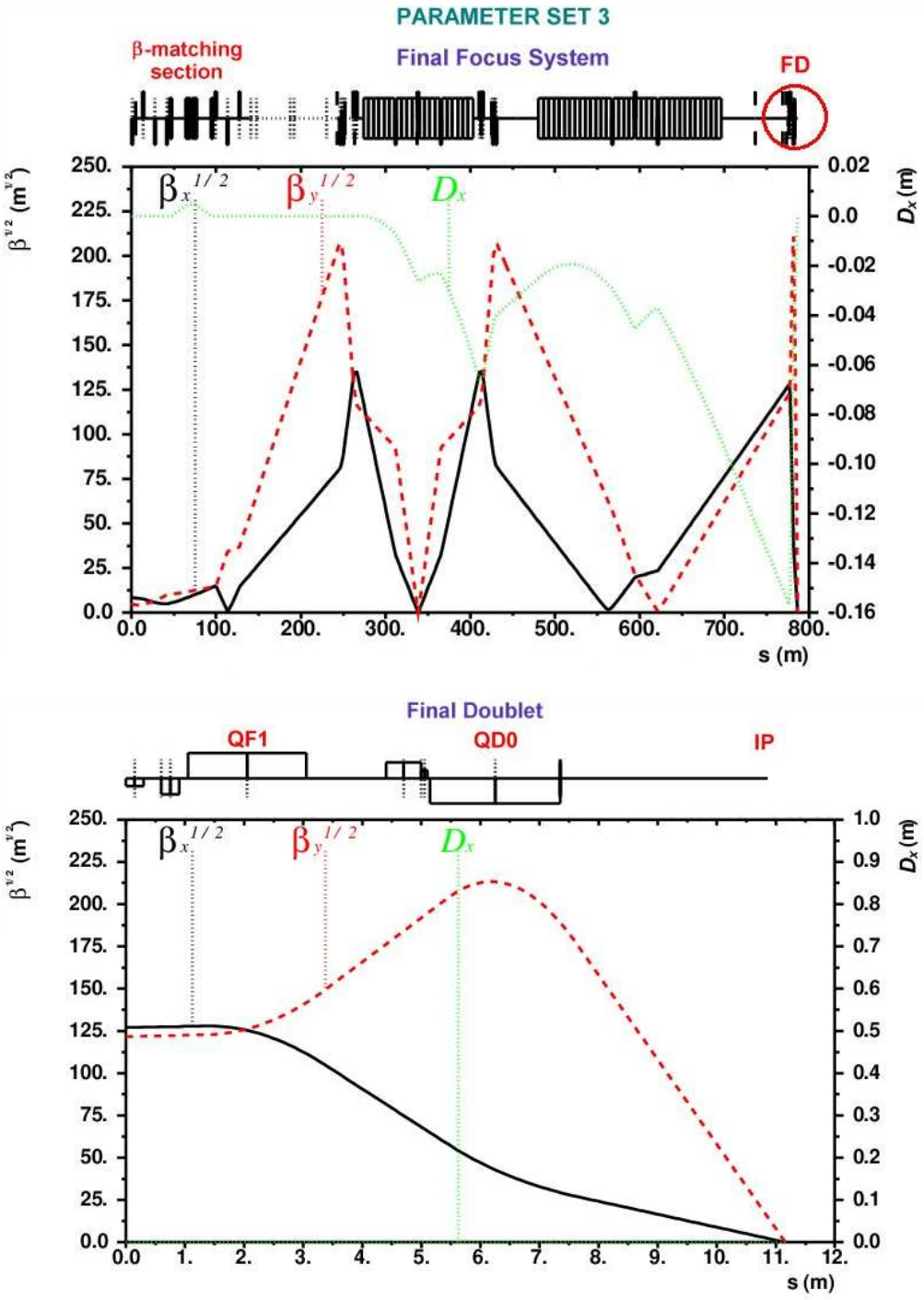

Figure 5.3: Optical functions of the ILC FFS (top) for the parameter set 3 in Table 4.1 (β_x^*=17.0 mm, β_y^*=0.4 mm). A zoom of the optical functions of the FD region is also shown (bottom).

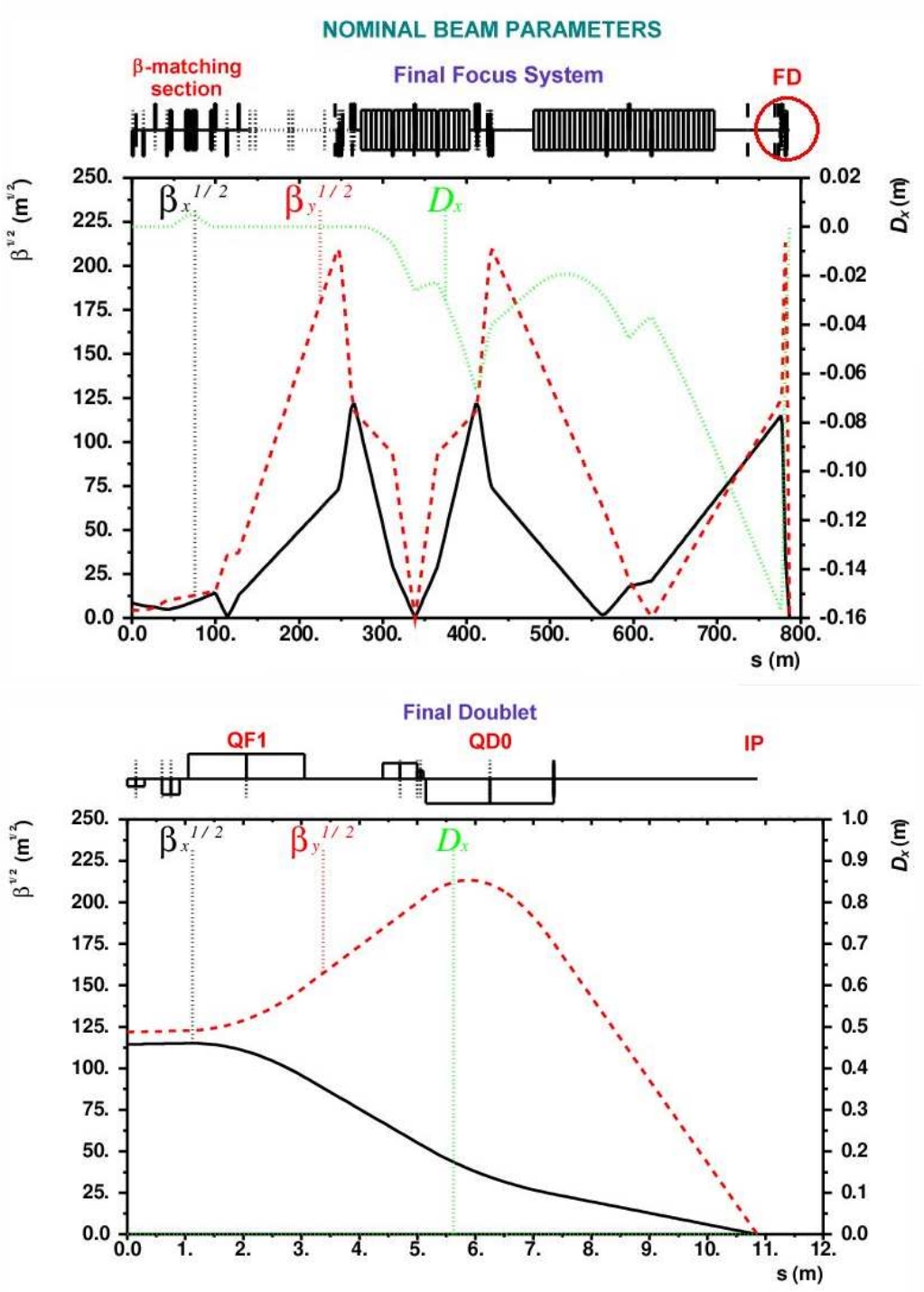

Figure 5.4: Optical functions of the ILC FFS (top) for the nominal parameters in Table 2.2 (β_x^*=21.0 mm, β_y^*=0.4 mm). A zoom of the optical functions of the FD region is also shown (bottom).

The proposed parameter sets 1, 2 and 3 are within the range of beam parameters defined for the ILC, and thus, from an optical point of view, are not difficult to achieve. Going to rounder beams to obtain these new β-functions at the IP decreases the maximum vertical β-function at the FD, whose maximum value for the nominal case is $\beta^{1/2} \approx 211$ m$^{1/2}$. This will neither increase the collimation depth, as the synchrotron radiation in the FD doesn't increase with respect to the set of ILC parameters considered in the current design for e^+e^- (see section 3.4.1), nor pose problems from the point of view of a possible impact of the beam with the apertures of the elements.

Optical bandwidth

A way to estimate the importance of the residual high-order chromatic aberrations from the FFS optics is to evaluate the momentum acceptance of the system. The performance of the different parameter sets can be studied from this point of view, through tracking simulations taking into account the higher order terms in the optical transport.

Transverse Gaussian beam distributions of 50000 particles with the β-functions corresponding to the entrance of the BDS ($\beta_{x/y}$=19.9/23.5 m) and the nominal normalized emittances ($\epsilon^*_{x/y,N}$=10/0.04 μm) are created with PLACET [51], for a flat energy distribution with 0.1% full width. Figure 5.5 shows the transverse phase space distributions and the energy distribution of the beam at the entrance of the BDS. The beam is then tracked through the BDS with MAD [57], and the obtained distributions of particles are used as an input for GUINEA-PIG [48], which simulates the collision to obtain the luminosity. Figures. 5.6, 5.7 and 5.8 show the transverse phase space distributions and the energy distribution of the beam at the IP, before the collision, after the tracking through the BDS, for the case of the parameter set 1, 2 and 3, respectively.

To evaluate the momentum acceptance of the FFS, different beam distributions have been created with an energy spread of 0.1%, for different central energies within ±1% of the nominal beam energy, and then tracked through the BDS and collided with GUINEA-PIG.

Figure 5.9 shows the optical bandwidth obtained for the different ILC proposed parameter sets in Table 2.2. Figure 5.10 shows the same result for the optics of the parameter sets 1, 2 and 3 for e^-e^- collisions in Table 4.1. The luminosities are normalized to the luminosity with nominal parameters without momentum offset. Dependencies with energy are rather flat in the vicinity of the nominal value, and the luminosity loss within the ±1% range is not bigger than 40% in any case. This is comparable to, and actually better than, the results obtained for the different ILC parameter sets in Fig. 5.9.

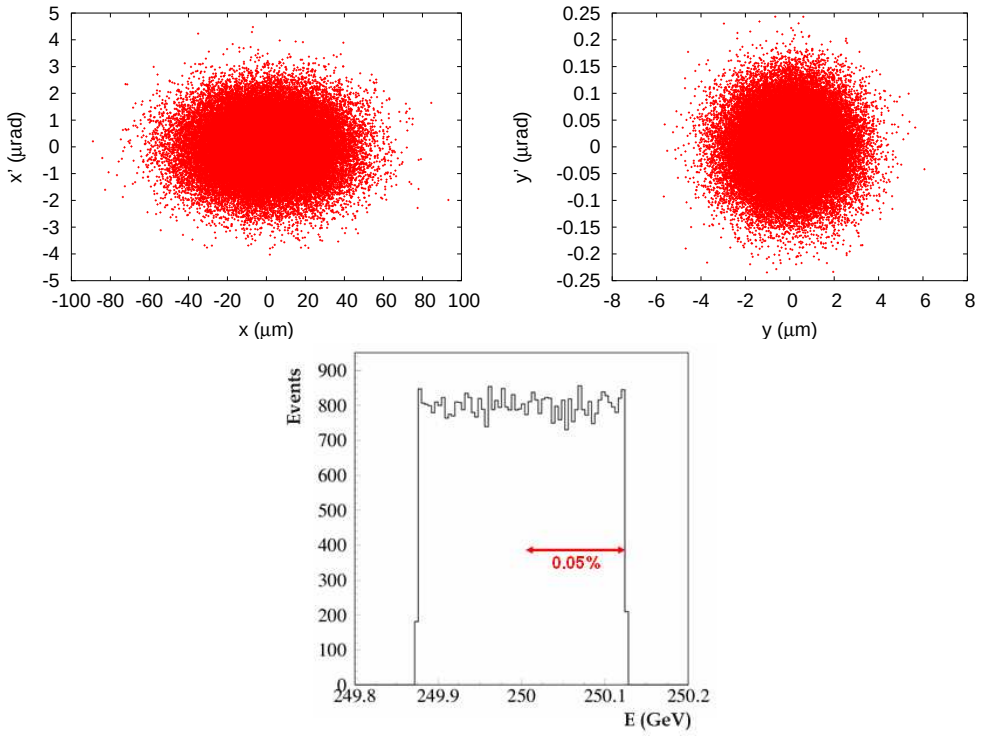

Figure 5.5: Transverse phase space (top) and energy distribution (bottom) of the beam at the entrance of the BDS. Distribution created with PLACET with 50000 macroparticles, with an energy spread of 0.1%.

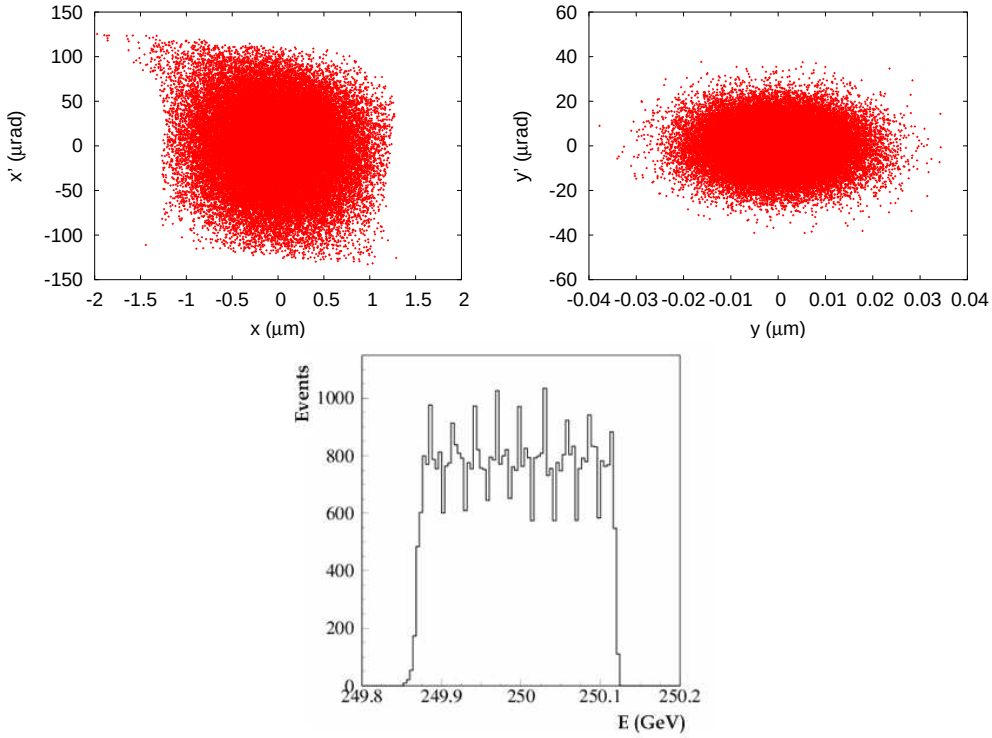

Figure 5.6: Transverse phase space (top) and energy distribution (bottom) of the beam tracked through the BDS, for the parameter set 1 in Table 4.1.

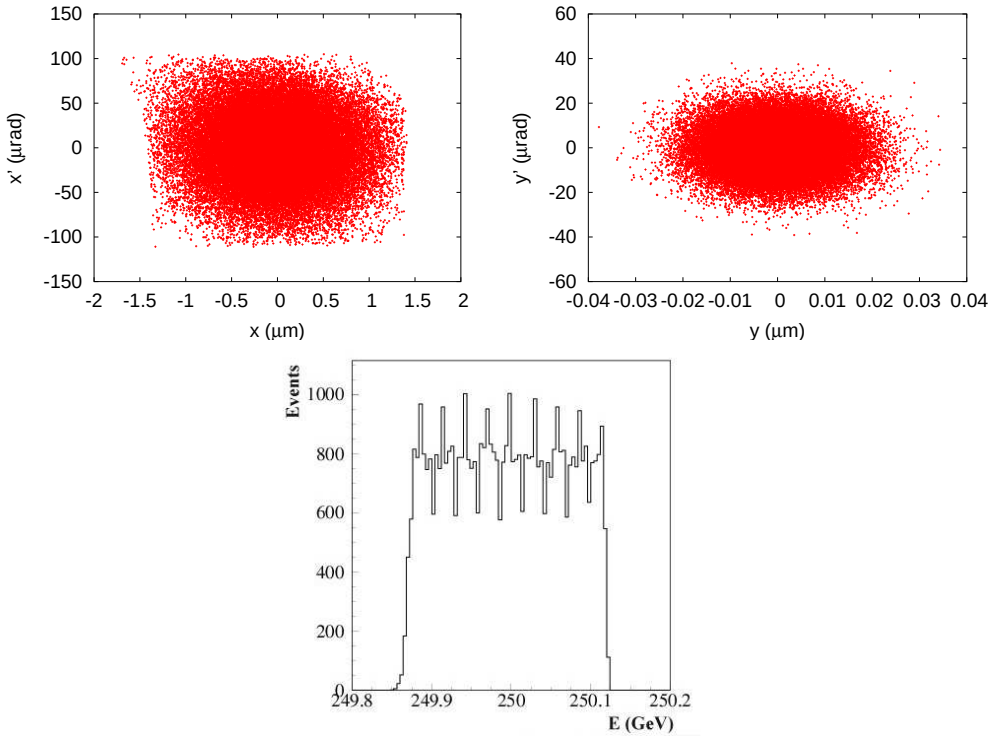

Figure 5.7: Transverse phase space (top) and energy distribution (bottom) of the beam tracked through the BDS, for the parameter set 2 in Table 4.1.

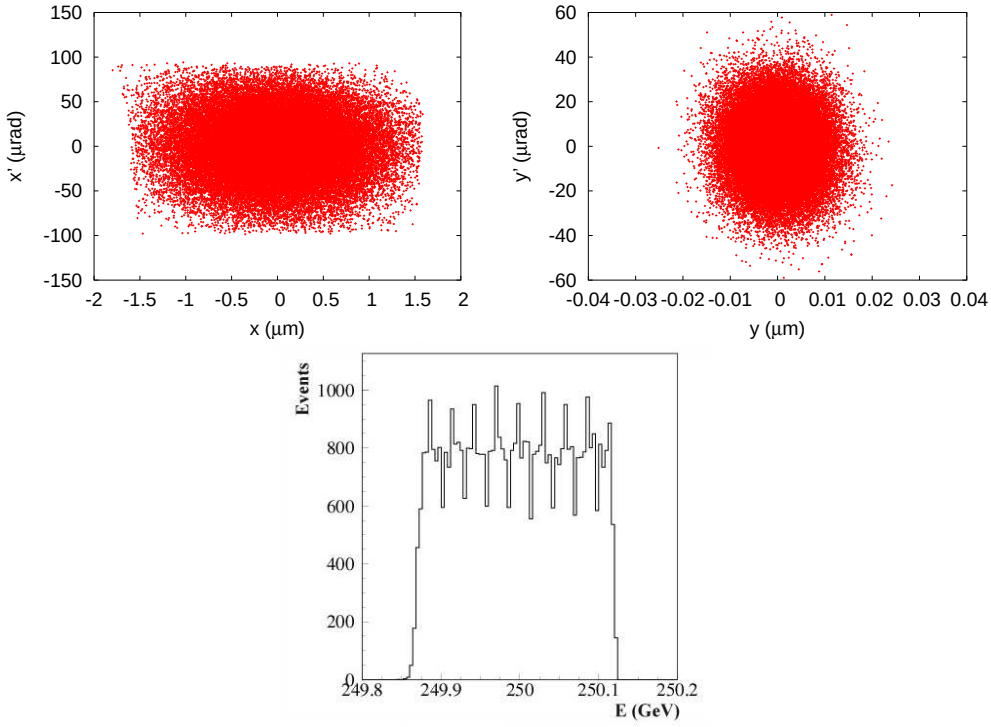

Figure 5.8: Transverse phase space (top) and energy distribution (bottom) of the beam tracked through the BDS, for the parameter set 3 in Table 4.1.

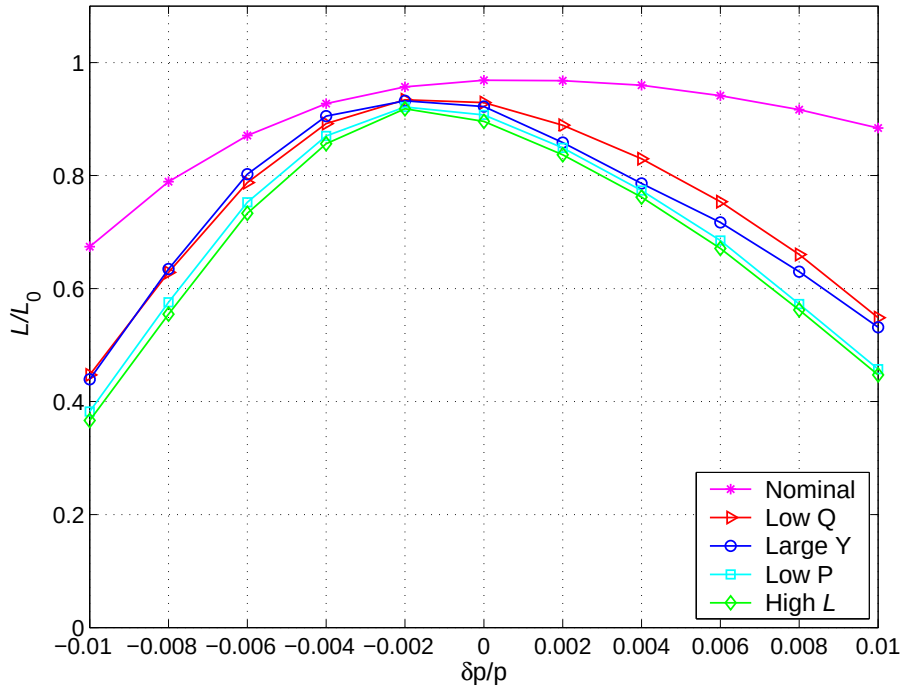

Figure 5.9: Optical bandwidth for the different ILC beam parameters at 500 GeV center-of-mass energy in Table 2.2. The luminosities are normalized to the luminosity obtained with GUINEA-PIG for ideal Gaussian beam distributions in each case.

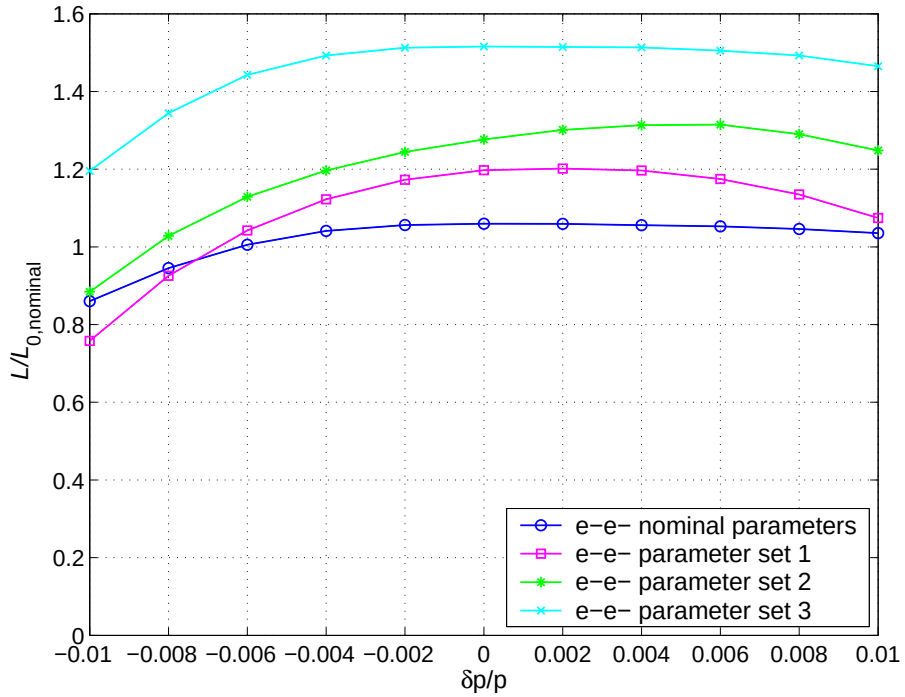

Figure 5.10: Optical bandwidth for the parameter sets 1, 2 and 3 in Table 4.1 for e^-e^- collisions. The luminosities are normalized to the ideal luminosity with nominal parameters.

5.1.2 Extraction line

Linear optics

The transport in the extraction line of the post-collision spent beam has been studied with the proposed parameters in Table 4.1 for the e^-e^- mode in the extraction line. Figures 5.11, 5.12 and 5.13 show the transverse phase space of the spent beam at the IP in the case of parameter sets 1, 2 and 3, respectively.

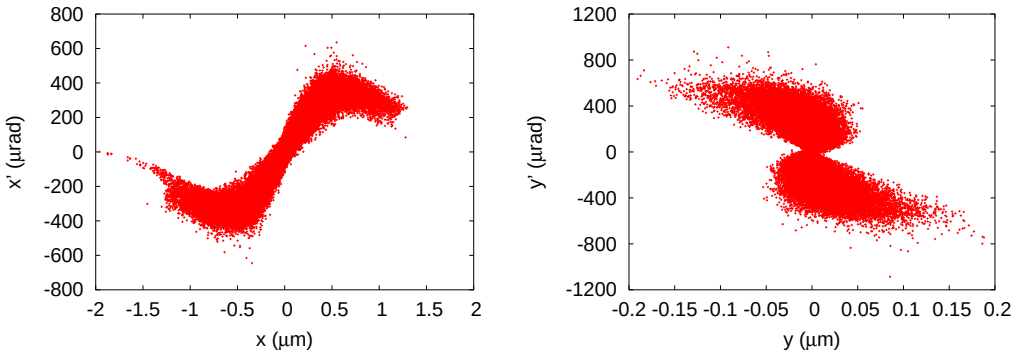

Figure 5.11: Beam phase space in the vertical and horizontal planes of the beam at the IP after the collision, corresponding to the parameter set 1 in Table 4.1.

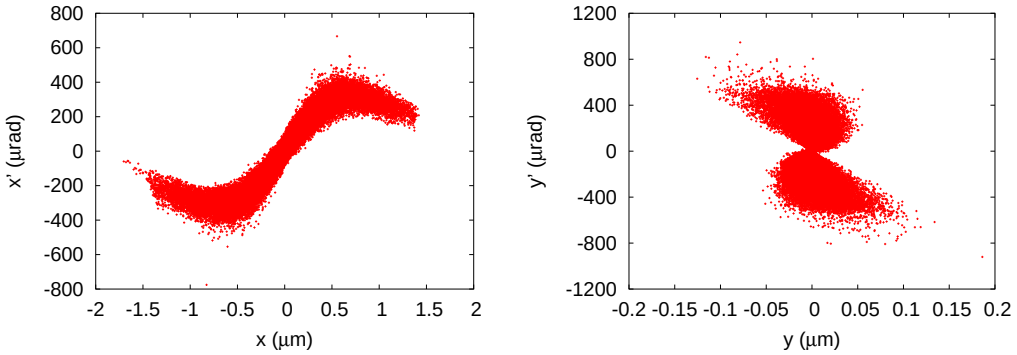

Figure 5.12: Beam phase space in the vertical and horizontal planes of the beam at the IP after the collision, corresponding to the parameter set 2 in Table 4.1.

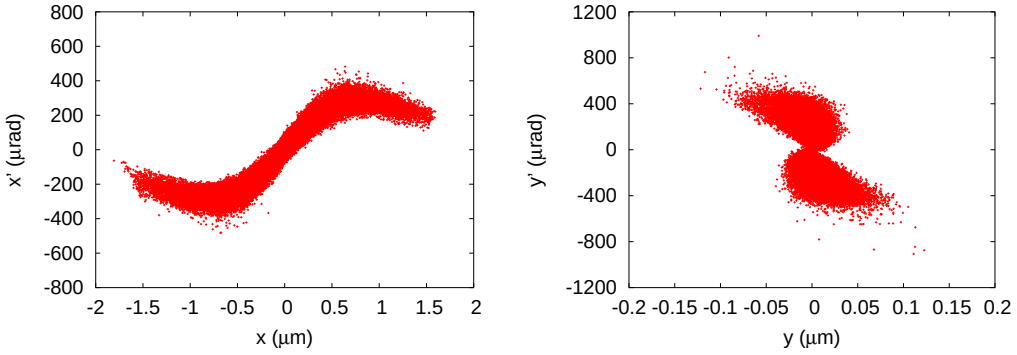

Figure 5.13: Beam phase space in the vertical and horizontal planes of the beam at the IP after the collision, corresponding to the parameter set 3 in Table 4.1.

The Twiss parameters of the disrupted beam are calculated from the distributions obtained with GUINEA-PIG after the collision as explained below.

The beam emittance ϵ_{xyz} represents the volume of the beam occupied in the phase space. Considering only the horizontal plane, the emittance ϵ_x can be obtained from [59]:

$$\epsilon_x = \sqrt{\langle x^2\rangle\langle x'^2\rangle - \langle xx'\rangle^2} \tag{5.1}$$

where the first moments or means of the distributions in position and angle have been subtracted, *i.e.*, the coordinates are defined with respect to the static position and angle offset of the core of the beam. The averages are taken over the distribution of the beam particles (see Appendix A).

The optical functions β and α are proportional to the second moments of the beam distribution, and can be written as a function of the emittance as[1]:

$$\beta_x = \langle x^2\rangle/\epsilon_x, \tag{5.2}$$

$$\alpha_x = -\langle xx'\rangle/\epsilon_x, \tag{5.3}$$

and analogously for the vertical plane.

The Twiss parameters obtained for the disrupted beams, corresponding to the different parameter sets for e^-e^- collisions are shown in Table 5.1. The Twiss parameters corresponding to the post-collision beam for nominal beam parameters and and for the High Luminosity set (High $\mathcal{L}$) for e^+e^- collisions are also shown for comparison. The High Luminosity set represents the worst case in terms of performances of the beam transport, since the beam spot sizes are smaller than for the nominal case.

The obtained Twiss parameters for the post-collision beams have been used as input to obtain the corresponding optical functions along the extraction line with MAD. Figures 5.14, 5.15, 5.16 and 5.17 show the optics of the extraction line, for the parameter sets 1, 2, 3 (e^-e^- collisions) and High Luminosity (e^+e^- collisions), respectively. For all the proposed parameter sets for e^-e^- collisions, rather similar β-functions are found along the extraction line. They are also rather similar to the β-functions obtained for the High Luminosity e^+e^- set, for which the extraction line is specified.

Table 5.1: Normalized emittances and Twiss parameters for the disrupted beams corresponding to the High Luminosity parameters for e^+e^- collisions and to the parameter sets 1, 2 and 3 in Table 4.1 for e^-e^- collisions.

	Nominal	**High $\mathcal{L}$**	**set 1**	**set 2**	**set 3**
$\epsilon_{x,N}$ (μm·rad)	27.5	29.9	24.2	24.1	24.1
$\epsilon_{y,N}$ (μm·rad)	10.1	10.0	2.80	1.89	1.38
β_x(mm)	7.3	3.36	4.18	5.35	6.74
β_y(mm)	0.36	0.17	0.14	0.08	0.09
α_x(rad)	2.08	2.02	-2.10	-2.22	-2.24
α_y(rad)	0.67	0.60	0.79	0.42	0.65

[1]The assumption of no x-y coupling is made.

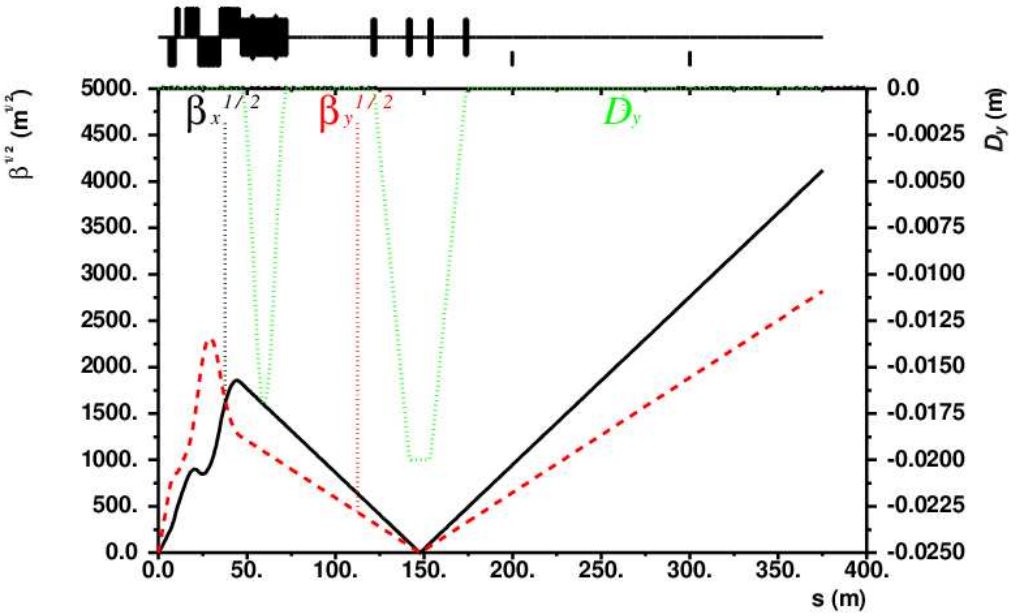

Figure 5.14: Optical functions of the extraction line for the input disrupted parameters corresponding to parameter set 1 for e^-e^- collisions in Table 4.1.

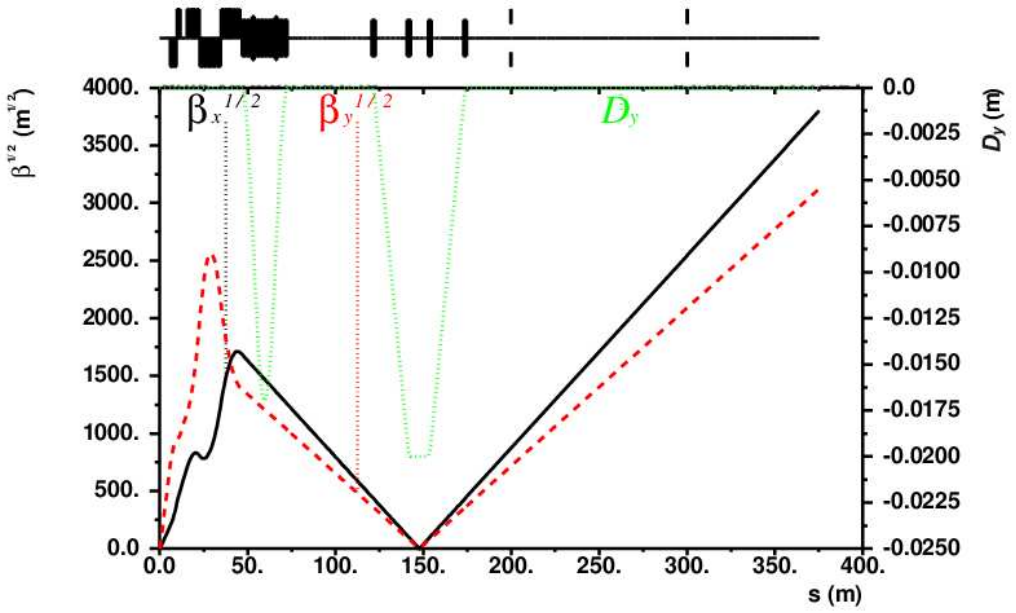

Figure 5.15: Optical functions of the extraction line for the input disrupted parameters corresponding to parameter set 2 for e^-e^- collisions in Table 4.1.

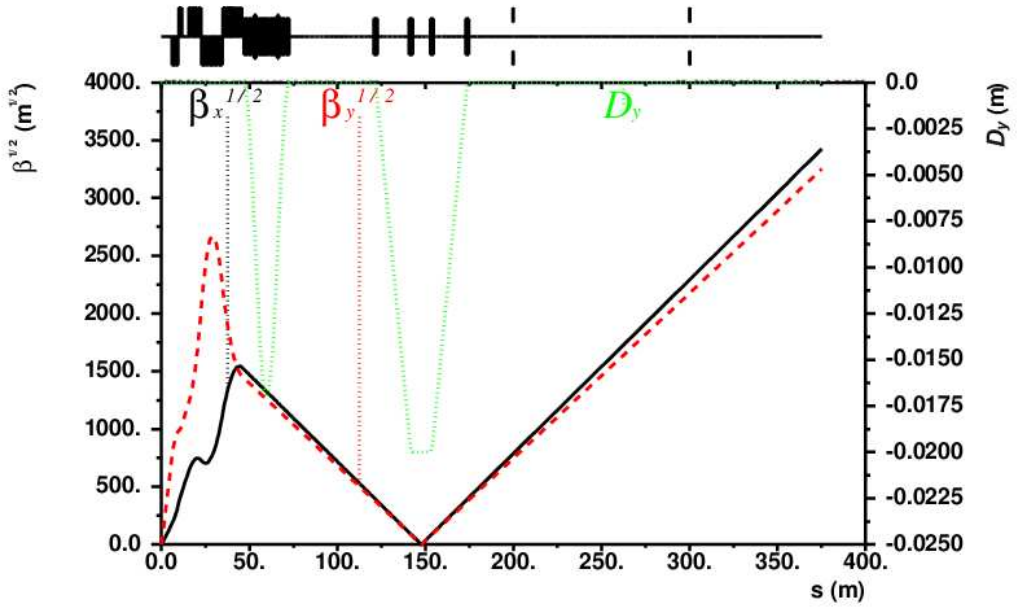

Figure 5.16: Optical functions of the extraction line for the input disrupted parameters corresponding to parameter set 3 for e^-e^- collisions in Table 4.1.

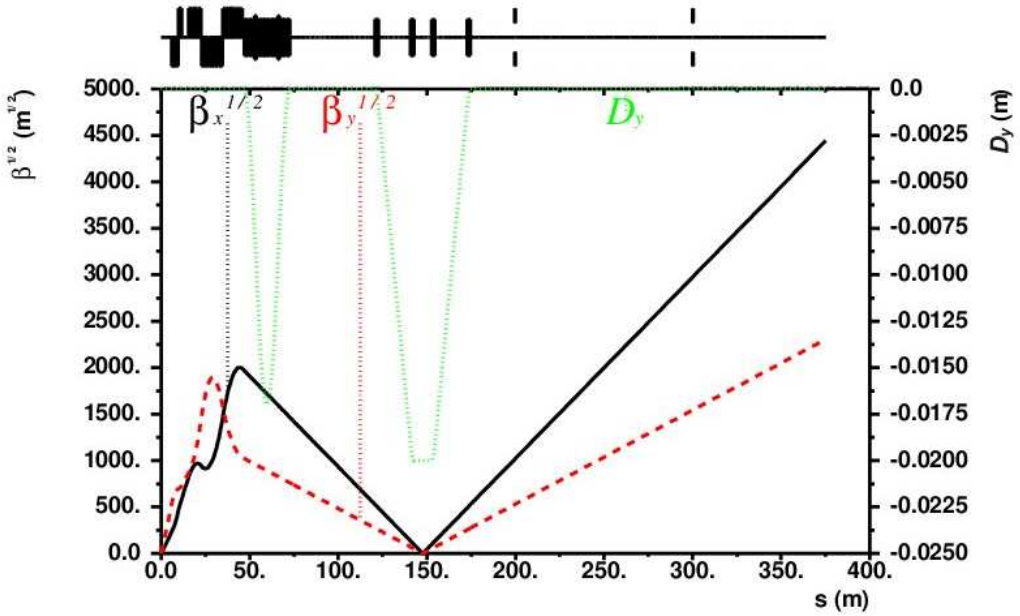

Figure 5.17: Optical functions of the extraction line for the input disrupted parameters corresponding to the High Luminosity set for e^+e^- collisions in Table 2.2.

Power losses along the extraction line

In addition to the linear optics, effects due to the particles in the lower end of the energy distribution must be studied. For this purpose, a complete tracking simulation has been done to compute the power loss deposition along the extraction line using the code BDSIM[2] [60]. The post-collision beam distributions obtained with GUINEA-PIG are used as an input for this simulation. For all the proposed parameter sets for the e^-e^- collisions, the post-collision beam at the IP gives rather similar Twiss parameters, and the optics along the extraction line are rather similar for all the cases. For the case of the parameter set 2, slightly higher β-functions are found along the extraction line. A comparison of the power loss deposition for this parameter set for e^-e^- collisions with the High Luminosity parameters for e^+e^- collisions is shown in Fig. 5.18. Besides the collimators at 200 and 300 m, the biggest losses found in the first part of the line do not exceed a couple of tens of W.

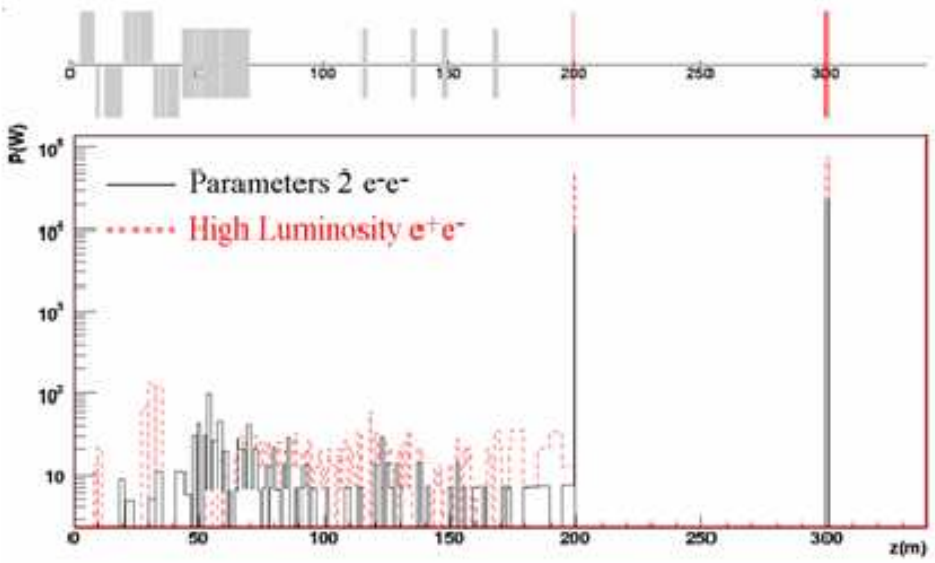

Figure 5.18: Power losses along the extraction line for the parameter set 2 in Table 4.1 for e^-e^- collisions and for the High Luminosity parameters for e^+e^- collisions at 500 GeV center-of-mass energy [60].

5.2 Optics studies for the 2 mrad crossing angle geometry

In the 2 mrad crossing-angle geometry the spent beam is transported off-axis through the last quadrupole of the FFS, which is defocusing in the horizontal plane. The kick produced by this quadrupole is used to extract the spent beam. Fig. 5.19 shows a schematic of this.

Such a scheme works in the case of e^+e^- collisions, but not for e^-e^-, since the spent beam passing through the last quadrupole would then experience a kick towards the incoming line, not away from it. To keep the same extraction geometry as for e^+e^-, in

[2]The computation of the power loss along the extraction line with BDSIM has been performed by O. Dadoun.

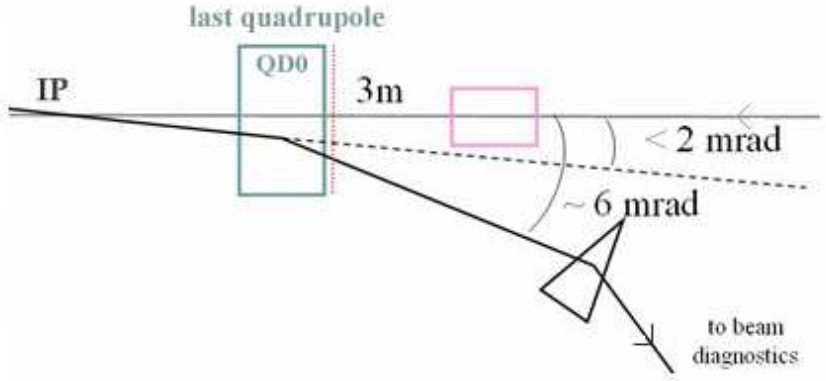

Figure 5.19: Scheme of the extraction of the spent beam in the 2 mrad crossing angle geometry for the e^+e^- mode of operation. The out-going beam passes off-axis through the last quadrupole of the FFS and receives a kick that moves it away from the incoming line.

the case of e^-e^- the signs of the focusing and defocusing final doublet quadrupoles have to be inverted while maintaining at least the strength of the last quadrupole to produce the appropriate kick needed for extraction. A first attempt in this direction [61] indicated that this was feasible, but a large β_y-value had to be used at the IP to limit the vertical beam size in the FD, in order to keep a reasonable collimation depth. In this case, the signs of the magnets of the FD where reversed, keeping the same strengths for both, and the quadrupoles upstream where used to retune the optics. The increase of the vertical β-function was a factor of 30, resulting in about only half the peak luminosity. Improvements with half the bunch length were also investigated, as well as possibilities to decrease the vertical β-function as much as possible while keeping an acceptable collimation depth. Fig. 5.20 shows the optical functions calculated with MAD along the FFS for $\beta^*_{x/y} = 10/3$ mm, for which enhanced overall performance can be expected. The luminosity for this beam parameter set, with half of the bunch length, calculated with GUINEA-PIG, is $\sim 3.7\times10^{33}$ cm^{-2}s^{-1}.

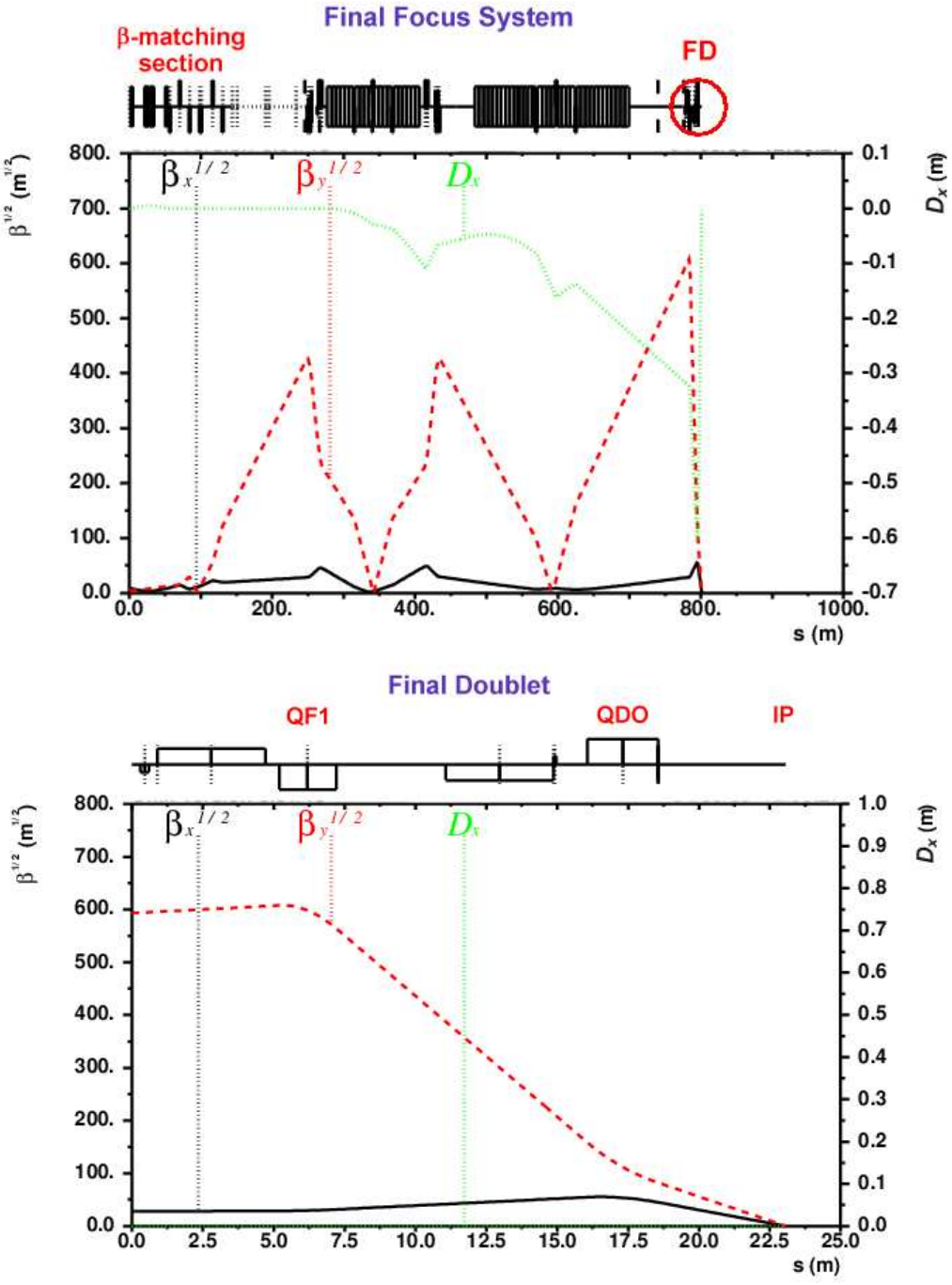

Figure 5.20: Optical functions of the ILC FFS (top) for the 2 mrad crossing angle geometry with $\beta^*_{x/y}$=10/3 mm. A zoom of the optical functions of the FD region is also shown (bottom).

Chapter 6

The Accelerator Test Facility (ATF) and ATF2

An important technical challenge in the construction of a future linear collider is the high gradient acceleration required, but what is similarly challenging is the collision of extremely small beams of a few nanometers in transverse size. In the latter challenge three distinct issues are involved: creating small emittance beams, preserving the emittance during acceleration and transport, and focusing the beams to nanometers. The Accelerator Test Facility (ATF) at KEK (Japan) was built to create small emittance beams. The ATF2 project has recently completed the construction of the ILC-type Final Focus beamline to create a tightly focused, stable beam by making use of the small emittance of the ATF. A study of the preservation of the small emittances along the transport from the ATF DR towards the ATF2 beamline, in particular during the extraction process, is addressed in this thesis.

6.1 ATF and ATF2 facilities

The ultimate goal of any colliding machine is high luminosity. The essential points to achieve such luminosity with an acceptable electric power consumption are the RF to beam power conversion efficiency and the small spot size at the IP, as seen in Chapter 3. The small spot-size at the IP requires small emittances and strong focusing, which implies an important challenge in the construction of a future linear collider. For that, the precise alignment of the components and the stabilization of the beam orbit are critical. Most studies have been done using computer simulations but many issues still remain that require experimental verification.

The ATF facility at KEK (Japan), completed in 1996, was built to demonstrate the small emittance beams needed for future linear colliders. The ATF DR has achieved world records for the normalized vertical emittance, with values as small as 1.5×10^{-8} m·rad at 1.3 GeV [7, 62]. R&D activities are ongoing to further reduce the ring emittance. Of course, there are many other issues which require much technical innovation, as beam diagnostics and instrumentation to characterize such small beams, and the suppression of the transient motions of bunches, since uneven emittances among bunches would lead to an effective loss of luminosity in a future linear collider, in which multi-bunch operation is planned.

ATF2 is a prototype final focus system, recently completed as a result of an interna-

tional collaboration to study the feasibility of focusing and stabilizing the damped ATF beam down to the nanometer scale [8]. The ATF2 final focus system is a down-scaled version that uses the same principle of local chromaticity correction as the ILC and CLIC projects (see Chapter 2). ATF2 will address successively two major challenges of the ILC BDS: focusing the beams to nanometer size and providing sub-nanometer stability.

6.1.1 ATF design

The ATF facility consists of two major parts: a 1.54 GeV S-band injector linac and a DR. It can operate in single or multi-bunch mode. The goal is to generate, accelerate and damp a train of 20 bunches with 2×10^{10} electrons/bunch and 2.8 ns spacing. Figure 6.1 shows the schematic layout of the ATF and ATF2 facilities. The beam is injected from the linac to the DR, by means of the Beam Transport line. The beam is then extracted from the DR and transported by means of the extraction (EXT) line to the ATF2 beamline, whose construction finished in 2008. Before this new EXT line and the ATF2 beamline were constructed, the beam was transported to a dump through an old EXT line, which was shorter than the present one. Figure 6.2 shows the schematic layout of the ATF facility, including the old EXT line.

ATF linac

The 1.54 GeV ATF linac is designed to accelerate multi-bunch electrons for injection to a low-emittance DR. The total length of the linac system is 80 m, which consists of an 18 m-long pre-injector section, a 70 m-long regular accelerator section with energy compensation structures and a remaining 12 m-long space for a beam-transport line to the DR and a positron test stand.

In the pre-injector linac, a laser-driven RF gun with a 1.6 cell S-band Cs_2Te photocathode generates an electron beam with an operational intensity of up to 3.2 nC per bunch. The pre-injector linac contains as well an accelerating structure, a matching section of the beam lattice, an energy analyzer and beam instrumentation.

In the 70 m 1.54 GeV S-band linac, the net length of 50 m is attributed to the accelerating structures, since a space of 20 m is reserved for the linac lattice, beam monitors and energy-compensation system. To achieve an energy of 1.54 GeV with this constraint the gradient has to reach 33 MeV/m with beam-loading. An accelerating field of 35.2 MeV/m is required to accelerate 20 bunches of 2×10^{10} electrons/bunch, assuming 6.3% beam-loading.

Table 6.1 shows the basic beam parameters of the injector linac, required from the DR. The linac is operated at a repetition rate of 25 pps (pulses per second) to allow circulating five bunch trains in the DR.

ATF Damping Ring

The basic beam parameters for the DR are summarized in Table 6.2. The ATF DR achieved in 2004 values for the normalized vertical emittance as small as 1.5×10^{-8} m·rad, which corresponds to a geometrical emittance of 6 pm·rad, for a bunch intensity of 10^{10} electrons [62]. The small emittance was achieved by special design of a strong focusing lattice with precise alignment of components and beam orbit control. The basic machine structure of the ATF DR consists of combined-function bending magnets and wiggler cells. The ring has a length of about 138.6 m.

Table 6.1: Basic design beam parameters of the ATF injector linac [6].

Beam energy, E_{beam}	1.54 GeV
Bunch population, N	2×10^{10}
Bunches per train, N_b	20
Bunch spacing, Δt_{bunch}	2.8 ns
Repetition rate	25 pps
Energy spread (Full Width), σ_δ	<1.0 % (90% beam)
Normalized beam emittance, $\epsilon_{Nx/y}$	$<3\times10^{-4}$ m·rad

Table 6.2: Basic design beam parameters of the ATF DR [6].

Beam energy, E_{beam}	1.54 GeV
Bunch population, N	2×10^{10}
Bunches per train, N_b	20
Bunch spacing, Δt_{bunch}	2.8 ns
Repetition rate	25 pps
Energy spread (Full Width), σ_δ	<1.0 % (90% beam)
Normalized beam emittance, $\epsilon_{Nx/y}$	$3\times10^{-6}/3\times10^{-8}$ m·rad

The value of the horizontal equilibrium emittance is basically determined by the structure of the unit cell. The role of wigglers is to help to reduce the damping time. The best way to reduce the equilibrium emittance is to suppress its source, *i.e.*, the horizontal dispersion at the radiation source. Thus, each bend is placed at the minimum of the dispersion in each periodic structure [6]. As a result, the bending magnet must play the role of a horizontal-defocusing magnet. Figure 6.3 shows the unit cell and its optical functions.

The ATF DR consists of 36 of these unit cells. The optical functions and the dispersion of the DR and the old EXT line, calculated with MAD, are shown in Fig. 6.4.

DR emittance diagnostics

The vertical and horizontal projected emittances at the ATF DR are obtained from measured beam sizes, dispersion and β-functions at a certain location, where an X-ray synchrotron radiation monitor is located. The beam sizes at this location are mainly given by the settings of the focusing magnets and the beam emittance [63]. Knowing the lattice, *i.e.*, the β-function $\beta(s)$ and the dispersion $D(s)$ at the monitor location s, the measured beam size $\sigma(s)$ is given by

$$\sigma_x^2(s) = \epsilon_x\beta_x(s) + \left(D_x(s)\frac{\Delta p}{p}\right)^2 \quad \text{and} \quad \sigma_y^2(s) = \epsilon_y\beta_y(s) + \left(D_y(s)\frac{\Delta p}{p}\right)^2. \tag{6.1}$$

If the momentum spread $\Delta p/p$ is known and the optical functions are measured, the emittances can be obtained. In the vertical direction the dispersion is zero in most cases ($D_y(s) = 0$), because only horizontal bending mangnets are used.

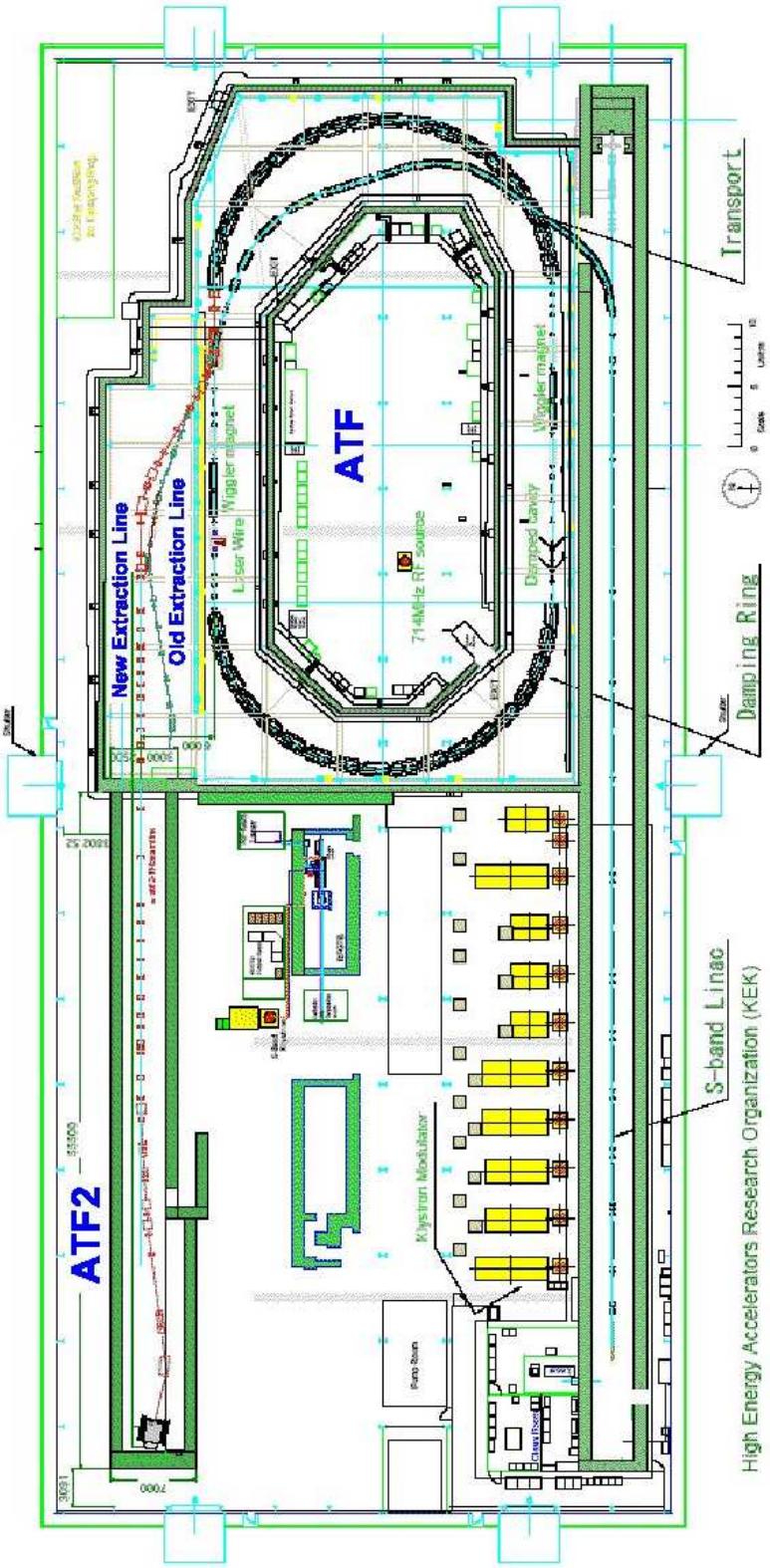

Figure 6.1: Schematic layout of the ATF and ATF2 facilities [8].

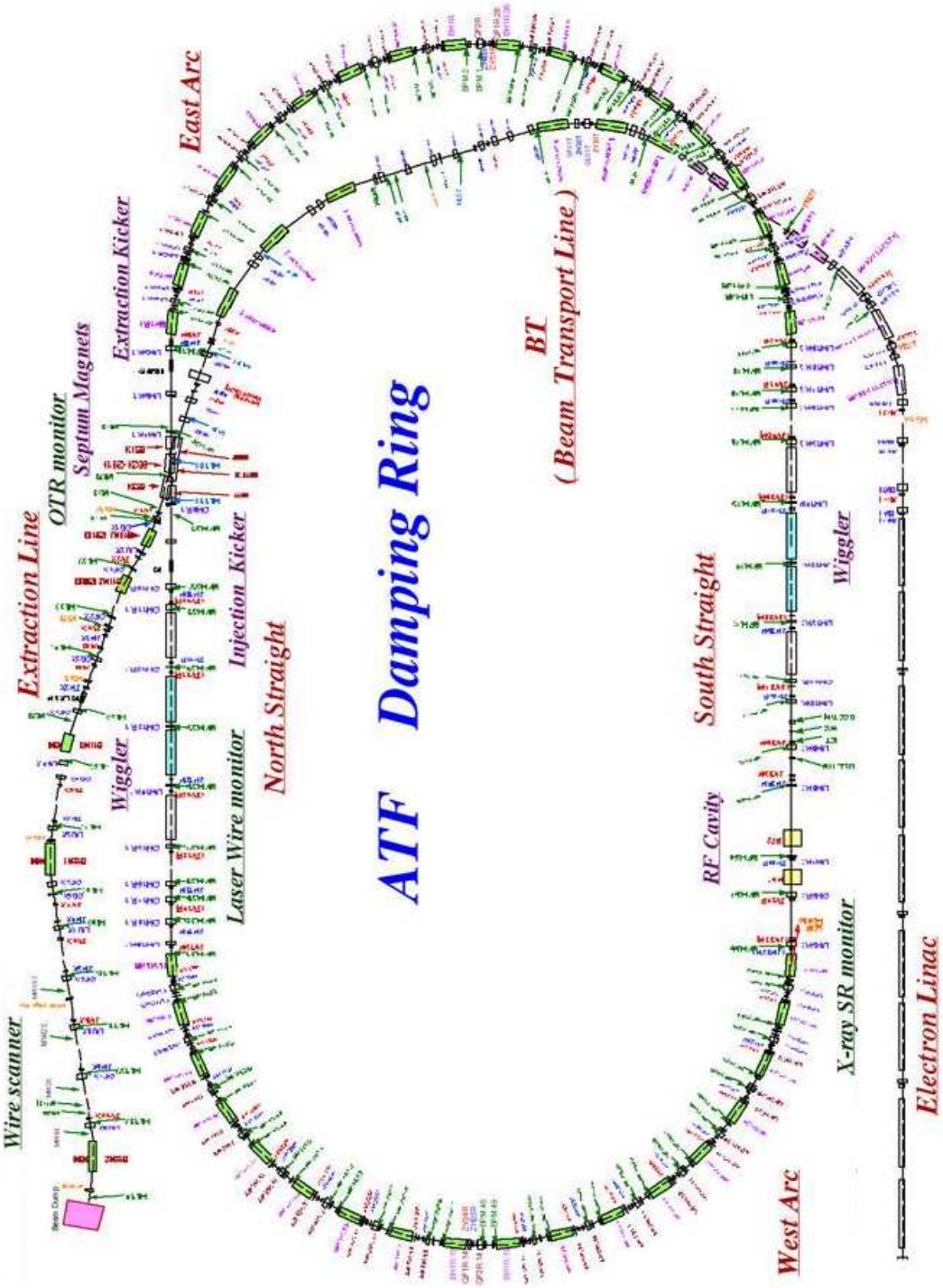

Figure 6.2: Schematic layout of the ATF facility: Linac, Beam Transport Line, Damping Ring and old Extraction Line [8].

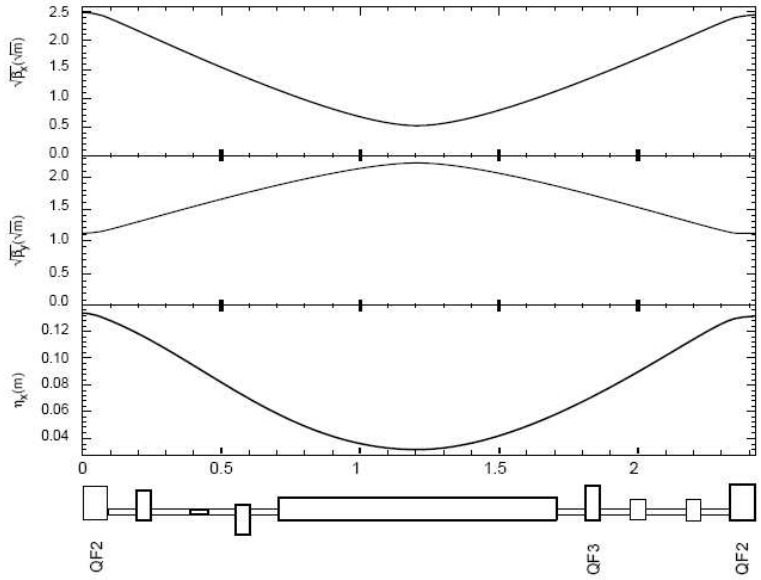

Figure 6.3: Lattice parameters of a single normal cell of the ATF DR [6].

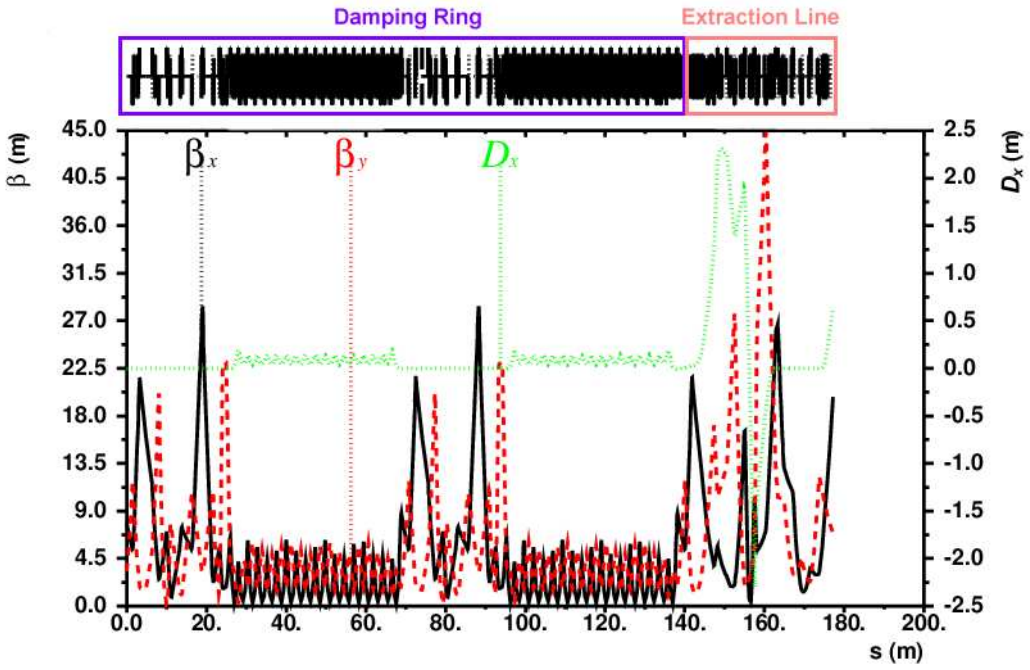

Figure 6.4: Horizontal dispersion and betatron functions of the ATF DR and the old EXT line.

X-ray Synchrotron Radiation monitor

For the diagnostic of the beam profile, an X-ray Synchrotron Radiation (XSR) monitor is used in the ATF DR. In such a device the light emitted when the electrons are bent in a dipole magnet is used to monitor its horizontal and vertical beam profile (see Fig. 6.5). Due to the high directionality of the synchrotron radiation, the spatial distribution of the emitted light reproduces fairly well the transverse distribution of charge density in the beam [63].

The schematic layout of the ATF XSR monitor is shown in Fig. 6.6. The SR source point is the final bend in the West arc section of the ring (see Fig. 6.2). The radiation is first reflected by a monochromator of Si crystal to choose 3.24 keV X-ray, and then transported through a magnification optics system which consists of two Fresnel Zone Plates (FZP). It was designed to realize a $\times 20$ magnified image of the source on an X-ray CCD camera. This monitor can measure beam sizes as small as 5 μm with 1 μm resolution [64].

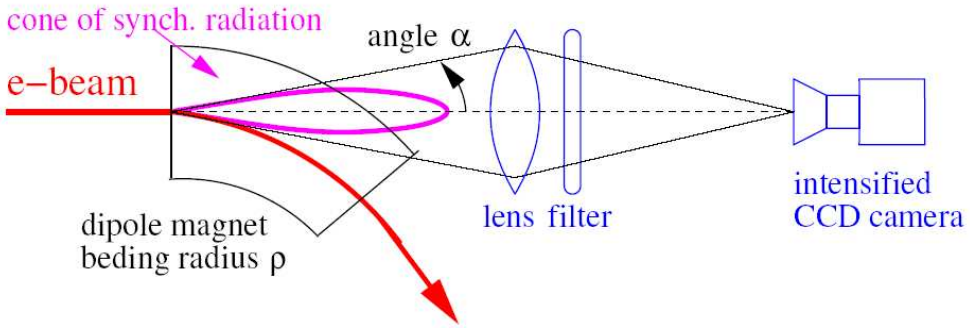

Figure 6.5: Scheme of a synchrotron radiation profile monitor observing the radiation from a dipole [63].

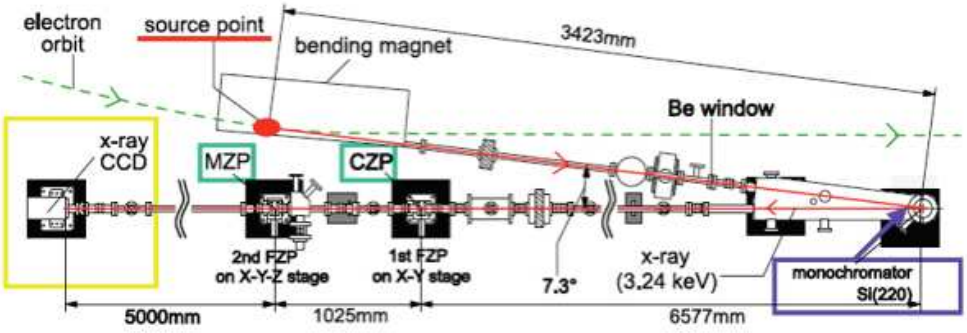

Figure 6.6: Schematic layout of the X-ray synchrotron radiation monitor in the ATF DR [64].

β-function measurement

Because there is no BPM at the source point, the β-function at the SR source point is obtained by measuring a shift of the betatron tune Q while changing the magnetic fields of three quadrupole magnets located upstream and downstream of the SR source point [65].

In a storage ring, the Q value, or betatron tune, is defined as the number of betatron oscillations per revolution [59]:

$$Q = \frac{\phi(L)}{2\pi} = \frac{1}{2\pi} \oint_L \frac{ds}{\beta(s)}, \tag{6.2}$$

where $\phi(L)$ is the betatron phase advance along the ring of circumference L, and the integral is taken around L.

If a quadrupole gradient is varied by a small amount Δk, the local β-function can be extracted from the tune variation as

$$\beta_{x,y} \approx \pm 4\pi \frac{\Delta Q_{x,y}}{\Delta k}, \tag{6.3}$$

as long as the tune is far from the integer and half integer resonances, where the plus or minus sign refers to the horizontal and vertical plane, respectively [59].

The absolute tune at five different trim currents of three DR quadrupoles (QM3R, QM4R and QM5R) is needed for the β-function calculation. The value of the β-function is obtained by a fit of the β-function at each quadrupole magnet. The betatron tune is measured by performing a FFT of the turn by turn transverse position of the beam at a fixed location [66]. In lack of an excitation kicker, the orbit oscillation due to injection error is considered [67].

Dispersion measurement

The horizontal dispersion function at the SR source point is measured from the change of the closed orbit due to change of the RF frequency. The change of the closed orbit is measured at every BPM position. The dispersion function at the SR source point is obtained by least squares fitting [65].

6.1.2 ATF2 design

The ATF2 project extends the extraction beamline of the ATF with an ILC-type final focus system to create a tightly focused, stable beam by making use of the small emittance of the ATF. The ATF2 facility will be a continuation of the Final Focus Test Beam (FFTB) at SLAC [24, 25]. The FFTB achieved a beam size of 70 nm, provided invaluable experience and confidence in design and operation of the final focus. However, it could not address many questions of reliably maintaining the beam size over the long term or of beam stability. In addition, in the last decade, the design of the BDS for a future linear collider in the TeV scale has changed significantly, with a local chromaticity correction scheme which has better performance in a much shorter system. But this new scheme has never been tested experimentally.

The ATF2 facility will serve for the demonstration of a compact FFS based on local chromaticity correction, with the achievement of 37 nm vertical spot sizes, and for maintaining the small beam sizes achieved over time. For that, the control of the beam position is a critical issue. ATF2 will serve as well for the demonstration of beam orbit stabilization with nano-meter precision at the IP, and for the establishment of beam jitter controlling techniques at the nano-meter level with an ILC-like beam.

Comparison of ATF2 and ILC Final Focus System

The proposed IP beam parameters for ATF2 are shown in Table 6.3 in comparison with those of the ILC. Many features of ATF2 are common to the ILC FFS in spite of the

two orders of magnitude lower beam energy. As stated above, the design of the ATF2 beamline is a down-scaled version of the ILC FFS, which is detailed in Section 2.3. It can be seen comparing the ATF2 optics shown in Fig. 6.7 with the ILC FFS optics shown in Fig. 2.17.

Table 6.3: Basic design IP beam parameters of ATF2 and ILC [2, 8].

Parameter	ATF2	ILC
E_{beam} (GeV)	1.3 GeV	250
l^* (m)	1	3.5
N_b (e^-/bunch)	1×10^{10}	2×10^{10}
$\gamma\epsilon_x$ ($m \cdot rad$)	3×10^{-6}	1×10^{-5}
$\gamma\epsilon_y$ ($m \cdot rad$)	3×10^{-8}	4×10^{-8}
β_x^* (mm)	4.0	20
β_y^* (mm)	0.1	0.4
σ_z (μm)	8	0.3
D_x' (rad)	0.14	0.094
σ_δ (%)	~0.08	~0.1
Chromaticity W_y	$\sim10^4$	$\sim10^4$

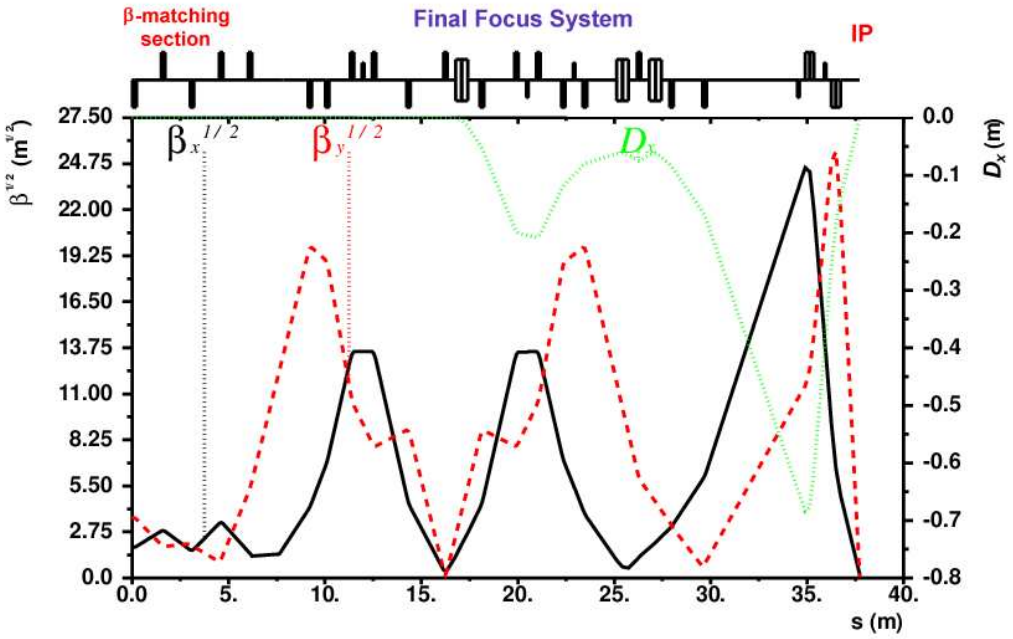

Figure 6.7: Optics of the ATF2 Final Focus System.

The natural chromaticity and the relative beam energy spread are quite similar in both ILC and ATF2 FFS designs. In Section 2.3 it was shown that the vertical beam size at the ILC would increase by about an order of magnitude if the chromatic aberration from the last strong quadrupole were not corrected. It was shown that the chromaticity is approximately $W \approx l^*/\beta^*$. From Eq. 2.12:

$$\frac{\Delta y^*_{rms}}{\sigma^*_y} \approx W_y \sigma_\delta, \tag{6.4}$$

and taking into account that $l^* = 1$ m, β^*_y=0.1 mm and $\sigma_\delta \approx 10^{-4}$ for the ATF2 FFS, the relative increase of the vertical beam size due to the chromaticity is a factor of 10, as in the case of the ILC.

Most of the tolerances of the subsystems for both accelerators are comparable, such as the tolerances on magnetic field, jitter vibration and power supply stability. While it is true that the ILC vertical beam size is about a factor of 5 smaller than that expected at ATF2, and thus the tolerances on magnet position jitter to achieve these spot sizes are less stringent ATF2, it is noteworthy that the jitter tolerance for the nano-meter level beam stabilization and control is similar to that for the ILC. In the same manner, the required resolution for the BPMs attached to the quadrupole magnets are about the same as for the ILC.

Some conditions at ATF2 will be different from the situation at the ILC FFS. Since the ATF2 beam does not come from a long linac, it will not show the time variation due to the integrated effects of ground motion and wakefields over the long ILC linac. The total length of the ATF2 FFS is an order of magnitude shorter than that for the ILC, and thus, the misalignments caused by the ground motion can be considerably smaller.

On the other hand, the ATF2 project entails some complications which are absent in the ILC. As explained in Chapter 4, at the ILC the position of the beam at the IP is diagnosed from the beam-beam interaction. In ATF2, a direct measurement of the beam position has to be performed, and thus a BPM with nanometer resolution is needed at the IP. Moreover, the longer ATF2 bunch requires a design of a cavity-type BPM with a lower resonant frequency. There are as well other environmental differences since the ILC will be built underground, and the ATF2 facility is not. Temperature differences and ground motion effect are considerably more important at ATF.

6.2 DR Extraction Line

Since the construction of the ATF facility, and before building the ATF2 beam line, an EXT line extracted the beam from the ATF DR and transported it to a dump. In Fig. 6.1 this line is shown. It comprises three parts: the beam extraction proper, a dispersion suppression section and a diagnostics section. Figure 6.8 shows a schematic layout of this EXT line, and Fig. 6.9 shows the optics of the line calculated with MAD, as well as a schematic indicating the different locations of the magnets involved in the extraction and the diagnostic devices in the line.

In this old extraction line, the beam was extracted from the DR by means of a first kick (KICKER1), and then passed off-axis through some magnets centered on the DR reference orbit. It passed first through the so-called QM6R and QM7R quadrupoles, nominally at distances of 0.65 and 2.2 cm from their centers, respectively. Then the beam went through three septum magnets, BS1X, BS2X and BS3X, which completed the extraction. The extracted beam was deflected by about 4.6 mrad by the extraction kicker into the first septum magnet. The three septum magnets successively deflected the beam by 28, 75 and 235 mrad. A schematic drawing of the beam extraction region is shown in Fig. 6.10.

After the extraction, the beam went through a dispersion suppression section, with a second kicker mirroring the extraction one (KICKER2 in Fig. 6.8), in order to reduce

fluctuations. Stabilization of the beam extracted from the DR is extremely important. The jitter must be less than one tenth of the beam size. For the septum magnets, DC magnets are chosen, because pulsed ones would introduce larger jitter. Assuming $\beta_x \approx 10$ m, the jitter tolerance on the kicker is estimated to be 5×10^{-4}. In order to achieve this tolerance, a double-kicker system, separated by a phase advance of π is located in order to cancel the jitter [68]. The pulse-to-pulse reproducibility in the total-deflection angle is thus better than $\pm3\times10^{-5}$.

The beam then goes through a horizontal dispersion-free zone, where five wire scanners are located in oder to allow emittance measurements (MW0X-MW4X) [69]. In 2007, an Optical Transition Radiation (OTR) monitor was installed just after the set of septum magnets, to allow fast diagnostics after the beam extraction.

In 2008, the construction of the ATF2 beamline was finished, and the EXT line was rebuilt, to transport the beam from the DR to the ATF2 beamline (see Fig. 6.1). Figure 6.11 shows the optics of the new EXT line. The extraction itself remained unchanged, but the rest of the line has been redesigned to optimize the beam diagnostic section. The dispersion suppression section has been also optimized to allow the matching of the beam parameters required to be injected on the ATF2 beamline.

6.3 Emittance growth in the Extraction Line of ATF

While small vertical emittances are consistently reproduced in the ATF DR [7, 62], measurements of the extracted beam, performed in the dedicated diagnostics section located immediately downstream, have since many years given significantly larger values than expected, of about a factor 3, and there are indications that the emittance growth increases with the beam intensity [9–11]. This long-standing problem has motivated studies of several possible sources of emittance growth induced during extraction, as well as the study of the proper emittance measurement process and reconstruction, which is complicated and could induce some uncertainty in itself [70].

One possible contribution is the non-linearity of the magnetic fields in the extraction region experienced by the beam when passing off-axis through a few magnets involved in the extraction process. As mentioned previously, the nominal extraction beam trajectory passes horizontally off-axis through the QM6R and QM7R quadrupoles shared with the DR. Then, it passes close to the conductor in the BS1X septum magnet, since this magnet is placed very close to the DR due to limitations in the space available. Moreover, in practical operation, the beam may deviate from the nominal trajectory.

Another possible contribution to the emittance growth, which is not studied in this thesis, could be the wakefields induced by the extraction kicker. The magnitude of this perturbation would depend on the beam intensity. The correlation between the emittance growth and the intensity could also be due to the dependent response of the BPM's with the beam intensity.

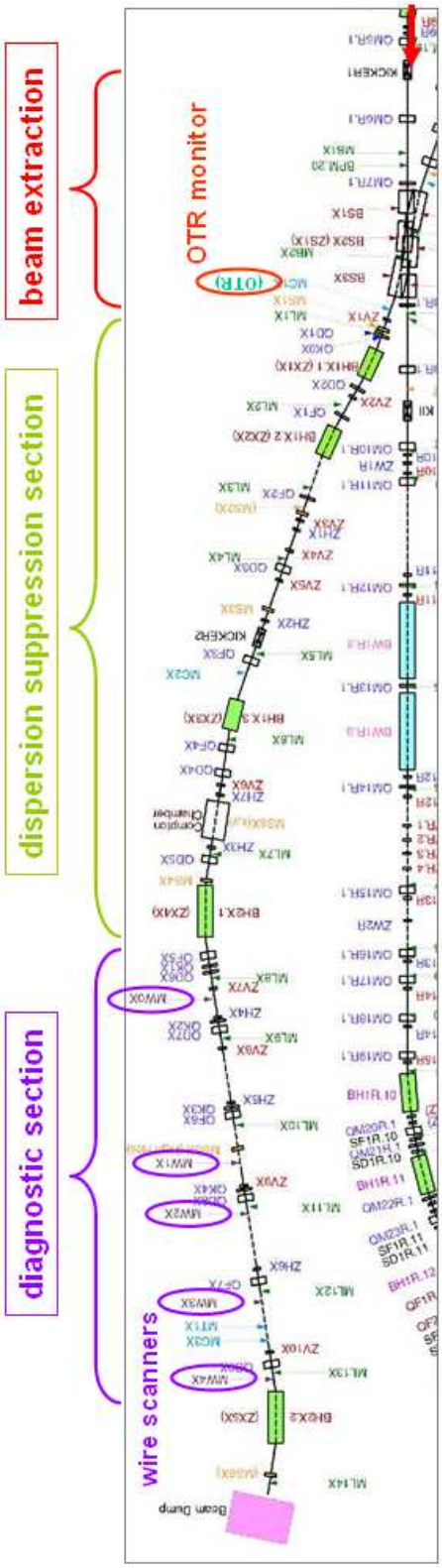

Figure 6.8: Schematic layout of the old EXT line indicating the different main parts of the line, and the location of the diagnostic devices.

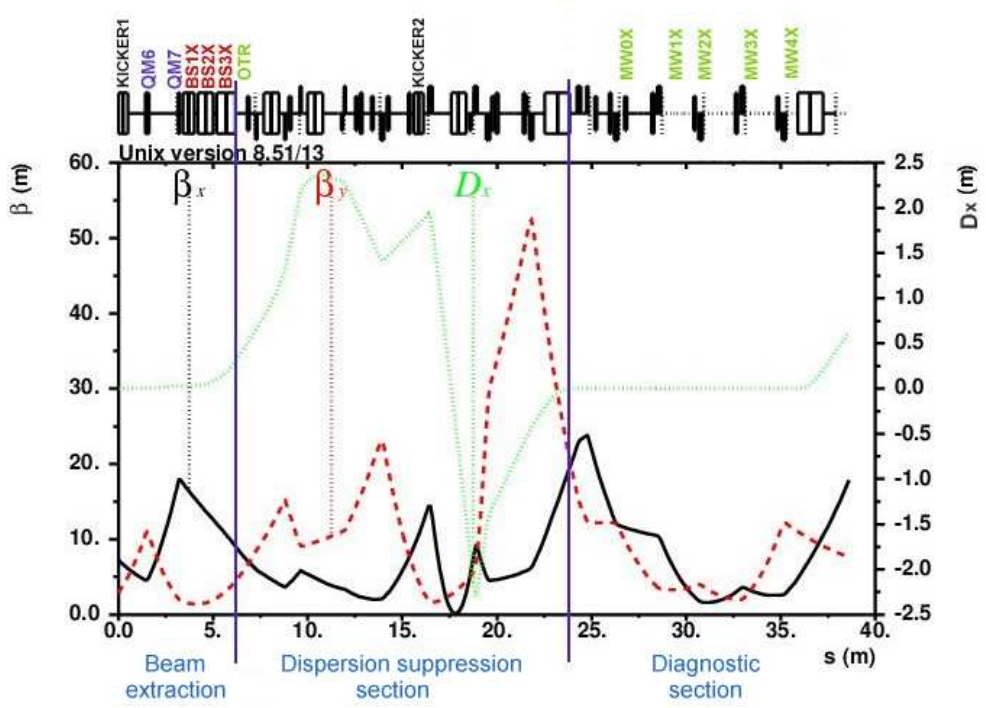

Figure 6.9: Optics of the old ATF EXT line which transported the beam to the dump.

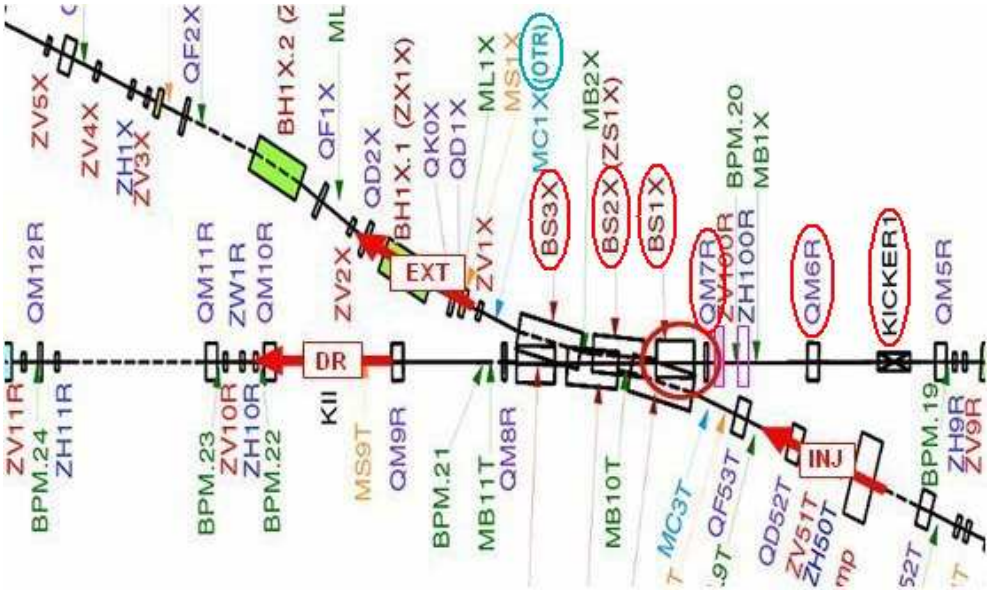

Figure 6.10: Schematic drawing of the extraction of the beam from ATF. The beam coming from the DR receives a first kick from the KICKER1, and then passes through two quadrupoles which are shared with the DR, QM6R and QM7R, and through three septum magnets, BS1X, BS2X and BS3X.

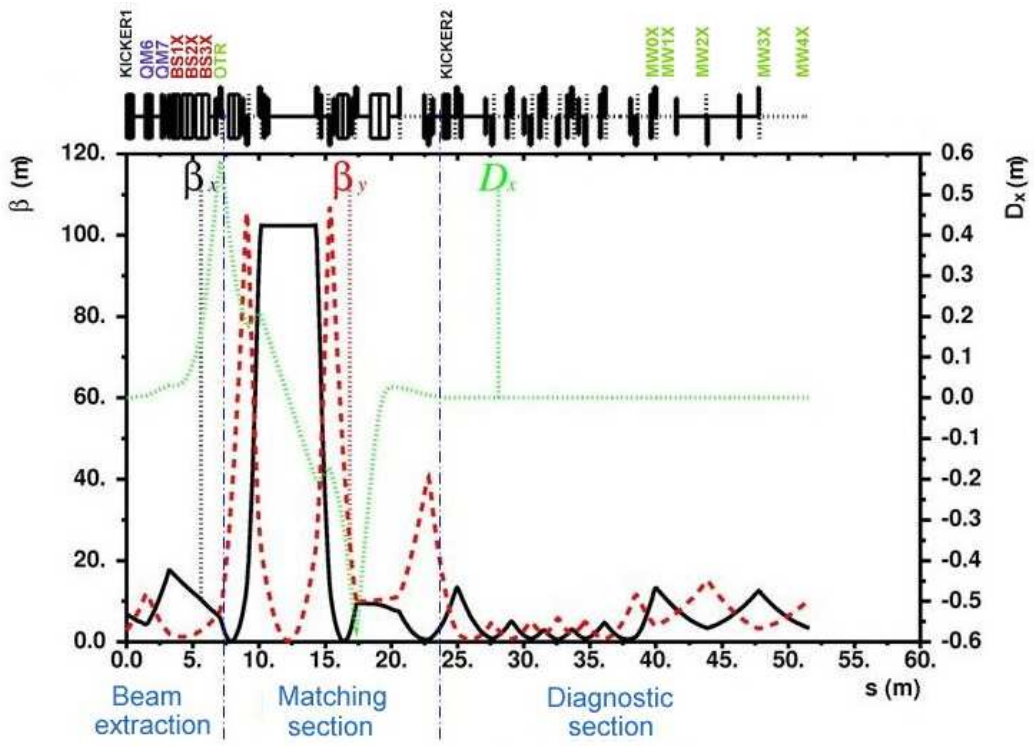

Figure 6.11: Optics of the new ATF EXT line constructed in 2008 which transports the beam to the ATF2 beamline.

6.4 Emittance growth studies

A study of the effect of the non-linear magnetic fields of the magnets involved in the extraction process on the emittance growth has been proposed and carried out. With this aim, the computation of the magnetic field of these magnets has been done with the finite element Poisson solver PRIAM [71], from the geometry of these magnets, which is presented in Chapter 7. Tracking simulations including the non-linear fields and with different vertical and horizontal displacements with respect to the ideal orbit have been carried out, and are presented in Chapter 8. They showed that the computed non-linear fields for QM7R had an important effect on the vertical emittance growth when the beam passed vertically off-axis. For the modeling of the beam at different orbits in the extraction channel, local bumps in the horizontal and vertical planes were generated, closing them in the DR. An experimental program was carried out during 2007-2008 to study the correlation between the extraction trajectory and the anomalous emittance growth. The results are presented in Chapter 9.

6.4.1 Local orbit bump generation

The beam orbit in the extraction region can be shifted locally in the vertical and horizontal planes by means of local orbit bumps [75]. For the DR bump generation, three correctors in each plane are needed (see Appendix B). For this purpose two correctors, ZV100R and ZH100R, were installed in the DR just upstream of the QM7R quadrupole in 2007. The

bumps can be opened in the DR by means of the ZV9R & ZV100R and ZH9R & ZH100R correctors and then closed with the ZV10R and ZH10R correctors, vertically and horizontally respectively. They can also be closed in the EXT line with ZV1X & ZV2X vertically and ZH1X & ZH2X horizontally. Details of corrector locations are shown in Fig.6.10. Figure 6.12 shows a vertical local bump closed in the DR generated with the code MAD8, with 1 mm of amplitude at the location of the QM7R magnet.

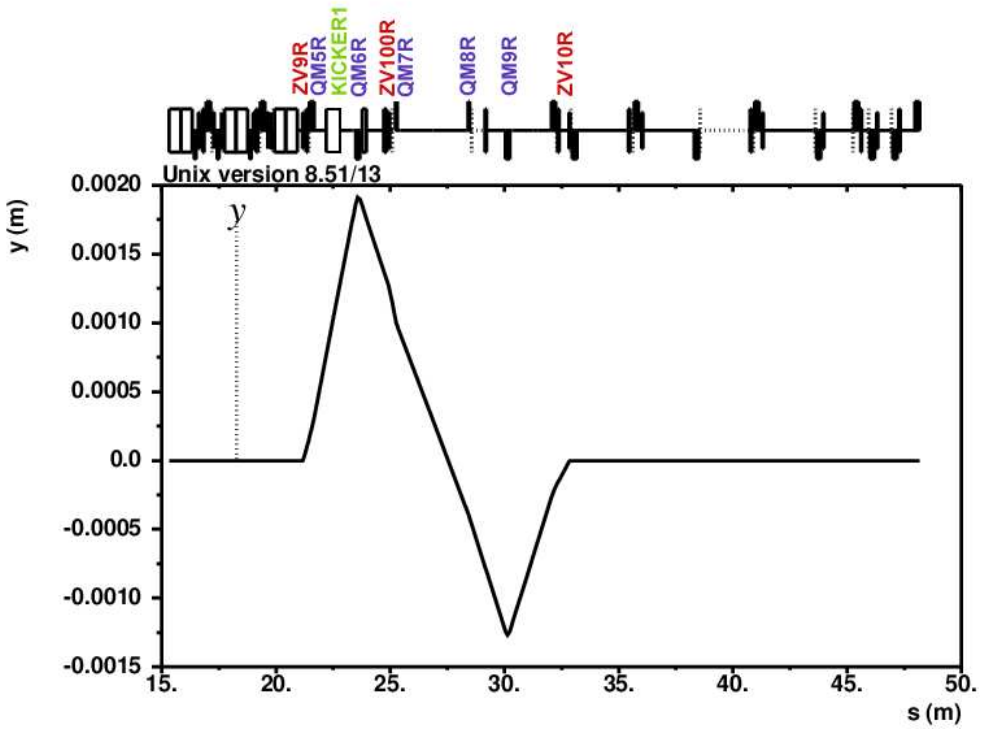

Figure 6.12: Generation of a vertical bump in the beam extraction region, closed in the DR. The bump amplitude at the QM7R magnet is adjustable by tuning the correctors.

6.4.2 Beam diagnostics

At the time of this study, four wire scanners (MW0X-MW3X) were available in the diagnostic section of the EXT line to allow emittance measurements as a function of the extraction trajectory. Measurements with multi-wire scanners were performed, but the betatron phase advances between the wire scanners could not be fully optimized to enable reliable emittance reconstruction. A complementary quadrupole scanning technique was also available, but because of practical constraints it could not be used easily during the shifts when trajectory bumps were applied [70].

An alternative method for beam size and vertical emittance diagnostics consisted in using an OTR monitor installed just after the septum magnets (see Fig. 6.8), at a location such that it imaged the beam angular spread out of QM7R quite well, with little influence from the beam size in QM7R. This allowed faster and more reliable results since the measured changes in vertical beam size at this location were correlated with the emittance growth and because the bumps did not need to be closed in EXT line during the measurements, as required for the emittance diagnostics at the wire stations.

The OTR monitor

Transition radiation is a classical electrodynamic process produced when a uniformly moving charged particle crosses the boundary between two media with different dielectric constants [77, 78]. In each medium the electromagnetic field associated with the particle is different. As the particle approaches and crosses the interface, the electromagnetic fields must reorganize themselves, leading to a time-dependent polarization at the medium boundary. The change of this polarization emits the radiation. Part of the photons are emitted in a cone centered at an angle with respect to the surface equal to that of the incoming beam, like in light reflection. The total transition radiation yield is proportional to the energy of the incoming particle. The radiation pattern produced by a beam of particles traversing a boundary can be analyzed to yield information about the beam.

At electron accelerators, as well as at high energy proton synchrotrons, the beam profile can be determined from the electromagnetic radiation emitted when it is intercepted by a thin metallic foil called OTR monitor, as shown in in Fig. 6.13 [63, 79]. The foil is inserted at 45° with respect to the beam path in most cases. The light is emitted in the forward direction as well as at 90°, because the metallic surface acts as a mirror. Typically, 100 to 1000 beam particles yield 1 photon in the optical wavelength range. With appropriate optics, an image of the foil can be recorded with a CCD camera.

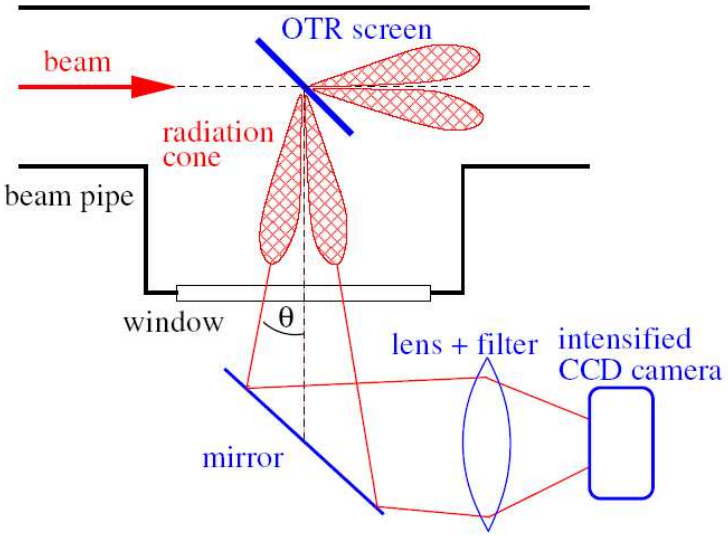

Figure 6.13: Scheme of an OTR monitor [63].

For relativistic particles crossing the boundary from the vacuum to a metallic foil with dielectric constant $\epsilon \gg 1$, the radiated energy dW into a solid angle $d\Omega$ per frequency interval $d\omega$ can be approximated by (see Appendix C)

$$\frac{d^2W}{d\Omega d\omega} = \frac{e^2}{\pi^2 c} \cdot \frac{\theta^2}{[\theta^2 + \gamma^{-2}]^2}, \tag{6.5}$$

where e, c and γ are the elementary charge, the velocity of light and the relativistic Lorentz factor, respectively.

The radiated energy is converted to the number of photons by $W = N_{photon} \cdot \hbar\omega$ observed within a wavelength interval from λ_{begin} to λ_{end} in the optical region by the

CCD camera, yielding the number of photons per solid angle [63]

$$\frac{dN_{photon}}{d\Omega} = N_{beam} \cdot \frac{e^2}{\hbar\pi^2 c} \cdot \log\left(\frac{\lambda_{begin}}{\lambda_{end}}\right) \cdot \frac{\theta^2}{[\theta^2 + \gamma^{-2}]^2}, \tag{6.6}$$

where N_{beam} is the number of beam particles. The radiation is more tightly focused for higher energies, as shown in Fig. 6.14. For the case of the ATF electron beam of 1.3 GeV, the radiation is emitted primarily in a cone with an opening angle of about 1 mrad. For low particle energies, like in most proton accelerators, the opening angle is too large for a practical application.

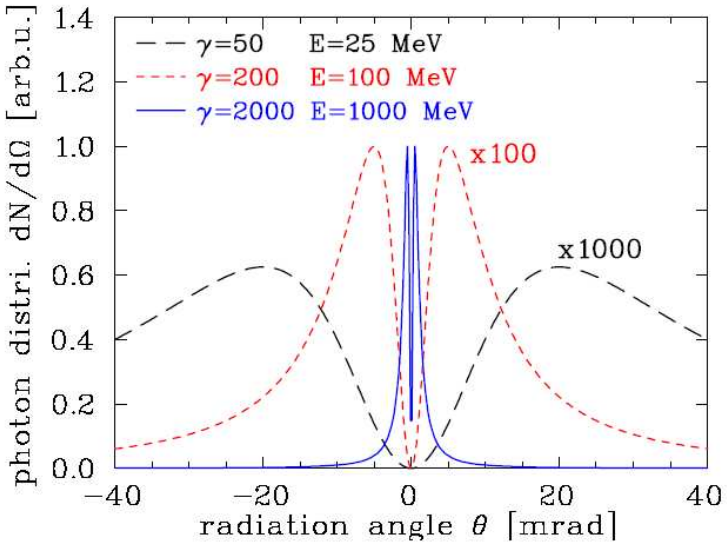

Figure 6.14: Intensity distribution of OTR as a function of the observation angle for three different electron energies. Note that the photon intensity is enhanced by a factor of 1000 and 100 for 25 and 100 MeV respectively [63].

The OTR monitor installed in the ATF EXT line is shown if Fig. 6.15. Its design is based on a long working distance microscope objective manufactured by Mitutoyo [82]. The 5× objective has a numerical aperture of 0.14, with a focal length of 40 mm and working distance of 34 mm. The lens is designed for use at infinite conjugate ratio and gives a depth of focus of approximately $\pm 7\mu$m. The lens has a resolution of 2 μm, corresponding to diffraction-limited performance. This is roughly equivalent to a resolution of 1 μm rms beam size. Beam sizes as small as 5μm have been measured with this instrument at the ATF EXT line [82].

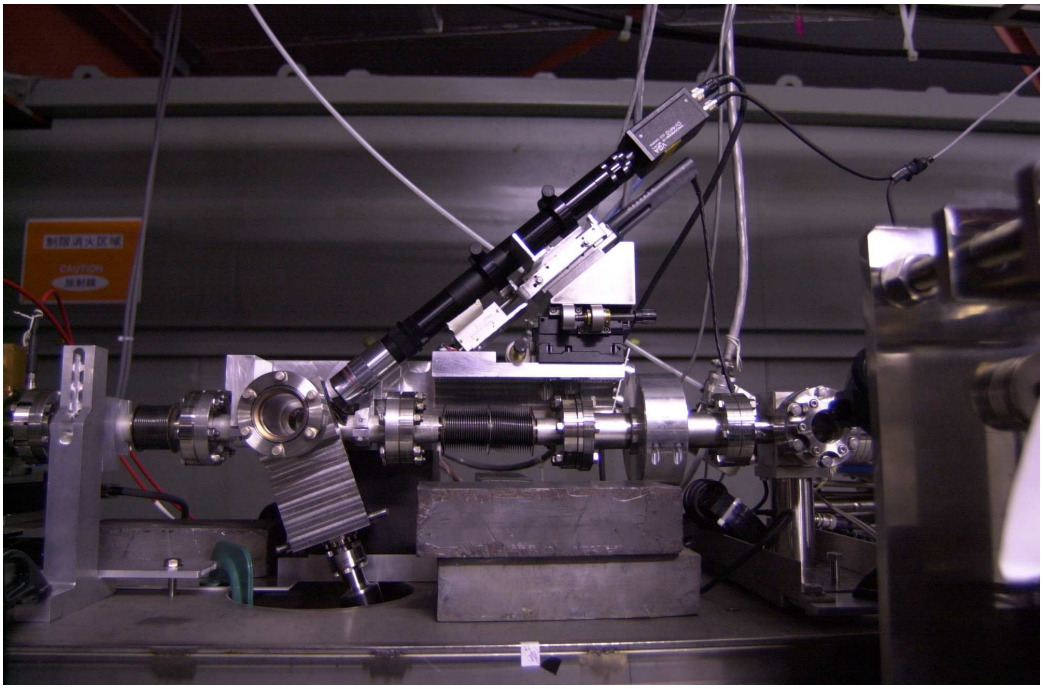

Figure 6.15: View of the OTR monitor installed in the ATF EXT line after the beam extraction.

Chapter 7

Modeling of the magnets involved in the DR beam extraction

Small vertical emittances have been consistently reproduced in the ATF DR, but measurements of the extracted beam in the diagnostic section located immediately downstream have since many years given significantly larger values than expected. One possible contribution to this emittance growth that has been under study is the non-linear magnetic fields that can arise during the extraction process, while passing the beam nominally horizontally off-axis with respect to the center of the magnets. In order to quantify the effect of the non-linearity of the magnetic field on the extracted beam emittance, a detailed study of the field maps of the magnets involved in the extraction has been done with the finite element Poisson solver PRIAM [71], using explicit magnet geometries and parameters, and is presented in this chapter.

7.1 Non-linear fields in the shared magnets with the DR.

As explained in Section 6.2, the DR beam extraction is initiated by firing the extraction kicker, and the extracted beam passes nominally off axis through the QM6R and QM7R quadrupoles, which are centered in the DR. The beam then goes through the BS1X, BS2X and BS3X septum magnets. After passage through the three septa, the extracted beam is transported in an independent magnetic channel. For example, the extracted beam path is significantly beyond the expected linear region of the QM7R quadrupole, close to the pole, as can be seen in Fig. 7.1. Table 7.1 summarizes the off-axis positions in the elements of the extraction region. For quadrupoles, distances are referred to the center of the magnet, while for septum magnets they are referred to the edge of the innermost conductor (see Fig. 7.9).

Type	**Element name**	x **[mm]**	y **[mm]**	
Quadrupole	QM6R	6.5	0.0	distance from
Quadrupole	QM7R	22.5	0.0	center of quad.
Septum	BS1X	8.2	0.0	distance from
Septum	BS2X	15.3	0.0	end of the top half
Septum	BS3X	16.0	0.0	septum conductor

Table 7.1: Displacement of the extracted beam while passing through the magnets involved in the extraction.

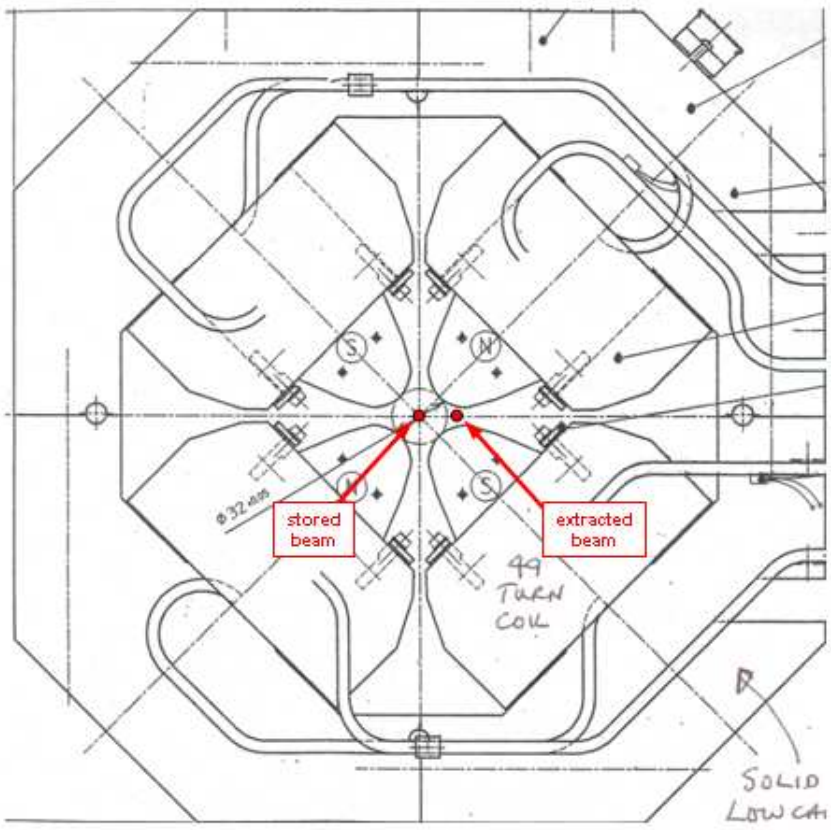

Figure 7.1: Draft of the QM7R quadrupole, with stored and extracted beam position.

The off-axis transport through the magnets in the extraction region is represented in the description of the optics by means of dipole components complemented by sets of normal multipoles. The non-linear fields are a potential source of vertical emittance growth in the ATF EXT line, and have been estimated. The field maps of the magnets involved in the extraction have been computed with the finite element code PRIAM [71]. The obtained magnetic fields have been fitted by polynomial functions in order to get a continuous representation in the complex plane[1] [72]. The results are compatible with the previous work based on the code POISSON [83].

Before computing and fitting the field maps, a description of the formalism used to obtain a continuous representation of the field in a magnet is presented in next section.

7.2 Local representation of the magnetostatic field in two dimensions

7.2.1 The potentials and magnetic field as analytical functions

The magnetic field of the majority of accelerator magnets has, to a good approximation, only transverse components, since the length of the magnets are long compared to their

[1]The computation of the magnetic field maps with PRIAM, as well as the corresponding polynomial fits have been performed by G. le Meur and F. Touze.

aperture.

The magnetic field $\vec{B}$ derives from a vector potential $\vec{A}$ through the relation : $\vec{B} = rot(\vec{A})$. When the magnetic field has only two components B_x and B_y, the last relation reduces to

$$B_x = \frac{\partial A_z}{\partial y} \; ; \; B_y = -\frac{\partial A_z}{\partial x}. \tag{7.1}$$

Setting the flux function $\Phi = A_z$ one gets:

$$B_x = \frac{\partial \Phi}{\partial y} \; ; \; B_y = -\frac{\partial \Phi}{\partial x}. \tag{7.2}$$

The curves $\Phi = constant$ are the field lines and their orthogonal trajectories, $V^* = constant$ are scalar potential lines from which derives the magnetic field: $\vec{B} = -grad(V^*)$. For a complex potential in the form of an analytic function:

$$\zeta(z) = \Phi(x, y) + iV^*(x, y), \tag{7.3}$$

where $z = x + i \cdot y$ is the complex variable, the conditions for analyticity are

$$\frac{\partial \Phi}{\partial x} = \frac{\partial V^*}{\partial y} \; ; \; \frac{\partial V^*}{\partial x} = -\frac{\partial \Phi}{\partial y} \tag{7.4}$$

which entails:

$$-\frac{d\zeta}{dz} = -\frac{\partial \Phi}{\partial x} + i \cdot \frac{\partial \Phi}{\partial y} = -\frac{\partial V^*}{\partial y} - i \cdot \frac{\partial V^*}{\partial x} = B_y + iB_x = B(z). \tag{7.5}$$

If ζ is analytical, so is B(z). The analyticity conditions for B then reads

$$\frac{\partial B_y}{\partial x} = \frac{\partial B_x}{\partial y} \; ; \; \frac{\partial B_x}{\partial x} = -\frac{\partial B_y}{\partial y}, \tag{7.6}$$

which are *Maxwell equations* in two dimensions (in the absence of currents):

$$rot(\vec{B}) = 0 \; ; \; div(\vec{B}) = 0. \tag{7.7}$$

7.2.2 The multipole fields

Let's consider the potential $\zeta(z) = -B_0 z$. The derivation leads to

$$B(z) = B_y = B_0, \tag{7.8}$$

which is a pure dipole field. The field lines are $\Phi(x, y) = -B_0 x = constant$, whereas the potential lines are $V^*(x, y) = y = constant$.

With the potential $\zeta(z) = -\frac{1}{2}G \cdot z^2 = -\frac{1}{2}G(x^2 - y^2 + 2ixy)$, the magnetic field reads

$$B(z) = Gx + iGy, \tag{7.9}$$

and thus, $B_x = Gy$ and $B_y = Gx$ which is a pure quadrupole field. The field lines are $\Phi(x, y) = -\frac{1}{2}G(x^2 - y^2) = cst$, *i.e.*, hyperboles, and the potentials lines are $V^*(x, y) = -\frac{1}{2}Gxy = cst$ as well.

To obtain a pure sextupole field, the potential has to be taken proportional to $\zeta(z) \propto -z^3$.

7.2.3 General multipole expansion

Usually the field in the magnets of a beam transport system is known at discrete points in a limited region, either from measurements or from computer simulations. For computer tracking purposes, it is generally necessary to know the magnetic field in continuous form in order to avoid instabilities in the computations. A solution is to represent the magnetic field by analytic expressions obtained by fits to the known values. A convenient way is to use an integer series of the complex variable, with complex coefficients, around a reference point, that can be expressed as

$$B(z) = B_y + iB_x \sim \sum_{n=0}^{N} a_n z^n. \tag{7.10}$$

The real part of the complex coefficients a_n is known as normal multipoles and the imaginary part as skew multipoles. Such a representation is consistent with the nature of the magnetic field. In particular, the property of analyticity entails that Maxwell equations are satisfied. This is generally not the case for other polynomial fits. Obviously, to benefit from this physical constraint, the fitting must be done in two dimensions.

In the particular case of symmetry with respect to the axis (plane $y = 0$), $B_x(x,-y) = -B_x(x,y)$ and $B_y(x,-y) = B_y(x,y)$, and the coefficients a_n become real. Indeed, for every z, this condition can be written as

$$B(\overline{z}) = \overline{B}(z), \tag{7.11}$$

or

$$\sum_{n=0}^{N} a_n \overline{z}^n = \sum_{n=0}^{N} \overline{a_n}.\overline{z}^n, \tag{7.12}$$

where $\overline{z}$ denotes the conjugate of z and which implies that $\overline{a_n} = a_n$.

Separate expansions of B_x and B_y can be obtained as polynoms of the variables x and y. Recalling that $(x+iy)^k = \sum_{p=0}^{k} C_k^p (iy)^{k-p} x^p$, with $C_m^p = \frac{m!}{p!(m-p)!}$ and the convention $C_m^0 = 1$, the magnetic field components can be expressed as

$$\begin{aligned} B_x &= y \sum_p \sum_{q=0}^{p} (-1)^{p+q} x^{2q} \left(a_{2p+1} C_{2p+1}^{2q} + a_{2p+2} C_{2p+2}^{2q+1} x \right) y^{2(p-q)} \\ B_y &= \sum_p \sum_{q=0}^{p} (-1)^{p+q} x^{2q} \left(a_{2p} C_{2p}^{2q} + a_{2p+1} C_{2p+1}^{2q+1} x \right) y^{2(p-q)}. \end{aligned} \tag{7.13}$$

It can be noticed that B_x is the product of y by a polynom $H(x,y)$. For a fixed x, H can be reordered with respect to the sole variable y, with only even powers y^{2h} appearing with coefficients

$$\alpha_{2h} = \sum_{q=0} (-1)^h x^{2q} \left(a_{2h+2q+1} C_{2h+2q+1}^{2q} + a_{2h+2q+2} C_{2h+2q+2}^{2q+1} x \right). \tag{7.14}$$

Multipole expansion in MAD notation

The multipole expansions for normal and skew field components defined in MAD8 are [57]:

$$B_y(x,0) = \sum_k \frac{B_{kn} x^k}{k!}$$
$$B_x(x,0) = \sum_k \frac{B_{ks} x^k}{k!}. \quad (7.15)$$

With the adopted symmetry with respect to the axis (plane $y = 0$), all the skew multipoles vanish and the successive normal multipoles are

- dipole : $B_{0n} = a_0$
- quadrupole : $B_{1n} = a_1$
- sextupole : $B_{2n} = 2 * a_2$
- ...
- 2k-pole : $B_{kn} = k! a_k$

The MAD8 coefficients $K_{kn} = B_{kn}/B_0\rho$ allow to specify the strengths of the multipoles $K_{kn}L$, in m^{-k}, multiplying $k!a_k$ by the length L of the element and dividing by the appropriate $B_0\rho_0$, where $B_0\rho_0$ [T m] = 10/2.998 E [GeV] is the magnetic rigidity.

7.3 Field mapping for the QM7R quadrupole

QM7R is a horizontally focusing quadrupole magnet, with an aperture of radius r = 0.015995 m and a length L = 0.078907 m. The focusing gradient is 21.8767 T/m. Figure 7.2 shows the field lines in the computed structure (1/8th of the quadrupole, taking into account the symmetries) obtained with PRIAM. A polynomial fit around the center

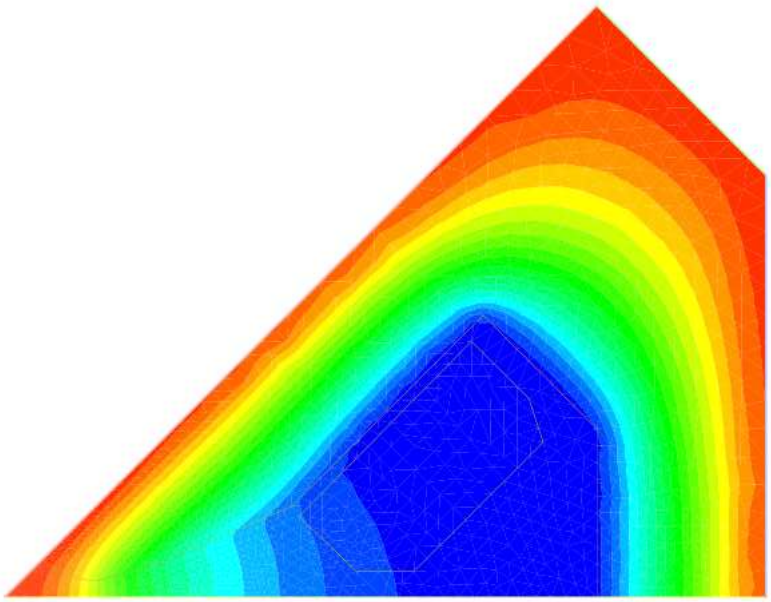

Figure 7.2: QM7R B field lines computed with PRIAM.

of the quadrupole (x = 0.0 m, y = 0.0 m) has been done with MINUIT [84], which provides the normal multipole coefficients listed in Table 7.2. The value of the χ^2 parameter for this fit, defined as

$$\chi^2 = \sum_{allsampled\ points} \left[\|B_x^{fit} - B_x^{priam}\|^2 + \|B_y^{fit} - B_y^{priam}\|^2 \right], \tag{7.16}$$

is 0.014 T^2 (using 40400 sampled points). The multipole coefficients to be used in the MAD program [57], $K_{kn}L = B_{kn}L/B_0\rho$, are added for completeness, where the length of the magnet (L) has the value of 0.078907 m and the magnetic rigidity $B_0\rho$ [T m] = 10/2.998 E [GeV] is calculated for 1.3 GeV. Notice that only some orders (1,5,9, 13,...) are permitted in accordance with the quadrupole symmetry.

Field Coefficients			**MAD Coefficients**		
a_1	2.1780989×10^{1}	[T m^{-1}]	K_1L	3.9633533×10^{-1}	[m^{-1}]
a_5	1.1406000×10^{6}	[T m^{-5}]	K_5L	2.4905761×10^{6}	[m^{-5}]
a_9	$-6.3613000 \times 10^{-15}$	[T m]$^{-9}$]	K_9L	$-4.200334 \times 10^{-11}$	[m^{-9}]
a_{13}	0.0	[T m^{-13}]	$K_{13}L$	0.0	[m^{-13}]

Table 7.2: Multipole coefficients for QM7R at the center of the quadrupole from the PRIAM mapping and fitted with a polynomial function using MINUIT.

The zone of interest for the tracking of the extracted beam is near x = 0.0225 m, y = 0.0 m. The fit performed in a region around this point, defined by $0.0175 \leq x \leq 0.0275$ m and $0.0 \leq y \leq 0.004$ m, provides the coefficients summarized in Table 7.3. The value of the χ^2 (defined in Eq. 7.16) for this fit is 0.0395 T^2 (for 5000 sampled points).

Field Coefficients			**MAD Coefficients**		
a_0	4.8119811×10^{-1}	[T]	K_0L	8.7560676×10^{-3}	
a_1	1.6721776×10^{1}	[T m^{-1}]	K_1L	3.0427593×10^{-1}	[m^{-1}]
a_2	-1.2801437×10^{3}	[T m^{-2}]	K_2L	-4.6587984×10^{1}	[m^{-2}]
a_3	-1.5580988×10^{5}	[T m^{-3}]	K_3L	-1.7011062×10^{4}	[m^{-3}]
a_4	-5.1401980×10^{6}	[T m^{-4}]	K_4L	-2.2447929×10^{6}	[m^{-4}]
a_5	-6.2084000×10^{5}	[T m^{-5}]	K_5L	-1.3556000×10^{6}	[m^{-5}]
a_6	1.4791000×10^{4}	[T m^{-6}]	K_6L	1.9377000×10^{5}	[m^{-6}]
a_7	5.5069000×10^{2}	[T m^{-7}]	K_7L	5.0501000×10^{4}	[m^{-7}]
a_8	3.7827000×10^{1}	[T m^{-8}]	K_8L	2.7752000×10^{4}	[m^{-8}]
a_9	0.0	[T m^{-9}]	K_9L	0.0	[m^{-9}]
a_{10}	0.0	[T m^{-10}]	$K_{10}L$	0.0	[m^{-10}]
a_{11}	0.0	[T m^{-11}]	$K_{11}L$	0.0	[m^{-11}]
a_{12}	0.0	[T m^{-12}]	$K_{12}L$	0.0	[m^{-12}]

Table 7.3: Multipole coefficients for QM7R at x = 0.0225 m and y = 0.0 m from the center of the quadrupole from the PRIAM mapping fitted with a polynomial function using MINUIT.

It can be noticed that due to the displacement in the horizontal plane all the normal multipole components are permitted for QM7R. The main components are a dipole field (a_0), a quadrupole field (a_1) which is about 24% less than on-axis, a sextupole field (a_2) and an octupole field (a_3). The other high order multipoles have decreasing values while

the series is limited to 8^{th} order.

Figure 7.3 compares the field values from PRIAM with the ones reconstructed from the fit for y = 1 and 2 mm. Figures 7.4 and 7.5 show this comparison in two dimensions over the defined range.

In the MAD optics description of the EXT line, QM7R is simulated as a bending magnet of length (L) 0.078907 m and angle -0.8942055×10^{-2} rad (the difference in the sign is a special convention in the MAD program), with a quadrupole component of strength 0.3980779044020 m^{-1}. Comparing with the value in Table 7.3, the dipole component has a slight difference of 2% while for the quadrupole component the difference is as large as 24%. The latter has a significant impact on the linear optics, as shown in Fig. 7.6, where it is compared to the design functions of Fig. 6.9. While effects on the horizontal dispersion (D_x) remain small, with a maximum deviation of ±2.5%, large deviations of up to ±20% in the vertical beta function (β_y) and between -400% / +66% in the horizontal beta function (β_x) result from the weaker strength of QM7R seen by the extracted beam.

7.4 Field mapping for the QM6R quadrupole

QM6R is a vertically focusing quadrupole of the EXT line which is also shared with the DR. It has an aperture of radius r = 0.016 m, a length L = 0.198745 m and a focusing gradient of -15.5377 T/m in the horizontal plane. As this magnet comes just after the kicker, the horizontal offset of the extracted beam is only 0.0065 m. As this is significantly less than the radius of the aperture, the non-linearity seen by the extracted beam is nearly negligible.

Figure 7.7 shows the magnetic field lines in the computed structure (1/8th of the quadrupole, taking into account the symmetries), computed with PRIAM.

The polynomial fit around the center of the quadrupole (x = 0.0 m, y = 0.0 m) has been done using MINUIT [84], which provides the normal multipole coefficients listed in Table 7.4. The value of the χ^2 for this fit is 9.720794×10^{-4} T^2 (for 40000 sampled points).

Field Coefficients			**MAD Coefficients**		
a_1	-1.5531000 × 10^1	[T]	K_1L	-7.1181198 × 10^{-1}	[m^{-1}]
a_5	1.7035000 × 10^5	[T m^{-1}]	K_5L	9.3689141 × 10^5	[m^{-5}]
a_9	-1.2743000 × 10^4	[T m^{-9}]	K_9L	-2.1193398 × 10^8	[m^{-9}]
a_{13}	0.0	[T m^{-13}]	$K_{13}L$	0.0	[m^{-13}]

Table 7.4: Multipole coefficients for QM6R at the center of the quadrupole from the PRIAM mapping and fitted with a polynomial function using MINUIT.

The zone of interest for the tracking of the extracted beam is near x = 0.0065 m, y = 0.0 m. The fit in a region around this point, defined by 0.005 ≤ x ≤ 0.008 m and 0.0 ≤ y ≤ 0.0015 m, provides the coefficients listed in Table 7.5. The value of the χ^2 for this fit is 4.391552×10^{-5} T^2 (for 5000 sampled points).

In the MAD optics description of the EXT line, QM6R is simulated as a sector bend of length (L) 0.198745 m and angle 0.462503985558 10^{-2} rad, with a quadrupole component of strength −0.7121175306066 m^{-1}. Comparing with the values in Table 7.5, the dipole and quadrupole components have only slight differences of −0.03% and 0.08%,

Field Coefficients			**MAD Coefficients**		
a_0	-1.0094000 $\times 10^{-1}$	[T]	K_0L	-4.6262508 $\times 10^{-3}$	
a_1	-1.5526000 $\times 10^{1}$	[T m^{-1}]	K_1L	-7.1158282 $\times 10^{-1}$	[m^{-1}]
a_2	-1.3721000 $\times 10^{0}$	[T m^{-2}]	K_2L	-1.2577132 $\times 10^{-1}$	[m^{-2}]
a_3	1.3220000 $\times 10^{3}$	[T m^{-3}]	K_3L	3.6353697 $\times 10^{2}$	[m^{-3}]
a_4	1.5352000 $\times 10^{6}$	[T m^{-4}]	K_4L	1.6886595 $\times 10^{6}$	[m^{-4}]
a_5	6.9339000 $\times 10^{2}$	[T m^{-5}]	K_5L	3.8135083 $\times 10^{3}$	[m^{-5}]
a_6	-1.0900000 $\times 10^{1}$	[T m^{-6}]	K_6L	-3.5968711 $\times 10^{2}$	[m^{-6}]
a_7	0.0	[T m^{-7}]	K_7L	0.0	[m^{-7}]
a_8	0.0	[T m^{-8}]	K_8L	0.0	[m^{-8}]
a_9	0.0	[T m^{-9}]	K_9L	0.0	[m^{-9}]
a_{10}	0.0	[T m^{-10}]	$K_{10}L$	0.0	[m^{-10}]
a_{11}	0.0	[T m^{-11}]	$K_{11}L$	0.0	[m^{-11}]
a_{12}	0.0	[T m^{-12}]	$K_{12}L$	0.0	[m^{-12}]
a_{13}	0.0	[T m^{-13}]	$K_{13}L$	0.0	[m^{-13}]

Table 7.5: Multipole coefficients for QM6R at $x = 0.0065$ m and $y = 0.0$ m from the center of the quadrupole from the PRIAM mapping fitted with a polynomial function using MINUIT.

respectively. The impact on the linear optics is negligible, as shown in Fig. 7.8 where it is compared to standard optics of Fig. 6.9.

7.5 Field mapping for the BS1X septum magnet

BS1X is a septum magnet that together with the septa BS2X and BS3X complete extraction from the DR to the EXT line. The lengths and angles for each septum are: BS1X (L=0.6 m, θ=0.028035665 rad), BS2X (L=0.8 m, θ=0.074343366 rad) and BS3X (L=1.0 m, θ=0.235022025 rad). The field map of the BS1X septum magnet has been computed. Figure 7.9 shows the cross section top half of the BS1X septum magnet. The top part of the figure shows the different parts of the BS1X septum while the bottom part of the figure shows the field lines calculated by POISSON [83].

The origin of coordinates in the septum, (x=0.0 m, y=0.0 m), is assumed to be at the bottom left hand corner while the right hand septum is between x=0.0937 and 0.099 m. The zone of interest for the tracking of the extracted beam is around the point (x=0.0855 m, y=0.0 m).

Figure. 7.10 shows the field lines in the computed structure (1/2 of the septum, taking into account the symmetries) calculated with PRIAM.

The fit around the point $x = 0.0855$ m, within a circle of radius $r = 0.004$ m, was obtained by squared minimization and provides the normal multipole coefficients listed in Table 7.6. The value of the χ^2 for this fit is 10^{-7} T^2 (for 640 sampled points).

In the MAD optics description of the EXT line, BS1X is simulated as a sector bend of length (L) 0.6 m and angle 0.028035665 rad. Comparing with the value in Table 7.6, the dipole component has a difference of 1.5%. The most important normal multipole from the harmonic analysis is a small quadrupole component of 0.0070853673 m^{-1} and a small sextupole component of 0.042628153 m^{-2}. These differences in dipole and quadrupole components have only a small impact on the linear optics. This is shown in Fig. 7.11,

Field Coefficients			MAD Coefficients		
a_0	1.9961476×10^{-1}	[T]	K_0L	2.7619357×10^{-2}	
a_1	5.1208429×10^{-2}	[T m^{-1}]	K_1L	7.0853673×10^{-3}	[m^{-1}]
a_2	1.5404429×10^{1}	[T m^{-2}]	K_2L	4.2628153×10^{0}	[m^{-2}]
a_3	2.2251138×10^{3}	[T m^{-3}]	K_3L	1.8472445×10^{3}	[m^{-3}]
a_4	5.7750633×10^{4}	[T m^{-4}]	K_4L	1.9177364×10^{5}	[m^{-4}]
a_5	-6.1819396×10^{7}	[T m^{-5}]	K_5L	-1.0264243×10^{9}	[m^{-5}]
a_6	$-1.9358771 \times 10^{10}$	[T m^{-6}]	K_6L	$-1.9285513 \times 10^{12}$	[m^{-6}]
a_7	$-3.6242908 \times 10^{12}$	[T m^{-7}]	K_7L	$-2.5274029 \times 10^{15}$	[m^{-7}]
a_8	$-5.0782180 \times 10^{14}$	[T m^{-8}]	K_8L	$-2.8330405 \times 10^{18}$	[m^{-8}]
a_9	$-4.5714786 \times 10^{16}$	[T m^{-9}]	K_9L	$-2.2953062 \times 10^{21}$	[m^{-9}]
a_{10}	$-6.4259328 \times 10^{17}$	[T m^{-10}]	$K_{10}L$	$-3.2264143 \times 10^{23}$	[m^{-10}]
a_{11}	0.0	[T m^{-11}]	$K_{11}L$	0.0	[m^{-11}]
a_{12}	0.0	[T m^{-12}]	$K_{12}L$	0.0	[m^{-12}]
a_{13}	0.0	[T m^{-13}]	$K_{13}L$	0.0	[m^{-13}]

Table 7.6: Multipole coefficients for the BS1X septum at $x = 0.0855$ m and $y = 0.0$ m, obtained from the PRIAM field map by fitting a polynomial function through square minimization.

where the comparison is made with respect to the standard optics of Fig. 6.9 and where the only significant effect is on the horizontal beta function (β_x), whose maximum difference is about ±12%.

It should however be mentioned that the values obtained for the multipoles in this procedure are very sensitive to the details of the geometry of the shim introduced at the end of the conductor to extend the flat region of the main bend field (see Fig. 7.9). Moreover, it was difficult to get stable fit results using MINUIT in this region, as large dependences on various conditions were observed, e.g. on the number of points, the boundary of the region considered or the degree of the polynom fitted. As it was found that square minimization gave stabler results, this was used for BS1X. The results were also compared with those from another computation technique for the field maps, which is available in PRIAM based on using linear Lagrange finite elements [71]. This approach is close to the approximations used in the POISSON program. The fit around the point $x = 0.0855$ m and $y = 0.0$ m, within a circle of radius $r = 0.004$ m, by squared minimization of this alternative field map gives the normal multipole coefficients listed in Table 7.7. The value of the χ^2 for this fit is 1.1×10^{-7} T^2 (for 640 sampled points). The dipole component obtained is rather similar to the one in Table 7.6, while the quadrupole and sextupole components are slightly smaller, which means that they would have an even smaller impact.

7.6 Non-linear fields in BS2X and BS3X septum magnets

The septum magnets BS2X and BS3X are further away from the damping ring than BS1X. This makes the geometry less constrained and their placement easier. From the corresponding engineering drawings, the nominal position of the extracted beam is 15.3 and 16 mm from the septum conductor for BS2X and BS3X respectively, in comparison to 8.2 mm for BS1X (see Table 7.1). This means that the beam passes farther away from the delicate region near the edge of these magnet where shims are included to help flatten the

Field Coefficients			**MAD Coefficients**		
a_0	1.9958973×10^{-1}	[T]	K_0L	2.7615894×10^{-2}	
a_1	2.8153166×10^{-2}	[T m^{-1}]	K_1L	3.8953650×10^{-3}	[m^{-1}]
a_2	8.4796963×10^{0}	[T m^{-2}]	K_2L	2.3465575×10^{0}	[m^{-2}]
a_3	9.0493494×10^{2}	[T m^{-3}]	K_3L	7.5125871×10^{2}	[m^{-3}]
a_4	-1.0862597×10^{5}	[T m^{-4}]	K_4L	-3.6071635×10^{5}	[m^{-4}]
a_5	-7.2537976×10^{7}	[T m^{-5}]	K_5L	-1.2043913×10^{9}	[m^{-5}]
a_6	$-1.8931642 \times 10^{10}$	[T m^{-6}]	K_6L	$-1.8860001 \times 10^{12}$	[m^{-6}]
a_7	$-3.3105246 \times 10^{12}$	[T m^{-7}]	K_7L	$-2.3085977 \times 10^{15}$	[m^{-7}]
a_8	$-4.3748047 \times 10^{14}$	[T m^{-8}]	K_8L	$-2.4406197 \times 10^{18}$	[m^{-8}]
a_9	$-4.0128670 \times 10^{16}$	[T m^{-9}]	K_9L	$-2.0148314 \times 10^{21}$	[m^{-9}]
a_{10}	$-8.5399590 \times 10^{17}$	[T m^{-10}]	$K_{10}L$	$-4.2878515 \times 10^{23}$	[m^{-10}]
a_{11}	0.0	[T m^{-11}]	$K_{11}L$	0.0	[m^{-11}]
a_{12}	0.0	[T m^{-12}]	$K_{12}L$	0.0	[m^{-12}]
a_{13}	0.0	[T m^{-13}]	$K_{13}L$	0.0	[m^{-13}]

Table 7.7: Multipole coefficients for BS1X at $x = 0.0855$ m and $y = 0.0$ m from the center of the septum magnet from the PRIAM linear Lagrange method of mapping, fitted with a polynomial function by square minimization.

field. The non-linearity was checked to be small enough to be neglected in this region.

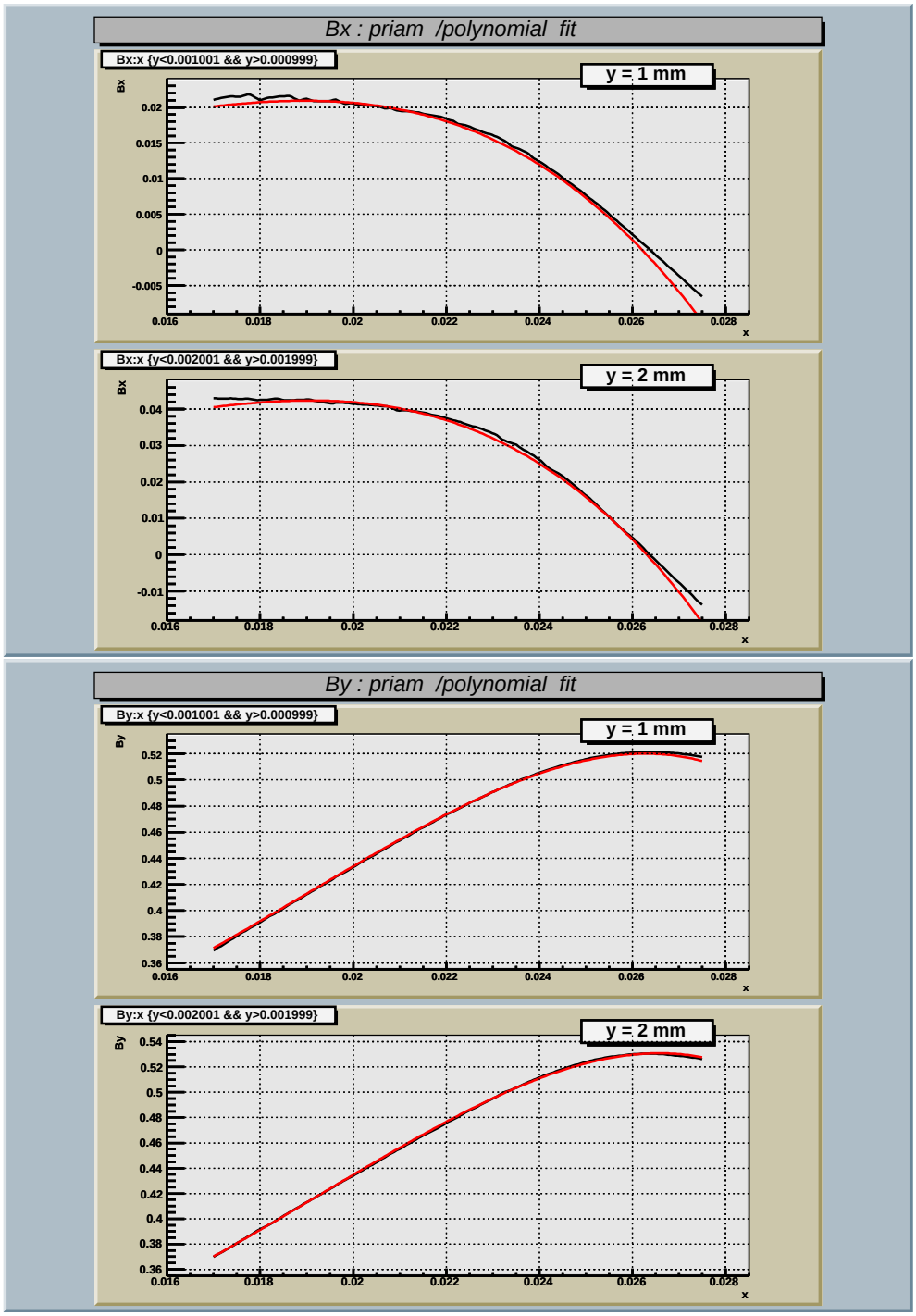

Figure 7.3: Comparison of the horizontal (top) and vertical (bottom) magnetic field of the QM7R magnet modeled with PRIAM (black lines) and the values reconstructed from the fit (red lines) at $y = 1$ and 2 mm, around the nominal horizontal beam extraction position.

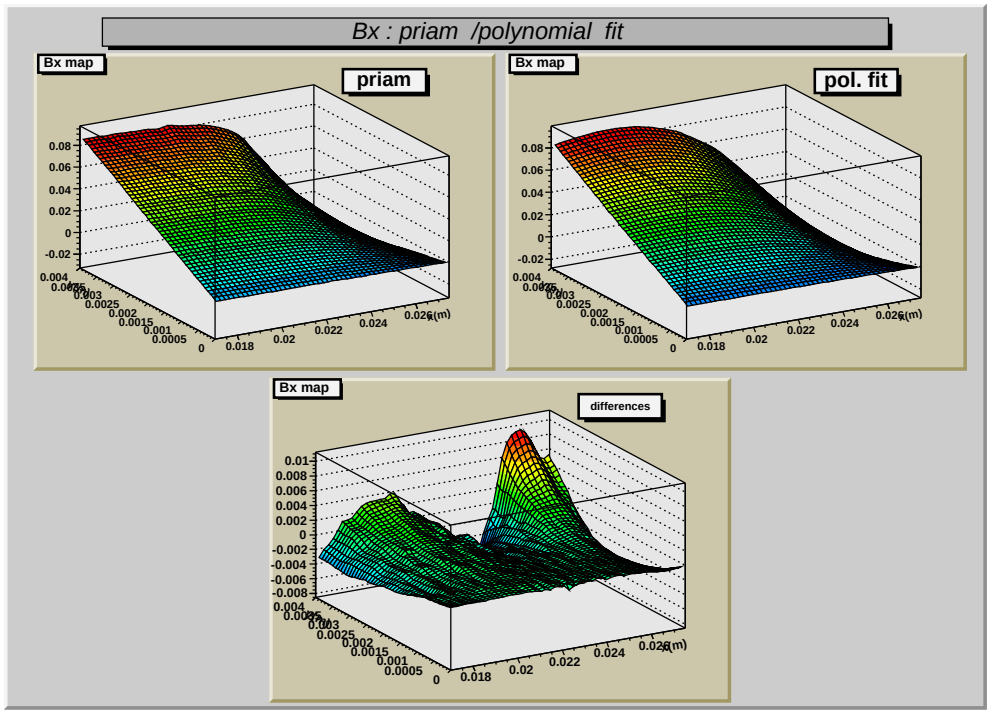

Figure 7.4: QM7R horizontal magnetic field B_x: comparison of PRIAM and fitted values.

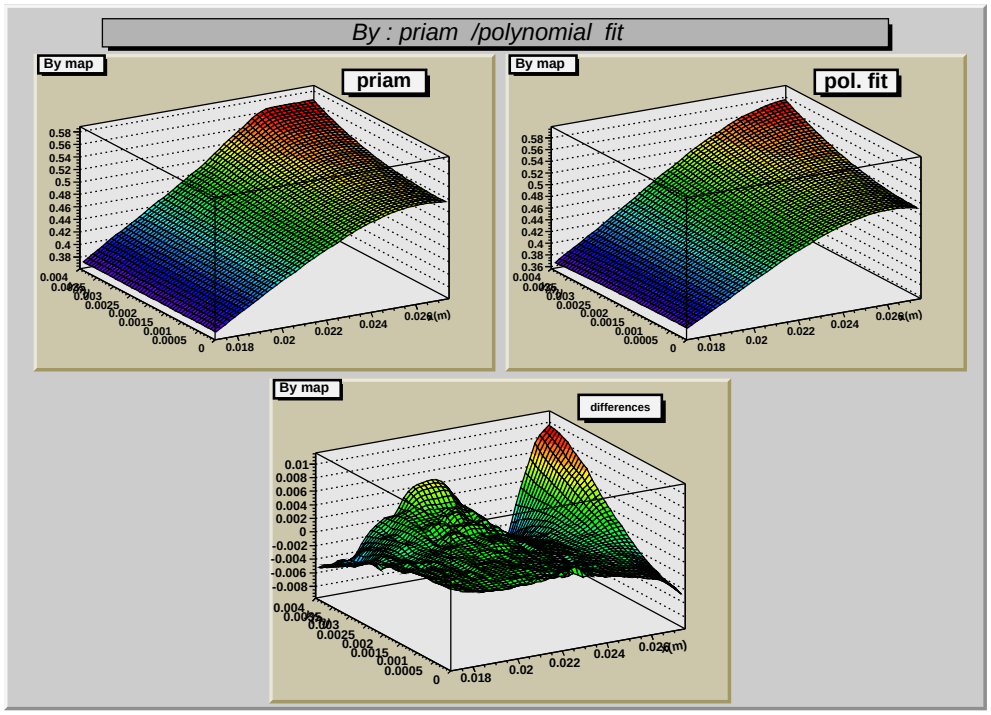

Figure 7.5: QM7R vertical magnetic field B_y: comparison of PRIAM and fitted values.

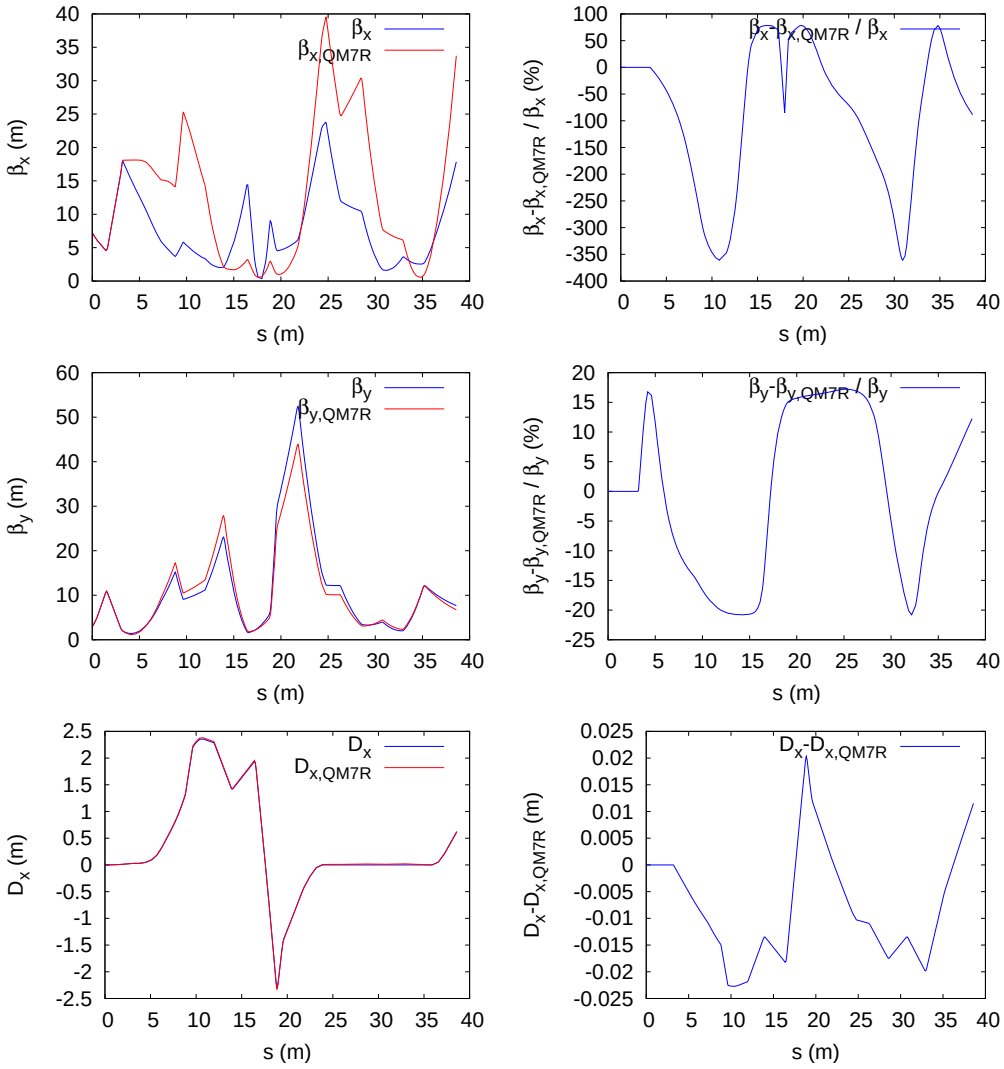

Figure 7.6: Relative differences between the standard optics functions in the ATF EXT line and those computed with the values of the dipole and quadrupole components of QM7R calculated by PRIAM for the extracted beam.

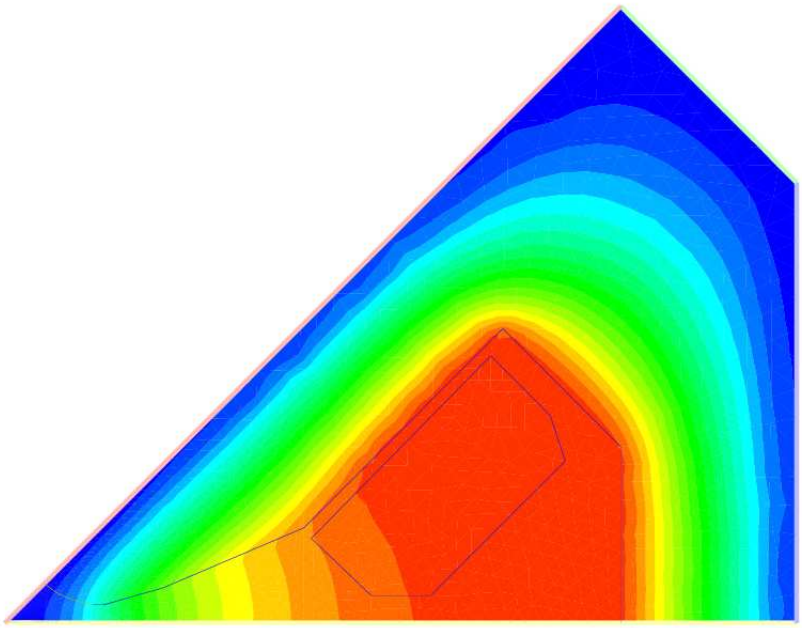

Figure 7.7: QM6R B field lines computed with PRIAM.

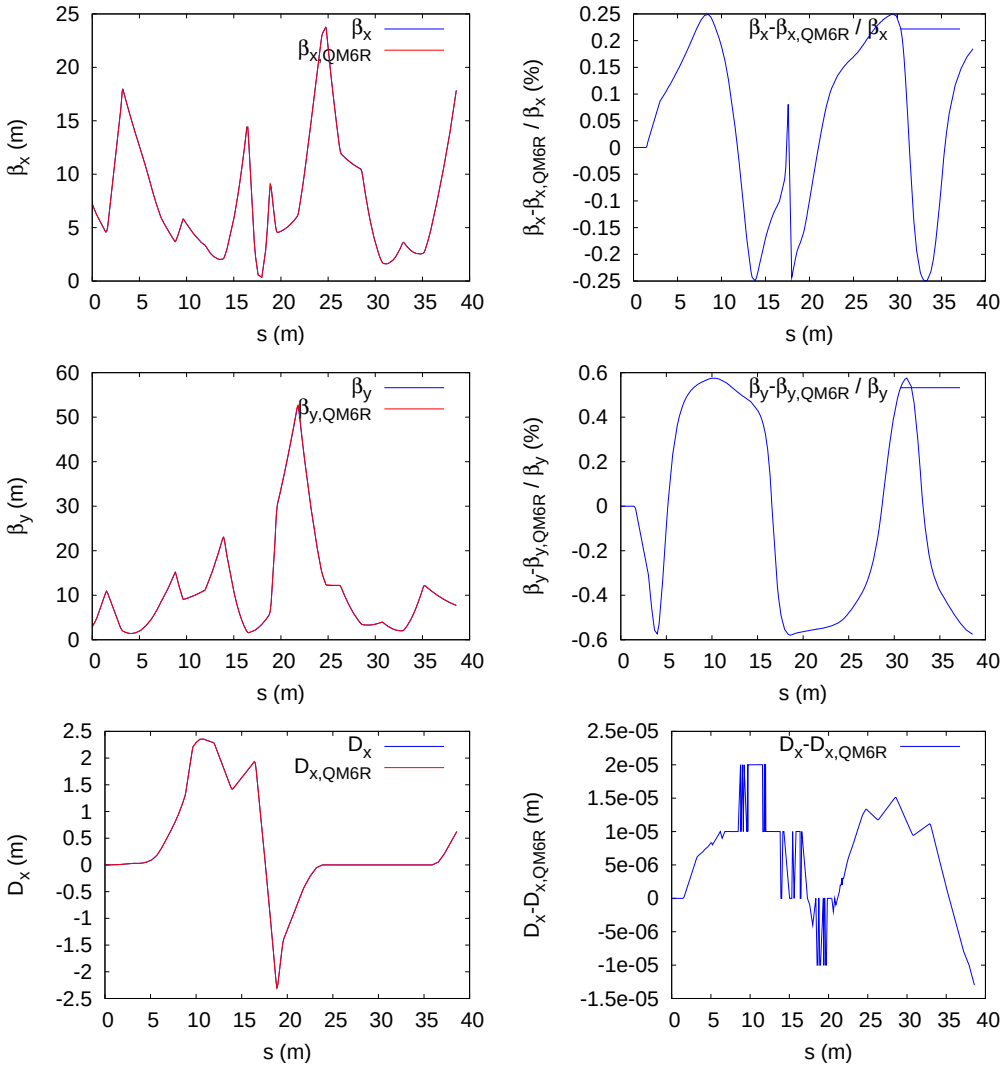

Figure 7.8: Relative differences between the standard optics functions in the ATF EXT line and those computed with the values of the quadrupole and dipole components calculated for QM6R by PRIAM at the location of the extracted beam.

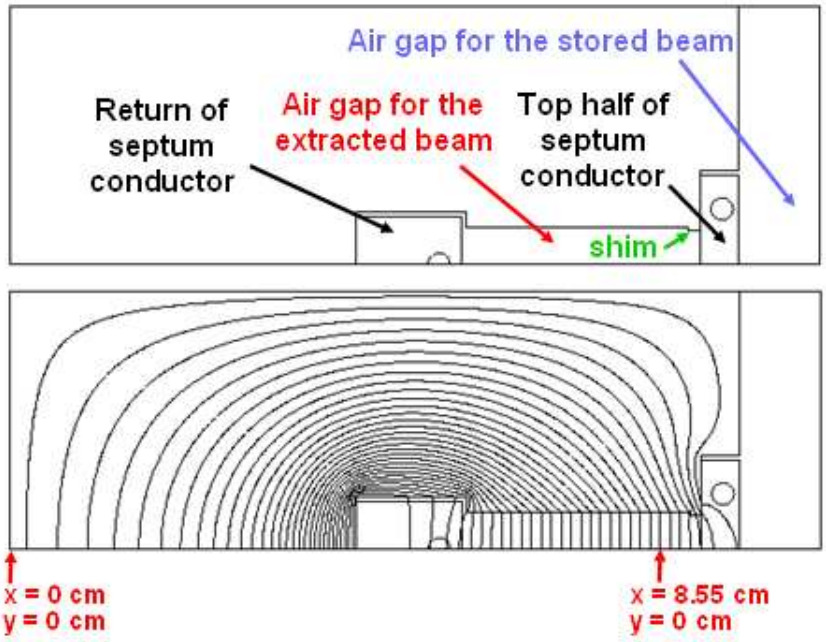

Figure 7.9: Top: Cross section through top half of BS1X septum magnet. Bottom: Field lines of BS1X calculated with POISSON [83].

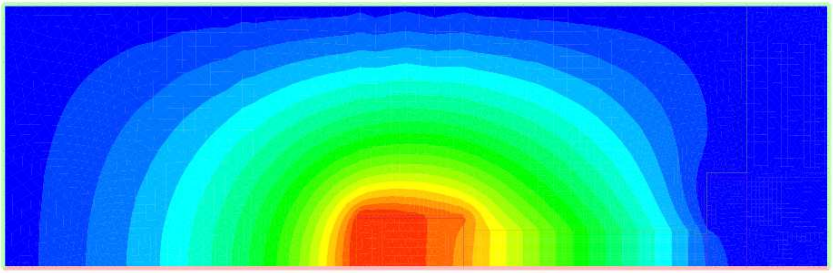

Figure 7.10: BS1X B field lines computed with PRIAM.

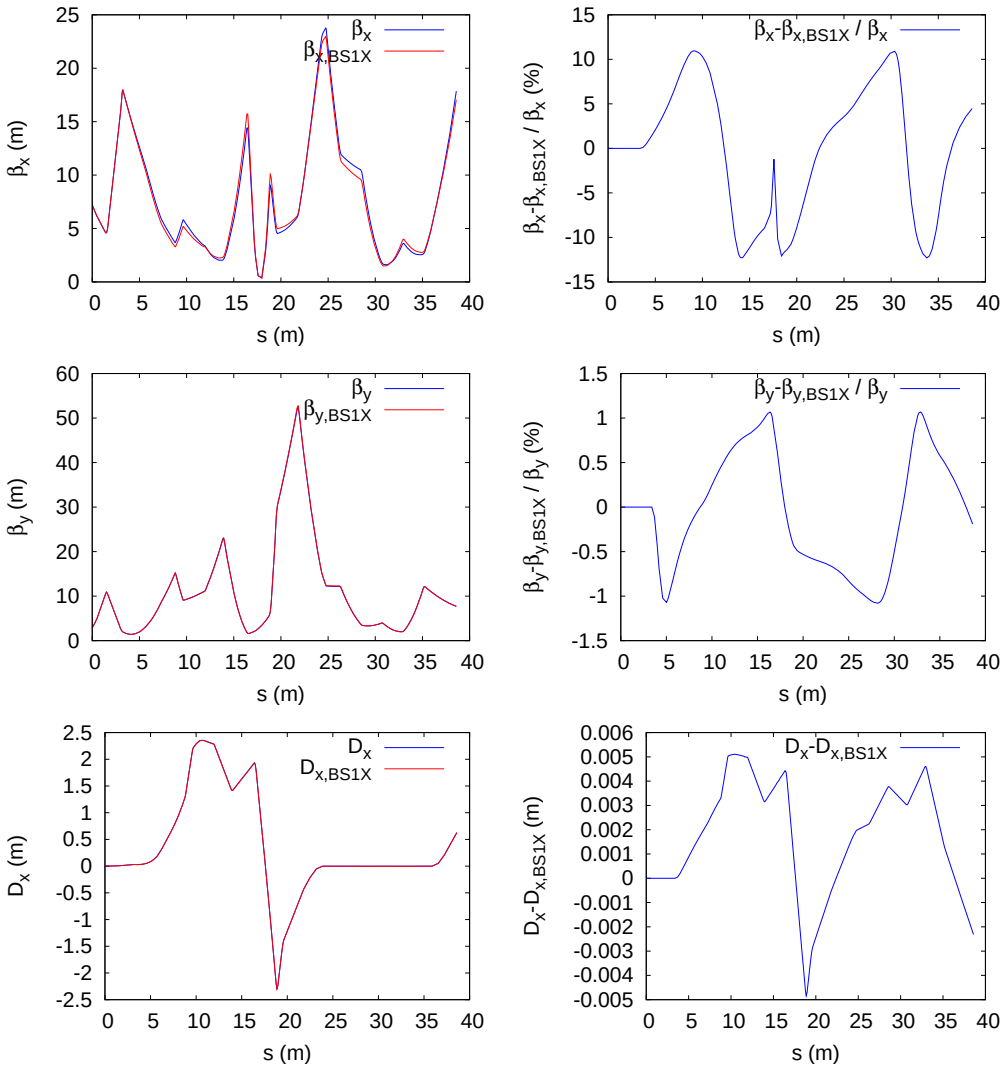

Figure 7.11: Relative differences between the standard optics functions in the ATF EXT line and those computed with the values of the dipole and quadrupole components calculated for BS1X with PRIAM at the location of the extracted beam.

Chapter 8

Tracking Simulations including Non-linear Magnetic Fields

With the purpose of studying the effect on the vertical beam emittance of the non-linear magnetic fields during the beam extraction from the DR, the magnets involved in the extraction have been carefully modelled in terms of multipole expansions, to enable tracking simulations. From the results of the corresponding field maps, presented in Chapter 7, a dominant contribution can be expected from the QM7R magnet. Tracking simulations have been performed including the non-linear fields for all these magnets, and with different vertical and horizontal displacements with respect to the ideal orbit, to study the corresponding sensitivities. The results are presented in this chapter.

8.1 Analytical approach to estimate the emittance growth due to the first order non-linear fields

Non-linear magnetic fields in the extraction region would induce coupling between the vertical and horizontal planes, inducing the undesired emittance growth.

As an example of the most common sources of coupling between two planes, there are the quadrupole rotations and the vertical sextupole misalignments [85, 86].

In a normal quadrupole, focusing in the horizontal plane, the horizontal and vertical components of the magnetic field are given by

$$\begin{aligned} B_x(x,y) &= -K_Q y \\ B_y(x,y) &= -K_Q x, \end{aligned} \tag{8.1}$$

where K_Q is the strength of the quadrupole [87]. This means that the horizontal force component depends only on the horizontal position and not on the vertical position of the particle trajectory, and vice versa:

$$\begin{aligned} F_y &= -evB_x(x,y) = evK_Q y \\ F_x &= evB_y(x,y) = -evK_Q x, \end{aligned} \tag{8.2}$$

where v is the velocity of light. Thus, the horizontal and vertical betatron oscillations are completely decoupled.

In a skew quadrupole (quadrupole rotated by 45°), the horizontal and vertical compo-

nents of the magnetic field are given by

$$\begin{aligned} B_x(x,y) &= K_{QS}\,x \\ B_y(x,y) &= -K_{QS}\,y, \end{aligned} \tag{8.3}$$

where K_{QS} is the strength of the skew quadrupole. In this case, the force component in each direction depends on the position of the particle trajectory in the other direction, coupling both planes:

$$\begin{aligned} F_y &= -evB_x(x,y) = -evK_{QS}\,x \\ F_x &= evB_y(x,y) = -evK_{QS}\,y. \end{aligned} \tag{8.4}$$

In a sextupole, the horizontal and vertical components of the magnetic field are given by

$$\begin{aligned} B_x(x,y) &= K_S\,xy \\ B_y(x,y) &= \tfrac{1}{2}K_S(x^2 - y^2), \end{aligned} \tag{8.5}$$

where K_S is the strength of the sextupole. In this case, the force component in each direction depends on the position of the particle trajectory in both directions:

$$\begin{aligned} F_y &= -evB_x(x,y) = -evK_S\,xy \\ F_x &= evB_y(x,y) = \tfrac{1}{2}evK_S(x^2 - y^2). \end{aligned} \tag{8.6}$$

A vertical sextupole misalignment, or a misalignment of the beam orbit with respect to the center of the magnet, of magnitude Δy would be equivalent to a skew quadrupole of strength $K_{QS} = K_S\Delta y$, coupling the motion in both planes.

In order to calculate the emittance growth due to the coupling induced by a skew quadrupole, let's consider an uncoupled beam at the entrance of the magnet. The beam matrix σ, in the case of the horizontal plane, is defined as

$$\sigma = \epsilon_x \begin{pmatrix} \beta_x & -\alpha_x \\ -\alpha_x & \gamma_x \end{pmatrix} = \begin{pmatrix} \langle x^2 \rangle & \langle xx' \rangle \\ \langle x'x \rangle & \langle x'^2 \rangle \end{pmatrix}, \tag{8.7}$$

where the bracketed terms are the second moments of the beam distributions. Note that the first moments or mean of the distribution have been subtracted [59].

The beam matrix σ_0 of the uncoupled beam just upstream of the skew quadrupole, generalized for both planes is

$$\sigma_0 = \begin{pmatrix} \sigma_{11} & \sigma_{12} & 0 & 0 \\ \sigma_{12} & \sigma_{22} & 0 & 0 \\ 0 & 0 & \sigma_{33} & \sigma_{34} \\ 0 & 0 & \sigma_{34} & \sigma_{44} \end{pmatrix}, \tag{8.8}$$

where the quadrants along the diagonal are the horizontal (top) and vertical (bottom) beam matrices, and the off-diagonal elements are zero.

The transformation between the initial beam matrix σ_0 to the beam matrix σ at the exit of the skew quadrupole is

$$\sigma = R\sigma_0 R^T, \tag{8.9}$$

where R is the transfer matrix and R^T is the transpose of R.

The transfer matrix of a skew quadrupole in the thin lens approximation is

$$R = \begin{pmatrix} 1 & 0 & 0 & 0 \\ 0 & 1 & -1/f & 0 \\ 0 & 0 & 1 & 0 \\ -1/f & 0 & 0 & 1 \end{pmatrix} \tag{8.10}$$

where the focal length is defined as $f^{-1} = KL$, with KL the integrated strength [50]. Thus, the beam matrix at the exit of the magnet is given by

$$\sigma_0 = \begin{pmatrix} \sigma_{11} & \sigma_{12} & 0 & -\sigma_{11}KL \\ \sigma_{21} & \sigma_{22} + \sigma_{33}KL^2 & -\sigma_{33}KL & 0\sigma_{21}KL + \sigma_{34}KL \\ 0 & -\sigma_{33}KL & \sigma_{33} & \sigma_{34} \\ -\sigma_{11}KL & \sigma_{12}KL - \sigma_{43}KL & \sigma_{43} & \sigma_{11}KL^2 + \sigma_{44} \end{pmatrix}. \tag{8.11}$$

Since the emittance can be calculated from the determinant of the beam matrix [59], $\epsilon = \sqrt{\det \sigma}$, the vertical projected emittance ϵ_y at the exit of the skew quadrupole is given by

$$\epsilon_y^2 = \sigma_{33}\sigma_{11}(KL)^2 + \sigma_{33}\sigma_{44} - \sigma_{34}^2 = \epsilon_{y,0}^2 + \sigma_{33}\sigma_{11}(KL)^2. \tag{8.12}$$

Using the analogous of Eq. 8.7 for the vertical plane, the vertical projected emittance can be expressed as

$$\epsilon_y^2 = \epsilon_{y,0}^2 + \beta_{y,0}\epsilon_{y,0}\beta_{x,0}\epsilon_{x,0}(KL)^2, \tag{8.13}$$

where $\epsilon_{y,0}$ is the vertical emittance at the entrance of the skew quadrupole.

As the skew quadrupole was equivalent to a sextupole magnet misaligned by an amount Δy in the vertical plane, the vertical emittance growth can also be expressed as

$$\epsilon_y^2 = \epsilon_{y,0}^2 + \beta_{y,0}\epsilon_{y,0}\beta_{x,0}\epsilon_{x,0}(K_2L)^2\,(\Delta y)^2\,, \tag{8.14}$$

where K_2L is the integrated strength of the sextupole magnet. Only the first order terms are considered.

It is worth noting that the emittance growth depends not only on the vertical beam size at the entrance of the magnet, but also on the horizontal one, $\sqrt{\beta_{x,0}\epsilon_{x,0}}$, which is much bigger in the case of flat beams.

For the case of ATF, assuming a sextupolar component in the QM7R quadrupole of $K_2L = 46.6$ m^{-2} (which corresponds to the value obtained from the modeling of this magnet, see Section 7.3, Table 7.3), with input initial emittances the nominal ATF ones, with typical values of the β-functions at the entrance of the QM7R quadrupole $\beta_{x/y} = 21.2/2.1$ m, respectively, and assuming that the beam is displaced vertically by 1 mm, the vertical emittance at the exit of the quadrupole would increase approximately by a factor of 3.3.

In order to carry out a more complete study, tracking simulations have been performed to determine the impact on the emittance not only of the first order non-linear fields, but also of the higher order multipole components of the magnets involved in the extraction.

8.2 Tracking simulations including non-linear magnetic fields in the magnets involved in the extraction

Simulations including non-linear fields in the different magnets of the extraction region (QM6R, QM7R and BS1X) have been performed. The multipole field components computed in Chapter 7 are introduced in the middle of the magnets by thin element kicks. The particles have been tracked from the drift that precedes the corrector ZV9R, which serves as starting point to create the bumps in the DR and the EXT line (see Section 6.4.1), until the OTR monitor, located after the extraction (see Fig. 6.10). Transverse Gaussian beam distributions of 50000 macro-particles have been created with the code PLACET [51], using the nominal ATF2 emittances and optical Twiss parameters at the starting point of the simulations which are listed in Table 8.1. These parameters represent the beam phase space at the beginning of the drift that precedes the ZV9R corrector. The simulations have been performed with a beam of central energy 1.3 GeV and a flat energy distribution of 0.08% full width. The modeled energy distribution coming from the DR should be a Gaussian distribution with 0.08% of sigma value, and not a flat distribution, but with such a small energy spread and vertical dispersion, the difference by using the two mentioned distributions on the vertical beam sizes and emittances is negligible.

The input beam phase space for the simulations are shown in Fig. 8.1 for each transverse plane.

Table 8.1: Input beam emittances and Twiss parameters for the tracking simulations corresponding to the location just before the ZV9R corrector.

E (GeV)	1.3
$\delta p/p$ (%)	0.08
ϵ_x (pm·rad)	1200
ϵ_y (pm·rad)	12
β_x(m)	2.06210
β_y(m)	2.92901
α_x	-3.51293
α_y	1.15084
D_x (m)	-1.096×10^{-3}
D'_x	-1.691×10^{-3}

The beam is then tracked through the EXT line with the code MAD [57], until the OTR monitor, located after the beam extraction. The vertical projected emittance ϵ_y at this location is obtained from the phase space as:

$$\epsilon_y = \sqrt{\langle y^2\rangle\langle y'^2\rangle - \langle yy'\rangle^2} \tag{8.15}$$

where the first moments or means of the distributions in position and angle have been subtracted, and the averages are taken over the distributions of the beam particles [59].

Vertical beam sizes and vertical projected emittances at the OTR monitor, as a function of the vertical bump amplitude in the QM7R magnet are shown in Fig 8.2. The results of the simulations are shown for different cases: without any multipolar component in the

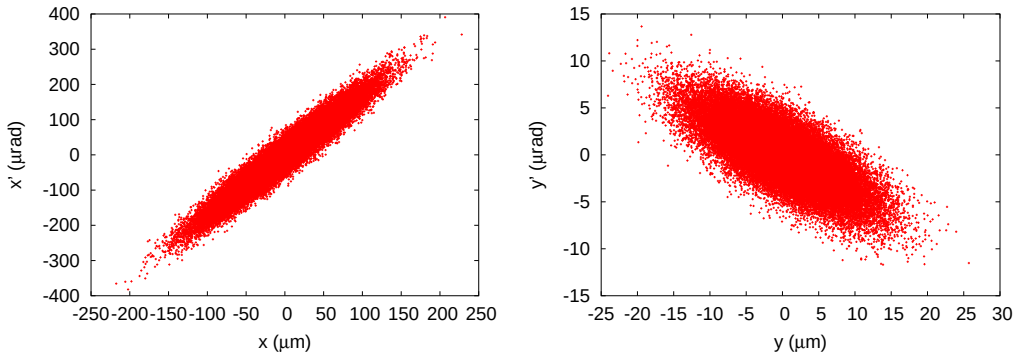

Figure 8.1: Transverse phase space of the input beam used for the simulations. The input distribution corresponds to the entrance of the drift that precedes the ZV9R corrector.

magnets involved in the extraction, and including successively the multipole components in QM6R, QM7R and BS1X.

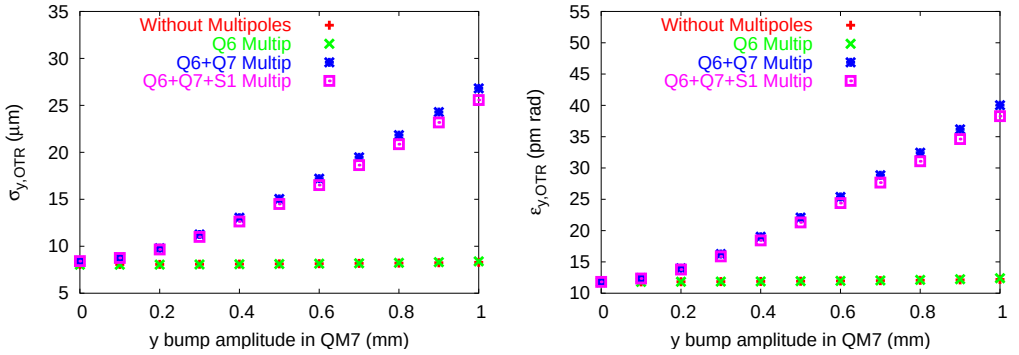

Figure 8.2: Vertical beam sizes (left) and vertical projected emittances (right) at the OTR location as a function of the vertical bump amplitude in the QM7R quadrupole including non-linear fields in the different magnets of the extraction region.

Without including in the simulation any non-linear multipolar component for the involved magnets, (red line in Fig. 8.2), the beam sizes and emittances are rather constant with the vertical offset.

As expected, the same occurs when including the multipolar components predicted in 7 for the QM6R quadruple, (green line in Fig. 8.2), since the nominal horizontal extraction position of the beam is very close to the center of the magnet, and the resulting non-linearity is hence small.

However, a significant increase occurs with the bump amplitude when including the QM7R multipolar components (dark blue line in Fig. 8.2), as the extracted beam passes off-axis horizontally significantly beyond the linear region of that magnet. The non-linearity in this magnet would have negligible effect if the beam were always centered vertically. As found in [73, 88], it however causes significant growth of the effective vertical emittance as soon as the beam goes vertically off-axis.

Fig. 8.3 shows the beam phase space at the OTR location corresponding to a 1 mm vertical bump in QM7R, for the cases in which no multipoles (green points) and QM7R multipoles (red points) are included in the simulation. The volume occupied by the beam

in the vertical phase space increases significantly when QM7R multipoles are included.

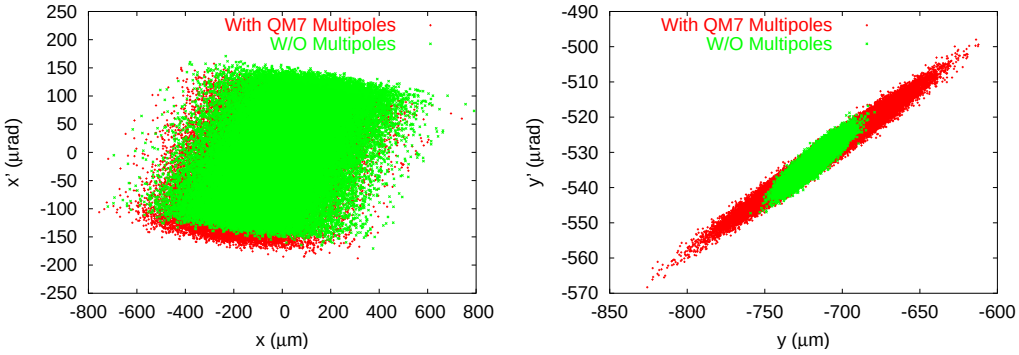

Figure 8.3: Transverse phase space of the beam at the OTR location corresponding to 1 mm of vertical bump amplitude in QM7R, for the cases in which no multipoles (green points) and QM7R multipoles (red points) are included in the simulation.

When including the multipole components for the BS1X septum magnet predicted in 7, (pink line in Fig. 8.2), almost no difference is found with respect to the simulation including the QM7R multipoles, as the predicted sextupolar component for BS1X is relatively small. About a 5% difference is found for a 1 mm vertical bump amplitude.

8.3 Tracking simulation for different vertical and horizontal bumps in the extraction region

Tracking simulations have also been done with combined vertical and horizontal bumps, to study the corresponding sensitivities. Results are summarized in Fig. 8.4. For ±1 mm vertical bumps in QM7R (Fig 8.4 left, top), there is a significant increase of the vertical projected emittance, while in the case of ±1 mm horizontal bump with the beam centered vertically (Fig. 8.4 right, top), the increase is still negligible.

As shown in Fig. 8.4 bottom left, having an additional horizontal bump of half a millimeter increases the emittance growth as a function of the vertical bump amplitude. In the case of a vertical bump of half a millimeter, the emittance growth for a +1 mm horizontal bump becomes important, while for a −1 mm horizontal bump the projected emittance decreases since the beam goes towards the center of the quadrupole, that is towards the linear region (see Fig. 8.4 bottom right).

8.4 Projected emittances at different locations along the EXT line

Furthermore, tracking simulations have been carried out to obtain the projected emittances at different locations along the extraction line: before and after the QM7R magnet, at the OTR monitor position, and at the location of the four wire scanners available in the diagnostic section, MW0X, MW1X, MW2X and MW3X. Results as a function of the vertical bump amplitude in QM7R are shown in Fig. 8.5.

Before the magnets where the non-linear fields arise, the projected emittance is rather

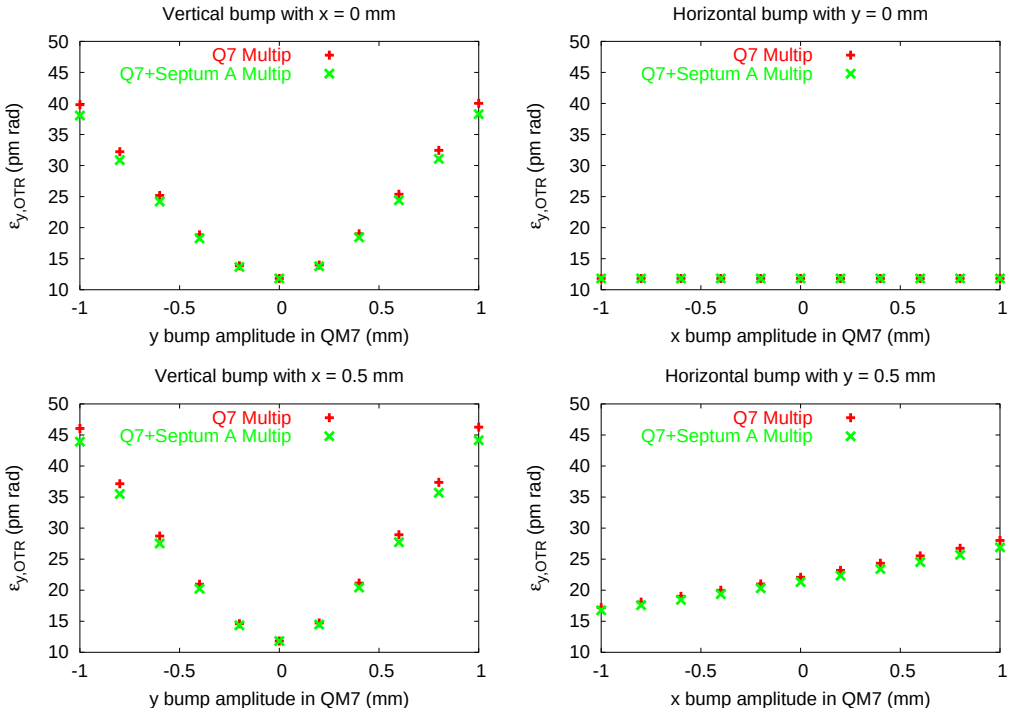

Figure 8.4: Vertical projected emittances at the OTR location as a function of combined vertical and horizontal bump amplitudes in the QM7R quadrupole. Simulations performed for two cases, including non-linear fields in the QM7R quadrupole and in both QM7R and BS1X magnets.

constant with the bump amplitude, while it increases after the extraction. It is not significantly increased along the EXT line where the different wire scanners are located.

During the experimental program carried out in order to study the correlation between the extraction beam trajectory and the emittance growth, and to asses the results of the simulations, beam diagnostics are performed with the OTR monitor (see Chapter 9). As explained in Section 6.4.2, it was not possible to succeed in obtaining reliable diagnostics in the wire scanner stations.

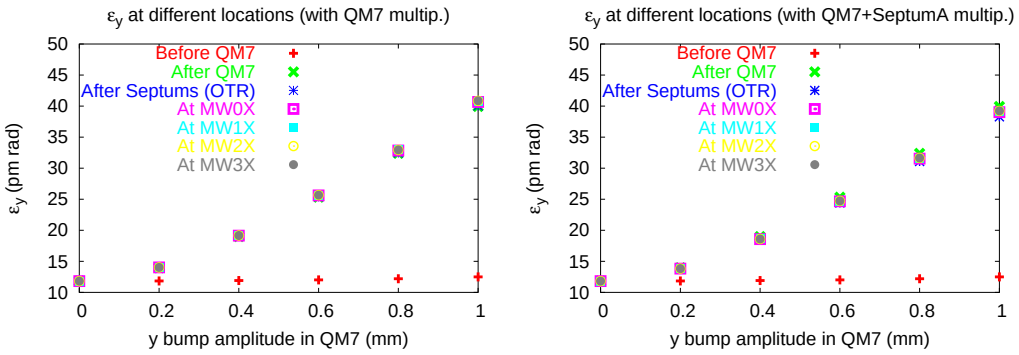

Figure 8.5: Vertical projected emittances at different locations along the EXT line, as a function of the vertical bump amplitude in the QM7R quadrupole. Simulations were performed including non-linear fields in the QM7R quadrupole (left) and in both QM7R and BS1X magnets (right).

Chapter 9

Experimental Studies of the Vertical Emittance Growth

Tracking simulations presented in Chapter 8, including modelled non-linear field errors in the magnets involved in the beam extraction process from the ATF DR, predict significant emittance growth when the beam is displaced vertically with respect to the nominal trajectory. The main contribution arises from the QM7R quadrupole, while the effect of the other magnets is nearly negligible. An experimental program has been carried out at KEK during 2007-2008 to study the relation between the extraction trajectory and the anomalous emittance growth. For the purpose of modeling the beam at different orbits during the extraction, closed orbit bumps in the DR were generated. In this chapter, the results of this program are reported and compared to simulations.

9.1 Overview of the experimental program

To study the dependence of the anomalous emittance growth on the extraction trajectory in QM7R during the beam extraction process from the DR, an experimental investigation was carried out, which involved creating closed orbit bumps in the DR, as explained in Section 6.4.1. Beam sizes were measured immediately downstream, after the beam extraction, to infer the corresponding beam emittances. For the diagnostics, an OTR monitor was used (see Section 6.4.2), installed just after the septum magnets, at a location such that it imaged the beam angular spread out of QM7R with little influence from the beam size in QM7R, thus representing the growth in projected emittance from non-linearities in QM7R quite well. This allowed faster and more reliable results since the measured changes in vertical beam size at this location were well correlated with the emittance growth (see the simulation study in Chapter 8) and because the bumps did not need to be closed in the extraction line during the measurements.

Beam sizes at this location were recorded as a function of bump amplitudes in QM7R. In order to discriminate between a possible emittance growth due to the non-linear fields in the extraction and variations arising within the DR itself, measurements of stored beam sizes were simultaneously performed with the XSR monitor (see Section 6.1.1).

9.2 Summary of beam time periods in 2007-2008

Table 9.1 shows the beam time used in the different periods in 2007-2008 to measure beam sizes at the XSR and OTR monitors, in the DR and EXT line, respectively.

Shift	Date	Time
1	2007 December 19	9 PM to 10 PM
2	2008 March 4	1 AM to 9 AM
3	2008 May 14	5 PM to 1 AM (+1 day)
4	2008 May 22	5 AM to 5 PM
5	2008 May 28	9 AM to 1 AM (+1 day)

Table 9.1: Beam time used in 2007-2008 for simultaneous XSR and OTR vertical beam size measurements.

During each shift, after initial checks of the orbits and dispersion corrections, a vertical bump was set up in the DR to generate offsets in QM7R. Typical amplitudes which could be achieved within the maximum strengths of the steering correctors used were in the ±1 mm range. Beam intensities and digitized size information at the XSR and OTR monitors were then acquired for each bump setting.

Table 9.2 summarizes the results obtained for minimum vertical beam sizes during these scans and for the vertical emittances, which could be inferred from propagating β and dispersion functions obtained using an optical model representing the magnet settings during the shifts. Simulated values are also shown for comparison, using DR measured emittances as input.

Beam conditions were different in the five data taking periods: while the measurements on the 19^{th} of December 2007 and 28^{th} of May gave values which could be compared with the simulation and interpreted in terms of coupling effects from QM7R, during the three other periods in March and May 2008, beam sizes at the OTR monitor were significantly larger and could not be explained in the context of the bump experiments subject of this study.

In the following sections, after summarizing the conditions in each data taking period, the corresponding measurement and simulation results are presented, focusing the analysis on the data from the 19^{th} of December 2007 and 28^{th} of May.

	$\epsilon_{x,XSR}$	$\epsilon_{y,XSR}$	$\sigma_{y,OTR}$ (μm)		$\epsilon_{y,OTR}$ (pm·rad)	
	(nm·rad)	(pm·rad)	Measurement	Simulation	Measurement	Simulation
19 Dec'07	2.4	36.5	12.8	11.8	40	35
4 Mar'08	1.4	41.9	25.9	13.4	155	41
14 May'08	2.5	44.6	22.6	13.1	127	44
22 May'08	3.8	27.0	30.8	10.3	228	27
28 May'08	2.1	22.5	15.1	9.4	40	22

Table 9.2: Smallest vertical beam sizes measured at the OTR for the different vertical offsets implemented during successive shifts and corresponding emittances calculated from the β-function and dispersion obtained from the model. Vertical beam sizes and projected emittances at the OTR predicted from simulations using as input DR emittances obtained during the shifts. Horizontal and vertical emittances measured at the XSR monitor.

9.3 Simultaneous measurements at OTR and XSR beam size monitors

9.3.1 Measurements on the 19^{th} of December 2007

On the 19^{th} of December the first simultaneous OTR and XSR beam size measurements were done parasitically in a shift of another group, as a function of the vertical bump amplitude. The machine was already tuned and running in the one bunch per train, one train per pulse mode. All measurements presented in this thesis were done with this mode of operation. The beam intensity was relatively constant (see Fig. 9.1). The corrector strengths needed to create a 1 mm vertical bump amplitude in QM7R are shown in Table 9.3. Negative vertical bumps were generated in QM7R, in steps of 0.1 mm, down to a -0.8 mm amplitude. It was not possible to go to positive values because the strength of ZV9R was at its upper limit.

ZV9R	1.94 A/mm
ZV100R	-1.56 A/mm
ZV10R	-1.42 A/mm

Table 9.3: Corrector strengths to create a closed bump in the DR with a 1 mm vertical amplitude in QM7R with the optics of the 19^{th} of December 2007.

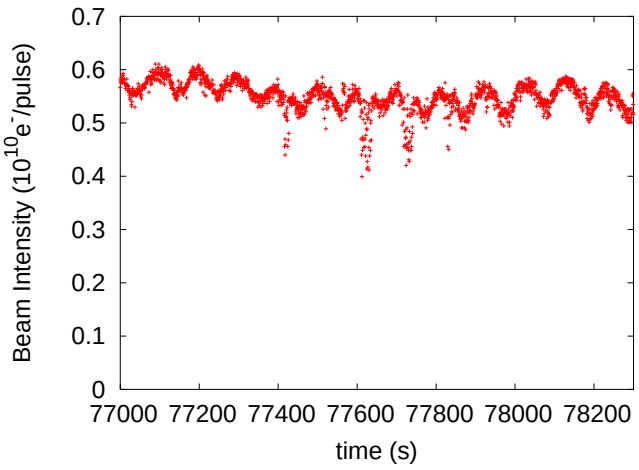

Figure 9.1: Beam intensity during the beam size measurements on the 19^{th} of December 2007.

The raw OTR and XSR beam size data are shown in Fig. 9.2 top, in channels and μm, respectively. They are also shown after cuts to remove the data in between each stable setting of the bump, see Fig. 9.2 bottom, and after averaging, see Fig. 9.3, where the error bars correspond to the standard deviation, the horizontal scale displays the bump amplitude and the vertical scale of the OTR measurements has been converted to μm by multiplying by a factor of 1.6. The XSR data recorded already included the required calibration factor of 1.2.

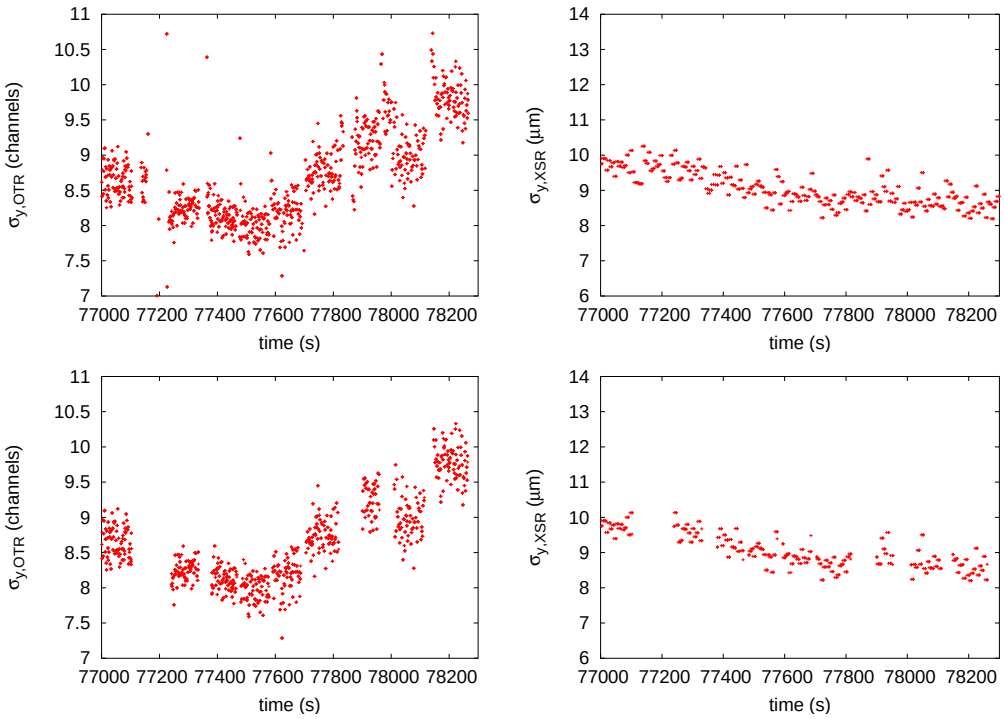

Figure 9.2: Vertical beam sizes recorded at the OTR (left) and XSR (right) on the 19^{th} of December 2007 as a function of time (top). Idem after removing data between each stable bump setting (bottom).

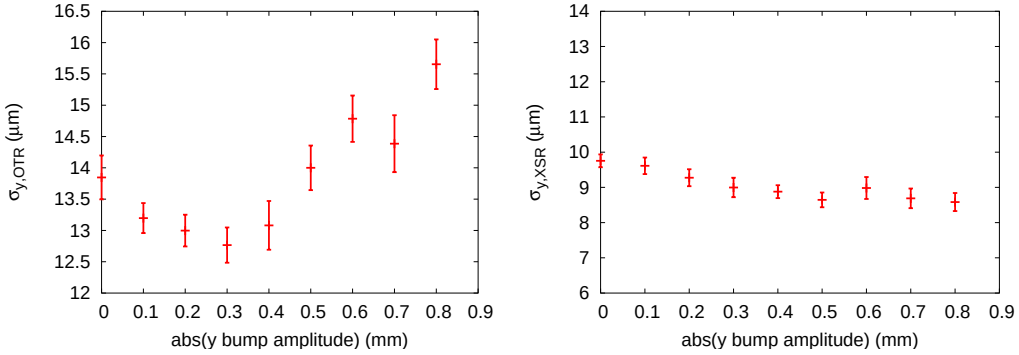

Figure 9.3: Vertical beam size at the OTR (left) and XSR (right) measured on the 19^{th} of December 2007 as a function of the bump amplitude in QM7R.

In the range from 0.3 to 0.8 mm bump amplitude, the XSR beam size was relatively stable (see Fig. 9.3 right). The minimum beam size, and thus the minimum emittance configuration, may correspond to a non-zero bump amplitude if the beam has an initial offset. Here, the minimum OTR beam size was for a 0.3 mm bump amplitude (see Fig. 9.3 left), which can hence be considered as origin for the vertical displacements with respect to the center of QM7R. In Fig. 9.4 left, (blue line) the OTR measurements are shown with respect to this reference, in the restricted range where XSR beam sizes remained stable. Simulation results using as input DR emittances measured during the shift (green line) or nominal values (red line) are also shown.

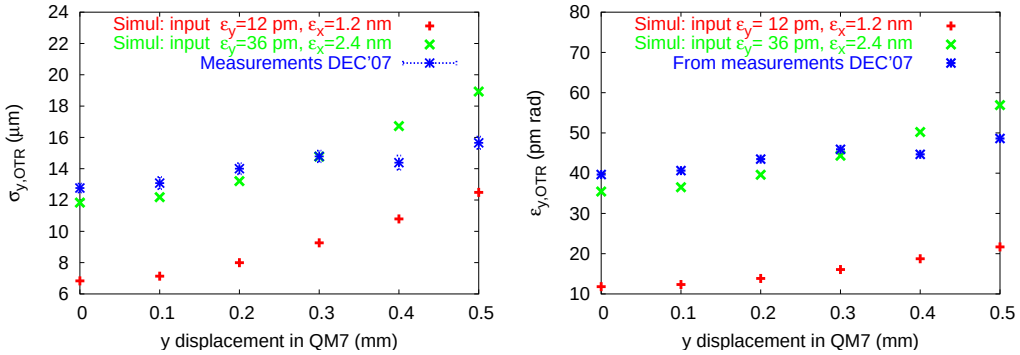

Figure 9.4: Vertical beam sizes at the OTR measured on the 19^{th} of December 2007 (left) and corresponding emittances (right) as a function of vertical displacement in QM7R. Simulation results using as input nominal and measured DR emittances are also shown.

The simulations tracked a Gaussian beam distribution of 50000 macro particles with energy 1.3 GeV and a flat energy distribution with 0.085% full width through the beam line, using an optical model representing the magnet settings during the shift and including the multipole coefficients computed in [72]. The vertical and horizontal DR emittances were computed from corresponding XSR beam sizes using the relation:

$$\epsilon_{y,x} = \left(\sigma^2_{y,x} - (\delta p/p \cdot D_{y,x})^2\right)/\beta_{y,x} \tag{9.1}$$

where the β-functions and dispersions were obtained from the on-line optical model of the DR (see Table 9.4).

Fig. 9.4 right shows the vertical emittances at the OTR computed from the same relation, using the measured beam sizes in Fig. 9.4 left and the vertical β-function and dispersion propagated to the OTR location using the model. Measured and simulated values for the minimum bump amplitude are also summarized in Table 9.4.

The simulation with nominal DR emittances (red line) and no bump gives much smaller OTR beam sizes than the measurement, while using the emittances determined during the shift (green line) improves the agreement. The growth when introducing the bump is however less than predicted by the simulation. Table 9.2 gives the minimum measured beam size and the corresponding value from the simulation. Small differences can be seen, which may due to differences between the optical model and the real machine. Such differences can also affect the conversion from measured beam sizes to emittances. Ideally, the β-function at the OTR location should be measured.

To better account for the variations in the DR during the experiment, the ratio of both beam sizes was also studied (see Fig. 9.5 left), using in this case the full range of bump

XSR				**OTR**	
$\sigma_{y,meas}$ (μm)	9.0	$\sigma_{x,meas}$ (μm)	40.7	$\sigma_{y,meas}$ (μm)	12.8
β_y (m)	2.2	β_x (m)	0.5	$\beta_{x,y}$ (m)	10.6, 4.0
D_y (mm)	-0.4	D_x (mm)	23.4	D_y (mm)	2.9
ϵ_y (pm·rad)	36.5	ϵ_x (nm·rad)	2.4	ϵ_y (pm·rad)	39.6

Table 9.4: Emittances in the DR and at the OTR location during the shift of the 19^{th} of December 2007, computed from the measured beam sizes and β-functions and dispersions at the XSR and OTR, obtained through an optical model of the DR and EXT line representing the settings of the magnets.

amplitudes. A second-order polynomial fit to this ratio gives:

$$f(y) = a(y-b)^2 + c = 0.78(y-0.054)^2 + 1.39 \tag{9.2}$$

where the reduced χ^2=0.53, $f(y)$ is the ratio of the OTR and XSR beam sizes and y is the absolute bump amplitude. The minimum of the parabola corresponds to a bump amplitude of $y = 0.054$ mm. The rationale of fitting a second-order polynomial is because the main component in the QM7R multipolar field expansion [72] is a sextupole, and it can be shown computing the transfer matrix that for a vertically displaced sextupole, the emittance squared has a quadratic dependence on the product of the displacement and corresponding strength (see Section 8.1).

Fig. 9.5 right shows the ratio of the OTR and XSR beam sizes, normalized to the minimum value, and in comparison with simulation predictions including the multipole coefficients computed in Chapter 7 for QM7R (blue lines) and for both QM7R and BS1X (magenta lines). Two cases are displayed, corresponding to the nominal extracted horizontal orbit of 22.5 mm in QM7R (blue crosses and magenta empty boxes) and to one displaced by about 1.5 mm towards the center of the quadrupole (blue cross-box and magenta full box). Since the magnet is more linear near its center, effects become smaller in this last case and the agreement with the measurements is improved.

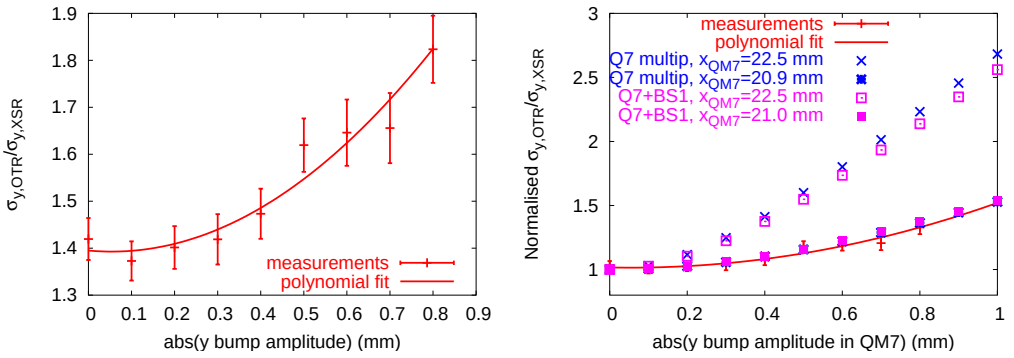

Figure 9.5: Ratio of vertical beam sizes at the OTR and XSR measured on the 19^{th} of December 2007 (left) and ratio normalized to the minimum value (right), as a function of the vertical bump amplitude. In the graph on the right, tracking simulation results are also shown, including the computed non-linearities in QM7R and BS1X, for the nominal horizontal orbit in QM7R (22.5 mm) and for one closer to the center of the QM7R by 1.5 mm.

9.3.2 Measurements on the 4th of March 2008

During this shift, DR and EXT line orbit and dispersions were corrected. Vertical dispersions need to be corrected down to less than about 10 mm in the diagnostic section to avoid biasing the emittance measurements. The beam intensity during the shift was about 1×10^{10} electrons per pulse and experienced small variations (see Fig. 9.6).

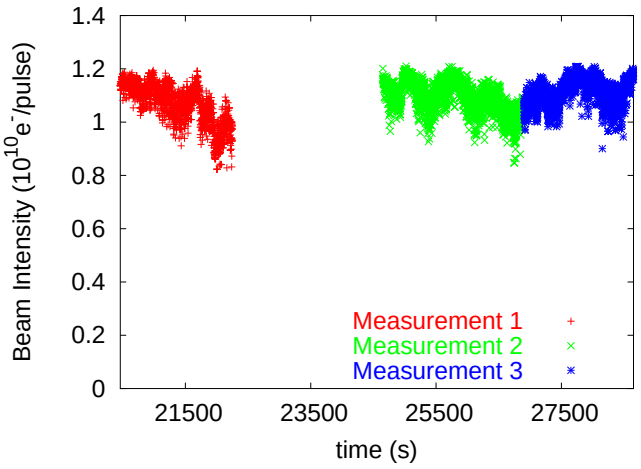

Figure 9.6: Beam intensity during data taking on the 4th of March 2008.

Beam sizes were recorded at the OTR and XSR as a function of a vertical bump in QM7R with amplitudes from 0 to 0.9 mm. The measurement was repeated twice about half an hour later (see Fig. 9.7). Since the three sets of data were fairly compatible, they were averaged (see Fig. 9.8). As can be seen, XSR beam sizes increased for large bump amplitudes, probably due to the fact that the bump was not perfectly closed in the DR. Some coupling between horizontal and vertical planes can in this case be induced through the sextupoles used for chromaticity correction in the DR.

Fig. 9.9 shows the measurements at the OTR (blue line) and simulated values using as input the DR emittances from the shift (green line) and nominal values (red line). Emittances in the DR were computed from Eq. 9.1 using the measured beam sizes at the XSR and the β-functions and dispersions obtained from the on-line optical model (see Table 9.5). The vertical emittances were inferred from the beam sizes at the OTR using Eq. 9.1 and vertical β-function and dispersion values propagated to the OTR using the model. The values for the minimum bump amplitude are listed in Table 9.5.

XSR				**OTR**	
$\sigma_{y,meas}$ (μm)	9.8	$\sigma_{x,meas}$ (μm)	33.9	$\sigma_{y,meas}$ (μm)	25.9
β_y (m)	2.3	β_x (m)	0.5	$\beta_{x,y}$ (m)	10.6, 4.3
D_y (mm)	0.18	D_x (mm)	23.4	D_y (mm)	0.3
ϵ_y (pm·rad)	41.9	ϵ_x (nm·rad)	1.38	ϵ_y (pm·rad)	155.4

Table 9.5: Emittances in the DR and at the OTR on the 4th of March 2008, computed from the measured beam sizes and modeled β-functions and dispersions at the XSR and OTR.

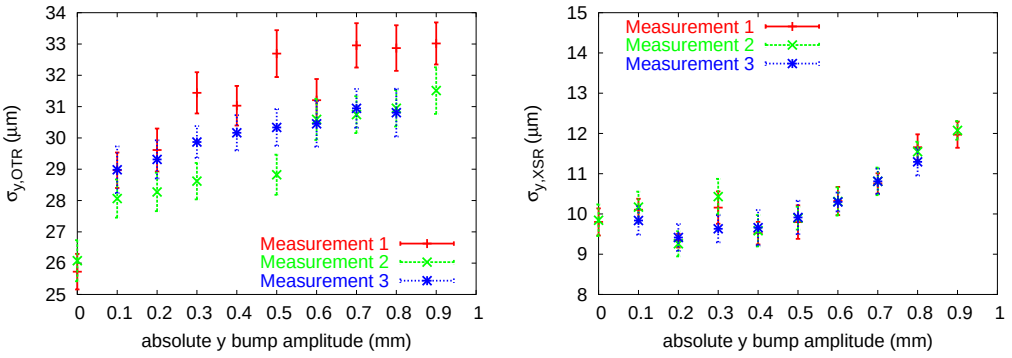

Figure 9.7: Vertical beam size at the OTR (left) and XSR (right) measured on the 4^{th} of March 2008 as a function of the vertical bump amplitude in QM7R. Three series of measurements are shown.

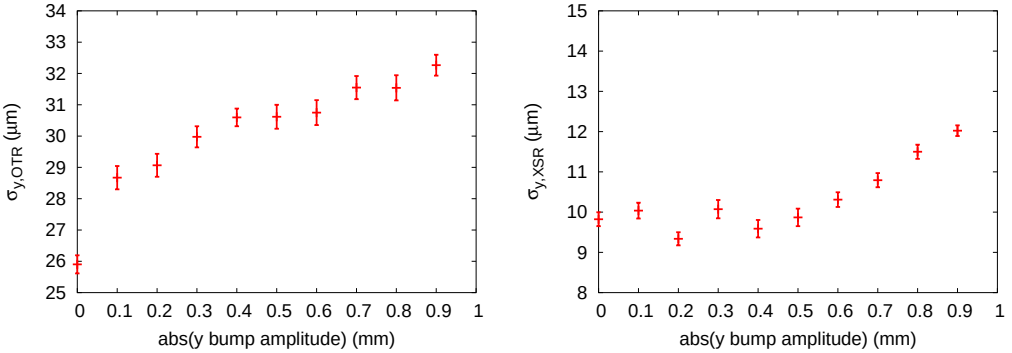

Figure 9.8: Average vertical beam size at the OTR (left) and XSR (right) measured on the 4^{th} of March 2008 as a function of the bump amplitude in QM7R.

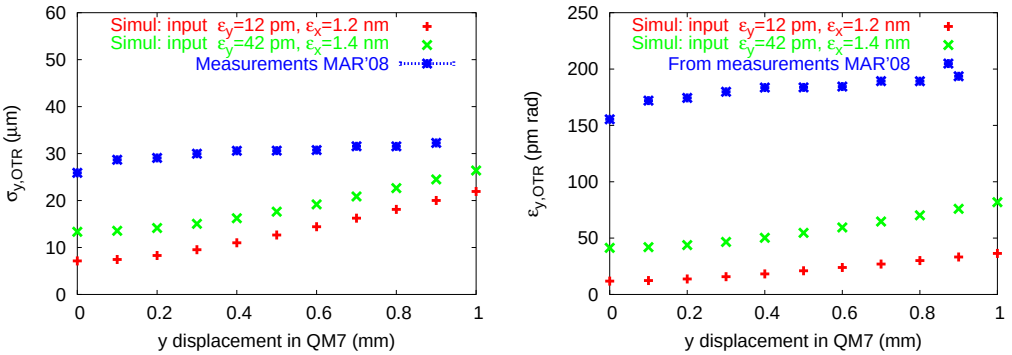

Figure 9.9: Vertical beam sizes at the OTR measured on the 4^{th} of March 2008 (left) and corresponding emittances (right) as a function of vertical displacement in QM7R. Simulation results using as input nominal and measured DR emittances are also shown.

As can be seen, measured beam sizes during the shift were two to three times bigger than can be explained with either nominal or measured input emittances in the DR. The emittances inferred at the OTR reach values as large as 155 pm·rad while in the DR it was only about 42 pm·rad (see Table 9.2). These anomalously large values could be due to an anomalous dispersion or to a coupled beam coming from the DR, though the latter is less probable, since it would also increase the dependence of the emittance with the bump amplitudes in the DR, which is not the case. It could also be due to other types of effects arising from larger offsets in the aperture of the extraction channel, as for instance, a large horizontal displacement of the beam towards the external part of the QM7R magnet, where it is more non-linear [73]. In the procedure to extract the beam during these shifts, neither the horizontal nor the vertical trajectory were controlled or reproduced at the level of a few millimeter. Moreover, the relative increase at the XSR was about as large as at the OTR. There is not enough information from the measurements to explain the observations.

9.3.3 Measurements on the 14^{th} of May 2008

During the measurements on the 14^{th} of May 2008, the beam intensity was about 0.55×10^{10} electrons per pulse but experienced some variations (see Fig. 9.10). Measurements of OTR and XSR beam sizes with vertical bumps were performed in the range of amplitudes 0-0.6 mm (see Fig. 9.11). As can be seen, the XSR beam size varied at least as much as the OTR one when applying the bump, probably due to the fact that, as in the shift on the 4^{th} of March, the bump was not perfectly closed in the DR, causing some coupling between horizontal and vertical planes through the sextupoles.

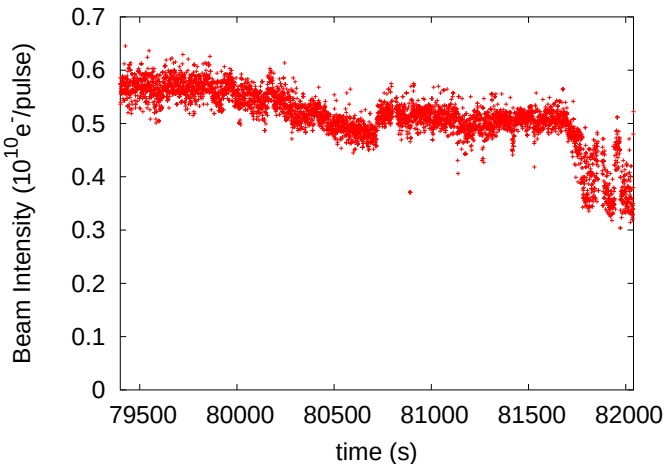

Figure 9.10: Beam intensity during data taking on the 14^{th} of May 2008.

The vertical and horizontal DR emittances computed during the shift from beam sizes measured at the XSR location are shown in Table 9.6. In addition to using the optical functions from the model as in previous shifts, explicit measurements of the β-function at the XSR location were performed by scanning DR quadrupoles and recording tune shifts. Simulation results for the OTR beam size using these DR emittances as input were obtained and are shown in Table 9.2, together with the smallest measured value, corresponding to a -0.4 mm bump. As in the shift on the 4^{th} of March, the measurement gave much larger values than the prediction and there is not enough information to determine the cause.

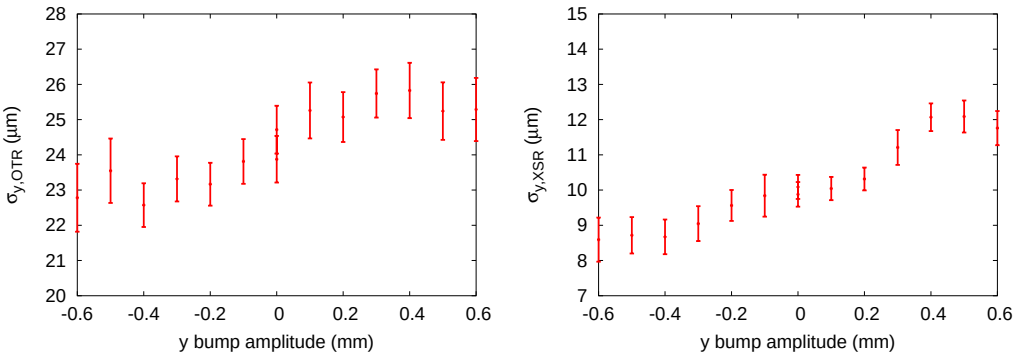

Figure 9.11: Vertical beam size at the OTR (left) and XSR (right) measured on the 14^{th} of May 2008 as a function of the absolute vertical bump amplitude in QM7R.

XSR				**OTR**	
$\sigma_{y,meas}$ (μm)	9.9	$\sigma_{x,meas}$ (μm)	41.3	$\sigma_{y,meas}$ (μm)	22.6
$\beta_{y,model}$ (m)	2.2	$\beta_{x,model}$ (m)	0.5	$\beta_{x,y}$ (m)	10.8, 3.9
$D_{y,model}$ (mm)	-0.3	$D_{x,model}$ (mm)	23.3	D_y (mm)	-3.9
$\epsilon_{y,model}$ (pm·rad)	44.6	$\epsilon_{x,model}$ (nm·rad)	2.48	ϵ_y (pm·rad)	127.1
$\beta_{y,meas}$ (m)	2.9				
$\epsilon_{y,meas}$ (pm·rad)	33.6				

Table 9.6: Emittances in the DR and at the OTR on the 14^{th} of May 2008, computed from the measured beam sizes and modeled β-functions and dispersions at the XSR and OTR. The vertical β-function measured at the XSR location during the shift and the corresponding emittance are also shown.

9.3.4 Measurements on the 22^{nd} of May 2008

During the measurements performed on the 22^{th} of May 2008, the beam intensity was not very stable (see Fig. 9.12), and the linac had to be retuned at some point to recover acceptable injection efficiency when it got below 0.2×10^{10} electrons per pulse. Measurements of OTR and XSR beam sizes with vertical bumps were performed in the range of amplitudes 0-0.8 mm (see Fig. 9.13). This time, the image of the beam at the OTR monitor was tilted (unlike the profile at the XSR monitor), and the beam was oscillating from left to right, probably due to some energy jitter.

Again, the measured OTR beam sizes were much larger than could be explained by simulating using measured DR emittances as input (see Table 9.7 and Table 9.2).

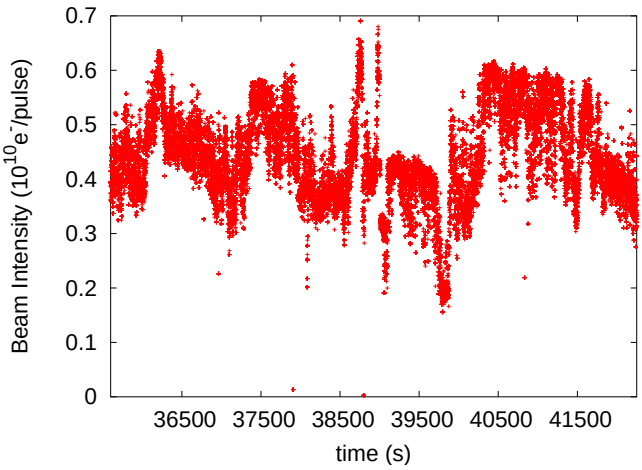

Figure 9.12: Beam intensity during data taking on the 22^{th} of May 2008.

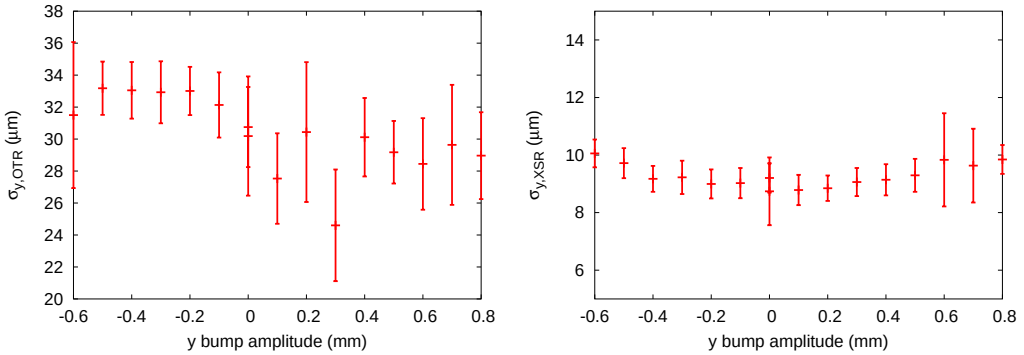

Figure 9.13: Vertical beam size at the OTR (left) and XSR (right) measured on the 22^{th} of May 2008 as a function of the vertical bump amplitude in QM7R.

XSR				**OTR**	
$\sigma_{y,meas}$ (μm)	8.7	$\sigma_{x,meas}$ (μm)	48.7	$\sigma_{y,meas}$ (μm)	30.8
$\beta_{y,model}$ (m)	2.2	$\beta_{x,model}$ (m)	0.5	$\beta_{x,y}$ (m)	10.6, 3.9
$D_{y,model}$ (mm)	4.9	$D_{x,model}$ (mm)	23.3	D_y (mm)	8.0
$\epsilon_{y,model}$ (pm·rad)	27.0	$\epsilon_{x,model}$ (nm·rad)	3.83	ϵ_y (pm·rad)	228.0
$\beta_{y,meas}$ (m)	3.3				
$\epsilon_{y,meas}$ (pm·rad)	17.8				

Table 9.7: Emittances in the DR and at the OTR on the 22^{th} of May 2008, computed from the measured beam sizes and modeled β-functions and dispersions at the XSR and OTR. The vertical β-function measured at the XSR location during the shift and the corresponding emittance are also shown.

9.3.5 Measurements on the 28th of May 2008

Measurements of OTR and XSR beam sizes with vertical bumps were repeated on the 28th of May 2008 in the range -1 to +1 mm. The beam intensity was not recorded, but it was checked for each measurement that it remained reasonably unchanged, with about 0.6×10^{10} electrons per pulse. Figure 9.14 shows the measurements at the OTR (left) and XSR (right) monitors as a function of the vertical bump amplitude.

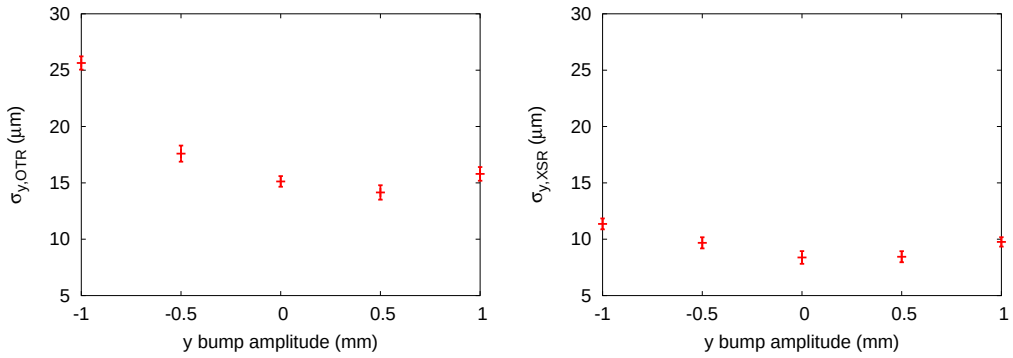

Figure 9.14: Vertical beam size at the OTR (left) and XSR (right) measured on the 28th of May 2008 as a function of the vertical bump amplitude in QM7R.

Fig. 9.15 shows the comparison of the measurements (blue line) with the simulation, including multipoles in QM7R and using DR emittances determined during the shift (see Table 9.8). Two input conditions were considered for the transverse phase space extracted from the DR, either with (green line) or without (red line) the presence of $x-y$ coupling. The skew quadrupoles in the DR were turned on during the measurements as part of the standard coupling correction procedure. Although the residual coupling in the DR results both from these skew quads and the misalignments and errors which they should correct, taking them into account in the simulation of the phase space of the extracted beam can give a representative estimate of the correlations between the horizontal and vertical coordinates. This was done to simulate the presence of x–y coupling effects. The measurement at the OTR corresponding to the minimum bump amplitude was bigger than predicted by simulating with an uncoupled input beam. Using a coupled input beam, it did get closer but still remained smaller than the measurement. In this case, the dependence on bump amplitude became rapidly stronger, indicating that the coupling effects introduced into the simulation of the input phase space may have been too large. The vertical emittance at the OTR was computed from the measured beam size and modeled vertical β-function and dispersion. Values for the minimum of the measurement, corresponding to an amplitude of 0.5 mm, are listed in Table 9.8.

For the purpose of taking into account the variations of the DR beam size during the experiment (see Fig. 9.14 right), the ratio of OTR and XSR beam sizes was studied (see Fig. 9.16 left) as for the data taken on the 19*th* of December. Fitting a second-order polynomial gives in this case:

$$f(y) = a(y-b)^2 + c = 0.19(y-0.76)^2 + 1.62 \tag{9.3}$$

where the reduced χ^2=0.70 and the minimum corresponds to a bump amplitude of y = 0.76 mm.

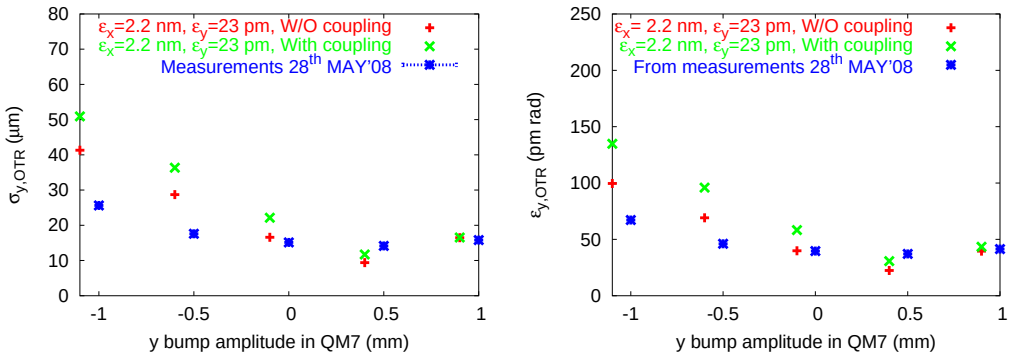

Figure 9.15: Vertical beam sizes at the OTR measured on the 28^{th} of May 2008 (left) and corresponding emittances (right) as a function of vertical displacement in QM7R. Simulation results using as input measured DR emittances, with a coupled or uncoupled input beam (see text) are also shown.

XSR				**OTR**	
$\sigma_{y,meas}$ (μm)	8.4	$\sigma_{x,meas}$ (μm)	38.6	$\sigma_{y,meas}$ (μm)	14.2
β_y (m)	2.2	β_x (m)	0.5	$\beta_{x,y}$ (m)	10.1, 3.9
D_y (mm)	5.4	D_x (mm)	23.3	D_y (mm)	7.4
ϵ_y (pm·rad)	22.5	ϵ_x (nm·rad)	2.14	ϵ_y (pm·rad)	37.1

Table 9.8: Emittances in the DR and at the OTR location during the shift of the 28^{th} of May 2008, computed from the measured beam sizes and β-functions and dispersions at the XSR and OTR obtained through an optical model of the DR and EXT line representing the settings of the magnets.

Fig. 9.16 right shows the ratio of the OTR and XSR beam sizes, normalized to the minimum value, and in comparison with simulation predictions including the multipole coefficients computed in Chapter 7 for the QM7R magnet (blue lines) and for both QM7R and BS1X (magenta lines). As for the data taken on the 19^{th} of December, two cases are displayed, corresponding to the nominal extracted horizontal orbit of 22.5 mm in QM7R (blue crosses and magenta empty boxes) and to one displaced towards the center of the quadrupole (blue cross-box and magenta full box), where it is more linear and effects can be expected to be less. For the data taken on the 28^{th} of May, since the measured emittance growth was weaker than on the 19^{th} of December, a larger horizontal displacement is needed to explain the data. As can be seen in Fig. 9.16 right, a reasonable agreement is found for a 2.7 mm offset compared to 1.5 mm on December 19, 2007.

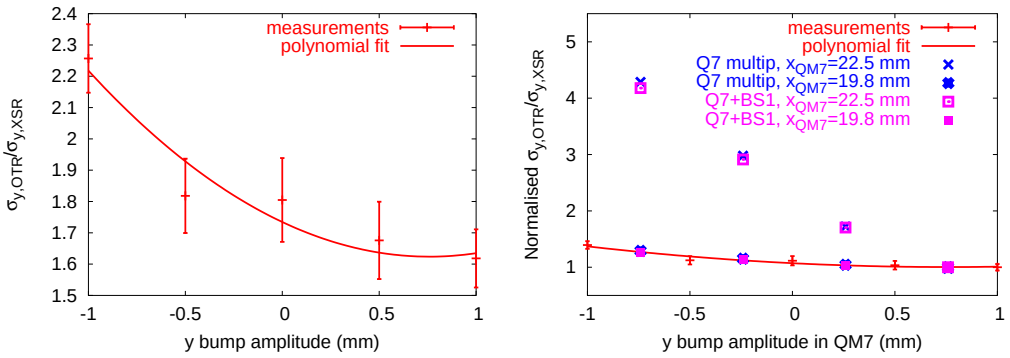

Figure 9.16: Ratio of vertical beam sizes at the OTR and XSR measured on the 28^{th} of May 2008 (left) and ratio normalized to the minimum value (right), as a function of the vertical absolute bump amplitude. In the graph on the right, tracking simulation results are also shown, including the computed non-linearities in QM7R and BS1X, for the nominal horizontal orbit in QM7R (22.5 mm) and for one closer to the center of the QM7R by 2.7 mm.

Chapter 10

Summary and Conclusions

The ILC is designed to collide e^+e^- beams at 500 GeV center-of-mass energy, with a luminosity $\mathcal{L}\sim 2\times10^{34}$ cm^{-2}s^{-1}. To obtain this high luminosity, very intense beams have to be delivered at the collision point, with tiny transverse beam spot sizes down in the nanometre range. One of the options at the ILC is to collide e^-e^- beams. The e^-e^- initial state is favored for some specific physics channels. The implementation of this option can be done without major changes in the accelerator. However, the overall ILC design and beam parameter optimization at the IP, done for the standard e^+e^- collisions, are not necessarily ideal for e^-e^- due to differences in the collision process. In the first part of this thesis, a study of these differences has been done to evaluate the feasibility of adapting the FFS to the e^-e^- mode of operation.

In the case of the e^+e^- collisions, the strong electromagnetic fields that each bunch experiences in the collision with the opposite bunch enhances the luminosity through mutual focusing. For e^-e^- collisions, on the other hand, repulsion occurs, which enhances the effective transverse sizes at the IP. This reduces peak luminosity to values of only typically about 20% of those for e^+e^- . Moreover, in e^-e^- collisions, because of the repulsive forces, the luminosity is much more sensitive to residual offsets at the IP than for e^+e^- .

At the ILC, the transverse positions of the beams must be stabilized at the IP to a fraction of the beam sizes to maintain the luminosity. The main way to stabilize the beam positions at the IP is to measure the overall transverse kicks which each bunch inflicts on the opposite bunch when colliding with a residual offset. For small offsets, there is a linear relation between the out-going angle and the offset, which is used in a feedback loop to compute the corrections needed to center the beams on subsequent bunch collisions. The out-going angles, which can reach typically $\sim$150 μrad, are obtained by measuring the beam positions a few meters downstream of the IP. A specific feature of e^-e^- collisions is that the deflection curve as a function of the IP offset is much steeper than for e^+e^- . This must be taken into account in the parameter optimization.

A study of the impact of this steeper deflection curve on the performance of the feedback system compared to e^+e^- collisions has been carried out using a simplified simulation. According to measurements of ground motion at different sites, the offsets at the beginning of an ILC bunch train can be of the order of hundreds of nanometres, while the amplitudes corresponding to the frequency between bunches are negligible in comparison to the beam sizes. A simplified simulation of the beam-based IP position feedback has been done for both e^+e^- and e^-e^- collisions, taking into account both initial offsets at the beginning of a train and uncorrelated residual bunch-to-bunch jitter. The latter cannot be

corrected by a feedback system. One should make sure it is not amplified by the feedback.

It was found that the correction for the e^-e^- collisions is slower compared to the e^+e^- case because the specified slope relating the correction of the IP offset to the measured outgoing angle must be, at least, a factor 5 greater for the e^-e^- case to avoid over-correction of small offsets. Under these assumptions, about 20 bunches are enough to correct initial e^+e^- beam-beam offsets of a hundred nanometres, while about 80 are needed in the e^-e^- case. However, given the large number of bunches within a train simulations, the loss of luminosity over a full train remains small even for e^-e^- and the results obtained are almost independent of initial offsets. Thus, the feedback for e^-e^- collisions, although slower, is still fast enough to avoid impacting the train luminosity in a major way. The steeper deflection curve for the e^-e^- collisions turns out not to be a problem from the point of view of the feedback performance.

Simulations for different bunch-to-bunch jitter amplitudes have also been done. The luminosity loss was found to be a factor 2 greater for e^-e^- compared to e^+e^- for the same assumptions. This is due to the greater sensitivity to the vertical IP offsets. The ability to decrease this sensitivity with alternative beam parameters could be important if jitter conditions are worse than expected, *e.g.*, during early ILC operation.

Beam-beam effects are characterized by the so-called disruption parameter, which is the ratio between the *r.m.s.* of the bunch length and the effective focal length. Decreasing the bunch length leads to smaller disruption between the bunches, which decreases the sensitivity to the IP offsets. Different parameter sets have been derived by decreasing the bunch length by factors in the range 0.5-0.7 and by optimizing the transverse beam sizes in order to maximize the luminosity, while limiting the maximum beamstrahlung energy loss to 5%. These alternative parameters have increased peak luminosity, up to ~40% compared with the nominal parameters for e^-e^- collisions. Some of the proposed parameters also have smaller sensitivity to IP offsets. The average train luminosity for different amplitudes of the jitter applied to each beam is improved for these sets of parameters compared to the nominal parameters.

A more complete simulation of the IP position beam-based feedback system has also been used to verify that the assumptions on ground motion amplitudes and distribution considered in the simplified simulation are acceptable. In this simulation, the elements of the BDS were misaligned through a generator based on ground motion measurements at one of the sites. The sampling frequency was set to that at which trains are delivered. In this case, transverse offsets of several hundreds of nanometres, as assumed in the simplified simulation indeed result from the misalignments of the beam line elements. It was also found that the feedback correction for the e^-e^- collisions must be slower than for e^+e^- ones in order to not amplify the small offsets, but that average feedback performance is still acceptable.

In the more complete simulation of the ground motion in the FFS, the displacements of the magnets do not only introduce offsets at the IP, but also along the entire beam line. Such offsets can degrade the IP beam sizes through focusing effects in the sextupoles used for the chromaticity correction. Because of this, the luminosity is degraded over time even if the beams are properly centered at the IP. Simulations done for successive time intervals show that as the ground motion applied increases over time, the final luminosity which can be recovered with the beam-based IP position feedback becomes smaller. After 1 s, about ~80 - 90% of the luminosity can be recovered, while after *e.g.* 5 minutes, the deterioration of the beam sizes due to these optical effects makes it impossible to recover more than ~30 or 40% of luminisity.

In addition to the position, an IP angle correction has been included in the simulation in order to correct the average positions of the beams along the FFS, and thus mitigate the beam size increase produced by passing off-axis through the sextupoles. The angle at the IP is corrected with a kicker located at the entrance of the FFS, at $n\pi$ phase-advance from the IP. The results indicate that about 20 % more of luminosity can be recovered for e^+e^- collisions by correcting the IP angle compared to the case where only the IP position correction was considered. In the case of the e^-e^- collisions with the nominal e^+e^- parameters, the big sensitivity to the vertical offsets at the IP means that there is no significant difference when correcting the angle. But it is expected that this would also benefit e^-e^- collisions when beam parameters with reduced disruption at the IP were under consideration. After several seconds of ground motion applied, the luminosity can be recovered approximately until 90%, while after several minutes it is expected that using other feedback loops to correct trajectories further upstream will also be necessary. This behaviour is rather similar for both e^+e^- and e^-e^- collisions.

Optics studies have also been done to verify the feasibility of adapting the BDS and the extraction line for the e^-e^- option with the proposed alternative beam parameters with smaller disruption parameter. The studies have been done for both, small (2 mrad) and large (20 mrad) crossing angle geometries.

To obtain the new beam parameters, new β-functions had to be obtained at the IP. Changing the demagnification factors of the FFS would achieve this but this could also spoil the careful minimization of chromatic and geometric aberrations, unless fully re-optimizing the FFS. Instead, the demagnification changes were obtained using the matching quadrupoles upstream of the chromatic correction section, and re-fitting the sextupoles. This was feasible for the proposed beam parameters, which are in the range of β-functions proposed for the ILC.

The extraction line optics and the post-IP beam power losses were also studied for the proposed e^-e^- parameters. The latter were found comparable to the results obtained for the High Luminosity beam parameters proposed for the e^+e^- mode for the case of the 20 mrad crossing angle geometry with separate injection and extraction channels. For the 2 mrad crossing angle scheme, however, performances are more difficult to assure in the e^-e^- mode, and require a more complex re-optimization of the optics. An initial attempt in this direction was studied, but resulting in about a factor 2 luminosity loss. Some possible improvements were discussed and evaluated in a preliminary way.

In the second part of this thesis, a study of the preservation of the extremelly small beam emittances achieved at the Accelerator Test Facility (ATF) along the extraction (EXT) line has been performed.

The big challenge in the construction of a linear collider in the TeV scale, together with the high beam energies that have to be reached, is to achieve the high luminosity that the experiments demand for which extremely low beam emittances have to be reached and preserved along the accelerator, and the beam has to be focused down to a few nanometers in the vertical dimension at the IP. This will require unprecedented alignment and stabilization to maintain the beams colliding at the IP within tolerances of the order of half a nanometer. To this end, ATF and ATF2, as well as several other international test facilities, have been built and planned to address key performance goals of beam delivery sub-systems.

ATF was built in 1996 at KEK (Tsukuba) to demonstrate the production and measurement of the small emittance beams needed for a future linear collider. ATF2, completed

in 2008, and presently under commissioning, has been built as a fruit of an international collaboration. It consists of a scaled-down prototype version of the final focus sections planned in the ILC and CLIC linear collider designs. The ATF DR has achieved world records for the normalized vertical emittance, with values as small as 1.5×10^{-8} m at 1.3 GeV. One of the main goals of ATF2 is the establishment of the hardware and beam handling technologies pertaining to achieving and measuring small beams of 37 nm at the final focus point in a reproducible and stable manner.

While small vertical emittances are consistently reproduced in the ATF DR, measurements of the extracted beam, performed in a dedicated diagnostics section of the EXT line, located immediately downstream, have since many years given significantly larger values than expected (about a factor of 3). This long-standing problem has motivated studies of several possible sources of this anomalous emittance growth. One of these, arising from non-linear magnetic fields in the extraction region, experienced by the beam while passing off-axis through magnets of the DR during the extraction process, was investigated and found important. A detailed evaluation of the impact of these non-linearitites on the extracted vertical emittance was carried out, both computationally and experimentally, in order to devise a suitable mitigation plan.

The beam extraction is initiated by means of a kicker. The beam then passes horizontally off-axis through the QM6R and QM7R quadrupoles, and through three septum magnets, BS1X, BS2X and BS3X, which complete the extraction.

In order to quantify the effect of the non-linear magnetic fields on the extracted beam, a detailed study of the field maps of the magnets involved in the extraction has been done with the finite element Poisson solver PRIAM, using explicit magnet geometries and parameters. The obtained field maps have been fitted by polynomial functions in the complex plane to get continuous representations in the form of local multipole expansions. The most important contribution to non-linearity comes from the QM7R magnet, for which a non-negligible sextupole component appears at the position of the extracted beam.

Tracking simulations including the known non-linear dependences of the fields in the magnets shared by the ATF DR and extraction line were performed to determine the impact on the observed vertical emittance growth. It was found that the main effect arises from the QM7R quadrupole, as expected from the non-linear field calculations. The non-linearity in this magnet would have a negligible effect if the beam were always centered vertically. It can however cause significant growth of the projected vertical emittance if there is a vertical offset. It increases by about a factor of 3 for a 1 mm vertical offset, using as input the nominal DR emittances. The magnitude of the growth also depends on the horizontal displacement, increasing or decreasing in the outer and inner parts of the magnet, where the non-linearity is respectively enhanced or reduced. The growth can be reduced by about a factor of 2 for a 2 mm offset.

To complete the analytical studies and simulations, an experimental program was carried out to study the dependence of the anomalous emittance growth on the extraction trajectory. For the modeling of the beam at different orbits in the extraction channel, local bumps in the vertical plane are generated, closed in the DR. Beam size measurements in the DR and immediately after extracting the beam were used to infer the corresponding emittances. The results from two datasets, collected in December 2007 and at the end of May 2008, show that the growth after extraction is clearly visible but is smaller than predicted from simulations for a beam at the nominal horizontal trajectory in QM7R. The measurements can be reproduced by the simulation if one assumes horizontal dis-

placements of a few millimeter (1.6 and 2.7 mm in December and May, respectively), with the extracted beam passing through a region of QM7R nearer its center, where the non-linearity is reduced.

Although the ATF orbit is usually stable at the level of about 100 μm during data taking, it could of course have offsets of several millimeters after extraction. The instrumentation available in 2007 and 2008 in the extraction line did not allow to monitor beam positions in the vicinity of QM7R and the septum magnets. Since the extraction procedure after establishing storage in the DR during initial beam setup was principally based on maximizing the transmission efficiency, it could easily result in different offsets for each data taking period. The comparison of the measurements and simulations in December 2007 and end of May 2008 do indicate that such millimeter level horizontal offsets were likely present. Measurements including also horizontal bumps would have been very interesting to ascertain this, but there was unfortunately not enough time to perform them.

The measurements from three datasets collected in March 2008 and in the first half of May 2008 gave larger emittance values, which could not be explained by non-linear effects in the magnets considered. It is difficult to conclude anything firm from the corresponding data. On the one hand, beam sizes also varied significantly within the DR, indicating that the calculated bumps were not closed and that the beam was perhaps not sufficiently well set up for this experiment. On the other hand, the size of the extracted beam was significantly larger than expected even before implementing any bump, with growth factors between 2.7 and 3, with magnitudes which cannot easily be explained by optical effects. Since in the procedure to extract the beam during these shifts, neither the horizontal nor the vertical trajectory were controlled or reproduced at the level of a few millimeter, one cannot exclude other types of effects arising from larger offsets in the aperture of the extraction channel. These large beam sizes could also be due to an anomalous dispersion in the extraction region, or to a combination of these effects.

After the measurements described in this thesis, the extraction line of ATF has been reconfigured and partly rebuilt to drive the beam to the ATF2 final focus beam line. In the new design, the magnitude of the dispersion is reduced in the initial part, and the diagnostic section has larger phase advances between wire scanners, to allow more reliable emittance reconstruction. The instrumentation to monitor the positions of the extracted beam is also being significantly improved. Moreover, to mitigate effects on the projected vertical emittance from the non-linearity in the QM7R quadrupole, this magnet was replaced by a similar one with larger aperture, for which magnetic measurements and simulations indicate that non-linear fields are negligible at the beam extraction position.

Bibliography

[1] LHC Desing Report, CERN-2004-003 (2004). See also http://www.cern.ch/lhc.

[2] ILC Reference Design Report, ILC-REPORT-2007-001, August 2007. http://www.linearcollider.org/cms/?pid=1000437.

[3] M. Battaglia *et al.*, "Physics at the CLIC-TeV Linear Collider: report of the CLIC Physics Working Group", CERN-2004-005; hep-ph/0412251 (2004).

[4] W. R. Assmann *et al.*, "A 3 TeV e^+/e^- Linear Collider based on CLIC technology", CERN-2000-008 (2000). See also http://ab-div.web.cern.ch/ab-div/Info/2006/CLIC_Web_Site/publication.htm.

[5] S. Döebert, D. Schulte and I. Syratchev, "Status report of the CTF3 Test Beam Line", CTF3 Note 076 (2006).

[6] "ATF Report". Study report JFY 1996-1999. http://atfweb.kek.jp./atf/Reports/ATF99new.pdf.

[7] K. Kubo *et al.*, "Extremely low vertical-emittance beam in the Accelerator Test Facility at KEK", Phys. Rev. Lett. 88, 194801 (2002).

[8] ATF2 Proposal, Vol. 1 & 2. ATF2 Collaboration, August 11 2005 and February 13 2006. http://lcdev.kek.jp/ATF2/proposal.

[9] J. Nelson, M. Ross, M. Woodley, "ATF Studies: Extraction line dispersion, beam stability and bunch length sensitivity, etc", ATF-00-06 Internal Report (2000).

[10] H. Hayano *et al.*, "ATF: Accelerator Test Facility Study Report JFY 1996-1999", KEK Internal Report No. 2000-6, 2000, A.

[11] S. Kuroda, "Current Dependence of the Vertical Emittance in the ATF EXT", International Linear Collider Workshop LCWS'07, June 2007.

[12] A. De Roeck *et al.*, "Physics at a $\gamma\gamma$, eγ and e^-e^- Option for a Linear Collider", 2003, hep-ph/0311138.

[13] C. Heusch, "Electron-electron Collisions at the International Linear Collider", International Journal of Modern Physics A Vol. 18, No. 16 (2003) 2733-2737.

[14] J. A. Aguilar-Saavedra, "Slepton cascade decays at ILC", talk presented at the *Workshop on the Future Linear Collider*, Gandia (2005).

[15] E. P. Wigner, "On the Behavior of Cross Sections Near Thresholds", Phys. Rev. Vol. 73, No. 9 (1948) 1002-1009.

[16] J. Feng and M. Peskin, "Selectron Studies at e^-e^- and e^+e^- Colliders", 2001, SLAC-PUB-8829, hep-ph/0105100.

[17] See, for instance, the ICFA Statement on Linear Colliders (1999), http://www.fnal.gov/directorate/icfa/icfa_LCstatement.html.

[18] TESLA Technical Design Report (2001). http://tesla.desy.de/new_pages/TDR_CD/start.html.

[19] "Zeroth-Order Design Report for the NLC", SLAC Report 474 (1996). http://www-project.slac.stanford.edu/lc/ZDR/Zeroth.html.

[20] P. Tenenbaum, "The JLC/NLC Baseline Design", *Proceedings of PAC03*, p. 681-683 (2003).

[21] H. Weise *et al.*, "The TTF/VUV-FEL (FLASH) as the Prototype for the European XFEL Project", *Proceedings of LINAC'06*, p. 486-490 (2006).

[22] The European X-Ray Free-Electron Laser Technical Design Report, DESY-2006-097 (2006).

[23] G. A. Blair, "Test Beams for ILC Final Focus", EUROTeV-Report-2006-007 (2006).

[24] V. Balakin *et al.*, "Focusing of Submicron Beams for TeV-Scale e^+e^- Linear Colliders", Phys. Rev. Lett. 74, 2479 (1995).

[25] D. L. Burke *et al.*, "Results from the Final Focus Test Beam", SLAC-PUB-6609 (1994).

[26] P. Raimondi and A. Seryi, "A Novel Final Focus Design for Future Linear Colliders", Phys. Rev. Lett. 86, 3779-3782 (2001).

[27] T. Raubenheimer *et al.*, "Suggested ILC Beam Parameter Range", 1^{st} ILC Workshop. http://www-project.slac.stanford.edu/ilc/acceldev/beamparameters.html.

[28] K. Moffeit *et al.*, "Comparison of 2 *mrad* and 14/20 *mrad* Crossing Angle Extraction Lines", SLAC-PUB-11956 (2006).

[29] G. Burt *et al.*, "Discussion of Possible ILC Crab Cavity Parameters", ASTeC-RF-LC-05-01 *document* (2005).

[30] J. Payet, O. Napoly *et al.*, "Design of an Interaction Region with Head-On Collsions for the ILC", EURO-TeV-Report-2006-083 (2006).

[31] J. Carter *et al.*, "Simulation of the ILC Collimation System using BDSIM, MARS15 and STRUCT", EUROTeV-Report-2006-048.

[32] N. Walker, "Beam Delivery System for Pedestrians", published in ICFA Nanobeam 2002 Workshop 25-29, Lausanne (2002).

[33] F. Jackson, "Estimation of Collimation Depths for 20 and 2 mrad ILC BDS Lattices.", EUROTeV-Report-2006-017.

[34] F. Zimmermann, "Octupoles in Front of the Final Doublet", NLC Accelerator Physics Note, July 14 (1998).

[35] R. Brinkmann, P. Raimondi and A. Seryi, "Halo reduction by means of nonlinear optical elements in the NLC final focus system", SLAC-PUB-8896, PAC01 (2001).

[36] S. Guiducci, "Chromaticity", *Lecture on the CAS CERN Accelerator School*, CERN-91-04.

[37] N. Walker, "Physics and Technology of Linear Collider Facilities", Lecture 1, *Introduction and Overview*, Santa Barbara (2003).

[38] K. Brown, "Basic Optics for the SLC Final Focus", SLAC-PUB-4811 (1988).

[39] K. Yokoya and P. Chen, "Beam-Beam Phenomena in Linear Colliders", Lecture at 1990 US-CERN School on Particle Accelerators, Hilton Head Island, So. Carolina, USA (1990).

[40] N. Walker, "Physics and Technology of Linear Collider Facilities", Lecture on *Beam-beam effects*, Santa Barbara (2003).

[41] P. Bambade *et al.*, "Observation of beam-beam deflections at the interaction point of the SLAC Linear Collider", Phys. Rev. Lett. 62, 2949-2952 (1989).

[42] P. Chen and K. Yokoya, "Disruption effects from the interaction of round e^+e^- beams", Phys. Rev. D38 (1989) 987.

[43] P. Chen, "Disruption Effects from the Collision of Quasi-Flat Beams", *Proceeding of PAC'93*, p. 617 (1993).

[44] L. Z. Rivkin, "Beamstrahlung and Disruption", *prepared for CERN Accelerator School: Course on Advanced Accelerator Physics (CAS)*, Rhodes, Greece (1993).

[45] K. Oide, "Synchrotron-Radiation Limit on the Focusing of Electron Beams", Phys. Rev. Lett. 61 (1988) 1713.

[46] J. Irwin, in "Zeroth-Order Design Report for the NLC", SLAC Report 474 (1996), p. 722.

[47] A. Seryi, "Physics and Technology of Linear Collider Facilities", Lecture on *Final Focus System and Beam Collimation in Linear Collider*, Santa Barbara (2003).

[48] D. Schulte, Ph.D. thesis, University of Hamburg 1996, TESLA-97-08. `http://flc.web.lal.in2p3.fr/mdi/BBSIM/bbsim.html`.

[49] C. Rimbault, P. Bambade, K. Mönig, and D. Schulte, "Incoherent pair generation in a beam-beam interaction simulation", Phys. Rev. ST Accel. Beams 9, 034402 (2006).

[50] H. Wiedemann, "Particle Accelerator Physics", Vol. I and II, 2nd Edition, Springer-Verlag, Berlin (1999).

[51] D. Schulte, A. Latina, N. Leros, P. Eliasson and E. D'Amico. The Tracking Code PLACET, `https://savannah.cern.ch/projects/placet`.

[52] A. Seryi, "Ground motion and vibration issues for accelerators", SLAC-PUB-8893, *Invited talk at IEEE Particle Accelerator Conference (PAC 2001)*, Chicago, Illinois (2001).

[53] G. White, N. Walker, D. Schulte, "An Example of Integrated Simulations- A LINAC to IP Simulation of the TDR TESLA Accelerator", CARE/ELAN Document-2004-013.

[54] A. Seryi, T. Raubenheimer, "Ground Motion Model of the SLAC Site", SLAC-PUB-8595, (2000).

[55] A. Seryi, "Stability and Ground Motion Challenges in Linear Colliders", Proceedings of the ICFA Nanobeam 2002 Workshop.

[56] P. Burrows, "Intra-train Beam-based Feedback Systems", *talk in the Linear Collider Workshop LCWS2004*, Paris (2004).

[57] H. Grote and F.C. Iselin, "The MAD program (Methodical Accelerator Design) version 8.16, User's reference manual", CERN/SL/90-13(AP), (rev. 4), (March 27, 1995). `http://hansg.web.cern.ch/hansg/mad/mad8`.

[58] M. Woodley, ILC MAD decks repository. `http://www.slac.stanford.edu/ mdw/ILC/`.

[59] M.G. Minty, F. Zimmermann, "Measurement and Control of Charged Particle Beams", Springer (2003).

[60] G. Blair, BDSIM code based on GEANT4. `http://flc.pp.rhul.ac.uk/bdsim.html`.

[61] A. Seryi, "Running 2mrad IR in the e-e- mode: BDS constraints", presented at Snowmass, August 2005.

[62] Y. Honda *et al.*, "Achievement of Ultralow Emittance Beam in the Accelerator Test Facility Damping Ring", Phys. Rev. Lett. 92, 054802 (2004).

[63] P. Forck, "Lecture Notes on Beam Instrumentation and Diagnostics", Joint Universities Accelerator School (2007).

[64] Y. Honda, "Beam Instrumentation Experience at ATF", *Proceedings of APAC'07*, p. 306 (2007).

[65] T. Naito *et al.*, "Emittance Measurement at KEK-ATF Damping Ring", *Proceedings of PAC'99*, p. 2143 (1999).

[66] M. Serio, "Tune Measurements", *Lecture on the CAS CERN Accelerator School*, CERN-91-04.

[67] E. Gianfelice, "Measurement of β-functions at the ATF DR", ATF-97-17 (1997).

[68] T. Imai, H. Hayano, J. Urakawa and N. Terunuma, "Highly Stable Beam Extraction by Double Kicker System", KEK Preprint 2002-16 (2002).

[69] H. Hayano, "Wire Scanners for Small Emittance Beam Measurements in ATF", *Proceedings of LINAC 2000*, p. 146.

[70] C. Rimbault *et al.*, "4D Emittance Measurements using Multiple Wire and Waist Scan Methods in the ATF Extraction Line", *Proceedings of EPAC'08*, p. 1257, LAL-RT 08/17, ATF-08-06 internal report (2008).

[71] G. le Meur, F. Touze, "PRIAM/ANTIGONE a 2D/3D Package for Accelerator Design", *Proceedings of PAC94*, p. 1321 (1994).

[72] M. Alabau Pons, A. Faus-Golfe, P. Bambade, G. Le Meur, F. Touze, "Modeling of the Shared Magnets of the ATF Extraction Line". CARE/ELAN Document-2008-013, ATF-08-13 Internal Report (2008).

[73] M. Alabau Pons *et al.*, "Simulation Studies on the Vertical Emittance Growth in the ATF Extraction Line". CARE/ELAN Document-2008-014, ATF-08-14 Internal Report (2008).

[74] M. Alabau Pons *et al.*, "Experimental Studies and Analysis of the Vertical Emittance Growth in the ATF Extraction Line in 2007-2008". CARE/ELAN Document-2008-015, ATF-08-15 Internal Report (2008).

[75] K. Wille, "The Physics of Particle Accelerators, an Introduction", Oxford University Press.

[76] E. Wilson, "Transverse Beam Dynamics", *Lecture on the CAS CERN Accelerator School*, CERN-94-01.

[77] V. L. Ginzburg and I. M. Frank, "Radiation from a Uniformly Moving Electron Passing from One Medium to Another", JETP 16, 15 (1946).

[78] G. M. Garibyan, "Contribution to the Theory of Transition Radiation", JETP 33, 1403 (1957), Soviet Phys. JETP 6, 1079 (1958).

[79] J. Bosser *et al.*, "Optical Transition Radiation Proton Beam Profile Monitor", Nuclear Instruments and Methods in Physics Research A238, (1985), 45-52.

[80] L. Wartski *et al.*, "Interference phenomenon in optical transition radiation and its application to particle beam diagnostics and multiple scattering measurements", PACS numbers: 29.25 (1975).

[81] F. G. Bass and V. M. Yakovenko, "Theory of Radiation from a Charge passing through an Electrically Inhomogeneous Medium", Sov. Phys. Usp. 8 420 (1965).

[82] M. Ross *et al.*, "A very High Resolution Optical Transition Radiation Beam Profile Monitor", SLAC-PUB-9280 (2002).

[83] F. Zhou, J. Amann, S. Selestky, C. Spencer and M. Woodley, "Simulation studies on the Vertical Emittance Growth in the Existing ATF Extraction BeamLine", SLAC-PUB-12892 December 2007.

[84] "CERN MINUIT Package", `http://www.cern.ch/minuit`.

[85] D. Douglas, "Effect of Misaligning Driver Trim Quads and Sextupoles", JLAB-TN-98-042 (1998).

[86] A. Wolski, “A Coupling Correction Scheme for the NLC Main Damping Rings”, LCC-0064 CBP, Tech Note-232 (2001).

[87] J. Rossbach and P. Schmüser, “Basic Course on Accelerator Optics”, *Lecture on the CAS CERN Accelerator School*, CERN-94-01.

[88] F. Zhou, J. W. Amann, S. Seletsky, A. Seryi, C. Spencer and M. Woodley, “Simulation Studies on the Vertical Emittance Growth at the Existing ATF Extraction Beamline”, Proceedings of EPAC’08, p. 652, SLAC-PUB-13279 (2008).

Appendix A

Beam emittance

Liouville's theorem states that under the influence of conservative forces the density of the particles in the phase space stays constant. This theorem provides a powerful tool to describe a beam in phase space. Knowledge of the area occupied by particles in phase space at a certain location of a beam transport line allows to determine the location and distribution of the beam at any other place along the transport line without having to calculate the trajectory of every individual particle [50].

Particle beams are conveniently described in phase space by enclosing their distribution with elipses. Let's consider a distribution of particles at a given location of the beam transport line. The volume occupied in phase space by the distribution (see Fig. A.1) is defined as the beam emittance, ϵ, and can be described as an ellipse called the phase ellipse, whose equation is given by

$$\gamma_x x^2 + 2\alpha_x x x' + \beta_x x'^2 = \epsilon_x, \tag{A.1}$$

in the xx'-plane, (and analogously in the yy'-plane), and where α_x, β_x and γ_x are the ellipse parameters, which depends on the longitudinal coordinate s, and are called Courant-Snyder invariants, Twiss parameters or optical functions [59].

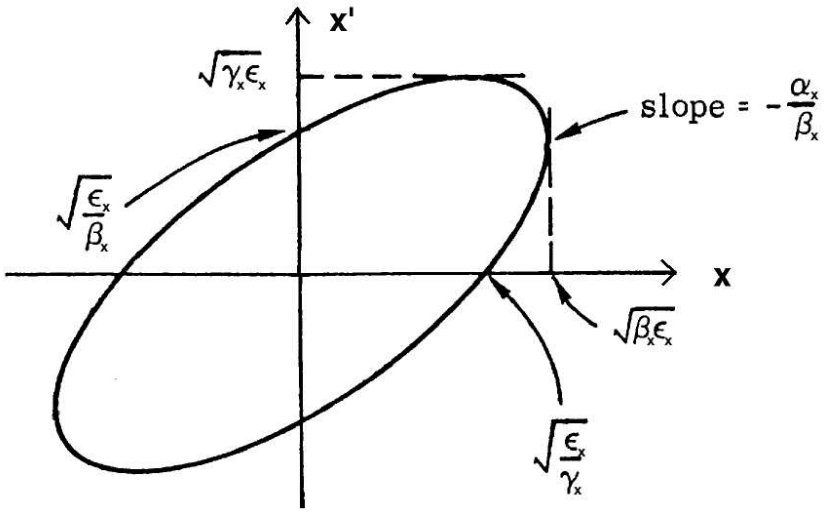

Figure A.1: Phase space ellipse in the xx'-plane [59].

The beam matrix σ in the horizontal plane, assuming that there is not $x-y$ coupling, is defined as

$$\begin{aligned}\sigma &= \epsilon_x \begin{pmatrix} \beta_x & -\alpha_x \\ -\alpha_x & \gamma_x \end{pmatrix} \\ &= \begin{pmatrix} < x^2 > - < x >^2 & < xx' > - < x >< x' > \\ < xx' > - < x >< x' > & < x'^2 > - < x' >^2 \end{pmatrix},\end{aligned} \tag{A.2}$$

where the bracketed terms are various moments of the beam distribution. $< x >$ is the first moment, or mean, of the distribution in position, $< x' >$ is the first moment, or mean, of the distribution in angle, and $< x^2 >$ and $< x'^2 >$ are the second moments of the beam distribution. Specifically, for a beam intensity distribution $f(x)$,

$$< x >= \frac{\int_0^\infty x f(x) dx}{\int_0^\infty f(x) dx}, \tag{A.3}$$

and

$$< x^2 >= \frac{\int_0^\infty x^2 f(x) dx}{\int_0^\infty f(x) dx}. \tag{A.4}$$

The rms of the distribution gives the beam size σ_x:

$$\sigma_x = \sqrt{< x^2 > - < x >^2}. \tag{A.5}$$

If the mean of the distribution in position and angle is neglected, *i.e.*, the static position offset and angle of the core of the beam are disregarded, or the coordinates defined with respect to these quantities, Eq. A.2 is reduced to

$$\sigma = \begin{pmatrix} < x^2 > & < xx' > \\ < xx' > & < x'^2 > \end{pmatrix}, \tag{A.6}$$

and the rms of the distribution is simplified to $\sigma_x =< x^2 >^{\frac{1}{2}}$.

The three Twiss parameters β_x, α_x and γ_x are proportional to the three second moments of the beam distribution, with the beam emittance as constant of proportionality:

$$\begin{aligned} < x^2 > &= \beta_x \epsilon_x \\ < xx' > &= -\alpha_x \epsilon_x \\ < x'^2 > &= \gamma_x \epsilon_x \end{aligned}, \tag{A.7}$$

and thus, the actual values of β_x, α_x and γ_x can be deduced from the beam distribution, since the beam emittance or two-dimensional volume occupied in the phase space can also be deduced from the distribution from:

$$\epsilon_x = \sqrt{\det(\sigma)} = \sqrt{< x^2 >< x'^2 > - < xx' >^2}. \tag{A.8}$$

Appendix B

Local Orbit Bumps

It is often necessary to deliberately distort the transverse beam position within a certain region, without affecting the orbit of the rest of the machine. This is done by means of the so called orbit bumps [75, 76]. The beam displacement is always performed using small dipole magnets, known as steering or correcting coils, that are distributed along the accelerator.

In the simplest case, an orbit bump can be created with only two steering or correcting coils spaced by π in betatron phase and centered about the place where the bump is required. This case is illustrated in Fig. B.1. The beam lies initially exactly along the axis, traveling from the left through the correcting coil H1 placed at the position s_1, and is deflected by an angle θ_1. It starts then to perform oscillations about the beam axis, and after an advance in betatron phase of $\phi = \pi$ it crosses the orbit again at an angle x_2' at the point s_2. At this point, the second steering coil is placed, and deflects the beam trajectory by an angle $\theta_2 = -x_2'$, bringing it back into the nominal orbit.

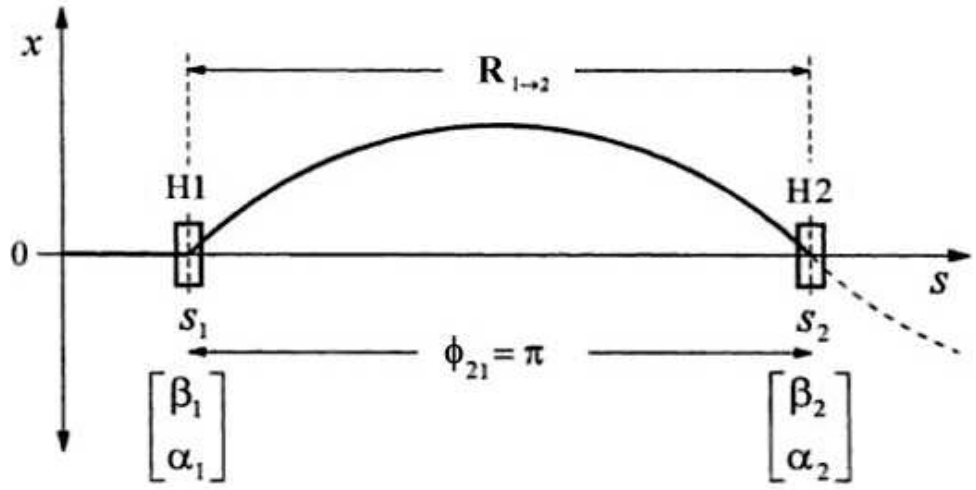

Figure B.1: The simplest case of an isolated orbit bump. Two correcting coils H1 and H2 spaced by π in betatron phase are used [75].

The trajectory vector at the point s_2 has the form

$$\begin{pmatrix} x_2 \\ x_2' \end{pmatrix} = \mathbf{R}_{1\to 2} \begin{pmatrix} x_1 \\ x_1' \end{pmatrix} = \begin{pmatrix} R_{11} & R_{12} \\ R_{21} & R_{22} \end{pmatrix} \begin{pmatrix} x_1 \\ x_1' \end{pmatrix}, \tag{B.1}$$

where $\mathbf{R}_{1\to 2}$ is the transfer matrix that gives the evolution from the position s_1 to the position s_2.

The transfer matrix $\mathbf{R}_{i\to f}$ from an arbitrary initial point i to a final point f, is given by

$$\mathbf{R}_{i\to f} = \begin{pmatrix} \sqrt{\frac{\beta_f}{\beta_i}}(\cos\phi_{fi} + \alpha_i \sin\phi_{fi}) & \sqrt{\beta_f\beta_i}\sin\phi_{fi} \\ -\frac{1+\alpha_f\alpha_i}{\sqrt{\beta_f\beta_i}}\sin\phi_{fi} + \frac{\alpha_i-\alpha_f}{\sqrt{\beta_f\beta_i}}\cos\phi_{fi} & \sqrt{\frac{\beta_i}{\beta_f}}(\cos\phi_{fi} - \alpha_f\sin\phi_{fi}) \end{pmatrix}. \tag{B.2}$$

where $\phi_{fi} = (\phi_f - \phi_i)$ is the betatron phase advance between the two locations.

In the case under consideration, in which the phase difference of the betatron oscillation between the initial and final positions is exactly π, the transfer matrix is simplified, and the trajectory vector at the s_2 position is given by

$$\begin{pmatrix} x_2 \\ x_2' \end{pmatrix} = \begin{pmatrix} -\sqrt{\frac{\beta_2}{\beta_1}} & 0 \\ -\frac{\alpha_1-\alpha_2}{\sqrt{\beta_1\beta_2}} & -\sqrt{\frac{\beta_1}{\beta_2}} \end{pmatrix} \cdot \begin{pmatrix} 0 \\ \theta_1 \end{pmatrix} = \begin{pmatrix} 0 \\ -\sqrt{\frac{\beta_1}{\beta_2}}\theta_1 \end{pmatrix}. \tag{B.3}$$

In order to close the bump at s_2, compensating for the angle of the trajectory, the corrector H2 must provide an angle θ_2

$$\theta_2 = -x_2' = -\sqrt{\frac{\beta_1}{\beta_2}}\theta_1. \tag{B.4}$$

The distortion produced at an arbitrary location s in between the correctors, is given by

$$y(s) = \theta_1\sqrt{\beta(s)\beta_1}\sin(\phi(s) - \phi_1). \tag{B.5}$$

If the location s_b where the bump is required, is in between the two correctors, at a betatron phase advance of $\pi/2$ with respect to the first corrector, Eq. B.5 is simplified, and the horizontal bump amplitude at this location is given by

$$y_b = \theta_1\sqrt{\beta_b\beta_1}. \tag{B.6}$$

In practice, generally it is not possible to fix the betatron phase difference between the steering coils at a value of π, and thus a third steering magnet is needed to create closed orbit bumps. The basic principle of the orbit bump with three correctors is illustrated in Fig. B.2.

In this case, the first corrector magnet, H1, deflects the beam by an amount θ_1. The trajectory vector at the point s_3 is given by

$$\begin{pmatrix} x_3 \\ x_3' \end{pmatrix} = \mathbf{R}_{1\to 3} \cdot \begin{pmatrix} 0 \\ \theta_1 \end{pmatrix}, \tag{B.7}$$

where $\mathbf{R}_{1\to 3}$ is the transfer matrix that gives the evolution from s_1 to s_3. The positions of the corrector magnets may in principle be freely chosen, and thus the resulting trajectory at s_3 in general has both a separation x_2 and an angle x_3' with respect to the ideal orbit. The second corrector magnet, H2, is thus used to induce a further shift in the trajectory, which on its own would give a trajectory vector at the point s_3 of

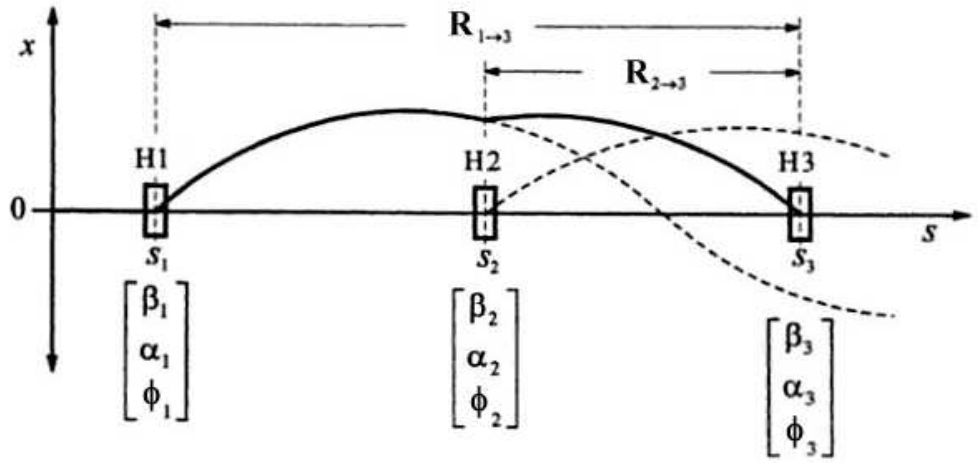

Figure B.2: Scheme of an orbit bump formed with three correcting coils. In this case matching is always possible, regardless of the phase between the individual coils [75].

$$\begin{pmatrix} x_3 \\ x_3' \end{pmatrix} = \mathbf{R}_{2\to3} \cdot \begin{pmatrix} 0 \\ \theta_2 \end{pmatrix}, \tag{B.8}$$

where here $\mathbf{R}_{2\to3}$ is the transfer matrix that gives the evolution from s_2 to s_3.

The corrections to the trajectory of these two corrector magnets are arranged so that at s_3 the separation goes to zero again, and the remaining angle is compensated by the bending angle θ_3 of the third corrector magnet H3.

At the point s_3 the trajectory thus has the vector

$$\begin{aligned} \begin{pmatrix} x_3 \\ x_3' \end{pmatrix} &= \mathbf{R}_{1\to3} \cdot \begin{pmatrix} 0 \\ \theta_1 \end{pmatrix} + \mathbf{R}_{2\to3} \cdot \begin{pmatrix} 0 \\ \theta_2 \end{pmatrix} \\ &= \begin{pmatrix} a_{11} & a_{12} \\ a_{21} & a_{22} \end{pmatrix} \cdot \begin{pmatrix} 0 \\ \theta_1 \end{pmatrix} + \begin{pmatrix} b_{11} & b_{12} \\ b_{21} & b_{22} \end{pmatrix} \cdot \begin{pmatrix} 0 \\ \theta_2 \end{pmatrix} \\ &= \begin{pmatrix} a_{12}\theta_1 + b_{12}\theta_2 \\ a_{22}\theta_1 + b_{22}\theta_2 \end{pmatrix}. \end{aligned} \tag{B.9}$$

Taking into account that the condition

$$\begin{pmatrix} x_3 \\ x_3' \end{pmatrix} = \begin{pmatrix} 0 \\ -\theta_3 \end{pmatrix} \tag{B.10}$$

must be accomplished in order to drive the orbit back to the nominal one, the strengths of the correctors are determined by the following equations

$$\begin{aligned} a_{12}\theta_1 + b_{12}\theta_2 &= 0 \\ a_{22}\theta_1 + b_{22}\theta_2 &= -\theta_3. \end{aligned} \tag{B.11}$$

For a given value of θ_1, the strengths of the other two correctors may be calculated. The elements a_{ij} and b_{ij} in Eq. B.11 are obtained from the optical functions at the positions s_1, s_2 and s_3, from Eq. B.2:

$$\theta_2 = -\frac{a_{21}}{b_{21}}\theta_1 = -\sqrt{\frac{\beta_1}{\beta_2}}\frac{\sin\phi_{31}}{\sin\phi_{32}}\theta_1 \tag{B.12}$$

and

$$\begin{aligned}\theta_3 &= -a_{22}\theta_1 - b_{22}\theta_2 \\ &= \theta_1\sqrt{\tfrac{\beta_1}{\beta_3}}\left\{\tfrac{\sin\phi_{31}}{\tan\phi_{32}} - \cos\phi_{31}\right\}.\end{aligned} \tag{B.13}$$

It is worth noting that by means of local bumps generated with three steering coils, the displacement or the angle at a certain location can be controlled. The most universal form of orbit bump consists of four steering coils, which allow simultaneously control of both the displacement and the angle at a certain location.

Appendix C

Transition Radiation

The transition radiation (TR) effect was predicted by I. Frank and W. Ginsburg in 1945 and demonstrated in 1959 by P. Goldsmith and J. V. Jelley. TR is emitted whenever a uniformly moving charged particle crosses the boundary between two media with different dielectric constants. More generally, the effect takes place in the presence of inhomogeneities in a medium. This effect can be understood by considering the electromagnetic fields that a moving charged particle carries with it, which depend on the dielectric constant ϵ of the medium. When the particle crosses the boundary between two different media, the fields must reorganize themselves. During this process of reoganization, some of the fields are thrown out in form of TR.

If a single particle of charge e crosses an interface (from the medium to the vacuum) at normal incidence the intensity of the transition radiation emitted into the vacuum (forward emission), in a frequency range $d\omega$ and a solid angle $d\Omega$, is given by the following formula [80, 81]:

$$\frac{d^2W}{d\Omega d\omega} = \frac{e^2\beta^2}{\pi^2 c}\cdot\frac{\sin^2\theta\cos^2\theta}{(1-\beta^2\cos^2\theta)^2}\cdot\left|\frac{(\epsilon-1)[1-\beta^2-\beta(\epsilon-\sin^2\theta)^2]}{[\epsilon\cos\theta+(\epsilon-\sin^2\theta)^{1/2}][1-\beta(\epsilon-\sin^2\theta)^{1/2}]}\right|^2, \quad \text{(C.1)}$$

where ϵ is the complex dielectric constant of the medium, θ the angle of emission with respect to the direction of the charge velocity v, and β the particle velocity expressed in units of c.

For extreme relativistic particles ($\beta \approx 1$), and in the case where $|\epsilon| > 1$, the third term in Eq. C.1 tends to unity and the radiation exhibits a high directivity ($\theta \ll \frac{1}{2}\pi$). The intensity in this case is given by

$$\frac{d^2W}{d\Omega d\omega} = \frac{e^2}{4\pi^2 c}\cdot\frac{\sin^2\theta}{(1-\beta\cos\theta)^2}. \quad \text{(C.2)}$$

This formula is identical with that obtained in the study of the well-known "internal bremstrahlung" occurring in a β-decay process. The radiation is then of the dipole type and is consequently linearly polarized, the electric vector lying in the plane containing the normal to the interface and the direction of emission. The intensity maximum occurs in a direction making an angle $\theta = \gamma^{-1}$ with respect to the normal to the interface, being γ the Lorentz factor.

Considering the small angle approximation, and $\beta \approx 1 - 1/(2\gamma^2)$, the intensity of the transition radiation emitted takes the form

$$\frac{d^2W}{d\Omega d\omega} = \frac{e^2}{\pi^2 c} \cdot \frac{\theta^2}{[\theta^2 + \gamma^{-2}]^2}. \tag{C.3}$$

When the particle goes from vacuum to the medium, the intensity of the transition radiation emitted into the vacuum (backward emission) is easily obtained by changing β to $-\beta$ in Eq. C.1. For relativistic particles, and in the case where $|\epsilon| > 1$, the third term in Eq. C.1 takes the form of a Fresnel reflection term, and the intensity in this case is given by

$$\frac{d^2W}{d\Omega d\omega} = \frac{e^2}{4\pi^2 c} \cdot \frac{\sin^2\theta}{(1-\beta\cos\theta)^2} \cdot \left|\frac{\epsilon^{1/2}-1}{\epsilon^{1/2}+1}\right|^2 \approx \frac{e^2}{\pi^2 c} \cdot \frac{\theta^2}{[\theta^2+\gamma^{-2}]^2} \cdot \left|\frac{\epsilon^{1/2}-1}{\epsilon^{1/2}+1}\right|^2, \tag{C.4}$$

where θ is now the angle of emission with respect to the direction of $-v$.

For optical frequencies in metals, for which $|\epsilon| \gg 1$, the reflection term in Eq. C.4 tends to unity, and the intensities of forward and backward emission (into the vacuum) are of the same order of magnitude.